

Exploring QCD matter in extreme conditions with Machine Learning

Kai Zhou^{a,*}, Lingxiao Wang^{a,*}, Long-Gang Pang^{b,*}, Shuzhe Shi^{c,*}

^a*Frankfurt Institute for Advanced Studies (FIAS), D-60438 Frankfurt am Main, Germany.*

^b*Institute of Particle Physics and Key Laboratory of Quark and Lepton Physics (MOE), Central China Normal University, Wuhan, 430079, China.*

^c*Center for Nuclear Physics, Department of Physics and Astronomy, Stony Brook University, Stony Brook, NY 11794-3800, USA.*

Abstract

In recent years, machine learning has emerged as a powerful computational tool and novel problem-solving perspective for physics, offering new avenues for studying strongly interacting QCD matter properties under extreme conditions. This review article aims to provide an overview of the current state of this intersection of fields, focusing on the application of machine learning to theoretical studies in high energy nuclear physics. It covers diverse aspects, including heavy ion collisions, lattice field theory, and neutron stars, and discuss how machine learning can be used to explore and facilitate the physics goals of understanding QCD matter. The review also provides a commonality overview from a methodology perspective, from data-driven perspective to physics-driven perspective. We conclude by discussing the challenges and future prospects of machine learning applications in high energy nuclear physics, also underscoring the importance of incorporating physics priors into the purely data-driven learning toolbox. This review highlights the critical role of machine learning as a valuable computational paradigm for advancing physics exploration in high energy nuclear physics.

Keywords: machine learning, heavy ion collisions, lattice QCD, neutron star, inverse problem

*Corresponding authors

Email addresses: zhou@fias.uni-frankfurt.de (Kai Zhou), lwang@fias.uni-frankfurt.de (Lingxiao Wang), lgpang@ccnu.edu.cn (Long-Gang Pang), shuzhe.shi@stonybrook.edu (Shuzhe Shi)

Contents

1	Introduction	3
1.1	Background	4
1.2	Machine Learning in a Nutshell	6
1.2.1	Bayesian Inference	6
1.2.2	Deep Learning	8
1.2.3	Generative Models	11
1.2.4	Physics-motivated New Developments	15
1.3	Outline	16
2	Heavy-Ion Collisions	17
2.1	Overview and Challenges for HICs	17
2.1.1	“Standard Model” of Simulating HICs	17
2.1.2	HIC Challenges	21
2.2	Initial States and Collision Geometry	22
2.2.1	Impact Parameter Determination	22
2.2.2	Unsupervised Centrality Outlier Detection	24
2.2.3	Nuclear Structure Inference	25
2.3	QCD Phase Diagram	26
2.3.1	Bayesian Analysis of QCD EoS at $\mu_B = 0$	26
2.3.2	Identify QCD Phase Transitions using CNN	27
2.3.3	Learning Stochastic Process with QCD Phase Transition	30
2.3.4	Point Cloud Network for Spinodal Clumping Identification	31
2.3.5	Dynamical Edge Convolution Network for Critical Similarity	32
2.3.6	Active Learning for Unstable Regions in QCD EoS	34
2.4	Dynamical Properties of QCD Matter	35
2.4.1	Shear and Bulk Viscosity	35
2.4.2	Jet Energy Loss in Hot QGP	38
2.4.3	Jet Classification and Jet Tomography	39
2.4.4	Chiral Magnetic Effect Detection	41
2.4.5	Anisotropic Flow Analysis	43
2.5	Fast Simulations for HICs	44
2.5.1	Efficient Emulator with Transfer Learning	44
2.5.2	Accelerating Hydrodynamic Simulations	45
2.6	Summary	46
3	Lattice QCD	47
3.1	Overview and Challenges in Lattice Field Theory	47
3.2	Field Configuration Generation	48
3.2.1	GAN-based Algorithms	49

3.2.2	Self-Learning through Effective Action	50
3.2.3	Variational Autoregressive Network	52
3.2.4	Flow-based Variational Learning	54
3.3	Observables Analysis for QFT	58
3.3.1	Thermodynamics and Phases	58
3.3.2	Variational Neural-Network Quantum States	65
3.3.3	Real-Time Dynamics Analysis	65
3.4	Sign Problem	69
3.4.1	NN-based Manifold	70
3.4.2	Normalizing Flow for Complex Actions	71
3.4.3	Path Optimization Method	71
3.5	Summary	72
4	Dense Matter Equation of State	73
4.1	Reconstructions from Neutron Star Mass-Radius	73
4.1.1	Statistical Inference	74
4.1.2	Deep Learning Inverse Mapping	77
4.1.3	Gradient-Based Inference	78
4.2	Constraints from Multimessenger Observations	80
4.3	Constraints from Nuclear Physics	83
4.3.1	Connections with Nuclear Symmetry Energy	83
4.3.2	Constraints from χ EFT, HICs, and pQCD	84
4.4	Summary	85
5	Advanced Developments – Physics Meets ML	86
5.1	Manifesting Physics Properties in NNs	86
5.1.1	Gauge Symmetry in Normalizing Flow	87
5.1.2	Inverse Renormalization Group Transformation	88
5.1.3	Fourier-flow Model Generating Feynman Paths	89
5.2	Fusing Physics Models into NNs	90
5.3	Solving Complex Inverse Problems	91
5.4	Summary	98
6	Summary and outlook	99

1. Introduction

High energy nuclear physics and machine learning, though being seemingly disparate, their interplay has already begun to emerge and been yielding promising results over the past decade. This review aims to introduce to the community the current status and report an overview of applying machine learning for high energy nuclear physics studies. From different

aspects, we will present how scientific questions involved in this field can be tackled or assisted with the state-of-the-art techniques.

1.1. Background

The study of nuclear physics focuses on comprehending the nature of nuclear matter, its properties under various conditions, its building blocks, and the fundamental interactions that govern them. The behavior of nuclear matter is fundamentally governed by the strong interaction, described by quantum chromodynamics (QCD) [1]. While nucleons serve as the main degrees of freedom for traditional low energy nuclear physics, high energy nuclear physics (HENP) cares more about QCD matter in extreme conditions, where the basic degrees of freedom are typically quarks and gluons.

A primary goal of HENP is to understand how nuclear matter behaves under extreme conditions, which remains an unresolved area of study [2–5]. Intuitively, when matter is subjected to extreme conditions, its basic constituents can be revealed. For example, when nuclear matter is heated to high temperatures, mesons and resonances are gradually excited out, and at some point causing hadrons or nucleons to *overlap* (the same can happen when nuclear matter is compressed to high densities) thus their constituent quarks and gluons can move freely inside a larger area. The induced state of matter, known as quark-gluon plasma (QGP) [6], is a deconfined state in which quarks and gluons are the basic degrees of freedom and strongly interacting. The existence of such primordial state of matter is believed to have occurred in the early universe after the Big-Bang, and may also exist in the dense interior of neutron stars [7]. The first-principle lattice QCD simulations predict that normal nuclear matter in the form of a dilute hadronic gas can undergo a crossover transition to the strongly-interacting, deconfined state of QGP at high temperature and low baryon chemical potentials, where chiral symmetry is also restored [8–10].

However, the situation at high baryon chemical potential is not well understood due to the fermionic sign problem that impedes direct lattice QCD simulations [11]. The structures of the QCD phase diagram and the properties of matter in these regions have to be studied through effective model calculations and experimental searches. The formation and study of hot and dense QGP can be accomplished through relativistic heavy ion collision (HIC) experiments [12], which act as a heating and compression machine to QCD matter to reach extreme conditions [13]. However, the collision of heavy nuclei creates a rapidly evolving and dynamic process with many entangled and not-fully understood physics factors [7]. Decoding the physics properties related to the early-formed QGP from the final measurements of heavy ion collisions therefore remains a challenging task. In general, both theoretical calculations and experimental facilities are crucial for advancing the field of HENP, which is anyhow becoming increasingly intricate and producing ever-larger amounts of data from sources such as detectors in experiments e.g., Relativistic Heavy Ion Collider (RHIC) at BNL and Large Hadron Collider (LHC) at CERN, etc., and model simulations such as relativistic hydrodynamics, transport cascades, and lattice QCD simulations. Nevertheless, performing the involved calculations, analyzing the involved data, and decode underlying physics from confronting theory with data, are routinely demanding due to factors such as high-dimensionality, background contamination, and potentially entangled physical influences.

Artificial Intelligence (AI) has grown rapidly in popularity with the goal of imparting intelligence to machines. The field of computer science, dating back to the 1960s, has experienced a revival in recent years with the development of modern learning algorithms, advanced computing power, and the vast amount of available data [14, 15]. Machine learning (ML), an essential part of AI, is viewed as a modern computational paradigm that gives machines the ability to learn without being explicitly programmed. It enables computers to go beyond being instructed by humans and learn how to

perform specific tasks on their own. This novel paradigm, particularly deep learning (DL) [16], a subfield of ML that uses deep neural networks for hierarchical representation, has shown successful applications [17] in computer vision(CV), natural language processing(NLP), game AI, and drug discovery. It also demonstrates great promise in transforming scientific research [18]. It allows for automatically recognizing patterns hidden in large, complex datasets, and has proven to be particularly effective in handling intricate structures and non-linear correlations that are beyond conventional analysis [18].

Therefore, a variety of scientific tasks can be aided from these new computational methodologies, such as extracting knowledge from measurements or calculations, improving simulations, detecting anomalies or discovering new phenomena. The deployment of machine learning in various scientific disciplines has become progressively ubiquitous. It is believed that machine learning has the potential to greatly enhance physics research as well (see e.g., [19] for pedagogical introduction). With its flexibility in tackling general computational physics tasks, machine learning is actively being explored to support physics studies [20]. Conversely, many concepts and foundations in machine learning can be traced back to physics, such as the Boltzmann machine and variational generative algorithms, which have close ties to statistical physics [21]. The synergy between these fields will not only benefit physics, but also deepen our understanding of the underlying working mechanisms of machine learning [22] or even intelligence.

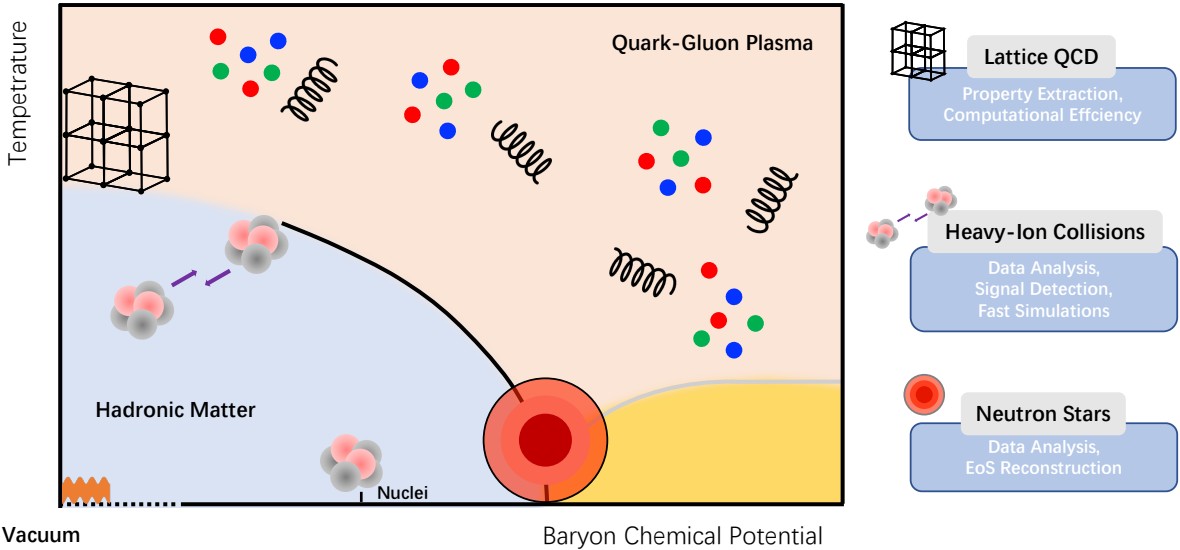


Figure 1.1: Schematic QCD phase diagram and the applications of machine learning in three domains, i.e., Lattice QCD, Heavy-Ion Collisions and Neutron Stars.

High energy nuclear physics can greatly benefit from machine learning techniques due to its computational and data-intensive nature. In recent years, the intersection of machine learning and HENP has shown great potential and unconventional possibilities [23, 24]. HENP has long been at the forefront of big data analysis, using techniques such as neural networks and statistical learning [25–28], but recent advancements in deep learning have brought new developments to the crossing of these two fields. Deep learning has improved the ability to handle large amounts of high-dimensional data, extended the feasibility of going beyond human-crafted heuristics, and generated new possibilities such as fast and effective simulation, sensitive observable design, and new physics detection (see a living review [29] and a collection of datasets in high energy physics [30]). This growing and influential research area deserves dedicated recognition and further study to release the full potential of such novel computational paradigms for high energy nuclear physics.

The use of machine learning in high energy nuclear physics encompasses a wide range of topics and tasks, from experimental data analysis with normal discriminative algorithms, to speeding up various simulations with generative models. We will review them systemically from three sectors, as shown in Fig. 1.1, i.e., heavy-ion collisions in Sec. 2, lattice QCD in Sec. 3 and neutron stars in Sec. 4. Besides, the involved studies are quite often with multi-scale and high-dimensional computations, and requiring customized ML methods that address the specific physics constraints and characteristics, e.g., physical differential equations, corresponding symmetries and conservation laws. This leads to the development of unique techniques for science automation and physics exploration with ML paradigm. A refined summary of some new and advanced developments and their applications in high energy nuclear physics will be discussed in Sec. 5. This review, although unavoidably being limited and with bias in terms of content selection, aims to offer a practical introduction to readers interested in exploring the rapidly developing field of applying machine learning into high energy nuclear physics. A general overview of the ongoing activities in this field will be covered. In the remainder of this section, we will briefly introduce the basics of machine learning for those unfamiliar with the terminology. These information and related techniques can be revisited when delving into the subsequent physics research discussions.

1.2. Machine Learning in a Nutshell

Before physics parts, we would like to provide a comprehensive but concise introduction to the basic concepts of machine learning, with a focus on deep learning and its current developments. The concepts and techniques touched here will be revisited later in this review. Although it can not cover all aspects of machine learning¹, the main objective is to introduce the advanced deep learning approaches. For a deeper understanding of machine learning, we recommend reading books [31, 32], or recent reviews for its practical applications in physics [19, 24, 33, 34].

1.2.1. Bayesian Inference

From a probabilistic perspective, one can infer the probability distribution of random variables (A) from limited trials/observations over its consequences (B), based on the Bayes' theorem [35],

$$P(A | B) = \frac{P(B | A)P(A)}{P(B)}, \quad (1.1)$$

where in scientific applications, A often represents parameters of theoretical models and B refers to experimental observations. The Bayes formula is used to update or revise our belief/knowledge of a theoretical model in terms of A using new experimental observations B . It involves the calculation of the posterior probability distribution $P(A | B)$, which takes into account the prior probability distribution $P(A)$ and the conditional probability $P(B | A)$, known as the likelihood. Uncertainties in the experimental observations B will impact the posterior distribution of A via likelihood, causing it to become wider. The posterior distribution $P(A | B)$ is a probability density function over A , which can be characterized by its mean, peak value, and variance. One way to determine the most likely value of A is by finding the group of parameter combinations $A = a$ that maximizes the posterior distribution $P(A | B)$, known as the maximum a posteriori estimation (MAP). This process allows us to locate the peak of the posterior distribution.

The variance of posterior $P(A | B)$ can be used to determine the uncertainty or confidence level of the theoretical model. If $P(A | B)$ is a narrow distribution with a sharp peak, its variance is small, indicating that the data are decisive and useful

¹The missing parts include but are not limited to dimensionality reduction, clustering, linear/Logistic regressions, (support vector machines)SVMs, and ensemble learning.

in constraining the model with small uncertainty. The marginal distribution $P(B) = \sum_a P(B | A = a)P(A = a)$ is called evidence, which provides a normalization factor by traversing the space of the theoretical model. For an n -dimensional parameter space $A = (A_1, A_2, \dots, A_n)$, if the random variable has m possible choices in each dimension, one must repeat the theoretical calculations m^n times to get the normalization factor $P(B)$. This procedure encounters the challenge of *curse of dimensionality* for high-dimensional parameter spaces. Fortunately, $P(B)$ is not needed using Markov Chain Monte Carlo (MCMC) methods, which work for an unnormalized posterior distribution as follows,

$$P(A | B) \propto P(B | A)P(A), \quad (1.2)$$

The way MCMC methods work for Eq. (1.2) is by importance sampling using random walk [36]. Starting from any position $A = a_0$ in the parameter space, walk to the next position using a random step size ϵ sampled from a uniform or normal distribution, following the Markov Principle that each update only depends on its current position, $a_{n+1} = a_n + \epsilon$. The trajectory of one random walk in the parameter space form a set $\{a_n\}$ for $n = 0, 1, 2, \dots$ whose density estimation produces a probability distribution. This probability distribution does not equal to $P(A|B)$ without any constraints to the process of random walk. The MCMC algorithms set an acceptance-rejection probability to each update such that $A = a$ values in the parameter space are visited more frequently with larger $P(A = a|B)$ than smaller ones to form a stationary distribution that is close to $P(A|B)$. E.g., in Metropolis-Hastings algorithm which is one kind of MCMC algorithm, the acceptance-rejection ratio is set to be $\min(1, \alpha)$ where,

$$\alpha = \frac{P(A = a_{n+1}|B)q(a_n|a_{n+1})}{P(A = a_n|B)q(a_{n+1}|a_n)} = \frac{P(A = a_{n+1}|B)}{P(A = a_n|B)} \quad (1.3)$$

where $q(a_{n+1}|a_n)$ is called proposal function that can be a uniform distribution or a normal distribution centered at a_n . The proposal function is symmetric in Metropolis-Hastings algorithm, which can be eliminated in Eq. (1.3). This is got from the detailed balance condition with $P(A = a_{n+1}|B)q(a_n|a_{n+1}) = \alpha P(A = a_n|B)q(a_{n+1}|a_n)$. In practice, one can sample a_{n+1} from a normal distribution $\mathcal{N}(a_n, \sigma)$ centered at a_n with standard deviation σ . The parameter σ can be adjusted adaptively for efficient sampling.

Gaussian Processes— Gaussian process(GP) is a probabilistic model that can be used for regression or classification [36, 37]. Formally, as a type of stochastic process, a GP dictates a probability distribution over functions, $f(\mathbf{x}) \sim \mathcal{GP}(m(\mathbf{x}), k(\mathbf{x}, \mathbf{x}'))$, which is fully specified by a mean function $m(\mathbf{x})$ (usually chosen to be zero) and a covariance function $k(\mathbf{x}, \mathbf{x}')$ (measures the similarity between two input values). The GP is defined as a collection of random variables (e.g., the evaluations of its sample function at different inputs $\{f(\mathbf{x}_i)\}$), with its any finite set following a joint Gaussian (i.e., multivariate normal) distribution, $f(\mathbf{x}_1), \dots, f(\mathbf{x}_N) \sim \mathcal{N}(\boldsymbol{\mu}, \mathbf{K})$ where $\boldsymbol{\mu}_i = m(\mathbf{x}_i)$ and $\mathbf{K}_{ij} = k(\mathbf{x}_i, \mathbf{x}_j)$.

For a regression task one can use GP to construct a non-parametric prior of the to be fitted function. Per observing a training set $\mathbf{X} = \{\mathbf{x}_i\}_{i=1}^N$ with its corresponding targets $Y = \{y_i\}_{i=1}^N$, one can update the prior by conditioning on the observations, which essentially restrict the functions from the GP to be in line with the training data. Specifically, one cares the prediction Y^* over new inputs \mathbf{X}^* , which together with the training targets Y have the joint prior distribution,

$$\begin{bmatrix} Y \\ Y^* \end{bmatrix} \sim \mathcal{N}(\mathbf{0}, \begin{bmatrix} \mathbf{K}(\mathbf{X}, \mathbf{X}) & \mathbf{K}(\mathbf{X}, \mathbf{X}^*) \\ \mathbf{K}(\mathbf{X}^*, \mathbf{X}) & \mathbf{K}(\mathbf{X}^*, \mathbf{X}^*) \end{bmatrix}),$$

and the conditioning of this joint Gaussian prior on the training data results in the posterior for the prediction,

$$p(Y^* | \mathbf{X}^*, \mathbf{X}, Y) = \mathcal{N}(\bar{Y}^*, \text{cov}(Y^*)),$$

with $\bar{Y}^* = \mathbf{K}(\mathbf{X}^*, \mathbf{X})\mathbf{K}(\mathbf{X}, \mathbf{X})^{-1}Y$ and $\text{cov}(Y^*) = \mathbf{K}(\mathbf{X}^*, \mathbf{X}^*) - \mathbf{K}(\mathbf{X}^*, \mathbf{X})\mathbf{K}(\mathbf{X}, \mathbf{X})^{-1}\mathbf{K}(\mathbf{X}, \mathbf{X}^*)$.

In practice, choosing the appropriate kernel function K for a GP is an important step in the modeling process. It determines the shape of the covariance function and thus the overall structure of the model. The choice of kernel function depends on the specific problem at hand, as well as any prior knowledge or assumptions about the structure of the underlying function. Some common kernel functions contain: *linear kernel*, $k(x, x') = x^T x'$, where x and x' are vectors representing the input values; *polynomial kernel*, $k(x, x') = (x^T x' + c)^d$, where c is a constant, and d is the degree of the polynomial; *squared exponential (SE)* or *Radial Basis Function (RBF)* kernel [38]. This is a popular choice for regression problems, as it can capture complex, non-linear relationships between inputs and outputs. The RBF kernel is defined as,

$$k(x, x') = \sigma_f^2 \exp\left(-\frac{1}{2l^2}(x - x')^2\right),$$

where σ_f^2 is the variance and l is the length scale, which determines the smoothness of the function. Besides, there are many other choices such as *Matérn kernel* [38] kernel for capturing a variety of functional shapes. Many other examples can be found in the book [38]. Once a kernel has been chosen, the parameters of the kernel (such as σ_f^2 , l , and d in the above examples) can be estimated from the data using a variety of optimization methods.

1.2.2. Deep Learning

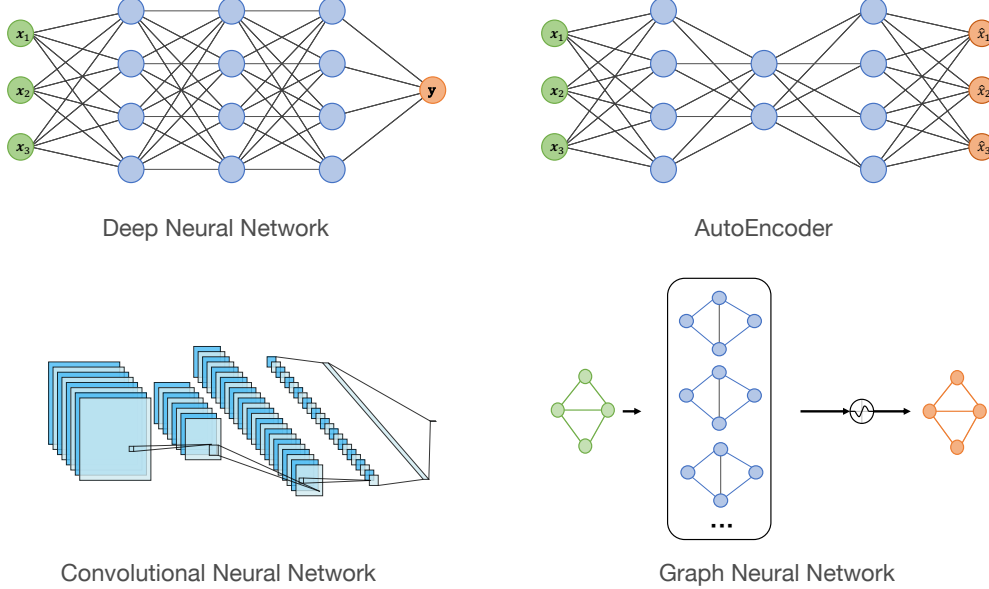


Figure 1.2: A demonstration of the common neural network structures that will be covered in this review. The Deep Neural Networks (DNNs), AutoEncoders (AEs) with "bottleneck latent" layers, Convolutional Neural Networks (CNNs) utilizing convolutional operations, and Graph Neural Networks (GNNs) capable of processing graph-type inputs.

Deep learning, as a modern branch of machine learning [16, 39] usually involving deep neural network usage, provides tools for automatically extracting patterns from the currently available massive multi-fidelity observation data. The **enormous data** makes it possible to establish a reliable mapping between input features and desired targets with deep models. **Deep models** are usually constructed using artificial neural networks(ANNs) which are originally designed to imitate functions of human brain [40], further proved having ability to represent arbitrary complicated continuous function [41, 42]. In an over-simplified picture, deep neural networks(DNNs) are a type of compound function which has multilayer nesting structures: $f_\theta(x) = z^l(\cdots z^2(z^1(x)))$, $z^i(z^{i-1}) = \sigma(\omega^i z^{i-1} + b^i)$, where x is input data defined in a set of samples \mathbb{X} , l labels the number of layers and i is the corresponding index, and $z^0 \equiv x$. $\sigma(\cdot)$ is a non-linear

activation function and $\{\omega, b\}$ are weights and bias respectively. Weights and bias are all trainable parameters, they could be abbreviated as $\{\theta\}$. Some common neural network structures are shown in Figure. 1.2. They will be mentioned tirelessly in the remainder of this review.

Given a well-definite **Loss function** $\mathcal{L}(f_\theta(x))$, these trainable parameters can be tuned in an optimization problem,

$$\theta = \underset{\theta}{\operatorname{argmin}} \mathcal{L}(f_\theta(\mathbb{X})) = \underset{\theta}{\operatorname{argmin}} \sum_j^m \mathcal{L}(f_\theta(x^{(j)})), \quad (1.4)$$

where j labels the index of a sample. If one can collect corresponding labels $y \in \mathbb{Y}$ for input x , the optimization process becomes a *Supervised Learning* task. Common Loss functions contain: Mean Squared Error(MSE), Mean Absolute Error(MAE) and Cross Entropy, etc.

In fact, one can understand the above optimization from a *probabilistic perspective*.

$$\theta = \underset{\theta}{\operatorname{argmax}} p_\theta(\mathbb{X}) = \underset{\theta}{\operatorname{argmax}} \prod_j^m p_\theta(x^{(j)}), \quad (1.5)$$

which is the *maximum likelihood estimation(MLE)* for parameters $\{\theta\}$ given the data-set \mathbb{X} . From such a perspective, training a deep model becomes approaching the conditional probability distribution $p_{\text{data}}(y|x)$. Moreover, it can naturally extend to the *Unsupervised Learning* task, which is approaching the underlying distribution $p_{\text{data}}(x)$ of data without labels. A useful trick is to maximize the log-likelihood, $\log(p_\theta)$, converting the product into a summation. Before introducing

Metrics	Formula	Probabilistic Description
MSE	$(f_\theta(x) - y)^2$	Gaussian
MAE	$ f_\theta(x) - y $	Laplace
Binary Cross-Entropy	$-\left[y \log f_\theta(x) + (1 - y) \log(1 - f_\theta(x))\right]$	Bernoulli

Table 1.1: Common Loss functions and their probabilistic descriptions.

the optimization algorithm, one should be aware of the *generalization ability* for deep models. Intuitively speaking, when training data is not enough to represent the underlying distribution $p_{\text{data}}(x)$ or the deep model is over-represented in the training data set, one will observe that metrics perform better in training than the testing data-set. That is *over-fitting*. On the contrary, it is called *under-fitting*. *Under-fitting* can be easily overcame by increasing complexity of deep models. However, *over-fitting* is thorny because it's from a **trade-off** between model flexibility and accuracy. Adding priors to the parameters is a conventional and efficient strategy to avoid the possible *over-fitting*. From a Bayesian perspective, it makes the MLE to the *maximum a posterior (MAP)* estimation,

$$\theta_{\text{MAP}} = \underset{\theta}{\operatorname{argmax}} p_\theta(\mathbb{X}|\theta) = \underset{\theta}{\operatorname{argmax}} \log p(\mathbb{X}|\theta) + \log p(\theta), \quad (1.6)$$

where the last term $\log p(\theta)$ is the prior distribution of parameters. The Gaussian and Laplace priors correspond to L_2 and L_1 regularization, respectively [32].

From an optimization perspective, once the loss function and model are given, one can choose many different methods to train the model. However, the **gradient-based optimizer** within the differentiable programming paradigm has been proven successful in deep models [16, 39, 43]. In fact, almost all current deep learning packages are adopting gradient-based methods, which are implemented in **automatic differentiation(AD)** frameworks. AD is different from either the symbolic differentiation or the numerical differentiation [44]. Its backbone is the chain rule, which can be programmed in

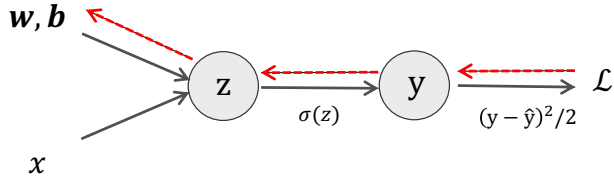


Figure 1.3: Computational graph of a logistic least squares regression in a vanilla net.

a standard computation with the calculation of derivatives. Lots of AD libraries have been developed in the past several years, rendering easy access to AD usage for researchers, such as Tensorflow [45], PyTorch [46] and JAX [47].

In a simplified example shown in Fig. 1.3, the computation of a logistic least squares regression consists of a series of differentiable operations. The forward mode is indicated by black arrows with derivatives. When calculating \mathcal{L} from the input x , the corresponding derivatives can be evaluated by applying the chain rule simultaneously. With this intuitive example, one could understand the **back-propagation(BP) algorithm** [32, 39] clearly. A generalized BP algorithm corresponds to the reverse mode of AD, which propagates derivatives backward from a given output. The adjoint is defined as $\bar{v}_i = \frac{\partial \mathcal{L}}{\partial v_i}$, which reflects how the output will change with respect to changes of intermediate variables v_i . The forward and reverse calculations can be demonstrated as follows,

$$\begin{aligned} z &= wx + b, \quad y = \sigma(z), \quad \mathcal{L} = \frac{1}{2}(y - \hat{y})^2, \\ \bar{\mathcal{L}} &= 1, \quad \bar{y} = y - \hat{y}, \quad \bar{z} = \bar{y}\sigma'(z), \quad \bar{w} = \bar{z}x, \quad \bar{b} = \bar{z}. \end{aligned} \quad (1.7)$$

The first line is the forward process and the second line indicates the reverse mode. Given a target \hat{y} , one can define a proper loss function $\mathcal{L}(y, \hat{y})$ and fine-tune the parameters $\theta = (\omega, b)$ with the gradient $\partial_\theta \mathcal{L}$, which is the gradient-based optimization introduced before. The BP is crucial for training a DNN because the derivatives can be used to optimize a high dimensional parameter set also layer by layer. In most deep learning tasks, models are trained to approximate a $\mathbb{R}^N \rightarrow \mathbb{R}^1$ mapping. In such a case, the reverse mode of AD holds dominant advantages in the gradient-based optimization compared with the forward mode or the numerical differentiation, see more details in Ref [44].

In the optimization problem defined in (1.4) or (1.6), a well-adopted **gradient-based optimizer** is the *stochastic gradient descent(SGD)* [43]. This algorithm updates parameters $\{\theta\}$ through subtracting the gradients derived from the BP algorithm,

$$\theta_{t+1} = \theta_t - \eta \partial_\theta \mathcal{L}_t, \quad (1.8)$$

where η is the *learning rate* and t indicates the t -th time repetition (*epoch*) for the training data. In each epoch, the *SGD* updates parameters on batches randomly selected from the training data set. It results in the stochastic updates of parameter θ on loss function landscape. This stochasticity has been shown necessary for escaping possible local minima [48]. Besides, we introduce a modified *SGD* algorithm which is also widely used, i.e., *Adam* [49]. It is designed to combine adaptive estimates of lower-order moments with the stochastic optimization for improving the stability. As a practical example, the optimizer implemented in our following discussions can be expressed as,

$$\theta_{t+1} = \theta_t - \eta \frac{\hat{m}}{\sqrt{\hat{v}} + \xi}, \quad (1.9)$$

$$\hat{m} \equiv m_{t+1} = \frac{\beta_1}{1 - \beta_1} m_t + \partial_\theta \mathcal{L}_t, \quad (1.10)$$

$$\hat{v} \equiv v_{t+1} = \frac{\beta_2}{1 - \beta_2} v_t + (\partial_\theta \mathcal{L}_t)^2, \quad (1.11)$$

where ξ is a small enough scalar for preventing divergence and β_1, β_2 are the forgetting factors (0.9, 0.99 in default setting) for momentum term \hat{m} and its weight \hat{v} .

Before entering the next section, it's helpful to introduce one specific architecture of neural networks, the AutoEncoder(AE) [50] shown in Figure 1.2. It consists of an encoder and a decoder. The encoder maps the input data x to a typically smaller dimensional variable in a latent space, $z = f_\phi(x)$, while the decoder tries to convert the latent variable z back to the data, $\tilde{x} = g_\theta(z)$. The two components can be designed as two neural networks. The AE can learn a compressed representation of the input data that captures its most important features, while minimizing the dissimilarity between input and output, to which the mean-squared error $L(x, \tilde{x}) = \sum_i (x_i - \tilde{x}_i)^2$ serves heuristically well as the reconstruction loss. This architecture can be used for manifesting the data in an interpretable latent space, which has been proven a successful paradigm in physics [51]. Similarly, principal component analysis (PCA) can also serve as a linear method for dimensionality reduction and feature extraction [52]. PCA computes the covariance matrix $C = X^T X$ and its eigenvectors and eigenvalues, where X is the centered data matrix in a d -dimensional feature space. These eigenvectors are termed as the principal components. Sorting the principal components in descending order of eigenvalues, the first k components with the largest eigenvalues are used to form the k -dimensional representation of a sample x_i by projecting it onto the first k principal components using $z_i = V_k^T(x_i - \mu)$. Here, V_k is the matrix of the first k eigenvectors of C . Later, many works introduced in this review involve applications of PCA, e.g., in Sections 2.2.2, 2.4.5, and 3.3.1.

1.2.3. Generative Models

In general, two typical tasks can be cast for categorizing deep learning algorithms: discriminative modeling and generative modeling. From probabilistic perspectives, discriminative modelling aim at capturing a conditional probability, $p(y|x)$, to be able to predict associated properties or class identities (y) of given object (x), while generative modelling target at learning and sampling from a joint probability (quite often lies in a high dimensional space), $p(x, y)$, to facilitate the generation of new data samples following the same desired statistics represented by the training data or specified distribution. There are several excellent tutorials [19, 53] tailored to physics research, which can be resorted to for details. In physics we often encounter such tasks like for statistical many-body system or lattice QFT simulation we use Markov Chain Monte Carlo (MCMC) to sample new configurations and further estimate the system's physical observables.

Currently, many generative models were developed from ML community with profound influence from and into physics. Basically, most (but not all) of the generative models at present are with the maximum likelihood principle as common guidance. Specifically, generative models can be viewed as parametric models, $p_\theta(x)$, to approach the probability distribution $p(x)$ of a system to which we may have or not have collected data. The Kullback-Leibler (KL) divergence (also called relative entropy), measuring the dissimilarity between the two distribution, can serve the objective for this task,

$$\mathcal{D}_{KL}(p(x) \parallel p_\theta(x)) = \int p(x) \log \frac{p(x)}{p_\theta(x)} dx, \quad (1.12)$$

the minimization of which under given observational data for the system, $\mathcal{D} = \{x\}$, is equivalent to minimization of the negative log-likelihood (NLL),

$$\mathcal{L} = \frac{1}{|\mathcal{D}|} \sum_{x \in \mathcal{D}} \log p_\theta(x), \quad (1.13)$$

thus the maximum likelihood principle.

In the following, we will briefly introduce several of the popular generative models with deep neural networks involved, include variational autoencoder (VAE), generative adversarial networks (GAN), autoregressive model and normalizing

flow (NF).

Variational autoencoder (VAE) [54] added probabilistic spins into classic autoencoder, with which variational inference can be performed under latent variable framework to the data distribution learning. For classic autoencoder (AE), the basic idea is learning to reconstruct the input data going through a bottleneck structured pipeline, where the bottleneck hidden layer describes the *code* to more efficiently represent the data also called latent variables usually with lower dimensional. The transformation from input data x to the latent code z is called encoder, and the left half in the network that reconstruct from the latent code to data manifold in output is called decoder or generator as Figure 1.4 shown.

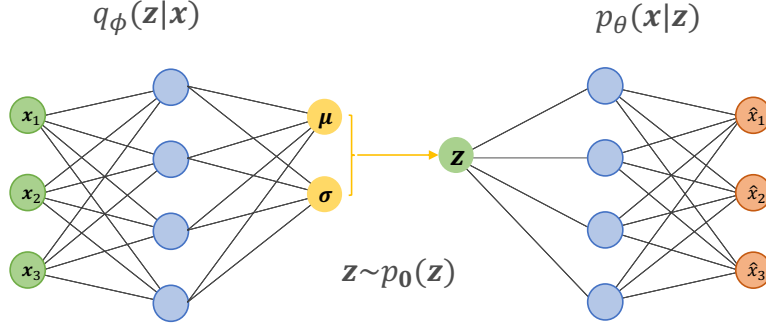


Figure 1.4: A demonstration of VAE whose latent layers output the parameters of prior $p_0(z)$.

In VAE the latent variable per generation convenient is assumed to follow a simple distribution called prior $p_0(z)$ such as a multivariate Gaussian distribution whose parameters, i.e., means μ and standard deviations σ , are from outputs of the encoder. The decoder consequently provides a generative model through the trainable conditional probability $p_\theta(x|z)$. However, the introduction of latent variable makes the whole data generation distribution intractable since the potentially high dimensional integration, $p_\theta(x) = \int p_\theta(x|z)p_0(z)dz$. This thus also results in the intractable encoder probability or the posterior distribution $p(z|x) = p_\theta(x|z)p_0(z)/p_\theta(x)$. To facilitate the MLE or equivalently minimizing the NLL on the training set, VAE employs variational approach. Basically VAE introduced a parameterized model $q_\phi(z|x)$ (modelled by a neural network, termed as encoder) to approximate the posterior for latent variable $p(z|x)$, naturally the KL divergence between $q_\phi(z|x)$ and $p(z|x)$, $\mathcal{D}_{KL}(q_\phi(z|x)||p(z|x))$, can be invoked for the training objective which derives the variational lower bound (also called evidence lower bound, ELBO) for the likelihood as the cornerstone for VAE:

$$\mathcal{L} = \mathbb{E}_{q_\phi(z|x)}[\log p_\theta(x|z) + \log p_0(z) - \log q_\phi(z|x)] \leq \log p_\theta(x), \quad (1.14)$$

where

$$\mathbb{E}_{p(x)}[A(x)] = \int dx p(x)A(x), \quad \int dx p(x) = 1, \quad (1.15)$$

denotes the expectation value over the normalized probability distribution $p(x)$.

Generative adversarial network (GAN) [55] also belongs to latent variable generative model, and introduces an adversarial training strategy to optimize the generator together with a discriminator (later soon will be explained). Basically the GAN framework contains two non-linear differentiable function, both of which being represented by adaptive neural networks. The first is the generator G , which maps random latent variable z from a prior distribution $p(z)$ (usually multivariate uniform or Gaussian) to the target data space, $\tilde{x} = G(z)$, which induces an implicit synthetic distribution $p_G(x)$ that per training to be pushed to the target distribution $p_{true}(x)$. The second one is named as the discriminator $D(x)$ with a single scalar output for each data (faked or real) sample, that tries to distinguish between real data x and

generated data \hat{x} by training to output $D(x) = 1$ and $D(\hat{x}) = 0$. These two networks will be trained in turn to improve their respective abilities going against each other, hence mimicking a two-player min-max game (also called zero-sum game) where their corresponding loss function sum to zero, $\mathcal{L}_G + \mathcal{L}_D = 0$. Upon optimization the respective parameters θ_G and θ_D in the GAN will converge to the *Nash equilibrium* state,

$$\theta_{G,D}^* = \arg \min_{\theta_G} \max_{\theta_D} (-\mathcal{L}_D(\theta_G, \theta_D)). \quad (1.16)$$

where the generator excels in synthesizing samples that the discriminator cannot differentiate anymore from real ones, therefore the data distribution has been captured by the generator after training. The original GAN uses the loss function

$$\mathcal{L}_D = -\mathbb{E}_{x \sim p_{\text{true}}} [\log D(x)] - \mathbb{E}_{z \sim p_{\text{prior}}} [\log(1 - D(G(z)))] , \quad (1.17)$$

and we used

$$\mathbb{E}_{z \sim p_{\text{prior}}} [A(G(z))] = \mathbb{E}_{\hat{x} \sim p_G} [A(\hat{x})] . \quad (1.18)$$

Mathematically it's proved that the training of GAN is equivalent to minimizing the Jensen–Shannon (JS) divergence generalized from the KL divergences,

$$\mathcal{D}_{JS}(p_{\text{real}} || p_G) = \frac{1}{2}(\mathcal{D}_{KL}(p_{\text{real}} || p_{\text{mix}}) + \mathcal{D}_{KL}(p_G || p_{\text{mix}})), \quad (1.19)$$

with $p_{\text{mix}} = (p_{\text{real}} + p_G)/2$. Thus, the GAN belongs to implicit MLE based generative model as well. To add more

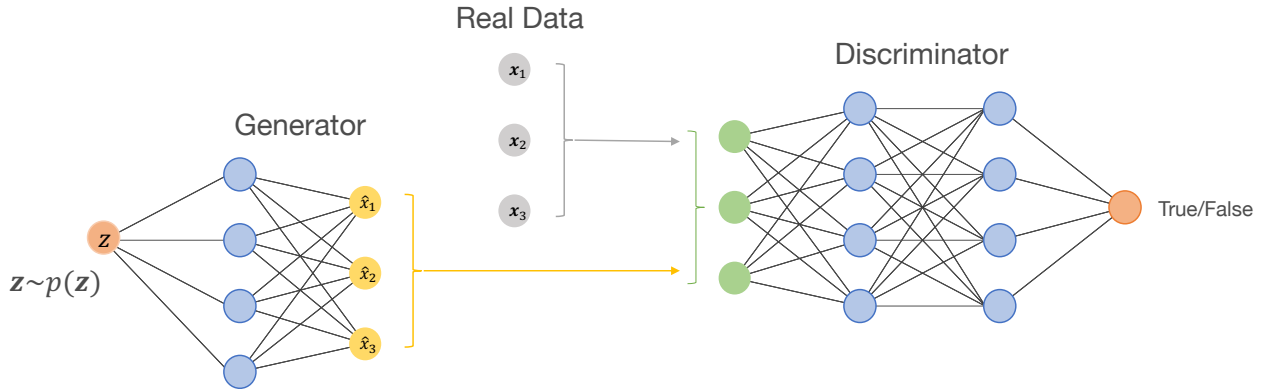


Figure 1.5: A demonstration of GAN, consisting of the generator and discriminator for generating and recognizing data.

flexible conditional-control and enhance the training stability, later a multitude of advanced development for GAN have been proposed, like ACGAN [56], Wasserstein-GAN [57], improved Wasserstein-GAN [58]. The most important difference of Wasserstein-GAN to the original GAN lies in the optimization object, which turns to the Wasserstein-distance (also called Earth Mover distance) being superior over the JS divergence in vanila GAN.

Autoregressive model [59, 60], as an explicit MLE based generative model, invokes the chain rule for decomposing a joint probability into a series of conditionals

$$p_{\theta}(x) = \prod_i^N p_{\theta}(x_i | x_1, x_2, \dots, x_{i-1}) \quad (1.20)$$

to model the data likelihood $p_{\theta}(x)$. Autoregressive model usually use neural networks to represent each of the involved conditional probability, the collection of which as a whole can be viewed as one network with triangular weight parameter matrix for simple fully connected network case (for cases using CNN or RNN the integral weight matrix is masked

accordingly), in order to respect the autoregressive properties specified by the probability decomposition (Eq. (1.20)). In other words, it's designed such that each output element of the autoregressive network is independent of those input elements with later index inside a predetermined order. Such construction for the generative model with Eq. (1.20) also renders efficient sampling from the joint distribution $p_\theta(x)$ by sequentially sampling from each conditional probabilities.

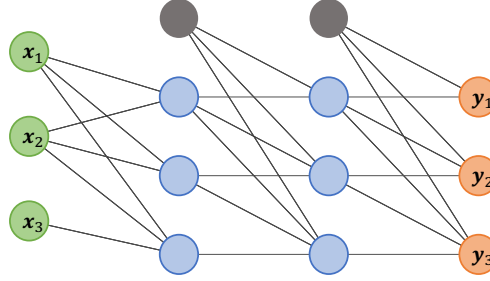


Figure 1.6: A neural network with autoregressive property, i.e., the value of outputs (red solid circle) at a given order only depends on its past inputs (green solid circles) and bias (black solid circle).

It was first designed into time-series data generation, like the recurrent neural network (RNN) in principle also holds such autoregressive property. For structured systems it was further developed to employ the convolutional layer and correspondingly the PixelCNN [61, 62] structure is constructed to fulfil the autoregressive transformation. Once the parameterization (through network) for Eq. (1.20) is given then explicit MLE can be performed by minimizing the forward KL divergence $\mathcal{D}_{KL}(p_{real}||p_\theta)$ if there are collected samples available. Otherwise, with known unnormalized distribution one can also minimize the backward KL divergence $\mathcal{D}_{KL}(p_\theta||p_{real})$ by sampling to estimate the involved entropy term.

Normalizing flow (NF) [63, 64] puts more efforts in performing explicitly the maximum likelihood estimation (MLE), through introducing a bijective, invertible and differentiable transformation f_θ (parameterized with networks) between a simple latent space z and the complex data space $x = f_\theta(z)$. The essential idea lies in the change of variable theorem which manifests the conservation of probability in connecting the latent space and target data space,

$$p_\theta(x) = p(z) \left| \det \left(\frac{\partial z}{\partial x} \right) \right| = p(f_\theta^{-1}(x)) \left| \det \left(\mathcal{J}_{f_\theta^{-1}} \right) \right|, \quad (1.21)$$

through which the likelihood can be evaluated and maximized for optimizing the transformation thus the generator $f_\theta(z) = x$. Special network structures are usually adopted which render accessible and practically computable Jacobian determinant evaluations. like the NICE (Non-linear Independent Components Estimation) [65] or Real NVP (Real-valued Non-Volume Preserving) [66] both with triangular Jacobian matrix.

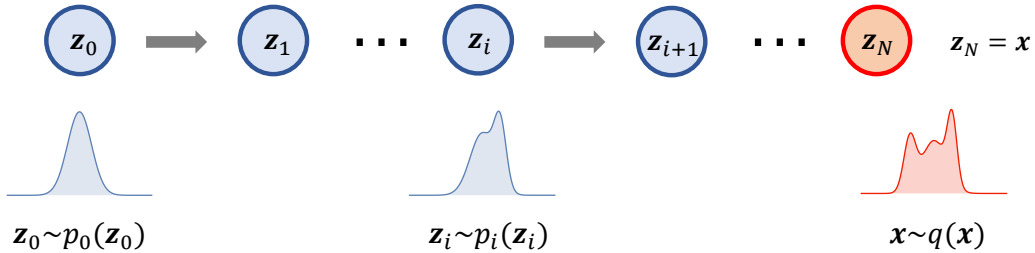


Figure 1.7: Sketch of a normalizing flow model, deforming a simple distribution $p(z_0)$ to a complex one $q(x)$ step by step.

Basically, NICE or Real NVP composes a sequence of simple affine coupling layers (represented by DNN) which split the sample (e.g., image, or field configuration as discussed in Sec. 3.2.4) into two subsets and transform one subset variables conditioned on the other, thus the transformation is with triangular Jacobian matrix, whose determinant can be efficiently evaluated. Specifically, the i^{th} affine coupling layer in NICE [65] reads

$$\begin{cases} z_{1:k}^i = z_{1:k}^{i-1} \\ z_{k+1:N}^i = z_{k+1:N}^{i-1} + m_\theta^i(z_{1:k}^{i-1}), \end{cases} \quad (1.22)$$

with z^i the output of the i^{th} affine coupling layer (thus $z^0 = z \sim p(z)$ and final output $z^L = x \sim p(x)$), and N the dimensionality or the number of variables in one sample. The above coupling layer operation can be easily inverted,

$$\begin{cases} z_{1:k}^{i-1} = z_{1:k}^i \\ z_{k+1:N}^{i-1} = z_{k+1:N}^i - m_\theta^i(z_{1:k}^i), \end{cases} \quad (1.23)$$

The neural network representation come into play for the mapping construction of the translation function ($m_\theta : \mathbb{R}^k \rightarrow \mathbb{R}^{N-k}$), or in Real-NVP for the involved scaling and translation functions (as will be introduced in Sec. 3.2.4). The non-linearity or complexity introduced by the network would not hurt the accessibility for the Jacobian determinant, which is the trace for the lower triangular matrix and in the case of NICE it is just unity. Usually, several such affine coupling layers are composed together to construct the normalizing flow transformation $f_\theta(z)$.

1.2.4. Physics-motivated New Developments

In the above, we reviewed the deep-learning techniques in detail. Deep learning is a powerful tool that can be broadly applied to different aspects of high-energy nuclear physics. If physics knowledge is encoded in the set-up of the learning process, one can further improve the efficiency, even applicability, of deep learning. In the history of its development, several concepts have been raised following this philosophy in deep learning — *physics-inspired*, *physics-informed*, and *physics-driven* deep learning.

The concept of *physics-inspired* machine learning is lacking of clear definition yet loosely summarized in Ref. [67]. It basically describes a paradigm that transfer ideas originating in physics into machine learning. Historically, many concepts from statistical physics deeply influence the foundations of machine learning, e.g., information entropy, information bottleneck and energy-based model, see a more systematic introduction in Ref. [68, 69]. In many modern applications, such as Restricted Boltzmann Machines(RBM)² [73, 74], Geometric Learning [75, 76] and Diffusion Models³ [78, 79], the physics origins are explicit. The backbone of modern physics, symmetry, is also widely manifested in the design of neural network architecture [32, 80, 81], e.g., translation invariance in CNNs [32, 82], Group Equivariant Convolutional Networks [83], permutation invariance in Point Nets [84], and rotational invariance in E3NN [85], and gauge invariance in the partition function of a lattice field theory [86–88].

²It consists of two layers of nodes: a visible layer, which represents the input, and a hidden layer, which models the underlying interactions. The nodes in the two layers are linked by weighted connections, and the RBM defines a probability distribution over the visible units given the hidden units and vice versa. The RBMs have been used to construct many-body quantum states [70] (mentioned in Sec. 3.3.1), also see more advanced researches in Ref. [71, 72] about recent developments in Neural Network Quantum State (NNQS).

³The Diffusion Model is a cutting-edge development in deep learning. It consists of a forward diffusion process and a reverse generation process. The forward diffusion process incrementally adds Gaussian noise to the samples in multiple small steps until it reaches a purely normal distribution. After training, generation can be initiated from a normal distribution by repeatedly applying the learned inverse denoising transformation until the sample is in the data space. See a recent review [77].

Physics knowledge is implemented in *physics-informed* deep learning [89, 90] in a different manner. Some physics properties cannot be encoded in the network architecture explicitly. Instead, one can include extra terms in the loss function to “punish” the violation of the desired properties. Let us take a dynamical system evolving in time as an example. One can train a network with the loss function, including the violation of the observation and the underlying equation of motion. A successfully trained network would be able to predict the observables at any given time without solving the differential evolution equation. Compared to *physics-inspired* DL, *physics-informed* ones take the physics knowledge as a soft constraint, as one can hardly guarantee the loss term to be exactly zero. More introduction can be found in recent review [90].

Last but not least, *physics-driven* deep learning is purposed to train differentiable problems. The Back-Propagation method discussed in Sec. 1.2.2 is designed to optimize the parameters in a network so that its output matches the desired observables. In some problems, the observables are not naively the network output but some function (or functional) of it. If such a function or functional relation is differentiable, one may incorporate their derivatives with the Back-Propagation method such that parameters can be efficiently optimized using gradient based methods. See also Ref. [91] as a comprehensive introduction.

Generally speaking, physics-driven machine learning implements more physics information into the training and therefore requires less amount of data, compared to the other two approaches. Additionally, the three approaches are not exclusive from each other. One can simultaneously apply more than one technique in above from different aspects on one problem. A concrete example, which attempts to reconstruct the nuclear matter equation of state from the neutron star mass and radius measurements, will be given in Sec. 5.

1.3. Outline

The organization of this review is summarized in Fig. 1.8. We cover ML applications in Heavy-ion collisions (Sec. 2), Lattice QCD (Sec. 3) and Neutron star equation of states (Sec. 4). Finally, in Sec. 5, we also demonstrate some new advanced developments.

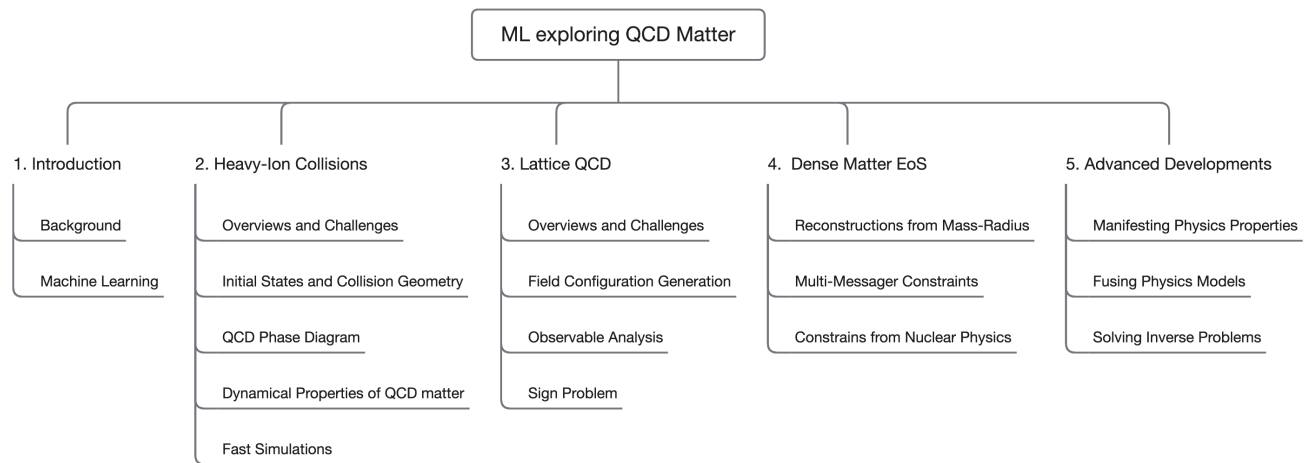


Figure 1.8: Outline of this review.

2. Heavy-Ion Collisions

2.1. Overview and Challenges for HICs

Relativistic heavy-ion collisions (HICs) create an extreme environment for QCD matter in the laboratory [92–98], e.g., at RHIC and LHC (also see Ref. [99] for a history background retrospect), with the highest temperature [100–102], the strongest magnetic field [103, 104], and fastest rotational angular velocity on Earth [105]. In this extreme environment, hadronic matter is expected to be deconfined to form a strongly interacting and free-roaming quark-gluon plasma (QGP), which is the same matter that was created in the early universe 10^{-6} s after the **Big Bang** [2–4].

The goals of the HIC physics include (but not limited to),

- **Look for evidence of deconfinement.** E.g., the strong collective flow [106], the enhancement of strange particles [107], the suppression of high- p_T particles explained by the jet-medium interaction in QGP [108] and the suppression of heavy quarkonium [109].
- **Study the QCD phase structure.** Such as, what is the nature of the phase transition between QGP and a hadron resonance gas (HRG) with equal proportions of matter and antimatter? What is the type of phase transition between QGP and normal nuclear matter with a finite baryon number? If there are crossover and first-order phase transitions in the diagram, is there a critical endpoint in between? What is the experimental evidence for the critical phenomena? See e.g., [110, 111].
- **Study the equation of state (EoS) of QGP**, e.g., the relations between local pressure, local energy density, entropy density, and local temperature. Will the EoS provided by lattice QCD lead to a reasonable dynamical evolution of QGP that can describe the momentum distribution of final state particles in HICs? See, e.g., [112–114] for more details.
- **Study the sensitivity of the physical observables to the physical parameters in the collisions.** For example, what are the effects of shear and bulk viscosity of QGP? What are the effects of the freeze-out temperature and the hadronic cascade? What are the effects of initial nuclear structure and gluon saturation? One may refer to [115–118] and the references therein.
- **Study the jet-medium interaction and in-medium effects for heavy bound states.** E.g., the shape and structure of the jet shower due to the jet-medium interaction, the sensitivity of the medium response to the underlying EoS of QGP, and the heavy quark potential inside the medium. Refer to [119–122] for an overview.
- **Search for CP violation and rotation/spin polarization (Chirality and Vorticity in QCD)** in the strong interaction. coupling between the classical, collective orbital angular momentum and the spin, an intrinsic quantum property, of a single-hadron.

2.1.1. “Standard Model” of Simulating HICs

To describe the whole process of a heavy ion collision, one has to construct hybrid models with different physics at different stages of the collision [2, 12, 123, 124]. Here we briefly summarize the state-of-the-art modeling for each stage. In the pre-collision state, a *Monte Carlo model* is used to determine the positions of the nucleons inside a 3-dimensional nucleus, to determine the collision patterns between two nuclei, e.g., the impact parameter of a collision, the orientation

of the deformed nucleus, which can lead to more complex tip-tip or body-body collisions. During the collision, *color-glass condensate and saturation models* are used to account for the physics of special relativity and vacuum fluctuations in the nucleus to calculate the fluctuating local entropy deposition in the overlap region. After the formation of locally equilibrated QGPs, *relativistic hydrodynamics* is used to describe the dynamical evolution of the local temperature and fluid velocity in the expanding QGP. Hadrons form at the boundaries of the QGP and will interact with each other via *transport models*. In parallel to the dynamical evolution of the soft(low energy) particles in HIC, the hard(high energy) partons with extremely high energy and momentum will pass through the QGP and interact with the thermal partons in the QGP. The physics is described by QCD, where partons will split and collide. The differential cross-sections are usually provided by pQCD calculations in leading order.

Monte Carlo models for the initial nuclear structure — According to the charge distribution of the nucleons in the nucleus, the density distribution of the nucleons is modeled using a deformed Woods–Saxon function [125, 126],

$$\rho(r, \theta, \phi) = \frac{\rho_0}{e^{(r-R_0(1+\beta_2 Y_{20}(\theta)+\beta_4 Y_{40}(\theta)))/a} + 1}, \quad (2.1)$$

where ρ_0 is the nucleon density inside the nucleus, R_0 is the radius, a is the diffusiveness, β_2 and β_4 are two deformation factors whose values determine the shape of the nucleus, e.g., whether it is prolate or oblate. For ^{208}Pb , whose proton number 82 and neutron number 126 are both magic numbers, the deformation parameters $\beta_2 = \beta_4 = 0$, its shape is a perfect sphere [127, 128]. Other heavy-ionic nuclei like Au, U, Cu, O, Xe, Ru, and Zr are deformed to varying degrees.

In Monte Carlo simulations, A nucleons are first sampled from the above deformed Woods–Saxon distribution for each nucleus. For each pair of the sampled nuclei, the probability $P(b) = 2b/R^2$ is used to sample the impact parameter b , where R is the maximum distance between two nucleons for overlap. In this procedure, each nucleon is sampled independently, without taking into account the nucleon-nucleon correlation, the clustering effect, and the difference between the proton and neutron distributions. These can be taken into account in specific studies.

Color Glass Condensate — Due to special relativity (Lorentz contraction and dilation effect, specifically), at extremely high energy with respect to the lab frame, the shape of the nucleus is compressed along the beam direction and the lifetime of quantum fluctuations in the nucleus is extended [129–134]. As a result, virtual quark-antiquark pairs and gluons live long enough to participate in high-energy collisions. As the collision energy increases, the gluons of typical longitudinal momentum correspond to a small momentum fraction(x) of the incoming nucleons. Noting the small- x region of parton distribution e.g., from Deep Inelastic Scatterings(DISc), the dominant contribution is from gluons, and the number of gluons in the projectile seen by the target increases with the collision energy. To leading order, the energy-momentum after the collision is given by

$$T^{\mu\nu} = \frac{1}{4}g^{\mu\nu}F^{\alpha\beta}F_{\alpha\beta} - F^{\mu\alpha}F_\beta^\nu, \quad (2.2)$$

where $F^{\mu\nu}$ is the field strength of the classical retarded color field A^μ described by the classical Yang–Mills equation,

$$[D_\mu, F^{\mu\nu}] = I^\nu \quad (2.3)$$

where $I^\nu = \delta^{\nu+}\rho_1 + \delta^{\nu-}\rho_2$ is the external current associated with the fast-moving partons in the projectile with density ρ_1 and in the target with density ρ_2 .

The IPGlasma model is a successful attempt is to describe the HIC initial condition by solving the classical Yang–Mills equation for gluons radiated from color sources [135, 136]. Solving the field equation is, however, computationally

expensive. One may adopt phenomenological models, such as the Trento Monte Carlo model [137]

$$s(\mathbf{x}_T) = \left(\frac{T_A^p(\mathbf{x}_T) + T_B^p(\mathbf{x}_T)}{2} \right)^{1/p}. \quad (2.4)$$

which generates the initial condition of entropy density(s) as a p -powered average of the thickness functions (T_A and T_B), where $T_A(T_B)$ is the nuclear matter in projectile(target) with the longitudinal direction integrated. p is a dimensionless parameter that can be tuned. Also note that such CGC inspired initial condition to HICs is also phenomenologically interesting by itself [138–141]. From a Bayesian global fit [142], it has been found that the anisotropy of entropy deposition in the transverse plane of IPGlasma can be approximated by choosing $p \approx 0$.

Relativistic Hydrodynamics — The dynamical evolution of created fireball (QGP and HRG in local equilibrium) from HICs can be described by relativistic hydrodynamic equations,

$$\nabla_\mu T^{\mu\nu} = 0, \quad \nabla_\mu J^\mu = 0, \quad (2.5)$$

where ∇_μ represents the covariant derivatives, $T^{\mu\nu} = (\varepsilon + P + \Pi)u^\mu u^\nu - (P + \Pi)g^{\mu\nu} + \pi^{\mu\nu}$ is the energy-momentum tensor of hot nuclear matter, with ε the local energy density, P the local pressure given by the equation of state $P = P(\varepsilon, \mu_B)$, Π the bulk viscosity, u^μ the fluid four-velocity satisfying $u^2 = 1$, $\pi^{\mu\nu}$ the shear viscous tensor, $g^{\mu\nu}$ the metric tensor. $J^\mu = nu^\mu + v^\mu$ is the charge current, where n is the net charge density, v^μ is the diffusion of the net charge, e.g., the net baryon diffusion. This set of equations is solved together with the Israel–Steward equations [143] for Π , $\pi^{\mu\nu}$ and the baryon diffusion current v^μ .

One merit of relativistic hydrodynamics is that it encodes the equation of state provided by lattice QCD calculations. Meanwhile, relativistic hydrodynamics is a complex dynamical evolution that involves many fundamental properties of hot QCD matter, e.g., shear viscosity over entropy density η/s , bulk viscosity over entropy density ζ/s , baryon diffusion parameter k_B , the initial time τ_0 , the freeze-out temperature T_f . With the accessible experimental results on HIC, one may determine these fundamental properties by performing Bayesian analysis in a global fitting [115–118]. Hydrodynamics provide the complete evolutionary history of the soft partons, e.g., the energy density, the pressure, and the temperature at any given space-time point (t, x, y, z) . This information is valuable because it provides not only the spectra and momentum anisotropy of soft hadrons but also the background information for jet quenching and the production of direct photons and dileptons. In this way, relativistic hydrodynamics provides multiple ways to study the properties of QGP.

There are many different implementations of the relativistic hydrodynamics, either in 2+1D or in 3+1D [144–169]. 2+1D hydro assumes the fluid to be boost invariant along the beam direction, whereas 3+1D hydro does not. The former is a good approximation for HIC phenomena in mid rapidity. Typically simulating one HIC event in 3+1D hydrodynamics with finite shear viscosity takes 40 to 60 times longer than simulating one event in 2+1D hydro. It is thus more convenient to accumulate a large amount of data using 2+1D hydro, which will also be beneficial for machine learning studies. For example, in the Bayesian analysis [142] that requires millions of events, VISH2+1 hydrodynamic model is used to generate data with event-by-event fluctuating initial conditions.

Transport models for the hadronic cascade — The particle-yield ratios between different hadrons are well described by the statistical model, assuming that the particles emitted from the freeze-out hypersurface obey the Fermi–Dirac distribution for baryons and the Bose–Einstein distribution for mesons, with mass m_i and chemical potential μ_i ,

$$\frac{1}{2\pi} \frac{dN}{dY p_T dp_T d\phi} = \text{dof} \int \frac{d^3 p}{(2\pi)^3} f(p \cdot u, T), \quad (2.6)$$

where $\text{dof} = 2 \times \text{spin} + 1$ is the spin degeneracy, f is the distribution function given by,

$$f = \frac{1}{e^{p \cdot u/T} \pm 1}, \quad (2.7)$$

where \pm stands for baryons and mesons respectively. In hybrid models, one can thus sample hadrons using the above distribution function in the comoving frame of each fluid cell with local temperature T and fluid velocity u^μ on the freeze-out hyper surface.

The hadrons from the freeze-out hyper surface can go through two different processes. Immediately after particle-isation, the hadron density is still very high and the many-body interactions between hadrons are still too strong to be described by transport models. At this stage, relativistic hydrodynamics still works well. At a later stage, hadrons become diluted, and their interactions should be described by hadronic cascade models such as UrQMD [170] and SMASH [171].

Jet quenching in QGP — There have been tremendous efforts in developing theoretical tools to model the interactions between energetic partons and thermal partons in QGP and simulate them in phenomenological studies [172–199]. While these models take different assumptions in the derivation, here we take the linear Boltzmann transport equations [183] as an example to demonstrate the theoretical framework,

$$p_i \cdot \partial f_i = \int \sum_{i,j,k} \prod_{a=i,j,k} \frac{1}{(2\pi)^3} \frac{d^3 p_a}{2E_a} (f_k f_l - f_i f_j) |\mathcal{M}_{ij \rightarrow kl}|^2 \frac{\gamma_j}{2} S_2(\hat{s}, \hat{t}, \hat{u}) (2\pi)^4 \delta^4(p_i + p_j - p_k - p_l) + \text{inelastic}, \quad (2.8)$$

where f_i is the distribution function for the hard parton i whose initial position is sampled from the distribution of binary collisions between nucleons and whose four-momentum is provided by the Pythia Monte Carlo model [200]. The right-hand side includes the gain term $f_k f_l$ and the loss term $-f_i f_j$ due to the collisions of hard partons with thermal partons. The scattering amplitude $\mathcal{M}_{ij \rightarrow kl}$ is given by tree-level pQCD calculations. γ_j is the spin and colour degeneracy of the thermal parton j . S_2 is a control factor to eliminate the collinear divergence, which is given by

$$S_2(\hat{s}, \hat{t}, \hat{u}) = \theta(-\hat{s} + \mu_D^2 < \hat{t} < -\mu_D^2) \theta(\hat{s} > 2\mu_D^2), \quad (2.9)$$

where $\hat{s}, \hat{t}, \hat{u}$ are three Mandelstam variables and $m_D = \frac{\sqrt{6}}{2} g T$ is the Debye screening mass for gluons and light quarks.

The last inelastic term accounts for the gluon radiation induced by elastic scattering. The gluon radiation rate Γ_a^{inel} is taken from higher-twist calculations,

$$\frac{d\Gamma_a^{\text{inel}}}{dz dk_\perp^2} = \frac{6\alpha_s P_a(z) k_\perp^4}{\pi (k_\perp^2 + z^2 m^2)^4} \frac{p \cdot u}{p_0} \hat{q}_a(x) \sin^2 \frac{\tau - \tau_i}{2\tau_f} \quad (2.10)$$

where z is the energy fraction of the emitted gluon with respect to the hard parton a , k_\perp is the transverse momentum of the emitted gluon, $\alpha_s = \frac{g^2}{4\pi}$ is the coupling constant, $P_a(z)$ is the parton splitting function, $\hat{q}_a(x)$ is the transverse momentum transfer per unit length due to elastic scattering. The sin function encodes the quantum interference between gluons emitted at different time. The τ_i is the production time of the parent parton a and $\tau_f = 2p_0 z(1-z)/(k_\perp^2 + z^2 m^2)$ is the formation time of the emitted gluon.

All simulation techniques and packages mentioned above are developed by different research groups, which makes it crucial to arrange them in a consistent and organized manner for a systematic phenomenological study in HIC. Thus, the JETSCAPE topical collaboration is formed, aiming to provide a comprehensive framework that implements the state-of-the-art simulation packages for every stage, so that soft and hard physics can be studied consistently. For jet-quenching phenomena in particular, the JETSCAPE framework construct a multi-stage jet-medium interaction model that takes into account different energy and virtuality scales of hard partons in the jet shower compared to the medium [201]. For

example, JETSCAPE uses MATTER [202] to simulate the parton splitting at early times when the parton a is highly virtual, it uses LBT [183], MARTINI [203], or AdS/CFT [204] to simulate the interactions between medium and hard partons with low virtuality. In this way, the JETSCAPE Monte Carlo model provides an integration of models for the production of simulating data in heavy ion collisions.

2.1.2. HIC Challenges

Theoretical simulations of high-energy heavy ion collisions (HIC) and experiments at RHIC and LHC have generated a huge amount of data. Unlike $e^+ + e^-$ collisions and $p + p$ collisions, HIC produces thousands of final-state hadrons at the highest energies of RHIC and LHC, in every single collision event of Au+Au and Pb+Pb. These produced hadrons contain both soft and hard particles, with the soft particles coming mainly from the freeze-out of the QGP while the hard particles from jet fragmentation or heavy quarkonium decay.

The data is routinely compressed to low-dimensional representations in physics space for data-model comparison, e.g., the charged multiplicity as a function of pseudo-rapidity, the p_T spectra, the anisotropic flow coefficients, the di-hadron correlation, etc. However, the initial state, the QCD matter EoS, the QGP properties such as shear and bulk viscosity are all coupled to final state observables intricately. For example, both the shear viscosity and the freezing temperature will change the slope of the p_T spectra. Traditional data analysis techniques encounter difficulties in determining a physical property using the final state observables, as its value will change adaptively with the values of other model parameters, as shown in Fig. 2.1.

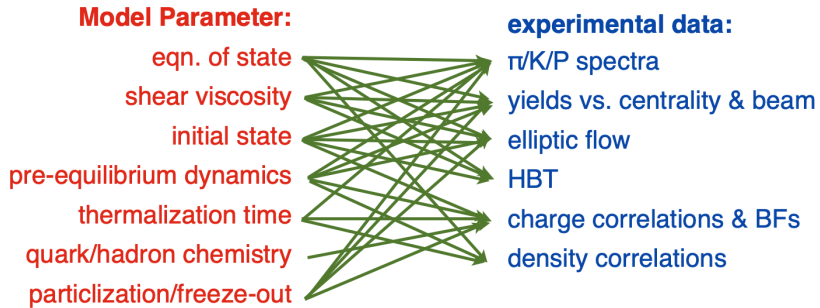


Figure 2.1: The entanglement between different model parameters and physical observables in heavy ion collisions. Taken from Ref. [205] with permission.

Data analysis in high-energy HICs is a typical *inverse problem*⁴: given all the different known physics factors, well-established standard computational models such as 3+1 D hydrodynamics can mimic the collision dynamics and obtain corresponding final state information, but given only limited and cross-impacted final state measurements, how to extract knowledge about the early time physics happened from the intricate entanglement influence, it is a very non-trivial inverse inference task. The lifetime of the formed QGP in high-energy HICs is only about 10^{-23} seconds, which is too short (also too small) to be resolved. What can be determined experimentally is the four-momentum of the final state hadrons or their decay products, but what we are interested in is the initial state and the properties of the QGP early in the collision evolution. It is unknown whether the physical information will survive the violent expansion and leave an imprint in the final state due to entropy production and memory decay induced by information loss. It is also unknown whether

⁴See Sec. 5.3 for more discussions on inverse problems.

this is an ill-defined inverse problem, where different parameter combinations may lead to degenerate output (final-state information).

In recent years, two techniques behave promising for extracting physical information from exotic final state particles of high-energy HICs. One method is the Bayesian analysis, where all available experimental data can be used together to determine multiple model parameters simultaneously through global fitting [115–118, 142, 205]. The other method is deep learning, which can search for observables that are sensitive to only one physical property [30, 206, 207]. Deep learning is currently the best pattern recognition method that can extract features and feature combinations from high-dimensional data and map them to specific physical properties.

2.2. Initial States and Collision Geometry

Since HIC challenges can be viewed as a type of inverse problems, it is natural to ask whether the initial state of HIC can be extracted from the momentum distribution of the final state hadrons. Due to entropy production and information loss, there is no guarantee that the initial state is recoverable from the final state particles' information. However, we know for sure that some of the initial state information survives the complex dynamical evolution of strongly coupled matter and is present in the exotic particles of the final state. For example, the momentum anisotropies have a strong correlation with the geometric eccentricity of the initial state as well as with the impact parameter. It is also known that the deformation of the nuclear structure leads to intrinsic collision patterns related to the distributions of the final state charge multiplicity and momentum anisotropy. It would also be interesting to know whether other initial state fluctuations as well as correlations are transformed into correlations of final state particles in momentum space. E.g., the neutron skin, the nucleon-nucleon correlation, the α clusters in heavy nuclei [208] and the gluon saturation at relativistic energies.

2.2.1. Impact Parameter Determination

If one wants to extract one number at the initial state from the final state particles using machine learning, the first one to try is the impact parameter, which is the transverse distance between two colliding nuclei. It is essential to know the impact parameter b for determining the event geometry and further analysis, e.g., the volume estimation in fluctuation analysis. However, we have no direct control or measurement over b in experiments. Usually, final state observables such as charged multiplicity are used to define centrality classes based upon models such as (Monte-Carlo)-Glauber simulation [209], through which one can get only a likely distribution of b for a given centrality class. Here the centrality classes are usually specified from percentiles of those final state observables, and further guide the grouping of events but in a rough manner. This impact parameter is so important that recently RHIC spent several million on the detector to improve the precision of impact parameter determination [210]. ML algorithms can provide a useful tool in discriminating initial conditions for HICs from the final state accessible information.

Early Attempts with ML to Determine Impact Parameter — Many early attempts with the usage of ML techniques for determining the impact parameter mainly resort to simple algorithms, e.g., feed-forward neural network using conventional observables [28, 211, 212] or support vector machine (SVM) [213] or Bayesian inference with also K-means clustering [214]. Later, working directly on the two-dimensional transverse momentum and rapidity spectra of final state particles, the DNN, Light Gradient Boosting Machine (LightGBM) and the Convolutional Neural Networks (CNN) algorithms were employed to estimate the impact parameter at intermediate energies [215–217] with UrQMD

provide the simulated events, and then also on realistic cases including detector responses of the S π RIT Time Projection Chamber into the simulation events [218]. Compared to conventional means, these ML-based methods show better performance in estimating the impact parameter, especially giving rise to the ability in recognizing the central collision events. Such strategy for impact parameter estimation using DNN and CNN was also discussed for Au+Au collisions at $\sqrt{s_{NN}} = 200$ GeV [219] using final state energy spectrum in (p_x, p_y) space as input. With data simulated from AMPT model, the trained CNN gives good prediction accuracy for impact parameter with a mean absolute error about 0.4 fm for $2 < b < 12.5$ fm, while for central and peripheral collisions the performance gets worse. For HICs at LHC energies, the Gradient Boosted Decision Trees (GBDTs) were used [220] for impact parameter regression in Pb+Pb collisions at $\sqrt{s_{NN}} = 5.03$ TeV with charged-particle multiplicity ($\langle dN_{ch}/d\eta \rangle$, $\langle N_{ch}^{TS} \rangle$) and mean transverse momentum ($\langle p_T \rangle$) as the input features, meanwhile, the transverse spherocity is obtained which characterize in two limits the hard and soft events⁵. In Ref. [221], besides the determination of impact parameter, two other quantities in characterizing the initial geometry–eccentricity and participant eccentricity, were also included as targets within ML-based regressions, where k-NearestNeighbors (kNN), ExtraTrees Regressor(ET) and the Random Forest Regressor(RF) models were employed based on the transverse momentum spectra as input features, model dependencies and generalizability of the trained were also discussed.

End-to-End b-meter with PointCloud Network — The detector’s record in HIC has an inherent point cloud structure (as will also be discussed in Sec. 2.3.4), which is defined as a collection of points as an unordered list with their record attributes, e.g., the position, charge, or momentum of particles. Such point cloud format in principle should hold the permutation invariance. Being specially developed, the PointNet provides an appropriate structure handling point cloud dataset and is meanwhile invariant under the ordering of the points (i.e., particles). Therefore, for HICs study, the PointNet-based models open up the possibility to work directly on the detector readout for physics exploration using pattern recognition strategy in the big data sense. As introduced in above, an accurate estimation of impact parameters on an event-by-event basis is non-trivial, much less the demand in working with detector output (hits or tracks) directly even before the particle identification. This actually forms an inverse problem, where the task of determining the initial impact parameter given purely detector output for the final state individual event is implicit by itself. In Ref. [222, 223], an end-to-end⁶ impact parameter meter is devised with PointNet-based deep learning models and demonstrated for the Compressed Baryonic Matter (CBM) experiment.

As is under construction within the FAIR program at GSI, CBM aims at studying the properties of strongly compressed nuclear matter through heavy ion collisions with beam energies ranging from 2 to 10A GeV. The key feature of CBM experiment is that it will have high event rate and trigger rate rendering rare particle detection and high statistic evaluation for some observables (e.g., higher order fluctuations or correlations), which however calls for fast real-time analysis in selecting events from the flooding stream of data produced from the collision experiment. To this end, thus being able to work with directly the detector output, Ref. [222, 223] adopted a supervised training strategy to construct an end-to-end impact parameter meter using PointNet, where the training data is prepared from UrQMD followed by the CBM detector simulation using CbmRoot. As input to the PointNet-based impact parameter estimator, each event is represented with particle hits or tracks information in point cloud format. One PointNet-based model consisting of two joint alignment networks as shown in Fig. 2.2 is constructed to capture the inverse mapping from the detector output of CBM to impact

⁵Transverse spherocity is defined for unit vector $\hat{\mathbf{n}}$ which minimizes the ratio $S_0 = \frac{\pi^2}{4} \left(\frac{\sum_i p_T i \times \hat{\mathbf{n}}}{\sum_i p_T i} \right)^2$.

⁶Here **end-to-end** means the inference is performed on direct detector output without much preprocessing for the data.

parameter and was trained supervisedly with training data simulated from UrQMD+CbmRoot.

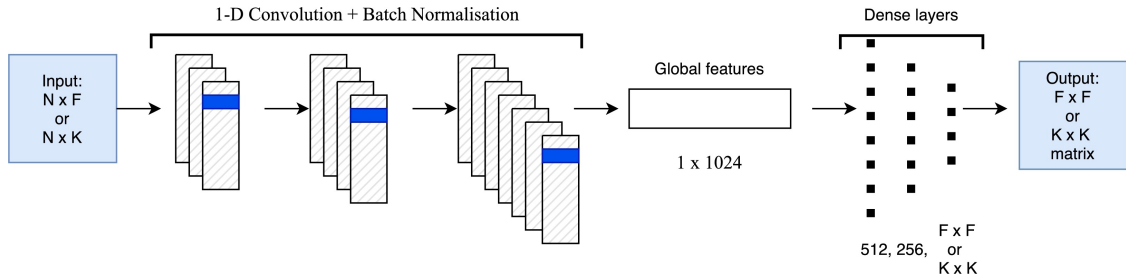


Figure 2.2: General structure of joint alignment network which induce transformations on input or features inside the PointNet. Taken from Ref. [222] with permission.

As seen from Fig. 2.2, the adopted 1-D convolutions with kernels of size 1 across point features for individual points (particles) ensures the operations to be order invariant, after which symmetric function like global Average or Max pooling is used to aggregate all global features for further processing (usually use dense layers), thus preserves the order invariance for the model. Note that the used 1-D CNN is equivalent to applying a shared dense layer operation to lift the feature space of each particle to a high-dimensional transformed feature space. As demonstrated in Ref. [222], such PointNet-based model provides fast and accurate, end-to-end and event-by-event impact parameter determination, showing around $0.5 fm$ mean squared error. By using such a trained model, It is promising to access event-by-event centrality estimation from the hits record for CBM experiment.

2.2.2. Unsupervised Centrality Outlier Detection

Though there is a well-established “standard model” for HICs simulations, due to the inaccessible first principle calculation to the collisional dynamics, new or not well-understood physics may be lacking in the models, e.g., the critical phenomenon. From the experimental point of view, in HICs the new and interesting physics might be hidden in rare events and/or rare particles and also their inter-correlations, such as higher-order cumulants of particle multiplicity distributions. In addressing such rare probes, *large event rate* is scheduled especially for the new experiments, like CBM or PANDA at FAIR, the RHIC beam energy scan, and the ALICE experiment at CERN. Efficient online event selection is then in urgent need, which for example could pop out events potentially containing different characteristics or statistics as compared to the background. Experimentally the disability in this issue may induce artifacts for the interpretation of the observable, such as an imperfect centrality determination or detector malfunction’s contamination induced different event types within a bulk background, manifested as two-bump distribution in the proton number distribution (which could also be induced by critical fluctuation physically), is discussed [224] to be able to explain the STAR observed deviation [225] for net-proton multiplicity distribution from simple binomial in Au+Au collisions at $\sqrt{s_{NN}} = 7.7$ GeV. Otherwise, this deviation may also signal a critical endpoint in the QCD phase diagram.

In such a context, outlier detection which in ML community has been well-developed is proposed to detect anomaly event in HICs [226]. As an exploratory study in testing the methodology, Ref. [226] generated an ensemble of mixed events with the majority to be central collisions (with impact parameter $b = 3$ fm) and a few portions to be peripheral ($b = 7$ fm) using UrQMD transport model, with the ratio of the two centrality classes set to be able to give the anomalous proton number distribution observed from STAR. The task is unsupervisedly select the outlier–peripheral collision events out of the background–large number of central events. Each event is represented by the 2D-histograms of transverse

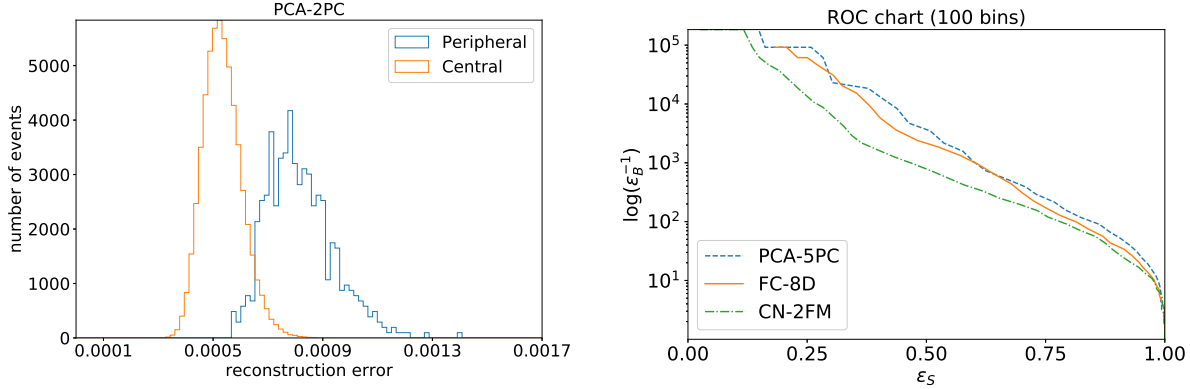


Figure 2.3: Taken from Refs. [226]. (left) the histogram of the RE in Eq. (2.11) for PCA using 2 PC; (right) the ROC curves for best models of each type: PAC, AEN-FC, AEN-CNN.

momentum (p_x, p_y) with normalization performed to eliminate the easy characteristic of total number of particles per event in distinguishing the centrality classes. Two kinds of algorithms were discussed for this outlier detection, principal component analysis (PCA) and autoencoder network (AEN), both can achieve dimensionality reduction over the training data-set while the output (for PCA i.e., the inverse transformation) largely reproduce the input. In the reduced feature space (e.g., with just 2 or 3 dimensions), the feasible visualization provides the most simple way for data clustering and outlier identification, which however is limited by the expressibility of the used feature space. Another way to realize outlier detection with arbitrary latent feature space is utilizing the *reconstruction error* (RE) of each event to guide the selection, e.g., the mean-squared error (see Fig. 2.3 for its histograms and performance in identifying outlier),

$$RE(x) = \frac{1}{N} \sqrt{\sum_{i=1}^N (x_i^{rec} - x_i)^2}, \quad (2.11)$$

where x_i^{rec} is the i^{th} component of the reconstructed event for x . Since the learning algorithms (PCA or AEN) is trained to reproduce the input event through reduced latent space on data-set with majority to be background types, the RE reflecting the reconstruction loss is expected to be different between two types of events if they possess distinct characteristics or statistics, thus provides also a promising indicator for anomaly identifier. It is found that the PCA with five principal components gives better outlier detection performance than complex AEN in the considered task [226].

2.2.3. Nuclear Structure Inference

The momentum distribution of final state hadrons produced in heavy ion collisions has a clear dependence on the initial nuclear structure, which provides an opportunity to determine the initial nuclear structure using the final state hadrons in heavy ion collisions [227]. The momentum anisotropy as a function of the charged particle multiplicity is quite different for Pb+Pb and U+U collisions, where ²⁰⁸Pb is a double magic nucleus whose shape is close to a perfect sphere, while ²³⁸U has a shape close to a prolate watermelon. As a result, the collision geometry is much more complex in U + U collisions than in Pb + Pb collisions. Of course, nuclear structure is not limited to shape deformations. Other nuclear structures include the neutron skin [228], which reveals the difference between the distribution of protons and neutrons in the nucleus, the α cluster, which is crucial for the light nucleus, and the nucleon-nucleon correlation. A deep residual neural network is trained to predict the initial nuclear deformation [229] parameters β_2 and β_4 . The network was found to obtain the absolute values of β_2 and β_4 using distributions of geometric eccentricity and total entropy. Deep learning

is also used to classify whether there is α cluster structure in ^{12}C and ^{16}O using AMPT simulations of collisions between light nuclei [208, 230].

One difficulty in determining the nuclear structure using high-energy heavy ion collisions is caused by the effect of special relativity. On one hand, the nuclear structure information along the beam direction is strongly destroyed due to Lorentz contraction. On the other hand, fluctuations of sea quarks and gluons will participate in the collision due to time dilation. The size of the nucleons inside the nucleus may increase due to the parton cloud surrounding the nucleons. This will definitely change the initial fluctuations in the overlapped region of the colliding nucleus, e.g., the sizes of the hot spots in the initial entropy-density distribution. Fortunately, the Trento Monte Carlo model has taken this change into account for the initial condition.

Another difficulty in determining nuclear structure from high-energy heavy ion collisions is due to the evolutionary processes that link the initial state to the final observed particles. Such processes include pre-hydro evolution, hydrodynamic expansion, and hadron scattering, where many transport coefficients are undetermined. It has been proposed [231] that such a subtlety might be avoided in a contrast experiment for isobar systems — a pair of nuclei that have the same mass number but different electric charge, and therefore different nucleon structures. The ratio of the final state observables between the isobar collisions is expected to be sensitive only to the nucleon structure and not to the transport parameters. The natural question then arises as to whether it is possible to determine the nucleon structures of the isobar pair by focusing only on the ratio of the final state observables. In Ref. [232], the authors attempted to answer this question by taking the Monte Carlo Glauber model as an “emulator” to map the nuclear structure onto the final state particle distribution, and performing Bayesian inference of the nuclear structure parameters from different combinations of “mock data”. The authors found that it was not possible to constrain the structure for both nuclei simultaneously if only the ratios of the multiplicity distribution and the elliptical, triangular and radial flows were fitted. However, the authors found that simultaneous reconstruction is plausible if one includes the multiplicity distributions for both collision systems. Such a pioneering investigation paves the way for further nuclear structure studies in HICs using Bayesian inference based on more computationally expensive but realistic models for the final state particle distribution.

2.3. QCD Phase Diagram

2.3.1. Bayesian Analysis of QCD EoS at $\mu_B = 0$

Although the Lattice QCD predicts that the transition between QGP and HRG is a smooth crossover in the high temperature and zero baryon chemical potential region, there is no clear evidence from experimental data produced at RHIC and LHC. Ref. [233] uses Bayesian analysis to extract the speed of sound square c_s^2 as a function of temperature, with the help of relativistic hydrodynamic simulations and experimental data. The $c_s^2 = dP/d\epsilon$ is a direct measure of QCD EoS, comparing $c_s^2(T)$ from data with that given by Lattice QCD provides direct evidence of a smooth crossover.

The c_s^2 is parameterized as a function of energy density in the following,

$$c_s^2(\epsilon) = c_s^2(\epsilon_h) + \left(\frac{1}{3} - c_s^2(\epsilon_h) \right) \frac{X_0 x + x^2}{X_0 x + x^2 + X'^2} \quad (2.12)$$

where $X_0 = \sqrt{12}RX'c_s(\epsilon_h)$, $x \equiv \ln \frac{\epsilon}{\epsilon_h}$, ϵ_h is the energy density at $T = 165$ MeV, R and X' are the two parameters in the EoS to be determined. Randomly choosing R and X' from the range $-0.9 < R < 2$ and $0.5 < X' < 5$ generate the unconstrained EoS that varies in a large region between $c_s^2 = 0.05$ and $c_s^2 = 0.33$, as shown in Fig. 2.4-a. This corresponds to the a priori distribution of c_s^2 parameters together with other 12 parameters in the model $P(\theta)$.

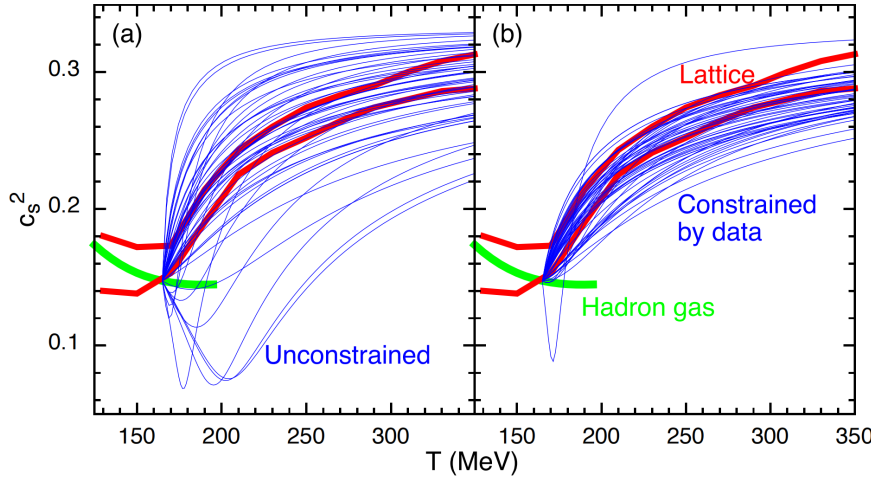


Figure 2.4: The prior and the posterior of the speed of sound square c_s^2 of hot nuclear matter using Bayesian analysis from Ref. [233].

The likelihood between experimental data and relativistic hydrodynamic outputs is given by,

$$P(D|\theta) = \prod_i \exp(-(z_i(\theta) - z_{i,\text{exp}})^2/2) \quad (2.13)$$

where D represent the experimental observables, $z_i(\theta)$ and $z_{i,\text{exp}}$ are the principle components of D from model outputs and the experimental data correspondingly. In Bayesian analysis, MCMC is used to sample θ from the posterior distribution of parameters $P(\theta|D) \propto P(D|\theta)P(\theta)$ to generate a batch of $c_s^2(T)$ curves. The EoS constrained by data is in good agreement with Lattice QCD calculations for $T > 150$ MeV.

Note that recently in Ref. [234] the Bayesian method has been successfully applied in constraining the density dependence of the QCD EoS for dense nuclear matter(at high μ_B) based on low energy HICs experimental data. Specifically, the mean transverse kinetic energy and integrated elliptic flow of protons from HICs in the beam energy range $\sqrt{s_{NN}} = 2 \sim 10$ GeV are taken as the evidence for the inference. Up to around 4 times nuclear saturation density ($4\rho_0$) the EoS is extracted from the analysis which describes other observables (the directed flow v_1 and the p_T dependent elliptic flow v_2).

2.3.2. Identify QCD Phase Transitions using CNN

Lattice QCD predicts that the transition between QGP and hadron resonance gas (HRG) at high temperature and zero baryon chemical potential is a smooth crossover [8]. It also produces the QCD EoS, which describes the pressure as a function of energy density. Using Bayesian analysis, the QCD EoS can be parameterized and used in relativistic hydrodynamic simulations of the HIC to extract the QCD EoS at the highest RHIC and LHC energies. The extracted EoS is in agreement with lattice QCD calculations [233]. It is conjectured that at high baryon chemical potentials, the transition between QGP and HRG is a first order phase transition. The endpoint of the first-order phase transition close to the crossover is called the critical endpoint. Tremendous efforts have been made to look for this critical endpoint (CEP) or region, including also the deployment of machine learning techniques.

Fig. 2.5 shows two different transition regions between QGP and hadron resonance gas (HRG) in the QCD phase diagram, the crossover region and the first order phase transition region. Different phase transitions lead to different equation of states (EOS). For crossover EOS, the pressure as a function of energy density (the blue dashed curve) is smooth in the region between QGP phase at high energy density and HRG at low energy density. For first order phase transition (the red solid line), the pressure as a function of energy density has a plateau between QGP phase and HRG

phase. As a result, the pressure gradient is zero in this region. Notice that the main driven force of fireball expansion is the pressure gradient. Difference of the pressure gradient in the phase transition regions between two EOS will lead to different evolution histories, which may encode the information of phase transition to the final state particles.

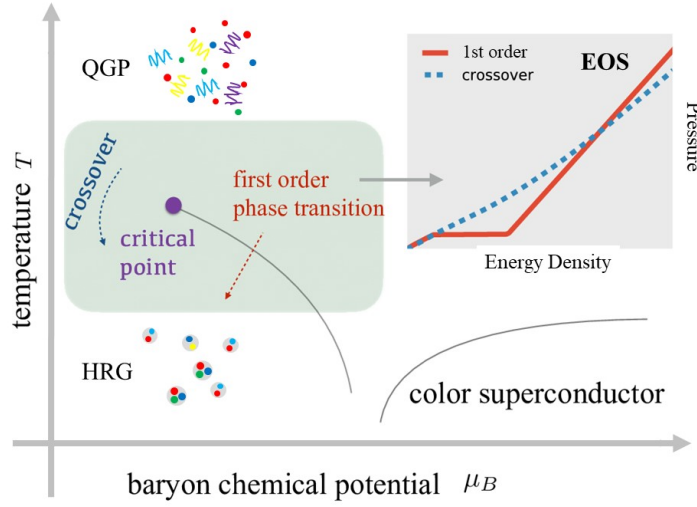


Figure 2.5: A schematic chart for QCD transition in the QCD phase diagram and the associated equation of state.

Fig. 2.6-(a) compares the energy density distributions in the transverse plane for 4 time snapshots, for two different EOSs in CLVisc relativistic hydrodynamic simulations. The evolution histories are visually different and can be easily distinguished by human. The energy density distributions using a EOS with crossover as shown in the first row is much smoother than that shown in the second row for a first order phase transition. However, the QGP will convert to hadrons through particlization and hadronic cascade, as shown in Eq. 2.6. What have been detected in experiment are the final state particles in momentum space. It is verified in [206] that the event-by-event distributions of traditional observables for 2 different EOSs almost overlap. The shape of the event-by-event distribution are also sensitive to the initial condition, the shear viscosity and the freeze out temperature. It seems that there is no way to identify the used EOS from the spectra of a single collision event.

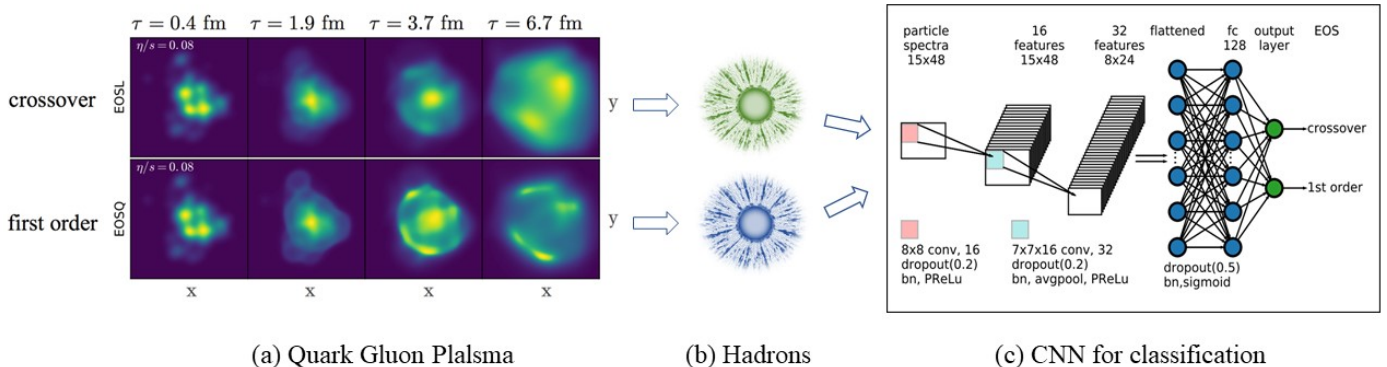


Figure 2.6: A schematic chart for QCD transition binary classification with CNN using final particle spectra from HIC as input.

Ref. [206] gives the first exploratory study of using deep learning techniques to directly connect the raw final state information from the HIC experiment to the bulk properties of this QCD phase transition type encoded in the EoS.

Inspired by the success of image recognition in computer vision, a deep convolutional neural network(CNN) is employed to learn and to directly represent the potentially existing inverse mapping from the final state information to the early time QCD matter bulk properties. Specifically, the CNN is used to classify two phase transition regions using simulated data from the parallelized relativistic hydrodynamics on GPU [206, 235, 236], with different EoS and phase transition types embedded in.

Fig. 2.6-(c) shows the schematic flow chart of the CNN. The input to the CNN is the the (p_T, ϕ) distribution of final state pions simulated by the CLVisc hydrodynamic model, with fluctuating initial conditions and different values of shear viscosity. The two dimensional spectra has 15 different p_T and 48 different azimuthal angle ϕ which serves as input images with 15×48 pixels. The output of the CNN have 2 neurons, representing the probability of the crossover and the first order phase transition, given by softmax activation as shown in Eq. 2.14,

$$\hat{y} = \begin{bmatrix} p_{\text{crossover}} \\ p_{\text{1st order}} \end{bmatrix} = \begin{bmatrix} \frac{e^{z_1}}{e^{z_1} + e^{z_2}} \\ \frac{e^{z_2}}{e^{z_1} + e^{z_2}} \end{bmatrix} \quad (2.14)$$

where \hat{y} is the discrete probability density distribution predicted by the network. z_1 and z_2 are the values of the last two neurons before the softmax activation. Multi-layer CNN and MLP are used to extracts correlations between particles in different momentum space in the input image, that can be used to make a final decision in the output layer.

The true label for crossover is $y = [y_1, y_2]^T = [1, 0]^T$, indicating that $p_{\text{crossover}} = 1$ and $p_{\text{1st order}} = 0$. The true label for 1st order phase transition is thus $y = [y_1, y_2]^T = [0, 1]^T$. The loss function contains a cross entropy loss between 2 distributions and the l_2 regularization term,

$$l(\theta) = -\frac{1}{m} \sum_{i=1}^m (y_1^i \log p_{\text{crossover}}^i + y_2^i \log p_{\text{1st order}}^i) + \frac{\lambda}{2} \|\theta\|_2^2 \quad (2.15)$$

where θ represents all the trainable parameters such as the matrix elements in the convolution kernels, the weights and bias in the MLP. m is the mini-batch size. The index i represents the i -th sample in the mini-batch. The $\|\theta\|_2 = \sqrt{\sum_k \theta_k^2}$ is the l_2 -norm used to constrain the magnitude of model parameters. The λ is a small number set manually. After trained, the network generalizes well to data generated with another relativistic hydrodynamic model (iEBE-VISHNU [161]), or to data generated with CLVisc with different initial conditions. In average, the prediction accuracy achieves 93%.

It is worth noting that, the demonstration in Ref. [206] of using deep CNN to identify the QCD transition types from the final pion's spectra is only on the level of pure hydrodynamic evolution, with its superb classification accuracy in the testing stage clearly indicating that: the early time transition information especially its types within hydrodynamics (mimicking HICs) evolution can survive to the final state. The constructed inverse mapping by the trained deep CNN also shows robustness to different initial fluctuations and shear viscosities. In modeling heavy ion collision with more realistic consideration, hybrid simulations combining hydrodynamics together with after-burner hadronic cascade transport become more appropriate. Accordingly, for HICs this strategy of using supervised learning to capture the inverse mapping from final accessible information to early time desired physics could be further deepened.

Indeed, later, the same method is used to classify the EoS using final state hadrons sampled from the freeze-out hypersurface and passing through the hadronic cascade via UrQMD [237]. Both the stochastic particlization being followed by hadronic rescattering and the resonance decay effects are taken into account in producing the final state pion spectra $\rho(p_T, \phi)$. Initially, it was found that the accuracy for CNN with event-by-event spectra is significantly lower than that using smooth particle spectra in pure hydrodynamic case. This performance decline manifests the concealing over the fingerprint of QCD transition inside final state, by the fluctuations due to finite particles and resonance decay. A

scenario with event-fine-averaged spectra as input is investigated, where the performance is showed to be greatly improved by feeding such averaged spectra with 30 events within the same fine centrality bin into the deep CNN. See Fig. 2.7 for a performance comparison from Refs. [237, 238].

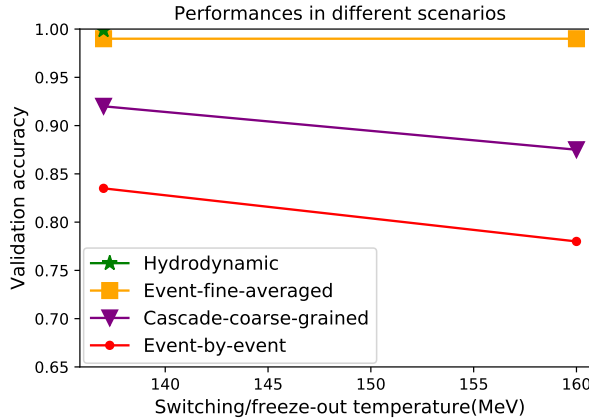


Figure 2.7: Taken from [237]. Comparison between the validation accuracy in all the different sub-scenarios studied. The green star depicts the pure hydrodynamic result [206]. The orange square, the purple triangle and the red filled circle symbols depict the results for the 30-events-fine-averaged, cascade-coarse-grained and event-by-event spectra, respectively, in different switching temperatures.

2.3.3. Learning Stochastic Process with QCD Phase Transition

The aforementioned EoS identification assumes that the phase transition process involved in the entire HICs evolution take place in equilibrium states. However, the actual collisional evolution dynamics, especially the phase transition process involved, should be a non-equilibrium evolutionary behavior. It is nontrivial to uncover the phase transition and involved dynamical information from a stochastically evolving dynamical system. Refs. [239, 240] generalized the idea of identifying transition type from HICs final state further, to recognize the phase order and extract the dynamical parameters in a stochastic dynamical process would happen in HICs. The general thermodynamics and phase behavior of QCD can be reasonably approximated by a linear sigma model [241], the effective potential of which describes the crossover transition at small chemical potentials and the first-order phase transition at large chemical potentials. As simplified modelling to the phase transition processes in HICs, the Langevin equation is adopted to describe the semi-classical evolution of the long wavelength mode of the sigma field,

$$\partial^\mu \partial_\mu \sigma(t, x) + \eta \partial_t \sigma(t, x) + \frac{\delta V_{eff}(\sigma)}{\delta \sigma} = \xi(t, x), \quad (2.16)$$

with the effective potential V_{eff} controlling the type of phase transition in the stochastic process. The damping coefficient η , and the noise term $\xi(t, x)$, follow the fluctuation-dissipation theorem. As a simplified description for HICs, Hubble-like decaying temperature field and constant baryon chemical potential are assumed for the heat bath. A Gaussian-type spatial noise with different overall strengths is adopted for ξ to inject fluctuations associated with the phase transition. Then a deep CNN, as shown in the left panel of Fig. 2.8, is devised to detect possible QCD phase transition order and predict the damping coefficient from the recorded σ field spatio-temporal configurations in later stage of the non-equilibrium evolution. It is shown that the trained CNN is able to identify the encoded phase transition to be cross-over or first-order based on the final stage stochastic evolution of the field, which works even on different magnitude of noise, see middle panel of Fig. 2.8. For the damping coefficient prediction, the network gives a performance with on average $R^2 = 0.97$ in

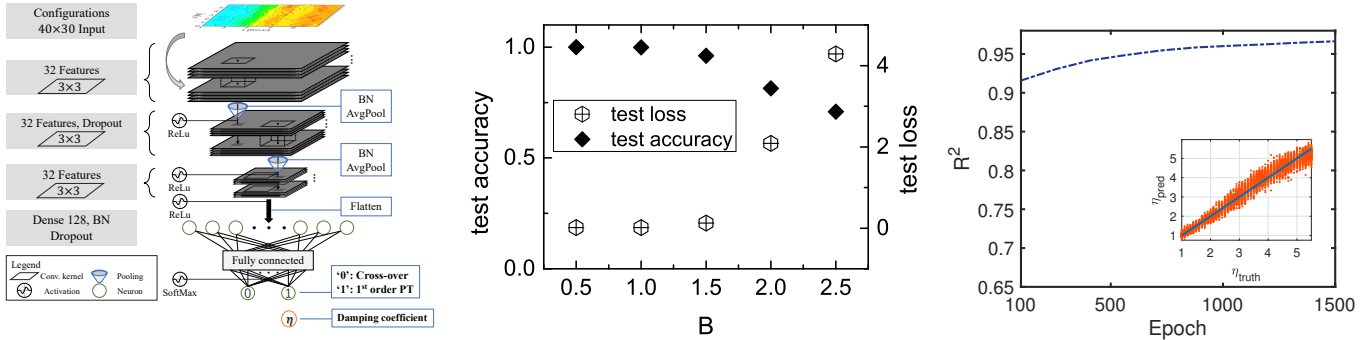


Figure 2.8: Taken from Refs. [239, 240]. (left) the deep CNN for phase transition identification and damping coefficient regression; (middle) phase order classification accuracy in the testing stage with different spatial noise magnitude B ; (right) the regression performance for damping coefficient during training and comparison to ground truth.

the scenario of first-order phase transition, as shown in the right panel of Fig. 2.8.

2.3.4. Point Cloud Network for Spinodal Clumping Identification

Several follow-up studies used convolutional neural networks (CNNs) to map final particle spectra to EoS types within hadronic transport models [242–244] or nuclear symmetry energy [245]. The CNN is the state-of-the-art for image recognition, so the momenta of the final state particles have to be converted into images. This is done by density estimation in (p_x, p_y) space or (p_t, ϕ) space using 2-dimensional histograms. In both cases, there is a loss of information just from this pre-processing to the final state. As also been introduced in Sec. 2.2.1, the natural data structure of particles in momentum space is a *point cloud*, where each particle is a point in momentum and feature space. The *PointCloud network* is used to classify two first-order phase transitions with Maxwell and spinodal constructions [207]. With the latter construction, QGP evolves into many blobs that hadronize separately. However, it is rather difficult to distinguish the equation-of-state type from the final state hadrons in momentum space. Another point cloud neural network is trained using reconstructed tracks of final state hadrons given by the CBM detector simulations [246]. It was found that the performance decreases when considering realistic detector acceptance cuts and resolution. On the other hand, the performance improves when multiple events are combined.

Shown in Fig. 2.9 is a simple point cloud network used classify two different equation of state. The point cloud network uses an MLP to transform the momentum and species information of each particle into a high-dimensional feature space (128 dimensions in this example). This MLP is shared by all particles in the cloud, so it is also called a 1-dimensional CNN. Notice that CNN is not a specific technique for image processing, any operations having the properties of local connection and weight sharing can be called CNN. Afterwards, a permutation-symmetric operations is used here to extract the multi-particle correlations hidden in the point cloud. A commonly used permutation-symmetric operation is the Global Max Pooling that is able to extract the boundaries of this point cloud in high-dimensional feature space, as shown below,

$$f_i = \max(\{f_{ij}\}, \text{along } j) \quad (2.17)$$

where $\{f_{ij}\}$ is the feature matrix with i denoting the i -th feature, j representing the j -th particle and $f_{ij} = \text{MLP}_i(\vec{p}_j)$, f_i is the maximum value of the i -th feature among all the particles in the cloud, extracted by the Global Max Pooling. Note that other permutation-symmetric operations can be used here to replace the global max-pooling. For example, the

widely used Global Average Pooling is shown below,

$$f_i = \frac{1}{N} \sum_{j=1}^N f_{ij} \quad (2.18)$$

where N is the number of particles in the cloud.

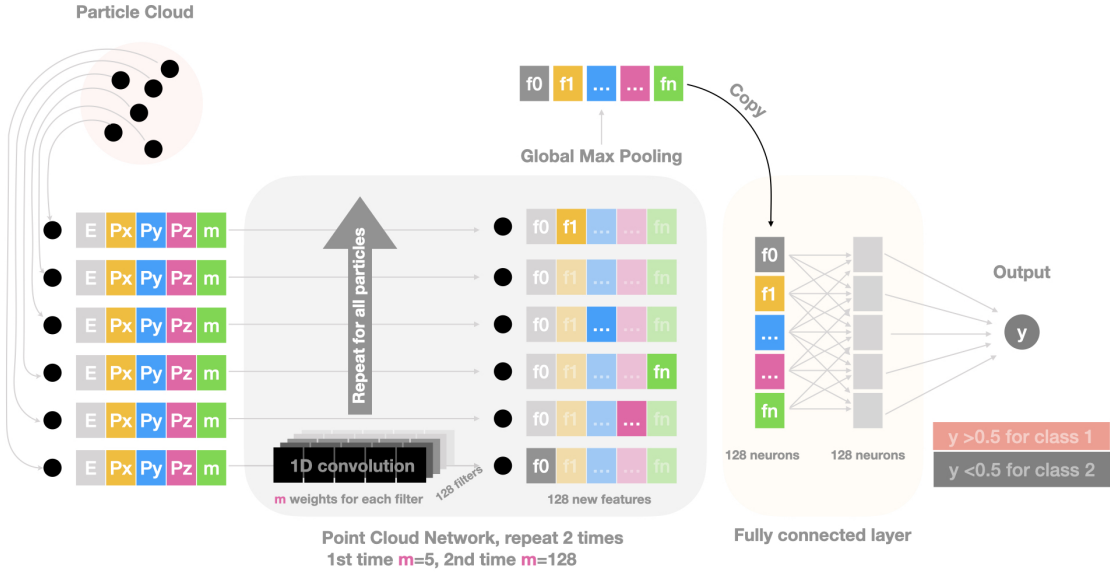


Figure 2.9: A simple point cloud network used to classify two kinds of first order phase transitions.

In principle, the point cloud network trained with 100 particles can be applied to a point cloud with 1000 or more particles, as the MLP is shared by all particles and the permutation-symmetric operation is not sensitive to the number of particles. The number of particles may be different for different particle clouds produced in different HIC events. However, implementing a deep neural network with varying number of input particles during training meet technical difficulties, because a mini-batch of input data are required to have the same shape for GPU parallel acceleration. Padding is usually used to produce the same number of particles in each cloud. There are different ways of padding, e.g., a list of virtual particles whose properties are all zeros, or particles from other events can be added which have no correlation with particles in the current event. To eliminate the effect of padding particles, another property can be added to each particle, called a "mask". The masks are equal to 1 for real particles in the cloud, but 0 for padding particles. Using these masks, the padding particles will not participate in the global max(average) pooling.

2.3.5. Dynamical Edge Convolution Network for Critical Similarity

There are rich critical phenomena near the critical endpoint, such as fluctuation enhancement and the emergence of self-similarity. The self-similarity in momentum space is modelled by Critical Monte Carlo (CMC) and encoded in the interparticle distances in momentum space. If self-similarity is present in only a few percent of all final state hadrons, the signal-to-background ratio is small. Traditionally, intermittency analysis is used to search for self-similarity in momentum space. However, this method fails at the current experimental p_T resolution of about 0.1 GeV/ c . A point cloud network and a dynamical edge convolution neural network are used to identify events with interparticle similarity and to label correlated particles [247]. The dynamical edge convolution network succeeds with a test accuracy of 92% on events with

5% signal particles. The method developed here appears to be powerful in searching for multi-particle correlations that are sensitive to specific physics.

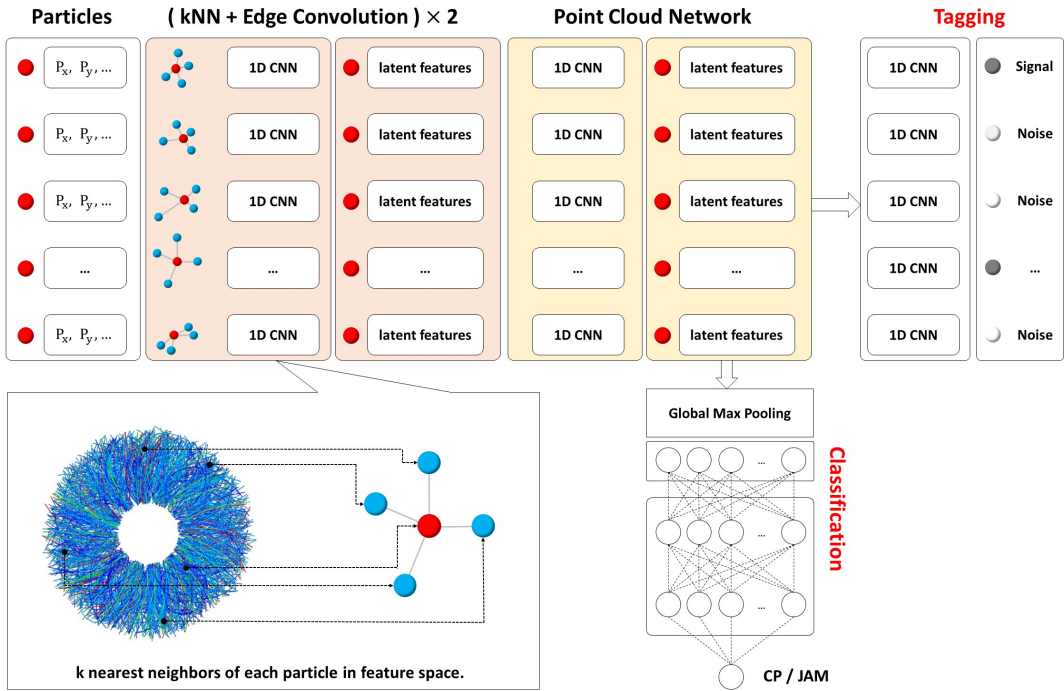


Figure 2.10: A schematic diagram of critical self-similarity search with a dynamical edge convolutional neural network using the HIC particle cloud as input. Taken from [247].

Fig. 2.10 shows the structure of the dynamical edge convolutional neural network used to search for multi-particle correlations in the particle cloud. The input to the network is a particle cloud produced in heavy ion collisions, with multiple features for each particle. The output of the network has two branches, one for classification and the other for tagging. The dynamic edge convolutional neural network extracts correlations between multiple particles to build a map between the input and output. Each input particle can have the four momenta, the charge, the baryon number, or the strange number as properties. In practice, the four momentum is usually normalized to the maximum energy of all particles in the cloud. Other quantum numbers can also be normalized to values between -1 and 1 .

In the dynamic edge convolution network, the k nearest neighbors of each particle are used to capture the multi-particle correlation. In the first layer, the distances between different particles in coordinate or momentum space are computed to explicitly determine the neighbors. A fully connected neural network (MLP) is used to compute the correlation between the central particle and one of its neighbors, using the following formula

$$e_{ij} = \text{MLP}(p_i, p_j) \quad (2.19)$$

where e_{ij} is the edge feature between particle i and particle j , the p_i represent the input features of particle i . This MLP network is shared by each pair of particles to produce edge features. The name "edge convolution" comes from the fact that the MLP is locally connected and its weights are shared among all edges. After the first edge convolution, there is a point cloud network that transforms the input of each particle together with its neighbors into a high-dimensional latent space, whose input is a concatenation of the central particle and its k edge features,

$$f_i = [p_i, e_{i1}, e_{i2}, \dots, e_{ik}]. \quad (2.20)$$

Using the features f_i in the high-dimensional latent space, the edge convolution can be applied again and again. As a result, the k nearest neighbors of each particle are determined by the distances between different particles in feature space afterwards. In other words, particles can be close in feature space but far apart in momentum space, allowing the network to capture long-range multi-particle correlation, which is critical for some specific classification or tagging tasks.

2.3.6. Active Learning for Unstable Regions in QCD EoS

Active learning is a sub-field of machine learning which can get higher accuracy using fewer labels [248]. This is achieved by allowing the machine to choose data from which it learns. The motivation of using active learning is that labels may be difficult to obtain in some tasks (expensive or time consuming) and the machine can learn better on some instances than on others. Active learning starts with a small labeled data set for supervised training. The trained model is used to make predictions about samples from a large unlabeled pool, as Figure 2.11 shows. If the network is uncertain about a sample, e.g., the sample is predicted to be stable with probability 51% and unstable with probability 49%, it is labeled and added to the labeled dataset for further supervised training. Labels can be made by human in the loop or by computer programs. The key of active learning is to propose samples for labelling, the first method is to use the uncertainty criterion as mentioned above, which is the entropy of the prediction,

$$s = - \sum_i p_i \log p_i \quad (2.21)$$

where p_i is the predicted probability that the sample is in the i th category. The entropy s is known to be maximized if the predicted distribution is uniform. The entropy criterion is similar to the margin criterion $m = p_1 - p_2$, where p_1 and p_2 are the first and the second most probable category labels for input x , predicted by the pretrained network. There are other criterions based on which the machines make their proposal. For example, four neural networks can be trained in parallel and vote on samples from unsupervised pool. If their judgements disagree the most on one sample, that sample will be voted for labelling. Another criterion is the gradient which quantifies how much the machine will learn from this instance. The negative gradients $-\partial l / \partial \theta$ have dependence on the input, it is thus possible to choose input that leads to the largest change to the network for labelling.

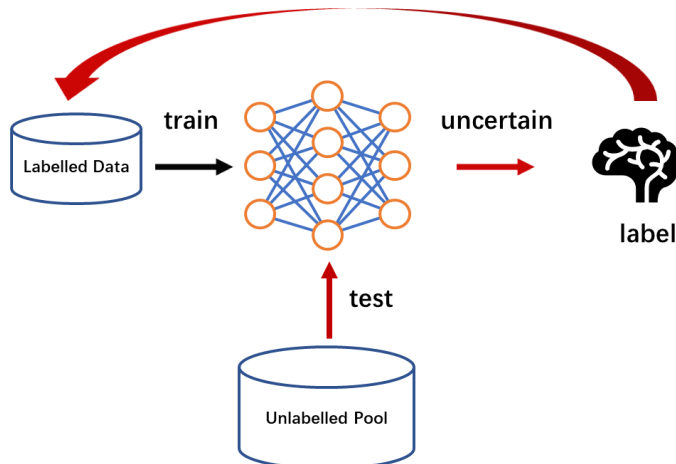


Figure 2.11: A schematic diagram of active learning.

Ref. [249] uses active learning to detect thermodynamically unstable and acausal regions in QCD EoS. Lattice QCD

fails to produce the QCD EoS around the critical endpoint region due to the sign problem (it will be discussed in the next section). The Beam Energy Scan Theory (BEST) collaboration [250] constructs a QCD EoS by mapping the 3D Ising model and the lattice QCD EoS. However, the shape and position of the critical region depend on several parameters. Some parameter combinations lead to unstable and acausal QCD EoS that should be discarded in the future model to data comparisons, as the hybrid model of HIC is computationally expensive and sensitive to acausal EoS in the medium.

The pressure is a sum of the contributions from Lattice QCD and the 3D Ising model as demonstrated in [250],

$$P(T, \mu) = P_{\text{lattice}}(T, \mu) + P_{\text{Ising}}(T, \mu) \quad (2.22)$$

where the pressure from Lattice QCD calculations at non-zero baryon chemical potential μ is given by the Tylor expansion around $\mu = 0$,

$$\frac{P_{\text{lattice}}(T, \mu)}{T^4} = \sum_n c_n(T) \left(\frac{\mu}{T}\right)^n \quad (2.23)$$

where the coefficients are $c_n(T) = \frac{1}{n!} \chi_n^B(T) = \frac{1}{n!} \frac{\partial^n P/T^4}{\partial(\mu/T)^n}$, the χ_n^B is the n th order baryon susceptibility. Using the pressure provided above, the complete thermal dynamic relations are given below,

$$\frac{n_B(T, \mu)}{T^3} = \frac{1}{T^3} \left(\frac{\partial P(T, \mu)}{\partial \mu} \right)_T \quad (2.24)$$

$$\frac{s(T, \mu)}{T^3} = \frac{1}{T^3} \left(\frac{\partial P(T, \mu)}{\partial T} \right)_\mu \quad (2.25)$$

$$\frac{\epsilon(T, \mu)}{T^4} = \frac{s(T, \mu)}{T^3} - \frac{P(T, \mu)}{T^4} + \frac{\mu n_B}{T T^3} \quad (2.26)$$

There are 4 parameters in total, whose combinations determine the size and the shape of critical endpoint in QCD EoS, as well as the stability and the causality of the derived EoS,

$$(\mu, \alpha_{\text{diff}}, w, \rho) \mapsto P(T, \mu) \mapsto \{\text{acceptable, unstable, acausal}\} \quad (2.27)$$

where stability requires the positivity of the energy density ϵ , the pressure P , the entropy density s , the net baryon density n_B , the second order baryon susceptibility χ_2^B and the heat capacity $(\frac{\partial s}{\partial T})_{n_B}$. The causality requires that the speed of sound square satisfies $0 \leq c_s^2 \leq 1$. Any parameter combinations that lead to unstable or acausal EoS will be discarded.

2.4. Dynamical Properties of QCD Matter

2.4.1. Shear and Bulk Viscosity

Relativistic hydrodynamic simulations indicate that the QGP produced in HIC is a strongly coupled plasma [251–253] whose shear viscosity over the entropy density ratio η/s is close to the universal limit $\frac{1}{4\pi}$ by AdS/CFT calculations [254]. Both η/s and ζ/s strongly influence the collective expansion of hot nuclear matter [255], leaving clear signals in the momentum anisotropy of final state hadrons produced in HIC. However, to quantitatively determine the values of η/s and ζ/s from the final state hadrons, one faces the difficult inverse problem described above. There are two difficulties, the entanglement between different model parameters and the temperature dependence of $\eta/s(T)$ and $\zeta/s(T)$. Ref. [256] shows that relativistic hydrodynamic simulations with different fluctuating initial conditions can all describe data, with different effective shear viscosity. For example, using “IPGlasma” initial condition in MUSIC hydrodynamic model, the simulation describes the event by event fluctuations of v_n , the mean v_n and the $v_n(p_T)$ with constant $\eta/s = 0.12$ at RHIC

energy and $\eta/s = 0.2$ at LHC energy [257]. Using ‘‘MC-KLN’’ initial condition in VISHNU hydrodynamic model, the simulation describes the charged multiplicity, the p_T spectra as well as the elliptic flow at both RHIC and LHC energy, with constant shear viscosity to entropy ratio $\eta/s = 0.16$ [258]. Using NLO improved EKRT initial condition in viscous hydrodynamics, it was observed that both the constant $\eta/s = 0.2$ and a temperature dependent $\eta/s(T)$ give equal good overall fitting to RHIC and LHC data. The used linear parametrization is $0.12 < \eta/s < 0.12 + (0.18/320)(T/\text{MeV} - 180)$ for temperature above 180 MeV in the QGP phase and $\eta/s(T) = 0.12 - (0.20/80)(T/\text{MeV} - 180)$ for temperature below 180 MeV in the hadron resonance gas phase. To quantitatively constrain the temperature-dependent shear and bulk viscosity, a global analysis on all available RHIC and LHC data using Bayesian parameter estimation is required [116–118, 142, 233, 259–261].

Ref. [116, 142] use Trento + IEBE-VishNew + UrQMD hybrid model to do a global fitting to the charged multiplicity, the transverse momentum spectra, the centrality dependence of the elliptic flow and the triangular flow, which helps to constrain both the parameters in the initial condition and the temperature-dependent shear and bulk viscosity. The study shows that the extracted initial condition agrees with the gluon saturation model, and there is a clear signal of non-zero bulk viscosity.

A set of nine model parameters in total are constrained using Bayesian analysis, whose posterior distributions are given in Fig. 2.12. These parameters include:

1. Norm, the overall normalization factor determining the initial total entropy that is responsible for the multiplicity of final state hadrons;
2. p , the entropy deposition parameter, which is used to mimic different kinds of initial entropy production, from MC-Glauber to saturation-based models;
3. k , multiplicity fluctuation shape parameter, which determines the multiplicity distribution in minimum-bias proton+proton collisions;
4. w , Gaussian nuclear width, which determines the size of nucleons during collision;
5. $(\eta/s)_{\text{hrg}}$, a constant parameter for the value of η/s in hadron resonance gas phase;
6. $(\eta/s)_{\text{min}}$, the minimum η/s at the critical temperature $T_c = 154$ MeV;
7. $(\eta/s)_{\text{slope}}$, the slope of $\eta/s(T)$ above the critical temperature T_c ;
8. ζ/s norm, one overall normalization factor for the given $\zeta/s(T)$ function;
9. T_{switch} , the particlization temperature.

These parameters form a nine-dimensional parameter space. Each point in this space represents one combination of model parameters. Without constraining, values of these parameters vary in a given range provided by physical a priori. According to Bayesian parameter estimation, un-normalized posterior distributions of these parameters are given by $P(\theta|D) \propto P(D|\theta)P(\theta)$, where the experimental data D used in the Bayes formula is composed of dN/dy , mean transverse momentum $\langle p_T \rangle$ for π^\pm , K^\pm , $p\bar{p}$ at mid-rapidity and two-particle cumulants $v_n\{2\}$ with $n = 2, 3, 4$ of charged hadrons, at various different centrality classes. The likelihood $P(D|\theta)$ is computed using the model output and experimental data. The prior $P(\theta)$ is usually chosen to be a uniform distribution. It shall be worth mentioning that the computationally

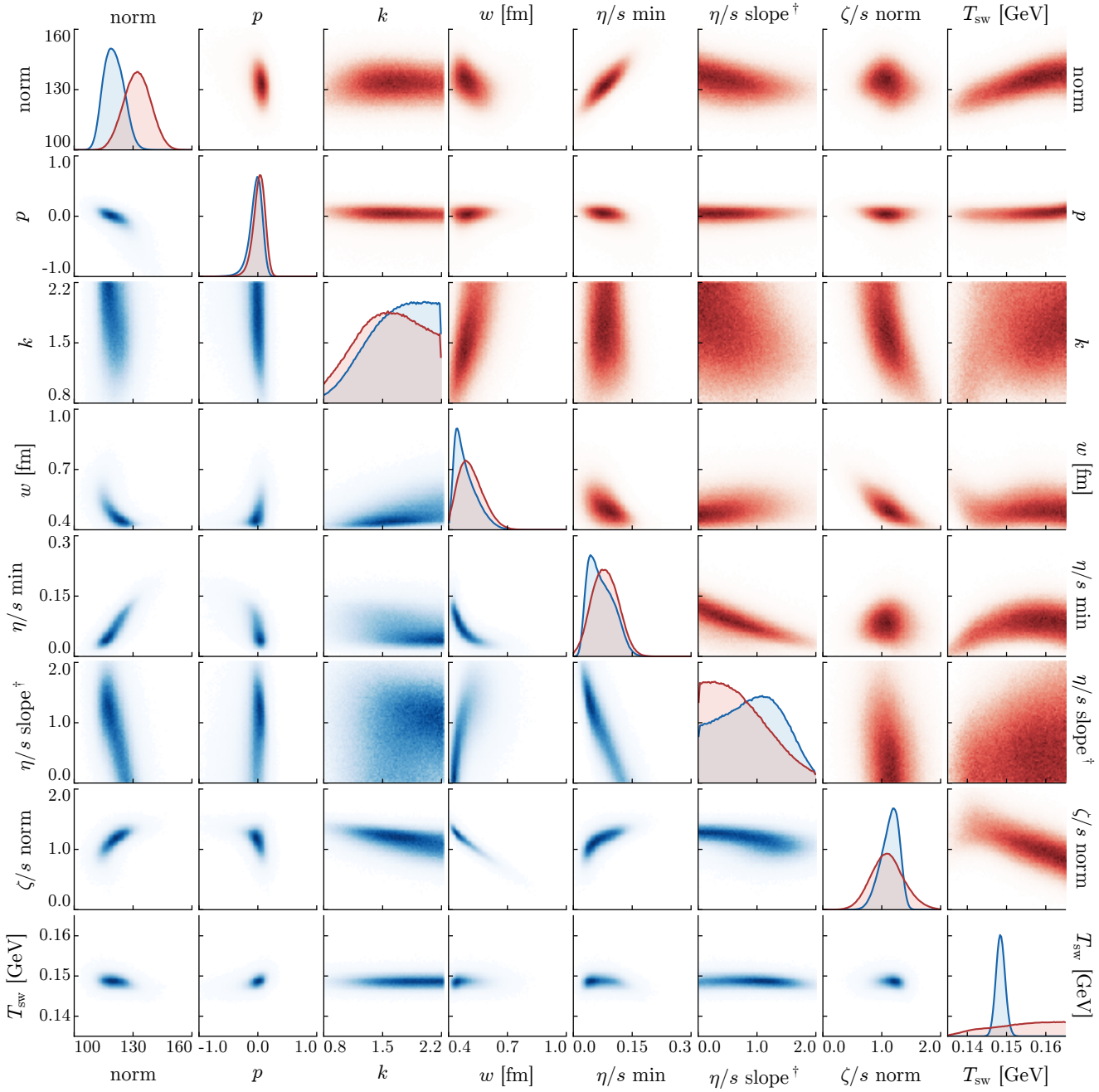


Figure 2.12: The posterior distribution of nine model parameters for initial condition and transport coefficients using Bayesian analysis. Taken from [142].

expensive HIC simulations are run for a finite number of parameter sets and then emulated by a Gaussian process (see Sec. 2.5.1 for more details).

The diagonal subplots in Fig. 2.12 show the marginal distributions of these 9 parameters. The posterior distribution in red color is constrained using charged particles, while the distribution in blue color is constrained using identified particles. For many parameters, the optimal values differ using these two groups of experimental data. However, the marginal distributions of p and ζ/s norm have narrow peaks whose locations agree with each other using two groups of data. The results indicate that the initial condition agrees with saturation-based models, and the bulk viscosity is clearly non-zero.

Follow up Bayesian Inferences of transport parameters are performed by the JETSCAPE collaboration [117, 260] and Nijs et al [118, 261]. These independent researches take different experimental results as evidence and focus on different parameters. The former focused on p_T averaged observables in both RHIC and LHC energies, whereas the latter looked into the p_T differential ones in LHC collisions. A clear tension is observed in the bulk viscosity, which reveals the model dependence in the parameter extraction and calls for further investigation.

Bayesian Inference provides a statistically systematic way to make full use of the low-dimensional observables⁷ provided by experiment as well as the physical prior, where the uncertainty of the inference can be properly estimated with the experimental error and theoretical modelling error being able to be incorporated. However, most of the Bayesian analysis in HICs use handcrafted parametrizations for many of the inference targets (e.g., EoS or shear viscosity's temperature dependence) thus the final results may be limited or dependent on the setup and also priors. The other concern lies in the probable information loss of using only low-dimensional processed “observations” instead of the original high-dimensional raw record. A naive pushing forward for Bayesian inference to, e.g., event-by-event quantity analysis would hugely increase the computational demanding and time. Direct mapping capturing by deep learning or combining deep generative models into traditional Bayesian Inference are thus necessary alternatives.

2.4.2. Jet Energy Loss in Hot QGP

As energetic partons pass through the hot QGP, they lose energy through elastic scattering and inelastic gluon radiation. The energy loss of the jet thus serves as a good probe of the properties of the medium. Bayesian analysis is used to study the temperature and momentum dependence of the heavy quark diffusion parameter [262], the jet quenching or transverse diffusion coefficient \hat{q} [263] and the jet energy loss distributions [264]. Bayesian analysis typically assumes a parameterized function whose parameters are determined by maximum a posteriori (MAP) estimation. Recently, the information field has been used to generate random functions that can be used as a model for Bayesian analysis to obtain the temperature-dependent $\hat{q}(T)/T^3$ using both RHIC and LHC data [265]. The information field provides a non-parametric representation of the unknown function, which can eliminate the unnecessary long-range correlations in the prior. Fig. 2.13 shows the application of Bayesian parameter estimation in determining the jet energy loss distribution [264]. The jet cross-section is approximated by the convolution between p+p jet cross-section and the jet energy loss distribution function, where the latter is parameterized using a Gamma distribution function,

$$W_{AA}(x) = \frac{\alpha^\alpha x^{\alpha-1} e^{-\alpha x}}{\Gamma(\alpha)}, \quad (2.28)$$

⁷i.e., preprocessed and projected from original detector raw record to expert designed quantities like elliptic flow or p_T spectra within rapidity cut and centrality bin.

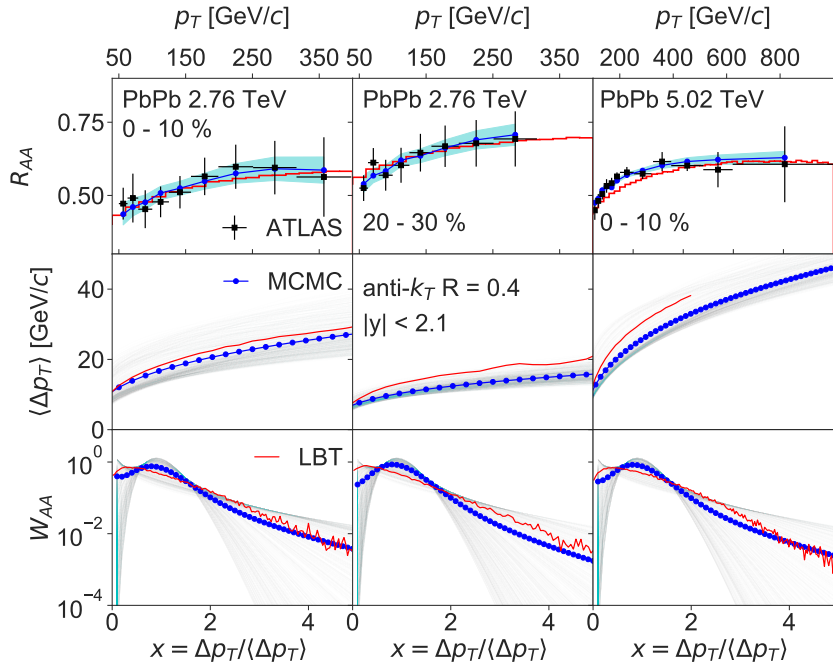


Figure 2.13: The extracted jet energy loss distribution and the computed R_{AA} as compared with Linear Boltzmann Transport model calculations. Taken from [264].

where $x = \Delta p_T / \langle \Delta p_T \rangle$, α can be interpreted as the average number of jet-medium scatterings that take energy out of the jet cone. The energy per scattering is thus $\langle p_T \rangle / \alpha$ with the mean transverse momentum loss as a function of p_T defined as follows,

$$\langle \Delta p_T \rangle (p_T) = \beta p_T^\gamma \log p_T. \quad (2.29)$$

Note that the function form of the averaged energy loss is motivated by theoretical calculations [183]. There are thus three parameters (α, β, γ) in the modification factor R_{AA} to be constrained using the Bayesian analysis. The first row of Fig. 2.13 demonstrate that the R_{AA} calculated from the constrained jet energy loss distribution is in good agreement with experimental data in Pb+Pb 2.76 and 5.02 TeV collisions. The second and the third row compare the mean p_T loss and the energy loss distribution $W_{AA}(x)$, as compared with Monte Carlo simulations using the Linear Boltzmann Transport model. The extracted value of α is small, indicating a large transverse momentum loss per scattering. The results suggest that the observed jet quenching is mainly caused by a few out-of-cone scatterings.

2.4.3. Jet Classification and Jet Tomography

Various studies have been carried out to study jets in particle physics[266–281] and heavy ion collisions [282–287], please refer [29] for a more complete list. The machine learning based jet-flavor and event classifications may find their applications in the future electron-ion collider[288]. The machine learning-assisted jet-flavor tagging, such as the u-d, ud-s, uds-c binary classification may be important to determine the collinear and transverse momentum dependent PDFs [289]. The qq/q̄ – g classification and the direct .vs. resolved photon classification may provide additional constraints to the parton-in-photon PDFs. The classifications of e+P and e+A collisions may help to find observables that are sensitive to the cold nuclear effect. It is also proposed that the charm and anti-charm tagging in di-jet events can help to constrain the gluon TMD and the gluon Sivers function [290]. Jet substructures are proposed to be able to constrain the gluon

PDF [291].

Ref. [284] uses deep learning to discriminate the vacuum-like jet ($p+p$ collisions) and the jet in medium ($Pb+Pb$ collisions). This helps to identify the effect of jet quenching in the presence of QGP in $Pb+Pb$ collisions. The lost energy as well as the charged particle distributions inside a jet cone can be used as input to a deep neural network to predict the initial jet energy and their production positions [285–287]. The machine learning assisted jet tomography can be used to select jet events with similar initial energy or production locations, for a more detailed differential study.

The machine learning assisted jet tomography is employed to study Mach cones produced in high energy heavy ion collisions [287]. Mach cones are expected to form in the smallest nuclear liquid droplet when energetic partons traverse through QGP and deposit energy and momentum in QGP [292–304]. The speed of hard partons is close to the speed of the light, which is much larger than the speed of sound c_s of QGP. There is a simple formula that relates the half-angle θ of Mach cone to the speed of sound c_s and the nuclear equation of state (pressure as a function of energy density),

$$\frac{dP}{d\epsilon} = c_s^2 = \sin^2 \theta \quad (2.30)$$

where P is the local pressure and ϵ is the local energy density of hot nuclear matter. The Mach cone angle thus provides a direct probe of the QCD EoS, if its effects on the final state hadrons are well understood.

In practice, the Mach cones are difficult to find because the jets are generated at different positions and travel in different directions [295]. The shape of the Mach cones will be affected by both the temperature gradients and the strong collective flow [305]. As shown in Fig. 2.14, the medium response is stronger for jets that travel a longer path length (jets initiated from $y = -3.0$) than those travel a shorter path length (jets initiated from $y = 3.0$) in QGP. On the other hand, the shape of the Mach cone and the associated diffusion wake is deformed depending on the initial jet production position and the collective flow on the jet trajectory. For jet initiated from $x = -3, y = -3$, the medium response is stronger for the right wave front than its left branch. This is caused by the increased temperature and parton density in the central region of QGP, which leads to increased number of scatterings between jet parton and thermal partons. The diffusion wake is also affected by the strong radial flow which pushes the medium response outwards. One can imagine that the effect of medium response, the signals of Mach cone and the diffusion wake will all be amplified if it is possible to determine the initial jet production positions for event selection.

Authors in Ref. [287] use a point cloud network to determine the initial jet production positions, which helps to select jets with similar path lengths and directions that is shown to be able to amplify the signal of 3D mach cones. The network in this study uses two different kinds of inputs, one is the point cloud in momentum space for particles with $p_T > 2$ GeV, the other is the global information of γ -trigger and the full jet. These features are manipulated differently. The particle cloud goes through a point cloud network and global max pooling, while the global information is processed using a simple MLP. Two inputs are concatenated to make the final decision. The neural network output two real numbers to represent the initial jet production locations. This is a regression task that is solved using supervised learning. The training data is generated using LBT and CLVisc. After trained, the network is able to predict the initial jet production positions approximately.

The machine learning assisted jet tomography is used to select events for jets initiated from the same region. Fig. 2.15 shows the angular correlation between the final state hadrons and the jet, for jet partons initiated from 4 different regions. The magnitudes of the angular correlation in sub-figures (f) and (h) are stronger than (e) and (g), as the path lengths in these events are selected to be larger. The suppression of hadrons in the opposite direction of jets is caused by the diffusion wake. Constraining initial jets to the left half of the QGP fireball will introduce asymmetric angular

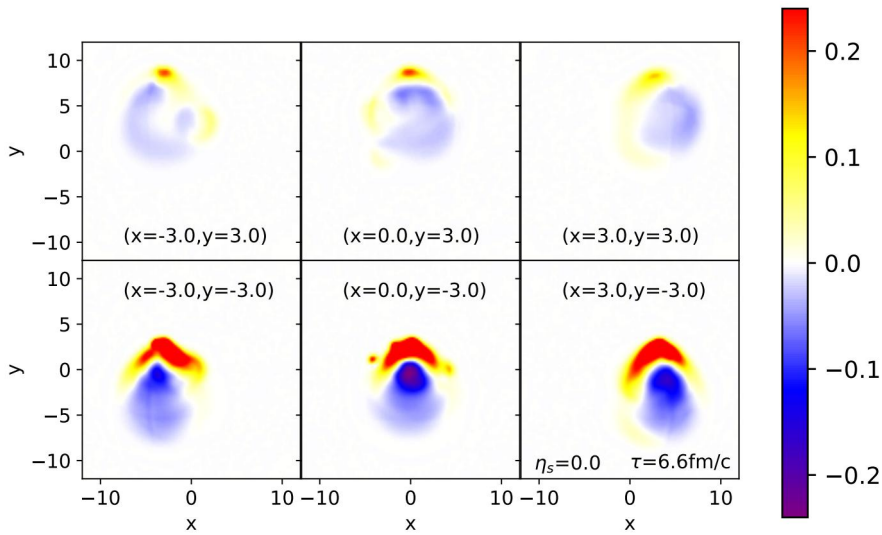


Figure 2.14: The shape of Mach cones for jets that are initiated at different positions and travel in the same positive- y direction. Reproduced from Ref. [287].

correlation, which reflects the effect of radial flow to the diffusion wake. Observing these features in experimental data using machine-learning assisted jet tomography will provide direct evidence of the existence of Mach cones and diffusion wake.

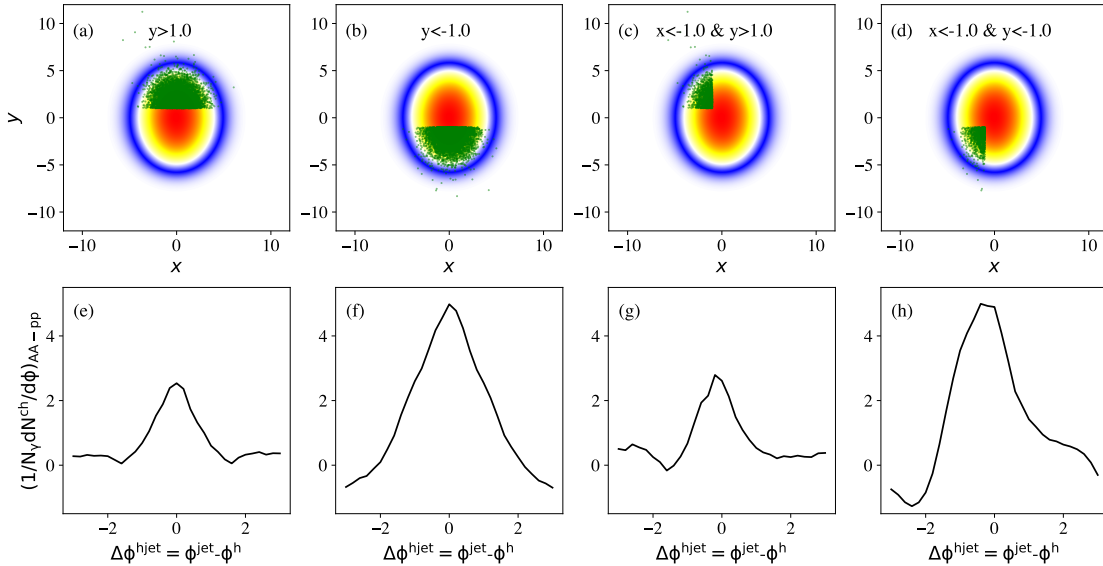


Figure 2.15: The hadron-jet angular correlation for selected jet events that are initiated from different regions in the transverse plane. Reproduced from Ref. [287].

2.4.4. Chiral Magnetic Effect Detection

The chiral magnetic effect (CME) is a phenomenon that occurs in chiral matter, where the combination of a chiral anomaly and a magnetic field leads to the separation of electric charges along the direction of the magnetic field [306]. The CME is important in the study of the quark-gluon plasma (QGP) created in HIC experiments [307]. Recently, researchers have been trying to search for this effect in HICs [308–310], but the traditional methods (e.g., γ -correlator) have proven

to introduce large amounts of background contamination, e.g., the elliptic flow, global polarization and indeterminate background noises. Zhao et al. have developed a *CME-meter* using a deep convolutional neural network (CNN), to analyze the entire final-state hadronic spectrum as big data and reveal the distinctive signatures of CME.

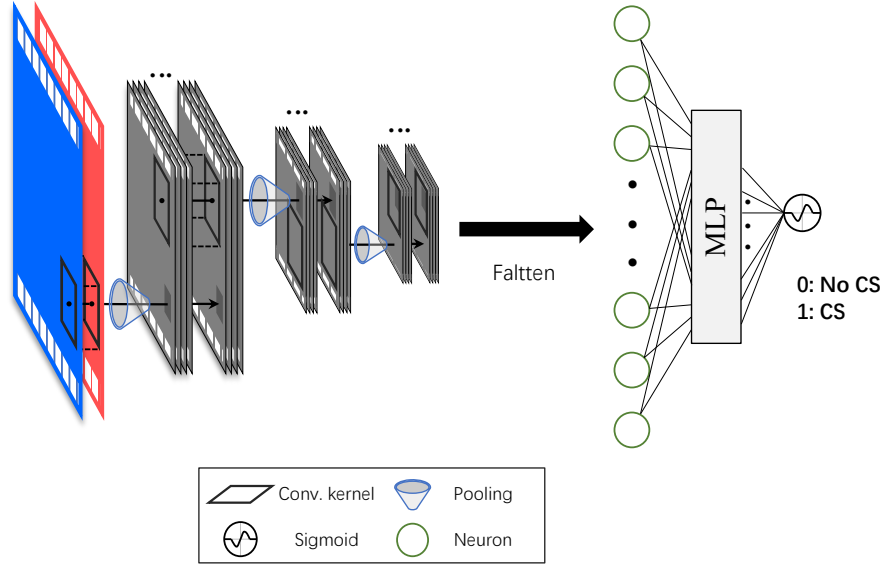


Figure 2.16: The convolutional neural network architecture with π^+ and π^- spectra $\rho^\pm(p_T, \phi)$ as input. Reproduced from Ref. [311].

They trained the meter using data prepared from a multiphase transport model(AMPT) [312–314] and found that it was accurate at identifying the CME-related charge separation in the final-state pion spectra. In data preparation, for CME events, the y-components of momenta of a fraction of downward moving light quarks and their corresponding anti-quarks were switched to upward moving direction, with the CS fraction, f , defining the events as “no CS” (labeled as “0”) for those with $f = 0$, and “CS” (labeled as “1”) for those with $f > 0$. Each event was represented as two-dimensional transverse momentum and azimuthal angle spectra of charged pions in the final state, $\rho_\pi(p_T, \phi)$. The training set includes multiple collision beam energies and centralities to ensure diversity in the dataset. With two different charge separation fractions as super parameters of the meter (5% and 10%), the meter is trained to recognize the CME signal under supervision. The sketch of the framework is shown in Fig. 2.16 and the detailed architecture can be found in Ref. [311].

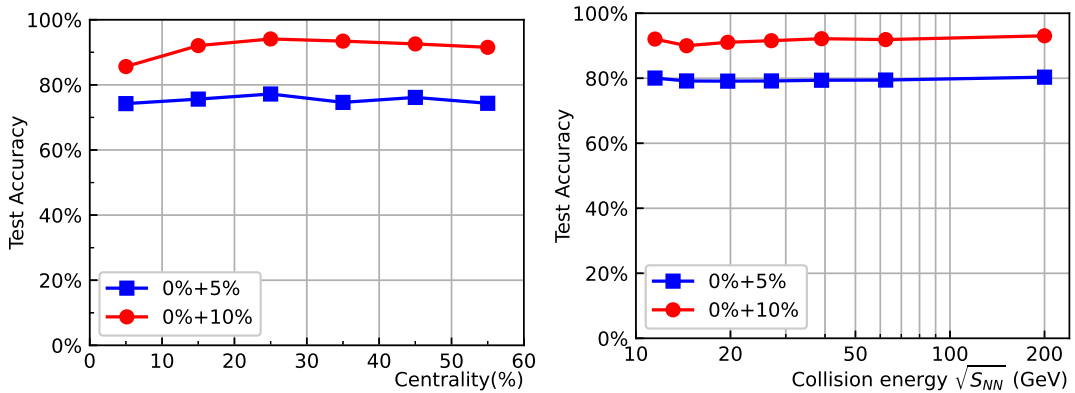


Figure 2.17: Taken from Refs. [311] with permission. (left) The test accuracy of models on different data-sets containing mixed collision energies along with centralities; (right) the test accuracy of models on different data-sets containing mixed centralities along with collision energies.

The well-trained CNN models are denoted as (0%+5%) and (0%+10%), respectively, in Fig. 2.17. Their ability to recognize the CS signal is also shown in the figure. Although there is a discrepancy between the two models, they both display robust performance under varying collision conditions, such as different $\sqrt{s_{NN}}$ and centralities. This indicates that the CS signals are not completely lost or contaminated during the collision dynamics, and can still be detected by our network-based CME-meter. In addition to its accuracy and robustness in handling collision conditions, it is noteworthy that the well-trained machine, embedded with the knowledge of CME in the final state of HICs, can extrapolate this pattern to different charge separation fractions, collision systems, and even different simulation model, i.e., Anomalous-Viscous Fluid Dynamics(AVFD) [315–317]. The well-trained machine also provides a powerful tool for quantifying the CME and is insensitive to the backgrounds dominated by elliptic flow (v_2) and local charge conservation(LCC), compared to the conventional γ -correlator.

To implement the trained CME-meter in real experiments, the first step would be to reconstruct the reaction plane of each collision event and form averaged events as input for the meter. In general, reconstructing the reaction plane requires measuring correlations among final state particles, which is subject to finite resolution and background effects. However, the well-trained CME-meter is still capable of recognizing the CS signals even with restricted event plane reconstruction. As shown in Fig. 2.16, the network output consists of two nodes, which can be naturally interpreted as the probability of the meter recognizing a given input spectrum as a CME event (P_1) or a non-CME event ($P_0 = 1 - P_1$). From a hypothesis test perspective, a characteristic distribution of $\max P_1(\phi)$ can be obtained, which can be used as a criterion for determining the existence of CME in HICs. Further details on deploying the CME-meter on single event measurements can be found in Ref. [311]. Finally, DeepDream, a method used to visualize the patterns learned by convolutional neural networks (CNNs), is applied as a validation test using P_1 to detect the CME. It helps us uncover the hidden physical knowledge in the well-trained machine, including charge conservation and specific charge distributions.

2.4.5. Anisotropic Flow Analysis

One of the signals for QGP production in HIC is the strong collective flow [112]. In semi-central and peripheral collisions, the geometric eccentricity of the initial state is transformed into the momentum anisotropy of final state hadrons, through the strong collective expansion. The azimuthal angular distribution $dN/d\phi$ in momentum space can be Fourier decomposed to get the famous elliptic flow v_2 , which is the second-order coefficient in the decomposition. The number-of-constituent-quark scaling of v_2 for identified particles in HIC is strong evidence that the underlying degree of freedom is partons. It is mysterious that the triangular flow which is sensitive to initial state fluctuations is discovered much later than the elliptic flow. Later, higher orders are also discovered and non-linear correlations are found between v_4 and v_2 , as well as between v_5 , v_2 , and v_3 . The correlations between different orders of harmonic flows (at different p_T) are used as new observables to constrain the properties of QGP.

Ref. [318] uses principal component analysis (PCA) to get the first several principal components of the single-particle distribution. As shown in Fig. 2.18, the v'_2 and v'_3 got from PCA are the same as v_2 and v_3 using Fourier decomposition, but higher order harmonic flows with $n \geq 4$ deviate from the Fourier decomposition method a lot. The correlations between different harmonic flows are reduced while the Pearson correlation between v'_n and the initial geometric eccentricity is enhanced, as compared with the traditional method. The results imply that the relativistic hydrodynamics might not be that non-linear which can couple different modes. The PCA rediscovers anisotropic flows to different orders. Compared with the flow analysis history, the importance of triangular flow emerge automatically in PCA as it is the next most

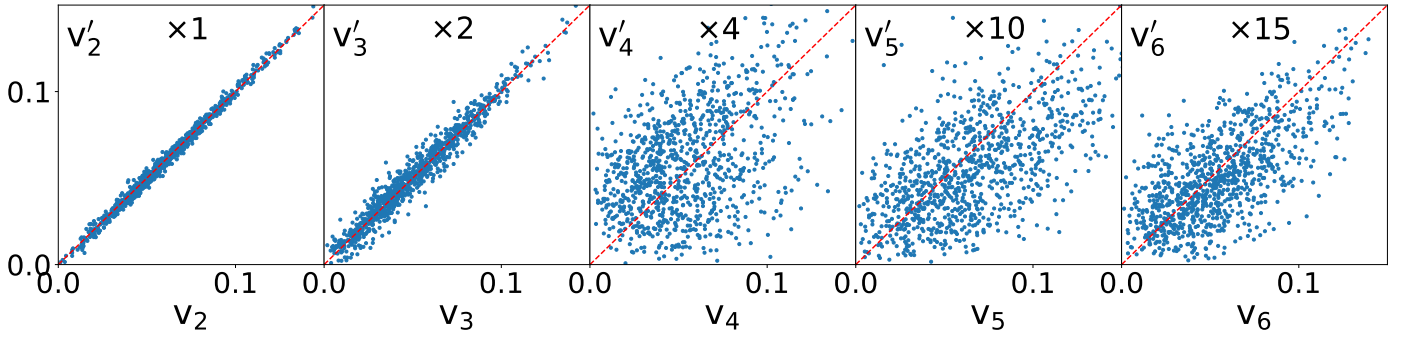


Figure 2.18: The anisotropic flow harmonics from principal component analysis as compared with traditional Fourier decomposition method. Taken from [318] with permission.

important component.

Ref. [220] uses a deep neural network to learn the elliptic flow from the final state particle kinetic information. This is a supervised learning which uses elliptic flow calculated from the event-plane method as labels. After training using minimum bias data from Pb+Pb 5.02 TeV collisions, the network succeeds in computing elliptic flows at various other beam energies and centrality classes. This may provide a way to replace time-consuming data analysis tasks using machine learning tools. Deep neural networks have the capability to compute critical physical observables such as anisotropic flow in heavy ion collisions, which suggests its potential for revealing new physical observables that are sensitive to a specific QGP property within the complex hybrid model. The machine-learned physical observable could be correlations among different traditional observables, or non-linear correlations between particles from different regions in the momentum space. The objective can be accomplished through supervised learning, which involves training a deep neural network to map the physical property of interest to the final state hadrons.

2.5. Fast Simulations for HICs

Simulations are a vital, albeit highly computationally demanding, element in linking experimental results with theoretical discoveries. This is especially true for the field of HENP, specifically in studying heavy ion collision physics. As mentioned in Sec. 2.1.1, relativistic hydrodynamics simulations have been shown crucial in modeling the heavy ion collisions, which thus serve as a powerful tool for studying the properties and evolution of the strongly interacting QCD matter under extreme conditions in the context of HICs. The deciphering of the driven physics from HICs requires a huge amount of collision event simulations to confront the experimental measurements. However, traditional numerical methods for HICs simulations are computational resources demanded and time-consuming, especially for a large amount of events simulations.

2.5.1. Efficient Emulator with Transfer Learning

As introduced in Sec. 2.4.1, when performing Bayesian inference to estimate the likely model parameters, the MCMC procedures which are needed to sample the posterior distribution for the to-be-inferred parameters would require huge model simulations to explore the parameter space. In practice, a model emulator or surrogate is necessary to largely reduce the computational demand in enabling the MCMC for inference. In general, a model emulator, usually constructed with machine learning, gives a fast map from any arbitrary point in multidimensional parameter space to the physical model

predictions on the desired observables with uncertainties associated. In the context of QGP properties constraints in HICs or other parameter estimation for computationally intensive models [319, 320], Gaussian Process (GP) emulators have been shown successful and taken as the standard practice for a decade. Notwithstanding, the training of a reliable emulator including preparation of training data is still highly computationally intensive, especially when different collision systems need to be considered jointly for the inference. Since each individual system needs a separate emulator for facilitating the global Bayesian inference.

By realizing that different collision systems share common physics are thus have related physical observables, Ref. [321] applied transfer learning to build an efficient emulator (or target task, $f_T(\mathbf{x})$) from emulator (for source task, $f_S(\mathbf{x})$) trained from limited existing training data simulated for a different situation. Specifically, the Kennedy–O'Hagan (KO) model is applied to model the discrepancy function between different nuclear collision systems or dynamical simulations, i.e., the systematic difference between target and source systems is modeled with one independent GP prior,

$$f_T(\mathbf{x}) = \rho f_S(\mathbf{x}) + \delta(\mathbf{x}), \quad \delta(\mathbf{x}) \sim GP\{\mu_\delta, k_\delta^{SE}(\cdot, \cdot)\}, \quad f_S(\mathbf{x}) \sim GP\{\mu_S, k_S^{SE}(\cdot, \cdot)\}, \quad (2.31)$$

where the squared-exponential kernels are used with different variance and length-scale parameters for the source emulator and the discrepancy function. With a collection of training data consisting of enough (suppose size to be m) model simulations for the source system ($\{\mathbf{X}_S, \mathbf{y}_S\}$) and a much smaller sized (suppose size to be $n \ll m$) simulations for the target system ($\{\mathbf{X}_T, \mathbf{y}_T\}$), the posterior distribution for the target system f_T at any given different parameter \mathbf{x}_{new} can be derived as

$$[f_T(\mathbf{x}_{\text{new}}) | \mathbf{y}_S, \mathbf{y}_T] \sim \mathcal{N}(\mu_T^*(\mathbf{x}_{\text{new}}), \sigma_T^{2*}(\mathbf{x}_{\text{new}})), \quad (2.32)$$

$$\mu_T^*(\mathbf{x}_{\text{new}}) = \rho \mu_S + \mu_\delta + \mathbf{k}^\top \boldsymbol{\Sigma}^{-1} \left(\begin{bmatrix} \mathbf{y}_S \\ \mathbf{y}_T \end{bmatrix} - \begin{bmatrix} \mu_S \mathbf{1}_m \\ (\rho \mu_S + \mu_\delta) \mathbf{1}_n \end{bmatrix} \right), \quad (2.33)$$

$$\sigma_T^{2*}(\mathbf{x}_{\text{new}}) = \rho^2 \mathbf{k}_S(\mathbf{x}_{\text{new}}, \mathbf{x}_{\text{new}}) + \mathbf{k}_\delta(\mathbf{x}_{\text{new}}, \mathbf{x}_{\text{new}}) - \mathbf{k}_{\text{new}}^\top \boldsymbol{\Sigma}^{-1} \mathbf{k}_{\text{new}},, \quad (2.34)$$

where $\mathbf{k}_{\text{new}} = [\mathbf{k}_{\text{new}}^S, \mathbf{k}_{\text{new}}^T] = [[k(\mathbf{x}_{\text{new}}, \mathbf{x}_i^S)]_{i=1}^m, [k(\mathbf{x}_{\text{new}}, \mathbf{x}_j^T)]_{j=1}^n]$ and

$$\boldsymbol{\Sigma} = \begin{bmatrix} \mathbf{K}_S(\mathbf{X}_S) + \gamma_S^2 \mathbf{I}_m & \rho \mathbf{K}_S(\mathbf{X}_S, \mathbf{X}_T) \\ \rho \mathbf{K}_S(\mathbf{X}_S, \mathbf{X}_T)^T & \rho^2 \mathbf{K}_S(\mathbf{X}_T) + \mathbf{K}_\delta(\mathbf{X}_T) + \gamma_T^2 \mathbf{I}_n \end{bmatrix}.$$

These thus serve the transfer learning emulator model with μ_T^* providing the prediction and σ_T^{2*} quantifying the uncertainty, which by construction and in spirit transfers the captured knowledge from an easily accessed or already existed source term emulator to a different target system.

2.5.2. Accelerating Hydrodynamic Simulations

Fast simulation via machine learning for heavy ion collision modeling with relativistic hydrodynamics is discussed in Ref. [322]. A stacked U-Net (sU-net) is designed and trained to capture the non-linear mapping from the initial state to final state profiles of the fluid field in the special case of being with ideal EoS ($p = e/3$), zero viscosity, zero charge densities and a fixed spatiotemporal discretization. The initial and final energy-momentum tensor profiles from hydrodynamics, $T^{\tau\tau}(x, y), T^{\tau x}(x, y), T^{\tau y}(x, y)$, are taken as the input and output for the deep neural network.

As a variation of the autoencoder structure with short-cut residual connections, the constructed sU-net architecture has been shown to be powerful for image synthesis or object segmentation, with the ability to identify local patterns. In the

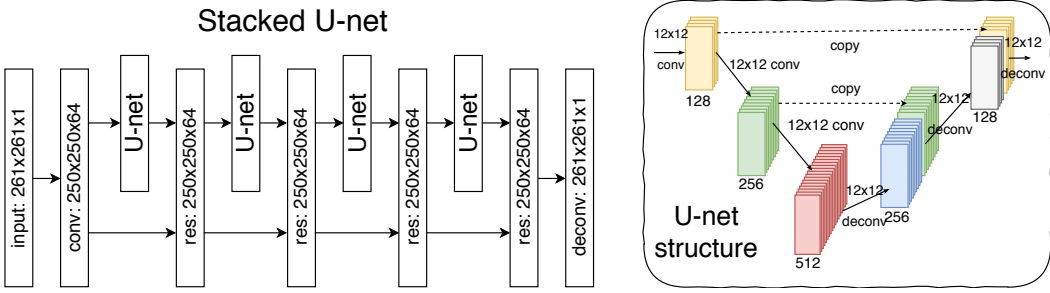


Figure 2.19: Taken from [322] with permission. The stacked U-net structure for predicting flow field in the relativistic hydrodynamic simulation of heavy ion collisions.

context of HICs, with simulation from hydrodynamic non-linear partial differential equations, sU-net, as shown in Fig. 2.19, was demonstrated to be able to predict well the final energy density and flow velocity profiles given any arbitrary initial profile from an initial condition model. Different initial conditional models were implemented for the generalizability test of the trained sU-Net, including MC-KLN, AMPT, and TRENTo with vanishing transverse flow-velocity, which were used for training the MC-Glauber initial condition. For physics interests in investigating the deformation and inhomogeneity of the created QGP medium, the eccentricity coefficients associated with the final energy density profiles from the sU-Net prediction were calculated and found to reproduce the results from VISH2+1 hydro simulation well. Note in Ref. [323] demonstrated on simple non-relativistic hydrodynamics, one single DNN was shown to be able to predict the fluid dynamics in extrapolation manner on both initial hydro profile and simulation duration. Another promising strategy not fully explored for HICs yet may come from a physics-informed neural network, which has been demonstrated for fluid dynamics [324–326] prediction in applied physics. It is also interesting to explore the inverse inference through such trained PINN for the relativistic Hydrodynamics simulations.

2.6. Summary

In this chapter, the “standard model” of high energy heavy ion collisions is reviewed. It is a hybrid model of gluon saturation, relativistic fluid dynamics for QGP expansion, hadronic transport, and the jet-medium interaction. The model is used to generate a vast amount of data that have been used in Bayesian analysis to constrain the QCD EoS at high energy, the initial state entropy deposition, the temperature-dependent shear and bulk viscosity and the jet energy loss coefficients/distributions. The data are also used in PCA or deep learning to rediscover physical observables, which verifies the representation power of machine learning. It is worthy noting that, besides the researches mentioned above, the determination of other bulk thermodynamics, like the entropy production [327], or related particle ratios [328] and particles multiplicity [329] have been very recently investigated with DNN or Bayesian approach [330]. The deep neural network is used in supervised learning to build mappings between the initial nuclear structure, the QCD EoS, the CME, the jet flavors, and the jet production positions to the final state hadrons. As an outlook, machine learning tools can be used as fast emulators of HIC simulations. The active learning algorithm can be used to propose important regions of the parameter space to be simulated with hybrid models to increase data generation efficiency. After training to build mappings between data and model parameters, the network $f(x, \theta)$ serves as a new physical observable, whose interpretation may inspire both experimentalists and theorists.

3. Lattice QCD

As the fundamental theory for describing the strong interaction, QCD is challenging to be solved due to its characteristic asymptotic freedom, which embarrasses perturbative treatment at low energy scales [1]. Therefore, non-perturbative methods for investigating nuclear matter in the context of strong interactions are required. Lattice field theory plays a significant role in the ab-initio computation⁸ of general many-body systems [332]. In this approach, the system's partition function or path-integrals are discretized on a lattice of Euclidean spacetime, and field configurations or paths can be generated using importance sampling for further evaluation of physical observables.

Typically, Markov Chain Monte Carlo (MCMC) related algorithms such as the Hybrid Monte Carlo (HMC) algorithm [333] are used to generate ensembles of configurations in lattice calculations [334], and have succeeded in giving important results e.g., for the QCD phase structure [8, 9, 335–337]. See also Ref. [338] for a recent review. However, the sequential nature and diffusive update involved in these Monte Carlo algorithms seriously hampers the sampling efficiency when moving to larger and finer lattices due to the critical slowing down(CSD) [339]. The computation becomes even more challenging for evaluating real-time dynamical properties. Recent advances in machine learning techniques may provide a promising way to overcome, or at least mitigate, the computational barriers involved in lattice QFT and further QCD studies [340]. From the methodology point of view, many of the algorithmic developments were firstly explored on simple many-body physics or QFT systems but with the potential to be generalized to QCD study. Therefore, the discussion in this chapter is with generality into lattice field theory.

3.1. Overview and Challenges in Lattice Field Theory

In general, Lattice QFT provides a non-perturbative solution of the path integral for the field system on a discretized Euclidean spacetime lattice. This allows the expectation value of an observable, $\mathcal{O}(\phi)$, to be represented by the discretized action,

$$\langle \mathcal{O} \rangle = \frac{1}{Z} \int \mathcal{D}\phi \mathcal{O}(\phi) e^{-S(\phi)}, \quad (3.1)$$

with $Z = \int \mathcal{D}\phi e^{-S(\phi)}$ the partition function, and $\int \mathcal{D}\phi$ the integration over all possible configurations of the discretized quantum field ϕ . All the dynamical and interaction information of the fields are encoded in the action $S(\phi)$. The specific numerical evaluation of Eq. 3.1 relies on sampling configurations following the action dictated probability distribution

$$p(\phi) = \frac{1}{Z} e^{-S(\phi)}. \quad (3.2)$$

Several obstacles or computational tasks for lattice field theory calculations are briefly introduced in following, to which we will later accordingly review the current progresses in utilizing ML techniques for a rescue.

- **Critical slowing down**

Monte Carlo (MC) simulation can provide unbiased sampling for lattice field theory, which has been proven to be ergodic and asymptotically exact to approach the target distribution $p(\phi)$ under detailed balance condition for the involved proposal probability [341]. Within a classical MCMC framework, the configuration sampling process typically involves proposing a new configuration from the previous configuration on the chain for further acceptance

⁸Fuctional methods e.g., functional renormalization group (fRG) and Dyson-Schwinger (D-S) equations form the other first principle approaches. See Ref. [331] for a review.

or rejection judgment, based upon evaluation of a specific target probability using the proposed and also the previous field configurations (e.g., within Metropolis-Hastings algorithm [342, 343]). In these diffusive updates based sampling approaches, the proposal for new field configuration is usually made by local perturbation of the previous one or heat bath updates, which thus is inefficient in drawing independent configurations. Improvements can be realized by HMC which relies on evolving the configuration $\phi(x)$ jointly with a “conjugate momentum” $\pi(x)$ under a classical Hamiltonian dynamics. Practically the computational cost involved are due to the strong autocorrelation of local updates, or the single local update itself is computationally expensive. The autocorrelation time is expected to scale as $\tau \sim \xi^z$, where ξ is the correlation length that diverges around the critical point or approaching the continuum limit, and z is the dynamical critical exponents which are ≈ 2 for standard local update algorithms [339]. Correspondingly, the induced severe inefficiency of sampling is called *critical slowing down* (CSD). Being related, in the context of lattice field theories with well-defined topological behavior like QCD, *topological freezing* can happen where topological observables usually have exponential scaling $\tau \sim e^{z\xi}$ [344, 345]. CSD and topological freezing form the main barrier of lattice QFT computations.

- **Observables measurements and physics analysis**

With ensembles of field configurations sampled from the desired distribution $p(\phi)$, correlation functions and further different physical observables can be evaluated, during which there'll be intensive operations on high-dimensional tensors (field configurations). Physics is thus also to be analyzed such as thermodynamics or phases transition (order parameter) of the system, different real-time dynamical properties, e.g., the reconstruction of spectral function or parton distribution functions (PDF) which form ill-conditioned inverse problem.

- **Sign problem**

The sign problem in lattice QCD calculations refers to the fact that the functional integral defined in the partition function is not positive definite in many cases (e.g., at finite density or for Minkowski-time dynamical physics), which makes it difficult to utilize standard Monte Carlo methods [346]. In lattice QCD, the partition function is defined as a functional integral over all possible configurations of quarks and gluons on a discrete four-dimensional lattice in the form [11, 347],

$$Z = \int D[A]D[\psi]D[\bar{\psi}]e^{-S[A,\psi,\bar{\psi}]}, \quad (3.3)$$

where S is the QCD action, A is the gauge field, and ψ and $\bar{\psi}$ are the quark and antiquark fields, respectively. In finite-density QCD, the nonzero chemical potential(μ) makes the fermion determinant complex within the partition function, $Z = \int D[A]\exp(-S_{\text{YM}})\det M(\mu)$, where S_{YM} is the Yang-Mills action. The problem is that the exponent in the integrand, $-S$, is not always positive, which leads to the non-positive definite integral. It induces the ill-defined probability when sampling configurations in standard Monte Carlo techniques. Even if some methods can bypass the predicament technically, they will inevitably encounter the highly fluctuating phase factors which result in exponential growth of computational cost as the volume increases [348, 349].

3.2. Field Configuration Generation

For lattice QFT study, it's expected that the generation of field configurations constructs the most expensive computation, because of the usually needed Monte Carlo simulation on Markov chains for the involved high dimensional distribution's

sampling, especially with also the need to push approach continuum limit for the simulation. In fact, for a general many-body system study within Monte Carlo simulation, much effort has been put into making a clever proposal or global update during the MCMC procedures to reduce the autocorrelation time, the increase of which usually hinders efficient sampling for MCMC. Besides the critical slowing down as introduced in Sec. 3.1, which is a crucial barrier when pushing the lattice calculation to the continuum limit, the other challenge facing conventional MCMC simulation is sampling from multimodal distributions. It's not trivial to traverse regions between the widely separated modes of the target distribution using update-based samplers. [344, 350]. This high-dimensional sampling and efficient proposal design task is also popular in the machine learning community, which motivated the rapid development of generative models [53]. It has been shown from both general classical/quantum many-body statistical physics study and lattice QFT research that the modern generative algorithmic development from AI/ML can bring in improved efficiency and support for traditional Monte Carlo computation on configuration generation for physical system.

3.2.1. GAN-based Algorithms

As introduced in Sec. 1.2.3, the Generative Adversarial Network(GAN), is a deep generative model to realize implicit MLE for distribution learning through adversarial training. This generative model has been recently explored for many-body statistical systems (e.g., for Ising model in [351]) and also for the configuration generation of quantum field systems. In Refs. [352–354], the GAN is used for configuration generation of complex scalar ϕ^4 field at non-zero chemical potential in the context of lattice QFT study. In Sec. 3.3.1 about **Regression in QFT** sector, this QFT system under worldline formalism was also introduced for regression exploration via deep learning. New configuration generation via Wasserstein-GAN scheme is also explored [352] at the task of producing uncorrelated configurations fulfilling the physical distribution, with training ensemble of configurations prepared from worm algorithm. Since the considered field system under the dualization approach should satisfy an important local divergence-type constraint reflecting flux conservation, the effectiveness of the generative algorithms, in terms of whether the generated configurations are physical or not, is verified by checking this divergence-type constraint condition for training. Surprisingly, as shown in the left of Fig. 3.1, it is found that this highly implicit physical constraint condition is realized in a converging manner (more and more together with training epochs) for configurations generated from the trained generator within GAN, without explicit guidance of this constraint. Also, the distribution with respect to normal physical observables from the generated samples was found to

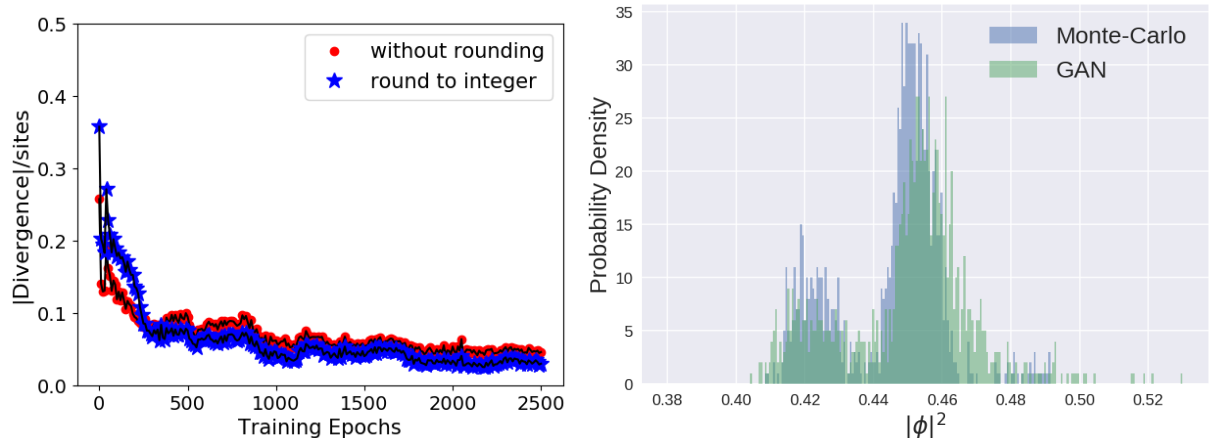


Figure 3.1: (left) The degree of divergence satisfaction for configurations from trained GAN generator; (right) the probability density distribution for the squared field ϕ^2 from GAN and from Monte-Carlo simulations at fixed chemical potential. Taken from Ref. [352].

agree well with the MCMC evaluation. And here, for the considered complex scalar field system, it even agrees reasonably well over the multimodally distributed number density and field square (see the right of Fig. 3.1), which is not trivial for conventional sampling approaches without special treatment. Moreover, a conditional generative network, cGAN, is proposed in [352] to generalize the configuration generation ability of the generator to be dependent/conditioned on physical observables (specifically the number density n was used for demonstration) and go beyond the distribution that it was trained on. Ref. [355] latter applied the conditional GAN in lattice Gross Neveu model to mitigate the critical slowing down when approaching the critical region.

This strategy with the conditional GAN was also used for the spin configurations generation of two-dimensional XY model [356], with several different architectures proposed including also one specific output distribution entropy maximization regulator to mitigate the mode-collapse issue. As the non-local defining feature for the involved topological phase transition, the vortices distribution is also specially scrutinized besides other relevant observables (e.g., magnetization and energy). With the trained GAN, Ref. [356] further proposed the GAN fidelity in terms of the discriminator network output which is shown to be able to detect the phase transition unsupervisedly.

The above demonstration, especially the consistency between the distribution from the GAN and the desired one, actually indicate that the trained GAN here can be taken as good enough proposal on a Markov Chain when one wants to guarantee the ergodicity and detailed balance properties for the sampling process, thus make sure the correct physics can be estimated in converging manner. This indeed is further demonstrated in Ref. [357] on scalar field theory together with Hamiltonian Monte Carlo (HMC) approach. Specifically, the trained GAN is proposed to serve as overrelaxation (i.e., configuration space exploration that keeps the action unchanged, $\delta S = 0$) procedure within action-based MCMC sampling algorithm. Start from some initial configuration ϕ after a number of HMC steps, the gradient flow is performed on the latent variable z to achieve the GAN overrelaxation proposal $G(z')$,

$$z'(\tau + \epsilon) = z'(\tau) - \epsilon \frac{\partial(S[G(z)] - S[\phi])^2}{\partial z}, \quad (3.4)$$

where ϵ is the learning rate and τ the training epochs. In Metropolis steps, proposal configuration with $\delta S = 0$ (w.r.t. the last configuration) is accepted automatically given the transition probability for proposal is symmetric. Heuristic arguments are provided in [357] on this issue for GAN's selection probability $P(G(z')|\phi)$. With demonstration on 2d scalar field theory, under such GAN overrelaxation method the autocorrelation time has been shown to be largely reduced.

Note that the GAN-based approach in general requires a training data set to be prepared from conventional sampling means, which hampers its ability to assist the field configuration generation purely from the physically known action or Hamiltonian. Also, though it can be taken as proposal in generating independent and physically promising configurations, the vanilla GAN has no evaluation to the likelihood thus the sample probability. More potential can be unlocked for GAN-based approach if the explicit likelihood estimation can be added inside the adversarial learning in the future. In contrast, the methods introduced in the following can render the self-training just from physical action or Hamiltonian, with also the sample probability to be accessible.

3.2.2. Self-Learning through Effective Action

Self-Learning Monte Carlo — Self-Learning Monte Carlo (SLMC) method is a general-purposed numerical algorithms for configuration generation of many-body system based upon machine learning. The development of SLMC originally is within classical spin systems[358] and shows clear improvement in curing the critical slowing down problem. It works also to other general quantum models that are concerned in condensed matter physics and quantum chemistry. [359]. The

basic idea is to learn a tunable and effective Hamiltonian or Action that can be associated with a more efficient update algorithm (such as cluster-update or other global moving ways to propose uncorrelated configurations), with which, the Metropolis-Hastings test using the real action can turn it to be exact sampler for the system.

As detailed in Ref. [358] on the example of a statistical spin model, the SLMC consists a learning phase and exploration phase within actual MC simulation in general: (1) a conventional MC simulation under local update can be performed to produce a series of configurations with its weight (energy or action evaluation) also being known; (2) based on these training data an effective Hamiltonian H_{eff} can be learned, to which one can use global update for a faster simulation (e.g., when only two-particle interactions are contained in H_{eff}); (3) the learned H_{eff} can be used to make proposal in actual MC simulation and (4) perform Metropolis Hasting test with the original Hamiltonian to correct (reject or accept). See Fig. 3.2 for a schematic illustration of SLMC in a simple spin model. The training over H_{eff} can also be

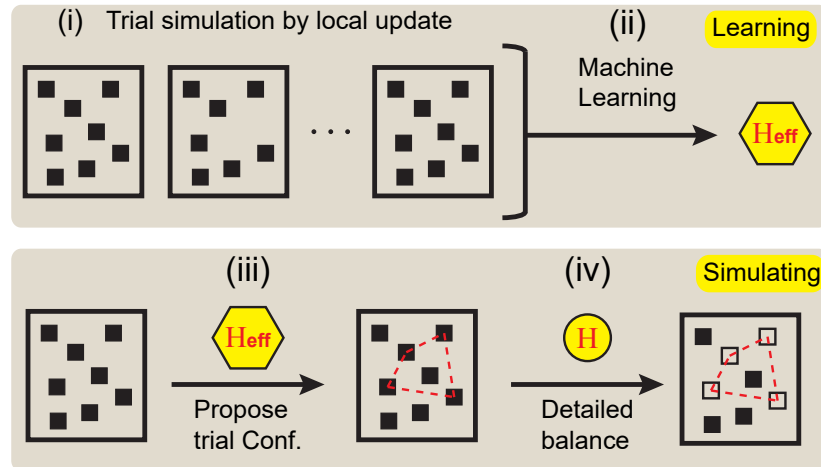


Figure 3.2: (From Ref. [358]) Schematic illustration of learning process (top panel) and simulating process (bottom panel) in SLMC.

self-improved by iteratively reinforce training H_{eff} with generated configuration from the last step self-learning update with H_{eff} . Basically, a more efficient MC update model can be obtained from the SLMC. It's demonstrated that the SLMC indeed largely reduced the autocorrelation time τ especially near the phase transition, and gives around 10 to 20-fold speedup on the considered 2D generalized Ising model. It's worthy noting that similar ideas by training and simulating Restricted Boltzmann Machines (RBM) [360] were adopted in Refs. [361–364] for proposing efficient Monte Carlo updates, which is not limited to Trotter decomposition for fermionic system and renders faster proposal since the used Gibbs sampling in RBM.

This self-learning MC strategy was further pushed forward into more realistic fermionic systems where Trotter decomposition is employed [365, 366] and for continuous time Monte Carlo simulation [367]. Deep neural network techniques are also additionally introduced into the effective action or Hamiltonian's construction in Ref. [368–370], which can further increase the flexibility of the effective action and improve the following acceptance rate in the Monte Carlo sampling stage.

The SLMC for non-abelian SU(2) gauge theory with dynamical staggered fermions at zero and finite temperature was developed in Ref. [371]. Ref. [372] devised gauge covariant neural network for 4-dimensional non-abelian gauge field theory, and adopted such network to construct effective action within HMC to achieve self-learning HMC scheme, with demonstration on the case of two color QCD including un-rooted staggered fermion.

Action parameter regression — In tackling the issue of CSD for lattice field theory study, with promise, multiscale

methods are proposed to overcome the CSD by refining ensemble of configurations at a coarse-scale. Such methods require **action matching** across different scales via renormalization group (RG), then the sampling at coarse-scale level can already render the approach to continuum limit physics evaluation together with a cheap re-thermalization with the original fine action. The key challenge involved is parametric regression for identifying the proper action parameters that best describe physics at coarse-scale from an ensemble of configurations generated at finer scale. It's thus proposed to use deep neural networks to tackle this action matching regression task[373], where the coarsened ensemble of SU(2) gauge field configurations are taken as input and the required action parameters being the output. It's worth noting that the mismatch from the regression can be corrected by re-thermalization steps in the finer scale with the corresponding action.

The simple fully-connected neural network was tried first and found to appear successful in validation, which however fails to generalize to different parameter cases or even new Hybrid Monte Carlo (HMC) simulation streams of the same parameters as of the training set. The failure of such naive neural network is argued in Ref.[373] to be induced by the lacking of symmetries of the gauge field configurations, and further proposed a customized symmetry-preserving network to reduce effective degrees of freedom for the task. The embedding of the symmetries is designed by featuring an initial preprocessing layer to yield possible symmetry-invariant quantities as input to following fully-connected layers. This gives accurate parameter regression and successful generalization for even ensembles not distinguishable to principal component analysis (PCA). It thus provides a solution to the action matching.

3.2.3. Variational Autoregressive Network

The key object for a general many-body system is the free energy, which contains all the information about the system in principle. From a probabilistic point of view, the usual MCMC approach basically is using importance sampling to implicitly approach the free energy, which is an intractable high dimensional integration. However, the direct evaluation of the free energy is not possible for naive classical MCMC approach (note that there are variants of MCMC developed to be able to approximately assess the free energy, which is computationally expensive). As another alternative strategy based on variational point of view, the *mean field approach* or related information transfer algorithms can be adopted for the free energy estimation, which then basically perform the minimization over the variational free energy. In probabilistic language this is equivalent to the minimization over the reverse (or backward) KL divergence between the variational distribution $q_\theta(\phi)$ and the target distribution in Eq. 3.2 or in statistical physics $p(\phi) = e^{-\beta H(\phi)}/Z$ (where β is the inverse temperature, $H(\phi)$ the Hamiltonian of the system, and Z is the partition function),

$$\mathcal{D}_{KL}(q_\theta(\phi) \parallel p(\phi)) = \int \mathcal{D}[\phi] q_\theta(\phi) \log \frac{q_\theta(\phi)}{p(\phi)} = \beta(F_q - F), \quad (3.5)$$

with the variational free energy defined as

$$\beta F_q = \mathbb{E}_{\phi \sim q_\theta} [\beta H(\phi) + \log q_\theta(\phi)], \quad (3.6)$$

Because of the non-negativity for KL divergence ($\mathcal{D}_{KL} \geq 0$, also known as *Gibbs-Bogoliubov-Feynman inequality* [374–376]), the true free energy F is upper bounded by the variational free energy F_q , and the equality happens when the variational distribution q_θ really reaches the target distribution p exactly. Note that in machine learning community as proposed in the beginning as general density estimation method, the autoregressive network usually uses the (forward) KL divergence between data empirical distribution (e.g., constructed with training data) and the variational distribution, $\mathcal{D}_{KL}(p_{data} \parallel q_\theta)$. For many-body physics or QFT study, the proposal to use the reverse KL divergence together with

the easily sampleable variational ansatz makes it possible for **self-training** starting solely from the unnormalized target distribution⁹, e.g., knowing the action or Hamiltonian for the physical system in equilibrium.

Despite its popularity and success, the *mean field calculation* is quite often limited by the assumed *variational ansatz* (e.g., factorized), especially when the system is with strong correlations between their degrees of freedom, thus most of the time it is valid only in high temperature cases or when the system's topological structure fulfills the requirement from mean field approximation. Here the autoregressive model naturally stands out, because both the direct sampling and tractable likelihood evaluation (which is desired in evaluating the variational free energy) can be simultaneously realized. Meanwhile, when the autoregressive model is constructed as variational ansatz, the variational free energy (Eq. 3.6), which serves as the loss function, can be estimated unbiasedly and stochastically by drawing ensembles of samples from the sequential stochastic process specified by the autoregressive model (see Eq. 1.20 as introduced in Sec. 1.2.3). Thus, in every optimization iteration, using data sampled from the autoregressive model it suffices to perform **self-training** on the model.

Ref. [377] for the first time proposed to introduce neural network to give a more powerful yet tractable variational ansatz, taking advantage of the strong representational ability of neural networks due to the universal approximation theorem. To keep the evaluation of the variational free energy tractable, one needs to design the network such that the variational distribution represented by the network to be accessible and efficiently computable. Accordingly, the autoregressive networks were adopted by the authors to decompose the joint probability over all lattices to a product of conditional probabilities, and parametrized each conditional with neural networks¹⁰. The idea got directly demonstrated on a simple 2D ferromagnetic Ising system, also generalized to the PixelCNN structure with convolutional layer included to respect the locality and the translational symmetry of the system. Compared to conventional MCMC evaluation, this variational autoregressive network can also give evaluation of the free energy by giving its well minimized upper bound. This strategy of using autoregressive probabilistic models was later combined with quantum circuits, and extended the variational quantum eigensolver (VQE) to investigate thermal properties and excitations of quantum lattice model, termed as β -VQE [378]. This quantum classical hybrid algorithm was also applied to Schwinger model at finite temperature and density [379], with large volume limit evaluated and continuum limit taken in obtaining the phase diagram.

Authors in Ref. [380] further generalized the above method to general many-body system with continuous variables, where the probability interpretation of the introduced autoregressive is devised to be a mixture beta distribution, instead of a Bernoulli distribution for Ising spins. This newly extended continuous-mixture autoregressive network (denoted as CAN in the paper) is well demonstrated on the 2D XY model which exhibits non-trivial topological KT phase transition. The thermodynamics of the systems were shown to be captured successfully (see Fig. 3.3), and the underlying emergent degree of freedom—vertex—is also found to be rediscovered by this CAN method. Furthermore, it is found that the trained CAN network can automatically give rise the vortices' distribution for any random given XY spin configurations with its conditional probability components output from plaquette (see Fig. 3.4), directly indicate that the network captured the underlying emergent physics about this many-body system. Note that this CAN method can capture the $O(2)$ symmetry for 2D XY model, which is equivalent to global $U(1)$.

⁹i.e., the training is performed with samples generated from the variational distribution, instead of collected samples from the true distribution in advance

¹⁰Note that to represent the conditional probability, the output of neural networks are interpreted as essential parameters of the distribution. More explanation about autoregressive network can refer to Sec. 1.2.3

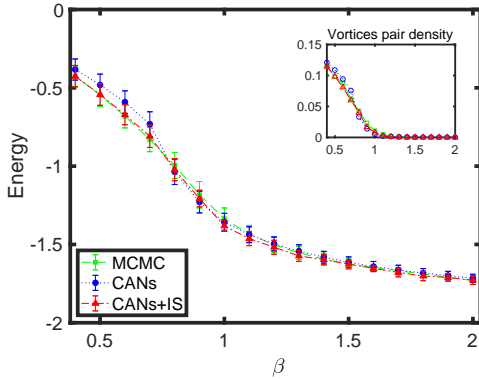


Figure 3.3: The energy per site of 2D XY model ($L = 16$) from CANs, CANs+IS and MCMC. The upper insert shows the number of vortex pairs density with inverse temperature. Taken from [380].

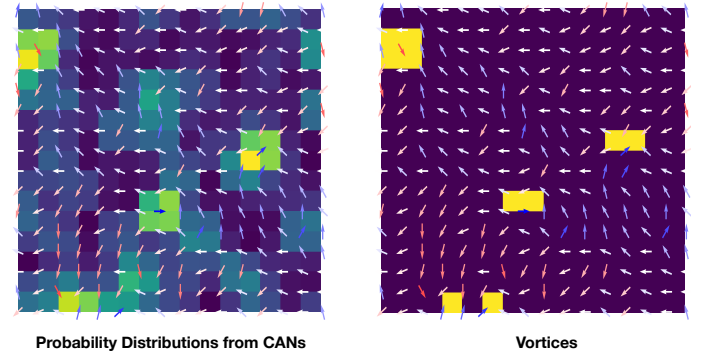


Figure 3.4: Probabilities analysis with CANs and corresponding vortices for a random 2D XY model configuration sampled from well-trained CANs at $\beta = 1.0$. Taken from [380].

Ref. [381] proposed symmetry-enforcing updates within MCMC with autoregressive neural network as global update proposer, since the system action or Hamiltonian remain invariant under specific symmetry operations (e.g., translation and reflections as considered in Ref. [381]). This introduced symmetry operation largely reduced the ergodicity problem from those exponentially suppressed configurations (i.e., those are with exponentially smaller $q_\theta(\phi)$ compared to $p(\phi)$ however will hardly influence the variational free energy evaluation). Additionally, a neural cluster update scheme is devised in Ref. [381] utilizing the decomposition structure of autoregressive model, which can lower the autocorrelation time by setting only a subset of the lattice to be changed instead of the whole in each Monte Carlo step.

3.2.4. Flow-based Variational Learning

Being similar to the above-mentioned variational autoregressive network models (see Sec. 3.2.3), the flow-based models construct the variational ansatz using normalizing flows (NF) for the target distribution, to further approach and learn the desired distribution via minimizing the variational free energy. Again, technically, it is minimizing the reverse mode of KL divergence between the flow constructed variational distribution and the target one.

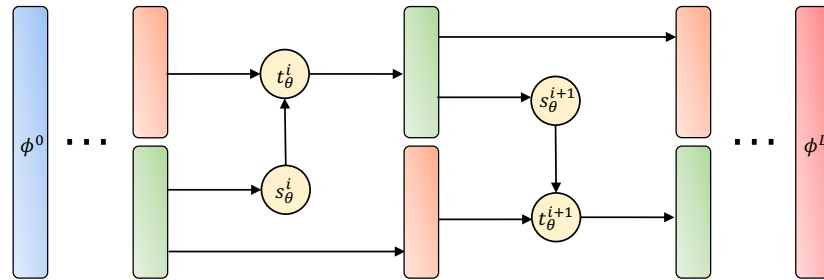


Figure 3.5: A schematic demonstration for the normalizing flow of the Real NVP, in which the yellow circles represent affine transformations represented by the neural networks.

Though introduced already in Sec. 1.2.3, we briefly explain the NF idea in the context of field configuration generation for the sake of terminology consistency in following. Generally speaking, NF construct a flexible and tractable probability distribution by providing a generative bijective transformation between a naive prior distribution $p_u(u)$ (e.g., multivariate Gaussians) and the variational distribution $q_\theta(\phi)$ (to approach the target distribution), $\phi = f_\theta(u) \sim q_\theta(\phi)$,

which is parametrized by neural networks with trainable parameters denoted as $\{\theta\}$ and specially designed to keep the transformation invertible. Through probability conservation (i.e., change of variable theorem for probability distribution) one easily get the connection between the variational distribution and prior, $q_\theta(\phi) = p_u(u) |\det \frac{\partial f_\theta(u)}{\partial u}|^{-1}$. With the prior probability easily evaluable and the Jacobian determinant J_f computable, one can calculate the variational probability $q_\theta(\phi)$ on any samples to allow for further minimization on the variational free energy. Thus the key recipe in constructing feasible flow model is to make the network represented transformation f_θ to be invertible, differentiable and composable. As the most common flow-based model, Real NVP structure (see Sec. 1.2.3 for details) are often applied, which constructs the transformation f_θ by composing a series of affine coupling layers (see its schematic diagram in Fig. 3.5) each looks like:

$$\begin{cases} \phi_{1:k}^i = \phi_{1:k}^{i-1} \\ \phi_{k+1:N}^i = \phi_{k+1:N}^{i-1} \odot e^{s_\theta^i(\phi_{1:k}^{i-1})} + t_\theta^i(\phi_{1:k}^{i-1}), \end{cases} \quad (3.7)$$

with ϕ^i the output of the i^{th} affine coupling layer (thus $\phi^0 = u \sim p_u(u)$ and final output $\phi^L = \phi \sim p(\phi)$), k the separation point of the configuration variables into two subsets, and N the number of variables in one configuration. The scaling and translation functions can be parameterized by DNNs as $s_\theta : \mathbb{R}^k \rightarrow \mathbb{R}^{N-k}$ and $t_\theta : \mathbb{R}^k \rightarrow \mathbb{R}^{N-k}$. The Jacobian determinant can be directly evaluated as well to be $(\det J_T^i) = \prod_j^{N-k} e^{s_\theta^i(X_{1:k})_j}$. Also, the above coupling layer can be easily inverted due to the splitting,

$$\begin{cases} \phi_{1:k}^{i-1} = \phi_{1:k}^i \\ \phi_{k+1:N}^{i-1} = (\phi_{k+1:N}^i - t_\theta^i(\phi_{1:k}^i)) \odot e^{-s_\theta^i(\phi_{1:k}^i)}. \end{cases} \quad (3.8)$$

With the above-mentioned flows, i.e., a series of bijective transformation layers one actually has a parametric model with explicit probability for each sample, $q_\theta(\phi)$, and with tunable parameters denoted as θ . Then similar to autoregressive models, the reverse KL divergence in Eq. 3.5 can be applied to guide the optimization of $q_\theta(\phi)$ in approaching the target distribution of $p(\phi)$ in Eq. 3.2,

$$\theta^* = \arg \min_{\theta} \mathcal{D}_{KL}(q_\theta(\phi) || p(\phi)) = \arg \min_{\theta} [\int \mathcal{D}\phi q_\theta(\phi) (S(\phi) + \log q_\theta(\phi)) + \log Z], \quad (3.9)$$

Ref. [86] delivered the first application of flow-based model to lattice field theory simulations¹¹. Taking the two-dimensional ϕ^4 field theory as example, this work showed that the flow-based sampler offers significant advantages over traditional sampling algorithms (local Metropolis sampling and HMC considered for benchmark), with the autocorrelation times found to be systematically reduced when combining the flow sampler as proposal inside the Markov Chain. The combination of the trained flow sampler and MCMC (e.g., Metropolis-Hastings) guarantee the asymptotic exactness of the sampling, since the Metropolis-Hastings acceptance/rejection step just provide a corrector to assure the sampling distribution to approach exactly the target distribution. This method is usually dubbed as *flow-based MCMC* in literature, of which one highlight is that the critical slowing down issue associated to the Markov Chain sampling is eliminated since the independent generation of samples from the well-trained flow model, and the cost correspondingly is shifted to the up-front training expense for the generative model. Note that when calculating observables ($\langle \mathcal{O}(\phi) \rangle$), besides the stochastic MCMC correction method, reweighting (i.e., importance sampling) can also be applied which just assign a weight $w(\phi) = p(\phi)/q_\theta(\phi)$ to each sample ϕ in computing the observables' expectation. A detailed introduction to *flow-based MCMC* on scalar field with code written in *PyTorch* can refer to Ref. [88]. We also summarize in Tab. 3.1

¹¹Earlier similar flow-based model was developed and demonstrated on the two-dimensional Ising model in its continuous dual version, with the novel concept of neural network based variational Renormalization Group approach[382] proposed.

some related applications of this strategy onto different systems. In Ref. [383], a simpler normalizing flow construction with Non-linear Independent Component Estimation (NICE, see Eq. 1.22) is adopted for lattice simulation of 2-D real scalar field theory. In this work, the \mathbb{Z}_2 -invariance is explicitly introduced by constraining the network to be with \tanh non-linearity and vanishing biases to ensure the transformation from the flow to be odd function, $f_\theta(-u) = -f_\theta(u)$. Interestingly, this work also proposed a direct estimator for the *free energy* ($\hat{F} = -T \ln \hat{Z}$)¹² from the trained flow model through Monte-Carlo approximation on the partition function,

$$\hat{Z} = \frac{1}{N} \sum_{\phi_i \sim q_\theta} [e^{-S(\phi_i)} / q_\theta(\phi_i)], \quad (3.10)$$

and it shows conceptual appeal since it bypasses the cumbersome integration error accumulation in conventional MCMC-based estimation for the partition function. With the free energy well estimated, other thermodynamic observables can be naturally obtained through taking derivative of the free energy, and be further corrected by the importance sampling [384]. Such capability from flow-based model is mainly attributed to their explicit likelihood estimation ability, which is also shared by variational autoregressive models like introduced in Sec. 3.2.3.

A conditional normalizing flow (c-NF) model was trained in Ref. [385] on samples pre-generated from HMC in noncritical region of the theory¹³. Such trained c-NF model is able to interpolate or extrapolate the dependence of configuration generation on the parameter and thus is applied to critical region (in i.e., phase transition situation or continuum limit seeking). Though the interpolation or extrapolation of the trained c-NF model in critical region for configuration generation may have bias, it can be corrected efficiently with few e.g., Metropolis-Hastings steps because of the tractable probability evaluation for each of the generated (“proposed”) configurations. Since the shared flow-model across the whole parameter space exclude the conditioning on them, it provides an economical way to reduce the cost of performing flow-based model for phase diagram exploration of the theory.

Table 3.1: Normalizing Flows applied to different physical system in terms of lattice study

systems	Ising	Scalar	U(1) gauge	SU(N) gauge	Yukawa	SU(3) gauge
dimensionality	2D	2D	2D	2D	2D	2D
fermions	no	no	no	no	Staggered	2 flavors
Ref.	[382]	[86, 386, 387]	[87, 388]	[389]	[390]	[391]

It is worth noting that, such normalizing flow (with networks) built diffeomorphic transformations f_θ between a naive simply distributed “prior field”, u , and the physical field configurations, ϕ , resembles the *trivializing maps* approach suggested by Lüscher in Ref. [392], under which actually one is constructing for the system an effective action,

$$S_{\text{eff}}[u] = S[f_\theta(u)] - \log \det J_{f_\theta}(u). \quad (3.11)$$

that decouples the field variables by using the transformation whose Jacobian hopefully cancel out the interaction part in the original action, such that easier sampling can be realized for the (inversely) transformed new system $u = f_\theta^{-1}(\phi) \sim e^{-S_{\text{eff}}(u)}$. Thus, one can in general view NF as neural network parametrizations for trivializing maps. By noting such perspective and taking the trained flow model inverse as an approximation of the trivializing map, Ref. [393] and Ref. [394]

¹²The temperature $T = \frac{1}{aN_T}$ where a is the lattice spacing and N_T is the number of lattice points in temporal direction.

¹³Note that being different from the variational strategy of flow-based MCMC method, this work trains the flow on existing samples, thus using forward KL divergence as the loss function.

performed HMC on the flow transformed system u for a 2-dimensional U(1) gauge theory and ϕ^4 scalar field theory, respectively. Then to the HMC resulted Markov chain $\{u_i\}_{i=1}^N \sim e^{-S_{\text{eff}}(u)}$ which is with shorter autocorrelation times, the application of the inverse flow transformation just gives the recovered field configuration samples, $\{f_\theta(u_i)\}_{i=1}^N = \{\phi_i\}_{i=1}^N \sim e^{-S(\phi)}$. It was also demonstrated for the 2-dimensional $U(1)$ theory that such deep learning assisted HMC (DLHMC) [388, 393] allows mix between modes of different topological charge sectors. Note that performing HMC on the inversely transformed system (can also be called the latent space for the original system) was proposed also by Ref. [382] on Ising system and showed enhanced efficiency, and later Ref. [387] adopted similar approach of the neural RG to complex ϕ^4 field theory with interpretation as automatic construction of exact holographic mapping of AdS-CFT.

The splitting operation in Real NVP (i.e., partitioning the field configuration into two parts before entering each flow coupling layer, as Fig. 3.5 shown.) may constrain the expressibility of the flow induced field transformation f_θ , such as in terms of the symmetry embedding. Ref. [395] introduced continuous normalizing flow to define this invertible map, $f_\theta : u \rightarrow \phi$, as the solution to neural ODE [396] with a fixed time \mathcal{T} (x indicate the lattice cites):

$$\frac{d\phi(t)_x}{dt} = g_\theta(\phi(t), t)_x, \quad \text{with } u \equiv \phi(0), \quad \phi \equiv \phi(\mathcal{T}), \quad (3.12)$$

where g_θ is a neural network represented vector field, to which symmetries can be built in more easily. The probability of the generated configuration ϕ follows the solution from a second ODE [396]:

$$\frac{d \log p(\phi(t))}{dt} = -(\nabla_\phi \cdot g_\theta)(\phi(t), t), \quad \text{with } p(\phi(0)) \equiv p_u(u), \quad p(\phi(\mathcal{T})) \equiv q_\theta(\phi), \quad (3.13)$$

Again, taking the two-dimensional scalar field theory as the testing ground, authors in Ref. [395] proposed a vector field for the neural ODE inspired by Fourier expansion, $g_\theta(\phi(t), t)_x = \sum_{y,a,f} W_{xyaf} K(t)_a \sin(\omega_f \phi(t)_y)$, with ω_f the learnable frequencies and W the learnable weight tensor and $K(t)_a$ the first several terms of Fourier expansion on the interval $[0, \mathcal{T}]$. With such vector field, the required symmetry and also the internal Z2 ($\phi \rightarrow -\phi$) symmetry of the scalar ϕ^4 theory can be easily satisfied. Compared to Real NVP, such continuous flow method shows quite enhanced sampling efficiency: the effective sample size (ESS)¹⁴ increases from 1% to 91% for 32×32 lattice size.

For target distributions with multimodal structure, it is well known that the usual (local) update-based sampling methods, such as MCMC, face the challenge of traversing regions between different modes, e.g., Higgs modes/double well potentials. “Freezing” may probably happen when modes are very widely separated that the sampler tend to collapse to only one or few modes. [344, 350]. It was pointed out [397] that the flow-based MCMC encounters such difficulties as well, due to the tendency of “mode collapse” from the original version of flow model. Then several different trials were performed in Ref. [397] to construct and train flow models in sampling multimodal distributional in lattice field theory with example on the \mathbb{Z}_2 -broken phase of real scalar field theory, including data preparation in mixture models and data-augmented forwards KL divergence training, or adiabatic retraining with flow-distance regularization. But these methods either need prior knowledge for the mode structure to be provided, or difficult to really control the multimodal sampling with action parameters adjustments. Recently one interesting development [398] related is to introduce the Fourier transformation layer into the flow construction and showed promising in solving multimodal distribution sampling problem, details can refer to Sec. 5.1 (Note that later very recently, similar ideas but named as *power spectral density layer* for flow models is introduced in Ref. [399] and applied in scalar ϕ^4 field).

¹⁴The effective sample size, ESS, can be computed as $\text{ESS} = \frac{[N^{-1} \sum_{i=1}^N p(\phi_i)/q_\theta(\phi_i)]^2}{N^{-1} \sum_{i=1}^N [p(\phi_i)/q_\theta(\phi_i)]^2}$ with $p(\phi)$ the target distribution and $q_\theta(\phi)$ the flow-sampler induced distribution

For lattice gauge fields, new architectures of flow-based models have recently been developed to preserve the relevant local symmetries. A gauge invariant flow model is designed for sampling configurations for a U(1) gauge theory in Ref. [87]. See Sec. 5.1.1 for more details. Soon this kind of flow-based scheme was developed further to system with $SU(N)$ links [389] and also to fermionic system as shown in Ref. [390, 391]. In the lattice community, it is now under progressing in translating these developments into real QCD simulations as reported in the recent proceeding [400]. Though being promising, note however that, such flow-based methods currently are with training costs growing very fast as approaching to the continuum limit, as pointed out recently [386, 399, 401]. Thus further efforts are needed in improving the approach e.g., incorporating transfer learning strategy.

3.3. Observables Analysis for QFT

In lattice QFT simulations, after the field configuration generation, usually the other big portion of the computations lie in the estimation of physical observables from the generated ensembles of field configurations or the accessible correlation functions, for examples, the thermodynamics evaluation, and real-time physics extraction. Some problem especially for real-time physics reconstruction will often encounter ill-posedness from an inverse problem perspective, such as spectral functions extraction, the parton distribution functions computation and other related transport coefficient analysis based upon Euclidean correlators from lattice calculation. ML and DL techniques has now been explored for tackling these problems in recent years.

3.3.1. Thermodynamics and Phases

Thermodynamic states of matter, especially the accompanying phase transition, is one very important and extensively observed phenomenon in various many-body physics systems. From whatever theoretical (i.e., analytical or numerical) or experimental point of view, the exploration of phase diagrams forms a long-standing physics focus. Usually estimators for physical quantities calculated on numerically generated samples (e.g., from MCMC) are constructed with close relation to phase related indicator such as order parameter. It is however not always easy to identify some physically important states with such estimators, like for topological phase. In this context, the data-driven machine learning well suits the scope of phase identification due to its relevant strengths in recognizing hidden patterns and correlations from complex data, and both supervised and unsupervised learning techniques have been explored for such a task [33].

Supervised Phase Classification — The very beginning of introducing deep learning methods into thermodynamics/phase identification in general many-body systems can be dated back to Ref [402], where it was firmly demonstrated on simple Ising systems that deep neural networks can be trained to recognize phases and phase transitions solely from the raw configurations sampled from Monte Carlo simulations¹⁵. This indicates the feasibility of using ML algorithms to identify order parameters of the many-body system per supervised training. A lot of further explorations along this strategy follows up, including also quantum phases identification for fermionic system [403]. See Fig. 3.6 for a general schematic view of such supervised phase classification network.

By training a convolutional neural network (CNN) to capture the correlation between the inverse temperature and the 2D Ising spin configurations, Ref. [404] found that the trained CNN can locate characteristic features for the phase transition of the system with scrutinization of the filters (weight parameters W) from the network. Accordingly, a

¹⁵This strategy is dubbed as “supervised” because labeled phases from domain/prior knowledge is relied on.

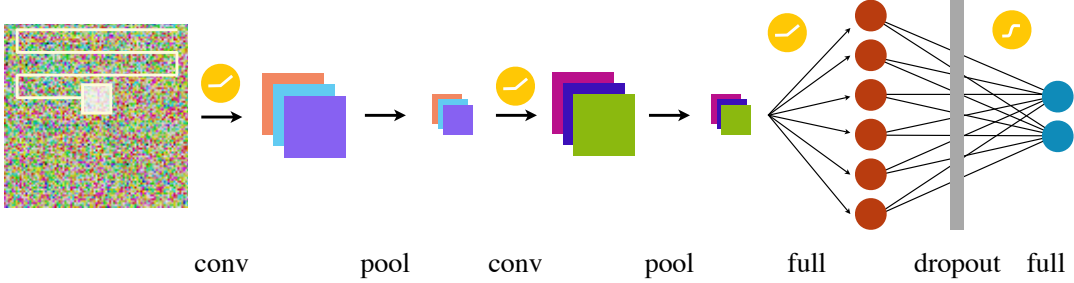


Figure 3.6: A typical convolutional neural network for phase binary classification. Taken from Ref. [403] with permission.

neural network assisted order parameter is defined to give rise to critical temperature estimation in this work. Ref. [405] generalized the phase identification with deep learning on Ising system to 3-dimensional case (employed 3D CNN on 3D Ising model), also discussed the average magnetization and energy regression, and the second-order and first-order phase transition learning. Being of special interest, it is expected that the QCD critical region have similar critical behaviors as in 3D Ising model because of their same universality.

Unsupervised Phase Clustering — Focusing on the phase classification task which is indeed one important physical goal in many-body physics, a lot of the machine learning approach based studies rely on prior knowledge of the order parameters of the system and ensembles of microscopic configurations of the physical system to be prepared, i.e., supervised training with correctly labelled “configuration-phase” large data set is needed as mentioned in above. However, phase labels for ensembles of field configuration are routinely not accessible, especially for a newly studied system. From machine learning, there is also unsupervised learning strategies which would find out the underlying important patterns in the collected data by itself and might be related to phase information in the context of phase identification, without knowing prior knowledge about the phase’s information under consideration.

The very first unsupervised learning application to phase transition recognition is proposed by Ref. [406] where neither the order parameter, thus the presence of a phase transition, nor the location of the critical point need to be provided. Specifically on the example of 2D classical Ising model, the principal component analysis (PCA) is adopted to extract the most significant components for the collected configurations of the system, then the projection of the spin configurations onto the first two principal components just automatically split into clusters matching well with the corresponding physical phases (see left of Fig. 3.7). The proposed simple PCA phase exploration approach was also shown successful in the Ising model with a conserved order parameter. In Ref. [407] this simple unsupervised learning techniques is also extended to different physical models, including the square and triangular-lattice Ising models, the Blume–Capel model, the biquadratic-exchange spin-1 Ising (BSI) model and the 2D XY model. It got confirmed that the extracted principal components can allow exploration of symmetry-breaking induced phase structure, can also help to identify the phase transition type and locating the transition points.

However, the naive PCA analysis by definition is limited to linear transformations, thus not suited for more complicated transitions with non-linear patterns. Like it is shown in Ref. [407] that the vorticity structure in the BSI model and XY model can not be captured from raw spin configurations by the PCA, and thus motivated to embark on nonlinear unsupervised machine learning algorithms. Ref. [408] proposed a *confusion scheme* which does not depend on labelled data and therefore can be taken as a generic tool to investigate unexplored phases of matter. Basically, the neural network is trained via deliberately by hand -“labelled” data for confusion purpose, then the performance of the trained network was

found to give a universal *W-shape* as a function of the guessed critical point for the parameter (e.g., chemical potential or temperature). This interesting idea got successfully demonstrated on Kitaev chain for topological phase transition, the classical Ising system for thermal phase transition and also the quantum many-body-localization transition in a disordered Random-field Heisenberg chain. However, this framework failed when applied on 2D XY model (with original unprocessed spin configurations as input) which shows unconventional topological phase transition, as demonstrated in Ref. [409]. It is found that significant feature engineering on the spin configurations is needed for the correct phase classification, which is closely related to the underlying vortex patterns of the KT transition.

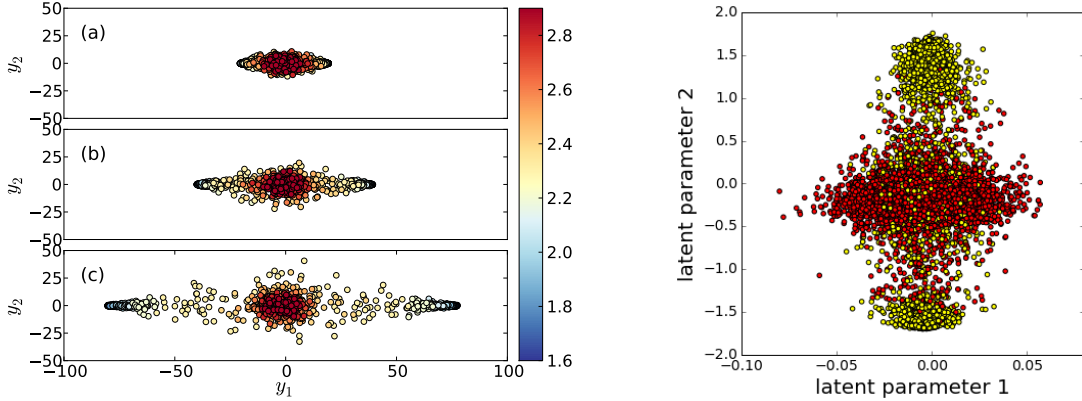


Figure 3.7: Taken from Ref. [406] (left) and [410] (right).

As another popular unsupervised learning method, deep generative models such as the variational autoencoder (VAE) and generative adversarial networks (GAN), were also applied to investigate phase transition detection of physical systems by learning latent parameters of the original configurations. In Ref. [410] the authors studied the phase transition with PCA and VAE on states of 2D Ising model (see right of Fig. 3.7) and 3D XY model. It was found that the unsupervisedly learned latent representation of the spin configurations are clustered by itself and correspond to the known order parameters of the system under investigation. Also, the reconstruction loss from the training can serve as an universal identifier for phase transition. In Ref [411] this strategy was further extended to explore crossover region identification to reveal deeper understanding of the latent space, which is achieved by studying the response of the learned latent variable mappings of the Ising configurations along with external non-vanishing magnetic fields and temperatures.

Unsupervised Anomaly Detection — With a different strategy, DNN autoencoder (AE) is also deployed by performing anomaly detection to explore phase diagrams of quantum many-body systems [412] in an automated and completely unsupervised manner. Intuitively, the anomaly detection can be realized by utilizing the reconstruction loss from the well-trained AE, as introduced in Sec. 1.2.2 and also applied for outlier detection in HICs in Sec. 2.2.2, to single out newly confronted data those are showing larger reconstruction error compared to training classes. Thus, by investigating the loss map of the trained AE on different parameter space of a physical system (with input could be full state vector or entanglement spectrum or correlations for the system), one can possibly map out the phase diagram without physical a priori knowledge for example of the order parameter. This anomaly detection scheme got tested on the extended Bose-Hubbard Model, which shows a rich phase diagram. Aside from the several standard phases, the method also reveals a new phase showing unexpected properties on the phase diagram.

Under a similar scheme, the generative adversarial network (GAN) is trained in Ref. [413] as the anomaly detector to identify gapless-to-gapped phase transition in different one-dimensional models. Specifically, the detection of the

elusive Berezinskii–Kosterlitz–Thouless (BKT) phase transitions in the XYZ spin chain, the Bose–Hubbard model and the generalized two-component Bose–Hubbard model (all at zero temperature) is demonstrated [413] with entanglement spectrum (measuring the degree of quantum correlation among sub-portions of the system) as dataset.

Interpretable Learning — Though phases of matter are shown to be detectable through supervised or unsupervised learning strategies, it’s not clear yet in physics interpretation what the learning algorithm captured from such classification tasks. Some early works explored under the supervised kernel framework of support vector machine (SVM)¹⁶ to give interpretable decision functions and further physical discriminators from the trained machines [414–416]. Ref. [417] proposed a *correlation probing neural network* to reveal the fact that the learned decision functions originate from physical quantities. It is also shown that a full explicit expression of the learned decision function can be reconstructed, from which one can further extract the quantities to facilitate the network’s decision-making in classifying phases. The proposed procedure get demonstrated first on Ising model, where it digged out the magnetization and energy per spin as the decision support of the trained network. Then on SU(2) lattice gauge theory, a whole ML pipeline combining PCA and the *correlation probing neural network* is constructed to examine the deconfinement phase transition related. The PCA with the average reconstruction loss serving as a universal phase transition identifier is shown to be able to capture the phase indicator, though the involved Polyakov loop is a non-linear order parameter in SU(2) gauge theory. This enables the awareness of an existing phase transition unsupervisedly. Then the *correlation probing network* is trained to correctly predict phases and further construct the explicit expression of the decision function, to which it is found that the decision is based upon the Polyakov loop as a non-local and non-linear order parameter.

In many of the ML based explorations for physics study, the more complicated algorithms though might be with better performance yet quite often lacking transparency and interpretability, especially when one seeks for new physical insight or comprehension of the learned representations from the data. In Ref.[418] it was proposed to adopt “explainable AI” techniques—specifically the layer-wise relevance propagation (LRP) method—to identify relevant features that influence the trained algorithms towards or against the particular recognition result. The work takes the (2+1) dimensional scalar Yukawa theory as demonstration context, which displays an interesting phase structure with two broken phases (ferromagnetic denoted as FM and antiferromagnetic denoted as AFM) separated by a symmetric paramagnetic phase (PM). These can be indicated by the normal magnetisation and the staggered magnetisation. With both the field configurations and preprocessed physical observables prepared, several machine learning models were trained to infer the action parameters (the hopping parameter κ is taken in this work) from the known observables (labelled as approach A) or solely from the raw field configurations (labelled as approach B). It should be noted that, the action parameter learning in this work is taken as just a pretext task to reveal the underlying phase structure or related physical insights. This is achieved by the adopted LRP to propagate the initially assigned relevance on the output to input layer by layer.

Observables’ Regression in QFT — The application of deep neural network for regressive tasks in lattice quantum field theoretical setting was explored in Ref [352] to unravel the dynamical information related to phase transition and physical observables. In Ref [352] the authors considered a complex massive scalar field with quartic coupling λ in (1+1)-dimensional Euclidean space-time at nonzero temperature, and a finite chemical potential μ is introduced to control the

¹⁶Briefly speaking, in the course of binary classification given training set $(\mathbf{x}^{(k)}, y^{(k)}) \in \{\pm 1\}$), the SVM aims at determining a decision boundary, $\omega \cdot \mathbf{x} + b = 0$, a hyperplane with parameters ω and b to separate data into two classes. To clearly separate the data, a margin without any training data contained is inserted, which is with the boundaries defined as $\omega \cdot \mathbf{x} + b = \pm 1$, and the margin width $2/\|\omega\|$ is expected to be maximized in generating the best separation of data. $\omega \cdot \mathbf{x} + b = d(\mathbf{x})$ provide the **decision function**.

charge density fluctuation, which also makes the action complex. The worldline formalism is taken for simulating the field configurations and circumvent the sign problem involved. Correspondingly, this $1 + 1$ -d charged ϕ^4 field is fully represented by 4 integer-valued dual variables: k_1, k_2 and l_1, l_2 . Observables like number density and field square can also be calculated with the re-expressed partition function under the dualization approach. The “silver blaze” behavior is expected for this system at low temperature and low chemical potential μ , that the particle density gets suppressed (with a mass gap) until some threshold value $\mu > \mu_{th}$ then enter the condensate region and increase considerably. Though for 2-dimensional systems there is no real phase transition related to symmetry breaking, one can refer to this pronounced change in density as a transition to condensation as treated in Ref. [352]. With the configurations training set prepared, two regressive tasks were attempted: phase identification and physical observable regression.

For the phase identification, a convolutional neural network (CNN) was devised to perform the phase binary classification task using the field configurations as input. Purposely, the training set is prepared to consist only two ensembles of configurations with one well above and one well below the transition point (μ_{th}), while the testing set is constructed with many ensembles of configurations at different chemical potential values sit in between the two chemical potential values of training ensembles. The network output is interpreted as *condensation probability*, $P(\phi)$, for each inputted configuration. Strong correlations were observed between the network output and number density or field square, without any specific supervision on the role of these observables in distinguishing the phases. The ensemble average of the network predicted condensation probability, $\langle P(\phi) \rangle$ serves as an accurate *phase classifier*, with its first non-vanishing point well indicating the transition threshold value. It is worthy to note that such concept of interpreting the network output P as an observable was also extended to undergo histogram reweighting [419]¹⁷ to construct an effective order parameter and perform scaling analysis (see also combination with transfer learning in studying unknown phase transitions [420]. Ref.[352] further tried to reduce the input features of this phase classification task, and found that with even restricted training input e.g., only l or even only k_1 variables, the network still can well distinguish the two phases. Note that the “order parameter”—number density of the system, n , is given by the sum of k_2 variables for this field system (See left panel of Fig. 3.8). This thus indicate that the network have captured hidden structures in k_2 variables, though it (k_2) conventionally is not able to distinguish the low-density and high-density phases.

The same supervised training paradigm was used for the observables (number density n and field square ϕ^2)¹⁸ regression task, with only the network output layer adapted to linear activation, and the loss function for training changed from cross entropy (for classification) to MSE. The same two ensembles of configurations were taken as the training set, with which the regression network is trained and then tested on previously unseen configurations at also different chemical potential showing different number density and field square. The regression performance was found to be successful over a broad range of chemical potentials, as shown in the right panel of Fig. 3.8. While for the number density regression the needed pattern may seem simple, the field square is a highly non-linear function of the high-dimensional input (i.e., field configurations with $4 \times N_1 \times N_2 = 8000$ entries). Thus, the good predictive ability of the network in regressing field square is non-trivial and impressive. Similar findings in the context of lattice Yang-Mills theories (SU(2) and SU(3)) about the transferability of the neural network learned regression function to a different parameter space are

¹⁷Specifically, the reweighting in terms of inverse temperature is performed for 2-dimensional Ising system as $\langle P \rangle_\beta = \frac{\sum_i^N P_{\sigma_i=1} \exp(-(\beta - \beta_0)H(\sigma_i))}{\sum_{i=1}^N \exp(-(\beta - \beta_0)H(\sigma_i))}$, with β_0 the place of inverse temperature where MCMC measurements for P is given.

¹⁸Specifically the number density is given by $n = \frac{1}{N_1 N_2} \sum_x k_2(x)$ and the squared field is given by $|\phi|^2 = \frac{1}{N_1 N_2} \sum_x \frac{W[s(k, l; x) + 2]}{W[s(k, l; x)]}$ where the weight $W[s] = \int_0^\infty r^{s+1} e^{-(4+m^2)^2 - \lambda r^4} dr$ and $s(k, l; x) = \sum_\nu [|k_\nu(x)| + |k_\nu(x - \hat{\nu})| + 2(l_\nu(x) + l_\nu(x - \hat{\nu}))]$.

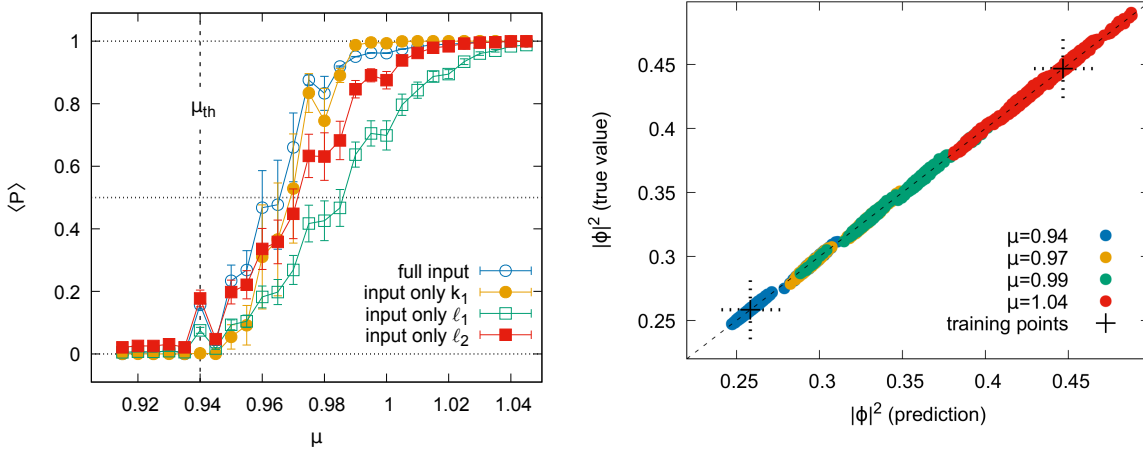


Figure 3.8: (left) Ensemble average of condensation probability in testing stage along with chemical potential; (right) Comparison of the network predicted squared field ϕ^2 and the true values at different chemical potentials. Taken from Ref. [352] with permission.

also reported in Ref. [421], where the Polyakov loop as gauge invariant deconfinement order parameter is the prediction target. For similar tasks investigated in Ref. [352], authors in Ref. [422] further explored the influences of translational equivariance satisfaction of the used network structure on the regression performance and generalization capabilities. Note also there's earlier trial [423] with traditional machine learning technique, specifically a boosted decision tree (BDT) regression algorithm, to reduce the computational cost of evaluating lattice QCD observables, by means of predicting observable from simpler and less compute-intensive observables' evaluation those are correlated with the target observable.

Enhanced Regression with Symmetries Embedded Networks — Interactions for physics systems always respect some symmetries, which possess fundamental importance to physics theories across all scales nowadays. The incorporation of the symmetries for the system into the analyzing procedures like machine learning architectures has been proven to be beneficial in improving the performance of the algorithms. One such popular simple example is the convolutional neural network (CNN), which is good at pattern recognition for image-like data structure because of the satisfied global translational equivariance (as manifested in the sharing of convolutional kernels). This concept has now been extended to yield up group equivariant CNNs (G-CNN) [424], where more general symmetries including rotations and reflections are discussed, with also local symmetry e.g., for data on curved manifolds [425]. See also a recent snowmass white paper [426] for a report about symmetry group equivariant architectures across physics studies. In the context of quantum field theory, symmetries provide important constraints on the action and thus are essential for lattice field theory study, their proper consideration is also crucial in obtaining meaningful results in lattice simulations.

As the fundamental theory for strong interactions that guide high energy nuclear physics phenomenon, QCD is a (non-abelian) gauge theory that the Lagrangian should be invariant under local symmetry transformations that form symmetry group $SU(3)$. Being relevant, there's lattice gauge equivariant (LGE) CNNs being proposed recently [427]. Consider a $SU(N_c)$ Yang-Mills theory on a lattice Λ and discretized in terms of links variables (parallel transporters) $U_\mu(x) = \exp[-igA^\mu(x + a\hat{\mu}/2)]$, the gauge links are transformed by group elements Ω_x as

$$U_\mu(x) \rightarrow \tilde{U}_\mu(x) = \Omega(x)U_\mu(x)\Omega^\dagger(x + \hat{\mu}), \quad (3.14)$$

with $\Omega : \mathbb{R}^4 \rightarrow SU(N_c)$ gauge transformations of the gauge fields. Taking the Wilson action as approximation for the

Yang-Mills theory with coupling g ,

$$S_W[U] = \frac{2}{g^2} \sum_{x \in \Lambda} \sum_{\mu < \nu} \text{ReTr}[\mathbb{1} - U_{\mu\nu}(x)], \quad (3.15)$$

with $U_{\mu\nu}(x)$ the plaquette (1×1 Wilson loop),

$$U_{\mu\nu}(x) = U_\mu(x)U_\nu(x + \mu)U_{-\mu}(x + \mu + \nu)U_{-\nu}(x + \nu), \quad (3.16)$$

and transform under gauge transformation locally as $U_{\mu\nu}(x) \rightarrow \Omega(x)U_{\mu\nu}(x)\Omega^\dagger(x)$. To construct lattice gauge equivariant network architectures, Ref. [427] devised several elementary layers to explicitly respect the gauge symmetry. One essential starting point is processing the input fields to be tuples $(\mathcal{U}, \mathcal{W})$, where $\mathcal{U} = \{U_\mu(x)\}$ the set of links of the configuration and $\mathcal{W} = \{W_i(x)\}$ with $W_i(x) \in \mathbb{C}^{N_c \times N_c}$ a set of locally transforming complex matrices like the plaquettes is used as example ($W_i(x) \rightarrow \Omega(x)W_i(x)\Omega^\dagger(x)$, note that Polyakov loops can also be included as stated in Ref. [427]). Then two gauge equivariant operations are introduced to act on the tuple data, $(\mathcal{U}, \mathcal{W})$, one is performing convolutions named as LGE convolution (L-Convs) and the other is LGE bilinear layer shortly named as L-Bilin, both leaving the gauge links variables unchanged while modifying only the \mathcal{W} part in covariant manner. Specifically, the L-Convs generalizes the normal convolutional operation to account for the parallel transport under geodesics to meet the requirement of gauge equivariance,

$$W'_i(x) = \sum_{j, \mu, k} \omega_{i, j, \mu, k} U_{k \cdot \mu}(x) W_j(x + k \cdot \mu) U_{k \cdot \mu}^\dagger(x), \quad (3.17)$$

with the kernel weights $\omega_{i, j, \mu, k} \in \mathbb{C}$ and $1 \leq i \leq N_{ch, out}, 1 \leq j \leq N_{ch, in}, 0 \leq \mu \leq D, -K \leq k \leq K$ where K specifies the kernel size and N_{ch} the feature map channel number. Such L-Convs operation combines data at different lattice sites with parallel transport well taken into account. The L-Bilin layer on the other hand is acting on a single lattice site, which combines two input tuples with bilinear product (note again the \mathcal{U} part are the same after operation):

$$W''_i(x) = \sum_{j, k} \alpha_{i, j, k} W_j(x) W'_j(x), \quad (3.18)$$

with the trainable weights $\alpha_{i, j, k} \in \mathbb{C}$ and $1 \leq i \leq N_{out}, 1 \leq j \leq N_{in, 1}, 1 \leq k \leq N_{in, 2}$. Besides L-Convs and L-Bilin,

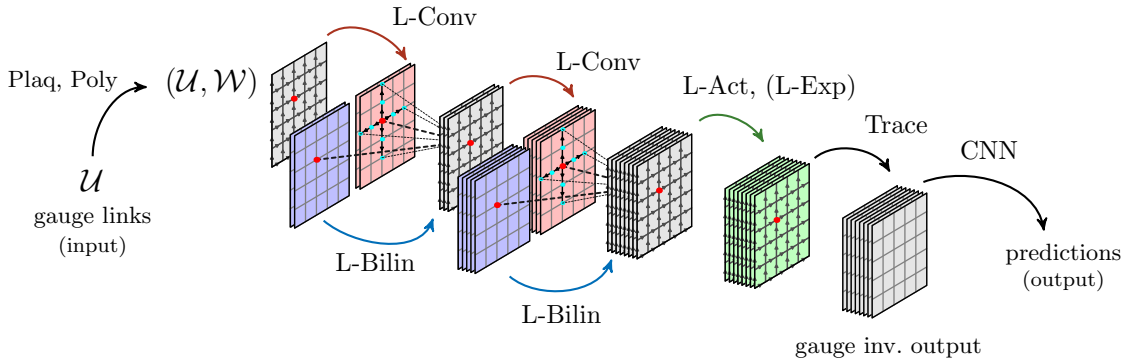


Figure 3.9: A generic lattice gauge equivariant CNN as from Ref. [427] with permission.

LGE activation function and LGE Trace layer, plaquettes and Polyakov loops calculation layers (pre-processing layer to prepare the \mathcal{W} information) are also proposed as elementary component to construct the gauge equivariant L-CNNs for lattice gauge field configuration treatment. See Fig. 3.9 for a typical L-CNNs comprising the above proposed LGE layers as from Ref. [427]. It is further demonstrated that such specially devised L-CNNs surpasses traditional CNN models in regression of gauge invariant observables.

3.3.2. Variational Neural-Network Quantum States

Many of the previous studies shown in above rely on existed or pre-prepared ensembles of configurations for the physical system, until Ref. [70] first introduced artificial neural networks to represent the wave function and presents a stochastic reinforcement learning scheme for solving the many-body problem without prior knowledge of exact samples. This gives state-of-the-art accurate description of both the ground-state and time-dependent quantum states for given Hamiltonian \mathcal{H} in several prototypical spin systems including 1 and 2-d transverse-field Ising (IFI) and anti-ferromagnetic Heisenberg (AFH) models. The corresponding wave function represented by a neural network which maps from the N discrete-valued degrees of freedom set $\mathcal{S} = (\mathcal{S}_1, \mathcal{S}_2, \dots, \mathcal{S}_N)$ to the complex phase and amplitude information, $\Psi(\mathcal{S})$ (taking the Restricted Boltzmann machine, RBM¹⁹, with M hidden spin variables $h_i = \{\pm 1\}$ for example),

$$\Psi_M(\mathcal{S}; \mathcal{W}) = \sum_{h_i} e^{\sum_j a_j \mathcal{S}_j + \sum_i b_i h_i + \sum_{ij} W_{ij} h_i \mathcal{S}_j}, \quad (3.19)$$

is termed as neural-network quantum states (NQS) with the trainable parameters $\mathcal{W} = \{a_i, b_i, W_{ij}\}$. Such RBM representation is formally equivalent to a two-layers feed-forward neural network with special activation functions, i.e., $z^1(x) = \log \cosh(x), z^2(x) = \exp(x)$. Through minimization of the energy expectation $E(\mathcal{W}) = \langle \Psi_M | \mathcal{H} | \Psi_M \rangle / \langle \Psi_M | \Psi_M \rangle$, the network parameters \mathcal{W} can be optimized via variational Monte Carlo (VMC) sampling. It's shown that this proposed scheme can accurately evaluate the ground state energy in the TFI and AFH examples. Later an extension for this approach to calculate excited states was also introduced with both RBM and deeper fully connected neural networks [429].

For dynamical properties of the many-body state which is upon solution of the time-dependent Schrödinger equation, the NQS also works with extension of the network parameters to be complex-valued and time-dependent $\mathcal{W}(t)$ [70]. Accordingly, per the Dirac-Frenkel time-dependent variational principle, the network parameter at each time t can be trained taking the variational residuals as the objective function,

$$R(t : \dot{\mathcal{W}}(t)) = \text{dist}(\partial_t \Psi(\mathcal{W}(t)), -i\mathcal{H}\Psi), \quad (3.20)$$

which is achieved stochastically by a time-dependent VMC method. On both TFI and AFH models, this time-dependent NQS scheme is demonstrated to capture with high accuracy the unitary dynamics induced by quantum quenches. There are further developments along using NQS for many-body physics studies, see Refs. [381, 430, 431] and Refs. [432, 433].

3.3.3. Real-Time Dynamics Analysis

Within modern theoretical physics, the dynamics of strongly correlated systems holds the central role for many pressing research problems, e.g., the hadronic spectrum/behaviors at zero temperature or immersed inside a thermal medium [434, 435], the non-equilibrium evolution and transport properties for the created QGP in heavy ion collisions [436, 437], the understanding for parton distribution functions of nucleons and nuclei [438–440]. The computation of these real-time physics is often noncompliance to perturbative analysis, thus calls for nonperturbative treatment such as lattice QFT simulations. These first principle Monte-Carlo based simulations are usually performed in Euclidean space-time (after a Wick rotation $t \rightarrow it \equiv \tau$) and provides only Euclidean correlators. Accessing real-time physics from imaginary-time correlation's “measurements” in quantum Monte-Carlo or lattice QFT simulation generally forms ill-conditioned inverse problems. Spectral representation forms a bridge to approach the real-time information of the dynamics from

¹⁹Note in Ref. [428] it was demonstrated that the RBM possess equivalence to tensor network states that widely used in quantum many-body physics

the Euclidean correlators. Also, quite often the relevant physics can be decoded directly from the spectral functions, like transport coefficients or in-medium hadronic behaviors [434].

Spectral Function Reconstruction — The involved spectral reconstruction problem can in general be cast from a Fredholm equation of the first kind, $g(t) = \int_a^b K(t, s)\rho(s)ds$, with the aim of rebuilding the function $\rho(s)$ given the kernel function $K(t, s)$ and limited numerical evaluation on $g(t)$. Once only a finite set of evaluation data with non-vanishing uncertainties are possible for $g(t)$, the inverse transformation of the above convolution becomes ill-conditioned (see Ref. [441] and Sec. 5.3 for more details). Basically, one can expand the convolution kernel (as a linear operator) by basis functions in a Hilbert space, within which it's shown in Refs. [442] and [441] respectively that the Laplace transformation kernel, $K(t, s) = e^{-st}$, and Källen-Lehmann (KL) kernel, $K(t, s) = s(s^2 + t^2)/\pi$, possess arbitrarily small eigenvalues thus correspond to eigenfunctions being able to induce negligible changes for the integral result of $g(t)$. Consequently, for the inversion operator these eigenfunctions, termed as null-modes, are related to arbitrarily large eigenvalues and will bring about numerically unstable inversion from noisy $g(t)$ to $\rho(s)$. In the context of QFTs the involved target function $\rho(s)$

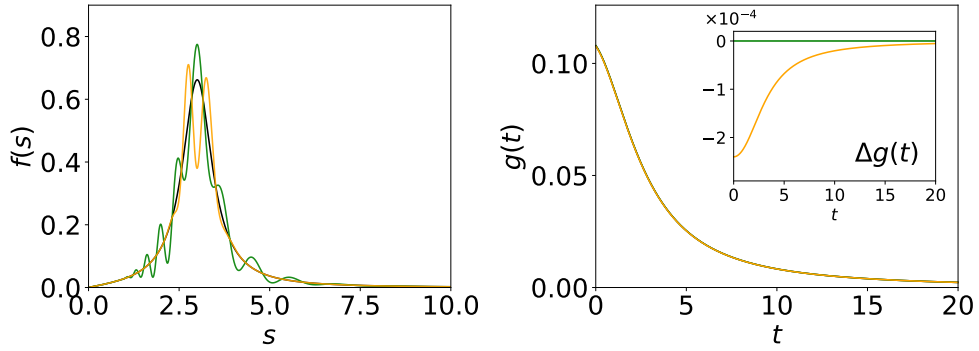


Figure 3.10: Spectral functions differed by null-modes (left) and their corresponding Källen–Lehmann correlation functions (right). The insert figure shows the differences-in-propagator caused by null-modes. Taken from [443] with permission.

is the spectral functions, and the integral $g(t)$ corresponds to correlator which can be measured from lattice calculations. To break the degeneracy for facilitating the inversion related, different regulator terms indicating prior domain knowledge have been proposed over the past several decades, such as Tikhonov regularization(L2 regularization) [444, 445], sparse modeling approach(L1 regularization) [446, 447], maximum entropy method (MEM) [434, 448] and related Bayesian Reconstruction (BR) method [449].

Recently there are also studies incorporating machine learning methods into solving this ill-posed problem, mainly in supervised manner under data-driven paradigm, including also unsupervised learning based trials. As the early stage ML application, in Ref. [450] the kernel ridge regression (KRR) and kernel quantile regression (KQR) models are adopted to invert the Fredholm integral of the first kind. Through the preparation of training database and also the restriction on basis functions and kernel involved, a regularization is naturally provided by such projected regression treatment to tame the ill-conditioned inversion.

Ref. [451] firstly introduced deep convolutional neural network (CNN) and variants of stochastic gradient descent optimizer into the spectral reconstruction from imaginary time Green's function, which is domain-knowledge-free as distinct from Ref. [450]. Being demonstrated on a Mott-Hubbard insulator and metallic spectrum, the deep CNN gives good reconstruction performance superior to the classical MEM method. It's also found that the usage of CNN structure achieved better reconstruction than fully connected neural network structure. A similar strategy was taken in Ref. [452] with the principal component analysis (PCA) also introduced to reduce the dimensionality of the QMC simulated imaginary time

correlation function. On a prototypical problem of quantum harmonic oscillator linearly coupled to an ideal heat bath, which is physically more relevant scenario, Ref. [452] demonstrated that the deep neural network with PCA processed input can outperform the MEM approach in reconstructing the spectral from the single particle fermionic Green's function, especially while the noise level increases for the data. Ref. [453] further pushed such data-driven supervised approach to QFT context, with the Källen–Lehmann (KL) spectral representation considered. The database is prepared in the form of combination of Breit–Wigner peaks, $\rho^{BW}(\omega) = 4A\Gamma\omega/((M^2 + \Gamma^2 - \omega^2)^2 + 4\Gamma^2\omega^2)$. Then in representing the network output – spectral function, two schemes are studied: one is with parameters of the Breit–Wigner peaks inside the spectral function and the other is with list of discretised data points of the spectral directly. The reconstruction performance is found to be at least comparable and again surpassing classical methods at large noise cases. Being inspired from the well-designed Shannon–Jaynes entropy term in regularizing the ill-posed inverse problem, Ref. [454] proposed a novel framework called SVAE based on the variational autoencoder (VAE) together with the entropy term “S” included in the loss function to reconstruct spectral functions from Euclidean correlators. A Gaussian mixture model is adopted to generate the spectral function database, while physically motivated spectral corresponded correlators are prepared for the test. Realistic noise level of lattice QCD data is implemented in both the training and testing data, and it was found that the trained SVAE in most of the cases gives comparable reconstruction quality as to MEM, and in cases with sharp spectral peaks with fewer data points for the correlator, SVAE shows superior results than MEM.

The above-mentioned studies more or less all rely on training data set preparation to regularize the inverse problem, thus may have dependency on the specific kinds of training data as well. There are also studies taking unsupervised learning strategy to perform the inversion directly, like Ref. [455] adopt the radial basis function network (RBFN) to represent the spectral, basically approximating the spectral as linearly combined radial basis function (RBF),

$$\rho(\omega) = \sum_{j=1}^N w_j \phi(\omega - m_j), \quad (3.21)$$

with ϕ the active RBF unit at adjustable center m_j and w_j the trainable weight. In discretized form, Eq. 3.21 can be rewritten in matrix format $\rho = \Phi W$, with which the Källen–Lehmann spectral representation integral becomes

$$G_i = \sum_{j=1}^M \sum_{k=1}^N K_{ij} \Phi_{jk} w_k \equiv \sum_{k=1}^M \tilde{K}_{ik} w_k, \quad i = 1, \dots, \hat{N} \quad (3.22)$$

with \tilde{K} an irreversible $\hat{N} \times M$ matrix. By setting $M = N$ then the truncated singular value decomposition (TSVD) method can be naturally applied to solve w_j . As compared to supervised learning applications, this method is fast in training and also free of over-fitting issue. Compared to traditional methods, RBFN resulted in better spectral reconstruction, especially about the low frequency part which matters to the transport coefficients extraction in Kubo formula.

As another alternative representation, Gaussian Processes (GP) are incorporated within Bayesian inference procedure for reconstructing 2+1 flavor QCD ghost and gluon spectral [456]. GP in general defines a probability distribution over a functional characterized by the chosen kernel function,

$$\rho(\omega) \sim \mathcal{GP}(\mu(\omega), C(\omega, \omega')), \quad (3.23)$$

where $\mu(\omega)$ is the mean function usually set as zeros, and $C(\omega, \omega')$ is the covariance dictated by the kernel function. Ref. [456] used the radial basis function (RBF) kernel. Actually, it's proved that GP is equivalent to infinite wide neural network. In this sense, the spectral representation in Ref. [456] somehow is limiting push for the one in Ref. [455] since the RBF activation usage. One distinctive point is that Ref. [456] plug such GP represented spectral priors into the Bayesian

framework to construct the likelihood of the ghost and gluon spectral. The corresponding reconstruction of the spectral function for ghost and gluons shows similar peak structure as to fRG reconstruction of the Yang–Mills propagator.

In Refs. [441, 443, 457] a different approach based upon automatic differentiation and general deep neural network representation [$\rho(\omega) = NN(\omega)$] has been devised (see Fig. 5.7 for the flow chart), which belongs to unsupervised category as well thus avoided the over-fitting issue and does not rely on training data preparation in advance. Since its general tackling of inverse problem as a strategy, we summarized them in Sec. 5.3, refer there for more technical details and explanations on the corresponding results.

In-medium Heavy Quark Potential — Another interesting and important real-time physics in the context of high energy nuclear physics lies in the in-medium effects of hard probes, for example the jets or heavy quarkonium (bound states of heavy quark and its anti-quark). Regarding as a smoking gun for the creation of QGP, heavy quarkonium has been intensively studied both theoretically [436, 437, 458–460] and experimentally [461, 462]. One central focus is to understand the in-medium heavy quark interaction, the computation of which represents a big challenge for non-perturbative strong interaction calculations. Because of the large mass and small relative velocities for the inter quarks inside the bound state, non-relativistic treatment of it is allowed, and also the color electric interactions inside will be dominant. It has been long expected that color screening will weaken the heavy quark interaction, in analogy with Debye screening phenomenon for QED. Additionally, studies from both the hard thermal loop (HTL) calculations [463, 464] and the recent effective field theory approach e.g., pNRQCD calculations [465, 466] point out that a non-vanishing imaginary part for the heavy quark interaction will appear in the QCD medium beyond just screening effect. For a complete understanding, the non-perturbative framework like lattice QCD is called for. In the past decade, there are studies for real-time heavy quark interaction based upon lattice QCD calculations, mainly with a Bayesian technique [467–469] used for spectral functions of the thermal Wilson loop. On the other hand, quantification of the in-medium Bottomonium masses and thermal widths are released from the very recent lattice QCD studies [470–472]. Empirically, it'd be interesting to know if one in-medium heavy quark potential $V(T, r)$ under a QM potential picture can accommodate these in-medium properties from lattice studies, since this can not be answered yet from field theoretic point of view.

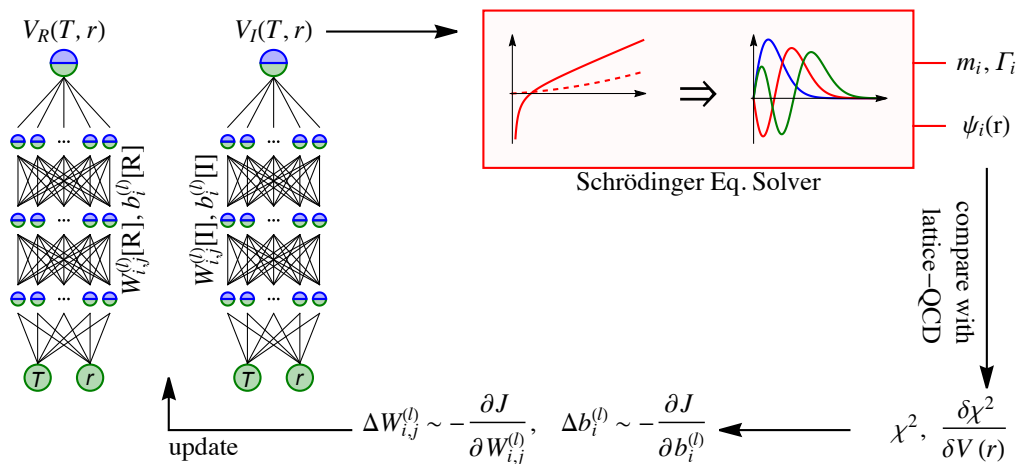


Figure 3.11: Flow chart of in-medium heavy quark empirical potential reconstruction from LQCD measurements of mass and thermal width. Taken from Ref. [473] with permission.

Ref. [473] accordingly devised a DNN-based method to infer the in-medium heavy quark interaction starting from the

lattice QCD released in-medium properties for Bottomonium. The DNN is introduced to parametrize the temperature and inter-quark distance dependent complex potential $V(T, r)$ in a model independent manner, and coupled to the Schrödinger equation to give rise to the bound state mass and thermal width. By comparing to the lattice QCD data correspondingly, the χ^2 can be evaluated serving as the loss function to optimize the DNN representation. Perturbative response analysis is performed to derive the gradient of the loss function with respect to network parameters which involves naturally the Feynmann-Hellman theorem, with which the optimization can be done using stochastic gradient descent algorithms. Fig. 3.11 displays the flow chart of this DNN-based automatic differentiation inference for heavy quark potential. The uncertainties of the reconstruction can be properly evaluated via Bayesian inference, which take into account both the aleatoric and epistemic uncertainty by construction. For more details, see Sec. 5.3.

Parton Distribution Function Reconstruction — The parton distribution function (PDF) is a fundamental property that reveals the hadron inner structure, which specifically depicts the probability distribution of the momentum fraction carried by the constituent quarks and gluons inside the hadron. It can be measured in high energy deep inelastic scattering experiments and also computed in theoretical calculations, such as lattice field theory. One may refer to [474, 475] for an overall review of recent developments on the study of PDF. There have been some pioneer efforts to employ deep learning techniques to help to extract the parton distribution function in a nucleon, where the NNPDF approach [476–481] for global QCD analyses has been systematically applied in determining the PDF in proton and also the fragmentation functions (FFs) in the light-hadron. With neural network parametrization for the PDF, NNPDF performs the global QCD fit based on high energy collider experimental data and higher order perturbative calculation in QCD and QED/Electroweak theory. This methodology was also implemented for the determination of the nuclear parton distribution function (nPDF) [482–484] with the χ^2 minimization achieved via stochastic gradient descent.

In the practice of lattice QCD calculation, a useful intermediate quantity is the Ioffe-time distribution — the Fourier transformation of the PDF, $Q_{\text{Ioffe}}(\lambda; \mu) = \int_{-1}^1 dx e^{ix\lambda} q_{\text{PDF}}(x; \mu)$, where μ is the energy scale, x the momentum fraction, and λ the Ioffe-time. Meanwhile, the observables that can be computed in lattice QCD calculation can be expressed as a convolution of the Ioffe-time distribution. Therefore, if $Q_{\text{Ioffe}}(\lambda; \mu)$ is obtained from lattice QCD calculation, one can then perform the inverse Fourier transformation and compute the PDF. Ref. [485] reconstructed the Ioffe time distribution using two approaches, i) a Bayesian Inference reconstruction and ii) DNN representation. In the latter, the network parameters are updated according to a generic algorithm, which takes random walks in the network parameter space and select the configurations that reduce the difference between the desired data and the reconstructed ones. In Ref. [486], the authors implemented DNN to represent $Q_{\text{Ioffe}}(\lambda; \mu)$ and applied the gradient driven update method that is described in Sec. 5.3 to optimize the network parameters. The new method significantly increases the efficiency and accuracy of the Ioffe-time distribution reconstruction. More applications can be found in Refs. [476, 487–490].

3.4. Sign Problem

There have been many efforts to find ways to overcome the sign problem in lattice QCD, but it remains a challenging and active area of research (see recent reviews in Ref. [11, 348, 349]). The most head-on method can be summarized as “statistical approach”, which aims to improve the statistic directly. *Reweighting* the observable with phase factors [491] and representing the actions with *density-of-states* [492] are two practical attempts. The alternative head-on methods contain, e.g., Taylor expansions to μ/T around zero chemical potential [493, 494], analytic continuation from imaginary chemical potential [495, 496]. The other branch of approaches is the “new variables” method. It attempts to tackle the

problem by redefining a new set of variables to reformulate the complex action. *Dualization* is one successful example, in which the dual variables can afford a representation of the partition function in terms of positive quantities [348, 497]. To handle with the action on the complex plane properly, people have developed complex Langevin methods and integration contour deformations. The former originates from stochastic quantization [498], processing the complex action with two coupled Langevin dynamics [499, 500]. The latter should rely on the *thimble method*, and the latest advances in using machine learning techniques focus on this approach [349]. Both the complex Langevin and Lefschetz thimbles methods rely on a complexification of the field degrees of freedom to move the integration over paths into the complex plane.

The key idea of the *thimble method* is to continuously deform the integration contour for the path integral from the original real fields ($\in \mathbb{R}^n$) into an N -dimensional real manifold \mathcal{M} immersed in the complexified field space ($\in \mathbb{C}^n$), on which the dramatic phase fluctuations induced by complex actions can be suppressed or even removed [501]. Earlier attempts chose the manifold \mathcal{M} as the set of Lefschetz thimbles resembling the high-dimensional generalization of the “steepest descent direction” or “stationary phase path”, and the induced integrand turns out to be real and positive up to an overall phase over the thimble [502, 503]. The reason is that the imaginary part of the action, $S_I[\phi]$, becomes locally constant and the real part, $S_R[\phi]$, is located as close as possible to the “saddle point”, which constructs the best landscape to perform stochastic evaluations of the path integrals. This further inspired the “generalized thimble method” [504, 505], where the integration contour is deformed to a manifold \mathcal{M}_T chosen as the evolution results of the so-called holomorphic gradient flow equation by a fixed flow time T starting from the original integration region,

$$\frac{d\phi}{dt} = \frac{\bar{\partial}S}{\bar{\partial}\phi}, \quad (3.24)$$

where S is a generic Euclidean action and the bar indicates the complex conjugation. The time t is an auxiliary variable, which denotes the evolution of the equation. Any flowed configuration $\phi(T)$ (which collectively forms the manifold \mathcal{M}_T) is uniquely corresponding to one original configuration, $\phi(t=0) = \zeta \in \mathbb{R}^n$ thus defines a one-to-one mapping $\tilde{\phi}(\zeta) = \phi(T)$. Starting from the initial point $\phi(0) \equiv \zeta$, as the flow time increases, $\tilde{\phi}(\zeta) \rightarrow \phi(T)$, the set of fields eventually approaches the right combination of thimbles which equals the original integral.

3.4.1. NN-based Manifold

To approach the proper thimbles for mitigating the sign problem in larger systems, large-enough flow time is necessary which would induce large computational consumption, especially for evaluating the required Jacobian. In Ref. [506], to avoid directly solving the gradient flow equation and Jacobian evaluation, the authors first proposed to train a feed-forward neural network to approximate the thimble (or the generalized manifold), accordingly the network can be termed as “*learnifold*” in approaching the flowed manifold by predicting its corresponding imaginary part based upon a real configuration input ϕ_R ,

$$\tilde{\phi}(\phi_R) = \phi_R + i\tilde{f}_\theta(\phi_R), \quad (3.25)$$

where the function $\tilde{f}_\theta(\cdot)$ is represented by a neural network. Compared with the standard generalized thimble method, the *learnifold* has inputs of the real part manifold and thus results in large Jacobian in practice, also the gaps between integral contributing regions (thimbles) are smaller which renders easy exploration of all relevant regions of integration. It can practically help to solve the problem of the time-consuming flow evolution and multi-modal search in Monte Carlo sampling. Translational symmetries can also be inserted for the *learnifold* network. The authors validated the method in a 1+1 dimensional Thirring model with Wilson fermions on sizable lattices.

This method has been further applied into the Hubbard model by Rodekamp et al. [507]. However, the standard (real-valued) neural networks still suffer from the computational effort, mainly because of severe volume scaling of the Jacobian determinant. Recently, the authors have developed complex-valued neural networks to instead learn the mapping from the integration manifold to the target manifold directly [508, 509], $\tilde{\phi}(\phi) = \tilde{f}_\theta(\phi)$. Meanwhile, given the affine coupling layers, the Jacobian can be evaluated high efficiently in this novel architecture, i.e., reducing the scaling of the Jacobian determinant from a general cubic scaling down to a linear scaling in the volume. This method has been demonstrated in systems of different sizes.

3.4.2. Normalizing Flow for Complex Actions

Recall the flow-based model introduced in Sec. 3.2.4, one will immediately find that it has similarities with the contour deformation. The main idea of a normalizing flow is to construct an isomorphic deformation on smooth manifolds. Although it cannot tackle the complex action naturally, it can be conceivably generalized, defining an integration contour along which the sign problem may be mitigated. In works of Lawrence and Yamauchi. [510, 511], they discussed the conditions for the existence of a manifold that can exactly solve the sign problem, which sets the requirement for building complex normalizing flows. The authors demonstrated the effectiveness numerically across a range of couplings for the Schwinger–Keldysh sign problem associated with a real scalar field in 1+1 dimensions. Manifolds that approximately solve the sign problem should be available in many physical systems, as the authors suggested in Ref. [512]. In addition, in a recent work [513], Pawłowski and Urban have proposed to compute the density with the normalizing flow directly, which is the core of the *density-of-states* approach for touching sign problems. They validated the method in a two-component scalar field theory, in which an imaginary external field breaks $O(2)$ symmetry explicitly.²⁰

3.4.3. Path Optimization Method

In Ref. [515, 516], Mori et al. first proposed the path optimization method. This new approach addresses the sign problem as an optimization problem of the integration path. They utilized a cost function to specify the path in the complex plane and adjust it to minimize a cost function that represents the degree of weight cancellation,

$$F[\phi(t)] = \frac{1}{2} \int dt |e^{i\theta(t)} - e^{i\theta_0}|^2 |J(\phi(t))e^{-S[\phi(t)]}|, \quad (3.26)$$

where $\theta(t)$ is the complex phase of the parameterized integrand $J(\phi(t))e^{-S[\phi(t)]}$, and θ_0 is the complex phase of the original integrand. The original partition function becomes $Z = \int_C \mathcal{D}t J[\phi(t)] \exp\{-S[\phi(t)]\}$. This method eliminates the need for solving the gradient flow found in the Lefschetz-thimble method. Instead, the construction of the integration-path contour becomes an optimization problem that can be solved using various efficient methods, e.g., gradient-based algorithms. This method has been successfully extended to e.g., 2D complex $\lambda\phi^4$ theory [516], the Polyakov-loop extended Nambu–Jona-Lasinio model [517, 518], the 0 + 1 dimensional Bose gas [519], the 0 + 1 dimensional QCD [520], as well as $SU(N)$ lattice gauge theory [521].

Simultaneously, in Ref. [522, 523], Alexandru et al. also investigated the path optimization method by parameterizing the manifold with neural networks \mathcal{M}_θ . They showed the results first for the 1+1 dimensional Thirring model with

²⁰Note in condensed matter physics, there are earlier trials using automatic differentiation to optimize a sufficiently general Hubbard–Stranovich transformation on fermionic system to mitigate the sign problem [514], which is in line with flow-based strategies in terms of field transformation optimization.

Wilson fermions on lattice sizes up to 40×10 . Then they demonstrated the performance in the 2+1 dimensional Thirring model [523]. The recent progress of the path optimization method can be found in the review [349].

Namekawa et al. further investigated the efficiency of gauge-invariant inputs [524] and gauge-covariant neural networks approximating integral path [525] for the path optimization method. The motivation is the path optimization method with a completely gauge-fixed link-variable input can tame the sign problem in a simple gauge theory, but does not work well when the gauge degrees of freedom remain. To overcome this problem, the authors proposed to employ a gauge-invariant input, such as a plaquette, or a gauge-covariant neural network, which is composed of the Stout-like smearing for representing the modified integral path. The efficiency is evaluated in the two-dimensional U(1) gauge theory with a complex coupling. The average phase factor is significantly enhanced by the path optimization with the plaquette or gauge-covariant neural network, indicating good control of the sign problem. Furthermore, another improvement of dropping the Jacobian during the learning process, which reduces the numerical cost of the Jacobian calculation from $O(N^3)$ to $O(1)$, where N means the number of degrees of freedom of the theory. Although a slight increase of the statistical error will emerge with the approximation, this practical strategy with invariant/covariant designs will push the path optimization towards solving complicated gauge theories.

3.5. Summary

This chapter introduces first some computational challenges in lattice field theory, the non-perturbative approach in tackling QCD calculation in understanding extreme nuclear matter properties. Then from three different sectors: field configuration generation, lattice data and physics analysis, and sign problem, we summarize some relevant explorations and present the status of using machine-/deep-learning techniques to facilitate the lattice field study. Many recent advanced developments are also discussed, including the symmetry embedding into learning algorithm, physics priors incorporation via automatic differentiation to solve inverse problems involved in real-time physics extraction, flow-based field configuration generation and series of novel trials in applying deep neural networks for mitigating the sign problems in lattice simulation.

4. Dense Matter Equation of State

In terrestrial laboratories, heavy-ion collisions compress nuclear matter to such high densities but inevitably involve high temperatures [4, 526]. In numerical calculations which serve as virtual laboratories, non-perturbative lattice QCD calculations can explore the finite-temperature region of the QCD phase diagram, yet leaves a long-standing challenge in finite-density part due to the inevitable sign-problem (see introductions in Sec. 3.4). Nevertheless, studies dedicated to probe the cold dense nuclear matter properties have benefited from astronomical observations in past decades [527]. Neutron stars (NSs) serve as cosmic laboratories for the study of neutron-rich nuclear matter, with densities far greater than the nuclear saturation density ($\rho_0 \sim 0.16 \text{ fm}^{-3}$). NS structures (e.g., mass and radius) are connected with their bulk properties [e.g., equation of state (EoS)]. Therefore, to understand QCD matter in such an ultra-high density, low temperature and large proton-neutron imbalance environment, one can infer the physical properties from NS observables, as an inverse problem (see, e.g., Refs. [528–532] for recent reviews).

The EoS, a relationship of pressure (p) and energy density (ε), can be employed to deduce many-body interactions in nuclear matter or the presence of de-confined quarks at high densities [533, 534]. For densities within the range of $n \simeq 1\text{--}2 n_0$, one can utilize a combination of *ab initio* techniques and the nuclear force derived from Chiral Effective Theory(χ EFT) [535]. In the extremely high density region of $n \geq 50 n_0$, perturbative QCD calculations provide a reliable understanding [536]. Accordingly, the neutron stars, with densities of up to a few times of the nuclear saturation density, covers the intermediate region($n \simeq 2\text{--}10 n_0$). Now, rapidly cumulating neutron star observations have opened a new window for extracting the EoS. The conventional measurements like the Shapiro delay provide observations of *massive pulsars*($M > 2M_\odot$), extending the mass upper limit of the neutron star realized before [528]. Quiescent low-mass X-ray binary systems(qLMXBs) and thermonuclear burst sources can determine the radius [537, 538]. The latest Neutron Star Interior Composition Explorer (NICER; see [539, 540]) collaboration provides more accurate X-ray spectral-timing measurements of pulsars' *masses*(M) and *radii*(R) [541]. In addition, there are also *compactness* (M/R), *moment of inertia*(I), *quadrupole moment*(Q) and *tidal deformability*(λ) can be measured. The last three observables can also be connected in I -Love- Q formula without knowledge of the inner matter [542]. Observations of long-lived and colliding NSs are growing since the advent of gravitational waves (GWs) and multi-messenger astrophysics [541]. The GW measurements from LIGO/VIRGO/KAGRA collaborations reveal an increasing number of events [543, 544], e.g., GW170817 [545, 546], GW190425 [547], and GW200105/GW200115 [548]. The former two have been analyzed sufficiently, which sets a tidal deformability boundary for undetermined EoSs [541, 549]. One can expect that more well-analyzed events will constrain EoSs to a more narrow area with statistical approaches and machine learning techniques. Meanwhile, the astrophysics observations themselves are beneficial from the rapid development of machine learning, but it is not our main topic in this review (one can read related references in Ref. [550]).

4.1. Reconstructions from Neutron Star Mass-Radius

As mentioned before, the mass-radius(M - R) curve of NSs is strongly dependent on the EoS of its internal dense matter. Its underlying physical law comes from the Einstein equation [529, 551], which relates the geometric structure of space-time with the distribution of matter within it. In a spherically symmetric body of isotropic matter, the Tolman–Oppenheimer–Volkov (TOV) equation [552, 553] gives a hydro-static description of the balance between pressure (p) and gravity (mass

m) included in a neutron star with radius (r) from the center

$$\begin{aligned}\frac{dp}{dr} &= -G \frac{m(r)\varepsilon(r)}{r^2} \left(1 + \frac{p(r)}{\varepsilon(r)}\right) \left(1 + \frac{4\pi r^3 p(r)}{m(r)}\right) \left(1 - \frac{2Gm(r)}{r}\right)^{-1}, \\ \frac{dm}{dr} &= 4\pi r^2 \varepsilon,\end{aligned}\quad (4.1)$$

where ε is the energy density. The observed mass and radius are set at the surface of neutron stars, as M and R where the pressure $p(r = R) \simeq 0$. The similar equals mean the boundary of a neutron star will depend on how to define the vacuum pressure. To solve the TOV equations, one needs EoS in each shell of NSs. In principle, EoS depends on two independent variables, i.e., temperature and baryon chemical potential. However, compared with its Fermi temperature ($> 10^{12}$ K), the dense matter in the NSs is actually cold enough ($10^8 - 10^{10}$ K) to be treated as in zero-temperature environments [541]. Then, there is only one independent thermodynamic degree of freedom, and one may represent the EoS as the relation, $\varepsilon = \varepsilon(p)$, between total energy density ε and pressure p .

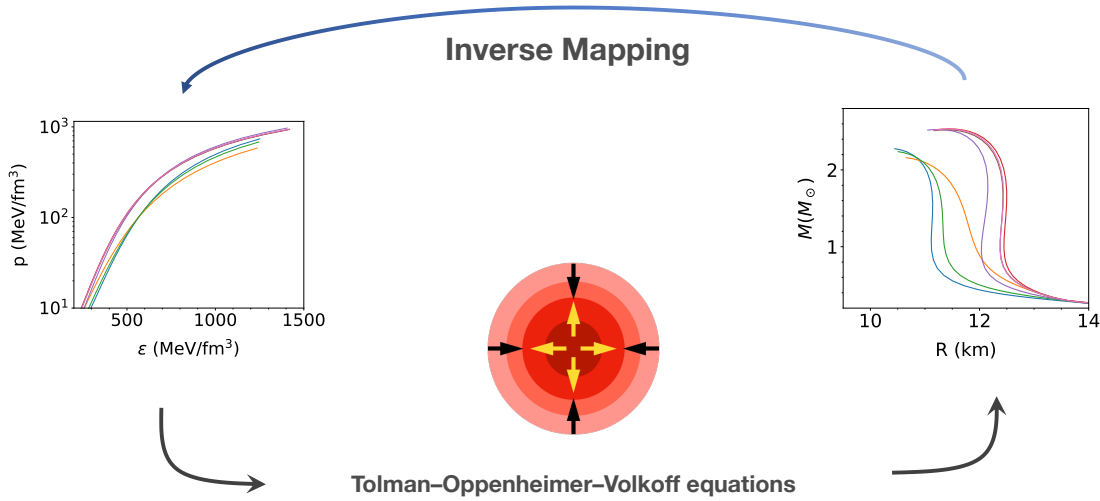


Figure 4.1: A flow chart of TOV and its inverse mapping. The red circle represents a compact star, whereas the black arrows represent the gravity and the yellow arrows indicate the pressure inside it.

4.1.1. Statistical Inference

Before inferring the equation of state, it is important to specify the parameterization schemes and the necessary physical constraints. For a realistic EoS which can reflect properties of the dense matter, it should satisfy [531, 554, 555],

- 1) the microscopically stable condition, i.e., $(dp/d\varepsilon) \geq 0$,
- 2) the causality condition, i.e., the speed of sound c_s obeys,

$$\frac{dp}{d\varepsilon} = \frac{c_s^2}{c^2} < 1, \quad (4.2)$$

where c is the speed of light in vacuum.

- 3) the experimental constraints, e.g., the massive star observations forcing the EoS to produce a neutron star with mass at least $M \sim 2M_\odot$, nuclear physics experiments suggesting the low-density part of the EoS.

The first two constraints should serve as a “hard” condition for reconstructed EoSs, while the fact such as the massive mass neutron stars(NSSs) would be introduced as priors of the Bayesian Inference. In fact, observations of $M > 2M_{\odot}$ NSSs, such as measurement of PSR J1614-2230 [556] effectively has ruled out too “soft” equation of states. A “soft” EoS, for which the pressure increases slowly as the energy density increases, leads to smaller maximum masses. In contrast, the pressure-energy density curve of the “stiff” EoS has a larger slope, making for a larger maximum mass of NSSs. Although the cores of the massive mass NSSs could be composed of quark-gluon matter, most non-baryonic EOS models(e.g., hyperons, kaons, pure quark stars, etc. [529]) have been ruled out.

Proper parametrization of EoSs means introducing as small as possible bias that is irrelevant to the physical priors ²¹. The common schemes, such as the spectral representation [558, 559] and the piece-wise polytropic expansion [560–564], have been proved to be useful in inferring EoS. In Ref [565], Raithel et al. manifest the feasibility of inferring pressures at five density segments from mock NS masses and radii. Although the authors demonstrate the five-polytropic model can infer possible phase transitions within 30% error, it is still limited by the coarse representation. Thus, non-parametric methods, e.g, the Gaussian process(GP) [566] and neural networks [555, 567, 568] have been proposed to avoid the biased outcome due to misspecification [569]. In addition to parametric forms, the self-consistent introduction of physical prior knowledge can also improve reconstructions. For instance, the meta-modeling EoS intuitively continue the Taylor expansions beyond the saturation density of symmetric nuclear matter [570, 571]. The well-measured nuclear empirical parameters can be used as priors [572]. Besides, parametrizing the speed of sound, c_s^2 , rather than ε itself, is beneficial for detecting phase transitions or crossover in dense matter [573–576]. Inspired by a similar form in spectral approach [558], a useful expression defines an auxiliary variable $\phi = \log(c^2/c_s^2 - 1)$, in which the stability and causality conditions can be naturally satisfied [566].

With the parametric EoS, $\varepsilon_{\theta}(p)$ [or speed of sound $c_{s,\theta}(p)$, auxiliary variable $\phi_{\theta}(p)$], one can infer parameters $\{\theta\}$ from observations following the Bayesian approach described in Sec. 1.2.1. The posterior is $P(\theta | \text{data})$ which describes the probability of obtaining a particular parametric EoS from a data set. Using Eq. (1.1), one can rewrite it as,

$$P(\theta | \text{data}) \propto P(\text{data} | \theta) \frac{P(\theta)}{P(\text{data})}, \quad (4.3)$$

where $P(\theta)$ and $P(\text{data})$ are priors on the parameters and observations, respectively. Given a set of EoS parameters $\{\theta\}$, one can derive the likelihood from data sets of observables O as,

$$P(\text{data} | \theta) = \prod_{i=1}^N P(O_i | \theta), \quad (4.4)$$

where N counts the number of observations and the observable O can be total mass-radius observations (M, R) or the observations from multi-messenger measurements. To combine uncorrelated observables from different sources, one can multiply the corresponding likelihood at the right-hand side of Eq. (4.4). Eventually the likelihood can be estimated through χ^2 fitting [577]

$$\chi^2(O | \theta) = \sum_{i=1}^N \frac{(O_i - \tilde{O}_i(\theta))^2}{\sigma_i^2}, \quad (4.5)$$

where σ_i is the measurement uncertainty associated with the observable O_i , and the prediction \tilde{O}_i is from calculations based on the corresponding $\varepsilon_{\theta}(p)$. Serving as an efficient alternative of maximizing likelihood, minimizing χ^2 can provide

²¹There is a fascinating work to explore correlations among different physics model-motivated EoSs by means of dimensionality reduction algorithms [557].

an approximation to the posterior $P(\text{data}|\theta)$ [578]. The MCMC algorithm introduced in Sec. 1.2.1 is widely applied for optimizing parameters $\{\theta\}$.

In the early works, although observations were limited, the Bayesian Inference of parametric EoSs anchored our basic understanding of dense nuclear matter. In Ref. [562], Steiner et al. estimated eight parameters of EoSs in four energy density regimes from six NS masses and radii. The determined EoS and symmetry energy around the saturation density are “soft”, leading to $R_{1.4M_\odot} = 11 - 12$ km. The predicted EoS is “stiff” at higher densities, leading to a maximum mass of about $1.9 - 2.2M_\odot$, consistent with the massive pulsar observation announced later [556]. In the following work [563], the authors extended the data set to 8 NSs, and attempted to combine more constraints from both HICs and quantum MC calculations at relatively low densities. In Figure 4.2, Ozel and Freire summarized NS observations can be used in Bayesian techniques at that time [528].

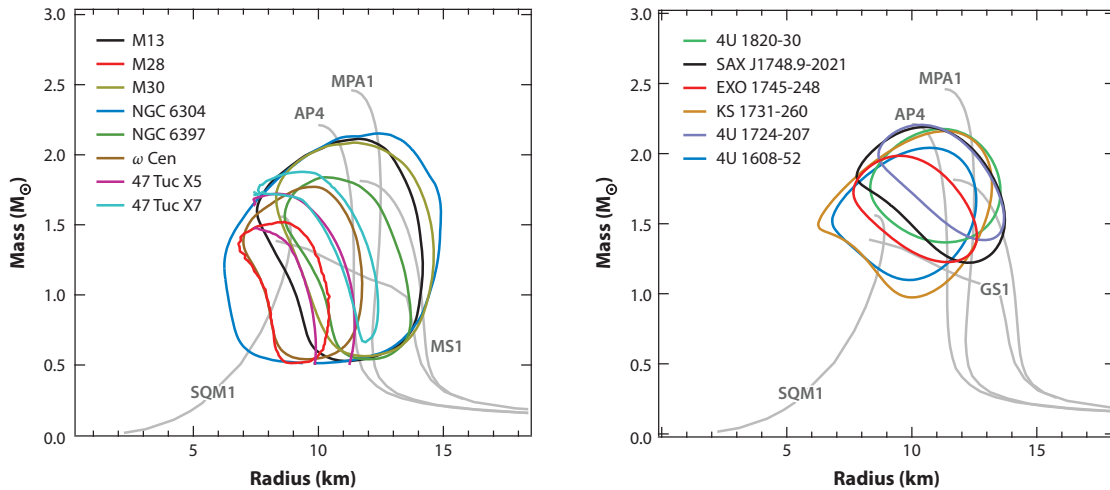


Figure 4.2: The neutron-star mass and radius constraints (68% Confidence Level), (left panel) low-mass X-ray binary neutron stars in a quiescent state, and (right panel) neutron stars exhibiting thermonuclear bursts. The mass relations corresponding to various EoSs are depicted using light gray lines. Figures are taken from Ref. [528].

Since 2017, GW observations have been playing a profound role in the study of dense matter EoSs [543–548, 579]. In Bayesian Inference, the measurements can be conveniently considered after marginalizing with multiple-source observations. They will be discussed in the next section. Moreover, the massive mass NSs (PSR J1614-2230 [580], PSR J0348+0432 [581], and PSR J0740+6620 [582]) set a baseline in inference when marginalizing over the mass measurement by taking into account the measurement uncertainty. The measurements of the NS moment of inertia, e.g., PSR J0737-3039 [583, 584] can also serve as a constraint in inference. Because mass and radius are jointly determined by the inner matter EoSs of NSs, more accurate M - R measurements can provide more precise constraints in inference. The NASA X-ray timing mission (NICER) which is currently in operation, has produced R and M measurements of a few of the radio millisecond pulsars that produce thermal radiation (J0030+0451 [585, 586], J0740+6620 [587, 588]).

Besides these observations, for improving the inference, another recent development is the application of machine learning in representing EoSs. For instance, Gaussian process is a non-parametric method [566, 589] can be used to represent the auxiliary variable ϕ at each pressure p as a multivariate normal distribution, $\phi \sim \mathcal{N}(\mu(p_i), K(p_i, p_j))$, where K is a kernel function for approximating the covariance. In priors composed of seven well-established EoS models, the GP process is implemented to estimate the posterior $P(\text{EoS}|\text{data})$ using the Markov Chain Monte Carlo (MCMC) algorithm. The alternative method introduced in Ref. [555] is a shallow neural network representation of EoS that can also handle

uncertainties from observations with MCMC while preserving flexibility. To alleviate the difficulty of sampling in a high dimensional space of parameters, the authors develop a variational auto-encoder(VAE) assisted framework for reducing the number of parameters in representing EoS [569].

4.1.2. Deep Learning Inverse Mapping

As shown in Fig. 4.1, the mapping from the M - R curve to the EoS relationship in the TOV equations is a one-to-one correspondence [590], which sets up a well-defined inverse problem when the observations are sufficient, i.e., constructing the EoS from a continuous M - R curve. The task becomes natural to build deep neural networks for constructing the complicated mapping from observed data to indeterminate physical variables [24, 591].

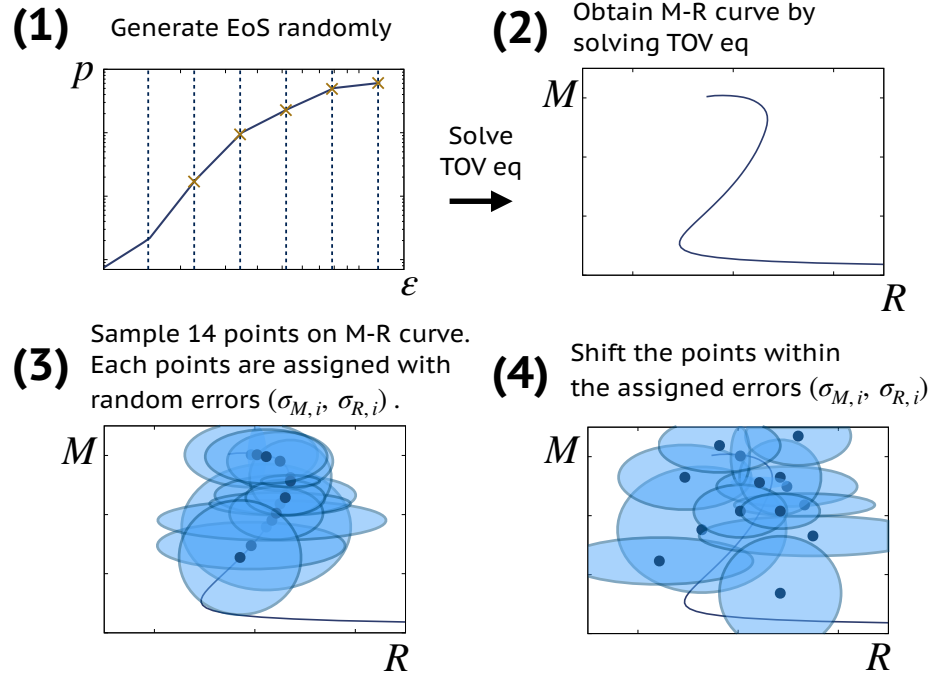


Figure 4.3: Schematic flowchart of data generation procedure for deep learning the inverse mapping, in which the step(3) introduces the data augmentation. Figures from Ref. [592] with permission.

Fujimoto et al. [593, 594] develop a supervised learning method to constrain the nuclear matter EoS, where a piecewise polytropic expansion is used to represent the EoS. The authors take the squared sound speed c_s^2 at the corresponding pressure as the output of the network, and the mass, radius, and their variances as the input, $(M_i, R_i; \sigma_{M,i}, \sigma_{R,i})$. Thus, one can use the NS observations to obtain the parameters of the nuclear matter EoS via the trained network. After a mock observation validation in the preliminary proof-of-concept study [593], the authors then use the mapping to construct the EoS from M - R distributions of 14 observed neutron stars [594]. In a more comprehensive work [592], the authors introduce data augmentation to improve the performance and compared the deep learning approach with polynomial regression, proving the robustness of their DNN method. The generation procedures of training data are shown in Figure 4.3, the new data augmentation strategy was introduced by assigning random uncertainty parameters($\sigma_{M,i}, \sigma_{R,i}$) for sampled 14 points from solved M - R curve. To build the uncertainty for the reconstruction, they further proposed the validation method and the ensemble method, but it is still a statistical estimation to the real uncertainties.

In Ref. [595], Morawski and Bejger further use a 4 hidden layer deep neural network to reconstruct EoSs from masses,

radii, and tidal deformabilities. This model can also construct EoS and produce a M - R curve that closely matches the observations within a range of approximately 1–7 times the nuclear saturation density. They demonstrate the effectiveness of this method by applying it to mock data generated from a randomly selected polytropic EoS, achieving reasonable accuracy with only 11 mock M - R pairs, similar to the current number of actual observations. They also validate the approach on mock data containing realistic EoSs. Different from Ref. [594], the authors also study how the NS radii can be determined using only the GW observations of tidal deformability. In their recent work [596], the problem of recognizing phase transitions is transformed into an anomaly detection task. The algorithm of normalizing flow, trained on samples of observations without phase transition signatures, interprets a phase transition sample as an anomaly. Although the results are inconclusive due to limited observations and large errors, it offers an alternative way to detect phase transitions may happen in dense matter.

In Ref. [597], Traversi and Char compare two methods for estimating the quark matter EoS: Bayesian Inference and Deep Learning. These methods are applied to study the constant speed of sound EoS and the structure of quark stars within the two-family scenario. The observations include mass and radius estimates from various X-ray sources, and mass and tidal deformability measurements from gravitational wave events. The results from both methods are consistent, and the predicted speed of sound is in agreement with the conformal limit.

All the works discussed in this subsubsection fall under the category of supervised learning, where the goal is to learn the inverse mapping from a large ensemble of training data. Well-trained deep neural networks can successfully approximate this mapping when the generated dataset is diverse and of sufficient size. This approach provides a new perspective for constructing EoS from mass-radius pairs, and can be extended to other observations as well. Meanwhile, it unavoidably requires preparing training data and faces difficulties in obtaining uncertainty from finite noisy observations. In the next section, a physics-driven approach will be introduced to address these challenges.

4.1.3. Gradient-Based Inference

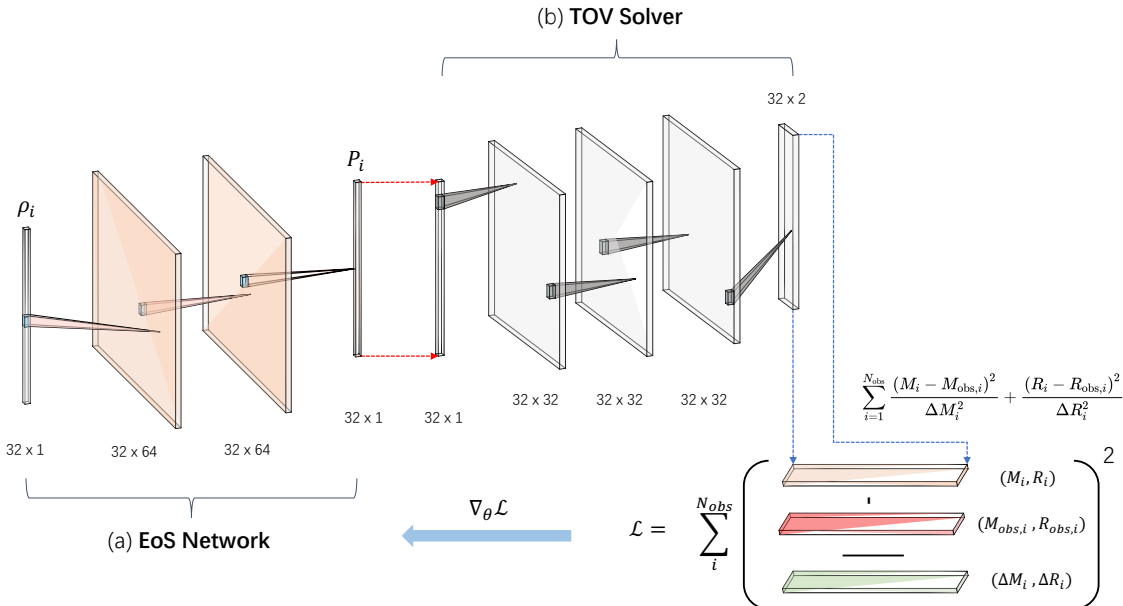


Figure 4.4: A flow chart of AD methods, with (a) the EoS represented by neural networks named as **EoS Network**. Note that in (b) the **TOV-Solver** is a well-trained and static network.

In recent works [567, 568], Shriya et al. propose an automatic differentiation (AD) framework to reconstruct the EoS from finite observations. A sketch of the framework is shown in Fig. 4.4. It consists of two differentiable modules: (a) the **EoS Network**, $p_\theta(\rho)$, an unbiased and flexible DNN parametrization of pressure as function of baryon number density; and (b) the **TOV Solver**, a DNN for translating any given EoS into its corresponding M - R curve. The latter is an emulator for solving TOV equations. With a well-trained **TOV-Solver** network, the **EoS Network** can be optimized in an unsupervised manner. Given N_{obs} number of NS observations, we train the **EoS Network** to fit the pairwise (M, R) predictions from the pipeline (**EoS Network** + **TOV-Solver**) to the observations.

A gradient-based algorithm within the AD framework is deployed to minimize the loss function, $\mathcal{L} \equiv \chi^2$, which is expressed as

$$\chi^2 = \sum_{i=1}^{N_{\text{obs}}} \frac{(M_i - M_{\text{obs},i})^2}{\Delta M_i^2} + \frac{(R_i - R_{\text{obs},i})^2}{\Delta R_i^2}. \quad (4.6)$$

Here (M_i, R_i) represents the output of the **TOV-Solver**, and $(M_{\text{obs},i}, R_{\text{obs},i})$ are observations which have an uncertainty $(\Delta M_i, \Delta R_i)$. With a static well-trained **TOV-Solver** network, the gradients of the loss with respect to parameters of the **EoS Network** are

$$\frac{\partial \chi^2}{\partial \theta} = \sum_{i=1}^{N_{\text{obs}}} \int \left[\frac{\partial \chi^2}{\partial M_i} \frac{\delta M_i}{\delta p_\theta(\rho)} + \frac{\partial \chi^2}{\partial R_i} \frac{\delta R_i}{\delta p_\theta(\rho)} \right] \frac{\partial p_\theta(\rho)}{\partial \theta} d\rho, \quad (4.7)$$

where the **TOV-Solver** is a functional mapping $f : p_\theta(\rho) \rightarrow (M_i, R_i)$. The partial/functional derivatives $\partial p_\theta / \partial \theta$, $\delta M_i / \delta p_\theta(\rho)$, and $\delta R_i / \delta p_\theta(\rho)$ can be directly computed with a back-propagation algorithm [44] within the AD framework. Optimizing the parameters of the **EoS Network** can obtain the best fit to the finite and noisy observational M - R data from the well-prepared **TOV-Solver** [567].

Uncertainty estimation. To evaluate the reconstruction uncertainty, one can adopt a Bayesian perspective and focus on the posterior distribution of EoSs given the astrophysical observations, $\text{Posterior}(\boldsymbol{\theta}_{\text{EoS}} | \text{data})$. In the computations, the authors first draw an ensemble of M - R samples from the fitted Gaussian distribution for real observations (see details in Ref. [568]). From this ensemble, one can infer the corresponding EoS deterministically with maximum likelihood estimation. Given the ensemble of reconstructed EoSs, one can then apply the importance sampling technique to estimate the uncertainty associated with the desired posterior distribution, where an appropriate weight is assigned to each EoS. In general, a physical variable \hat{O} can be estimated as

$$\bar{O} = \langle \hat{O} \rangle = \sum_j^N w^{(j)} O^{(j)}, \quad (4.8)$$

with the standard deviation can also be estimated as $(\Delta O)^2 = \langle \hat{O}^2 \rangle - \bar{O}^2$. The weights are

$$w^{(j)} = \frac{\text{Posterior}(\boldsymbol{\theta}_{\text{EoS}}^{(j)} | \text{data})}{\text{Proposal}(\boldsymbol{\theta}_{\text{EoS}}^{(j)})} \propto \frac{P(\text{data} | \boldsymbol{\theta}_{\text{EoS}}^{(j)}) \text{Prior}(\boldsymbol{\theta}_{\text{EoS}}^{(j)})}{P(\boldsymbol{\theta}_{\text{EoS}}^{(j)} | \text{samples}^{(j)}) P(\text{samples}^{(j)} | \text{data}) \text{Prior}(\text{data})}, \quad (4.9)$$

where j indicates index of samples and i indicates index of M - R observables. $P(\boldsymbol{\theta}_{\text{EoS}}^{(j)} | \text{samples}^{(j)}) = 1$, because it is deterministic. $P(\text{data} | \boldsymbol{\theta}_{\text{EoS}}^{(j)}) \propto \exp(-\chi^2(\boldsymbol{\theta}_{\text{EoS}}^{(j)}, \text{samples}^{(j)})/2)$ and $P(\text{samples} | \text{data}) = \mathcal{N}(M_{\text{obs}}, \Delta M^2) \mathcal{N}(R_{\text{obs}}, \Delta R^2)$ calculated from the corresponding Gaussian distribution. In practical, weights should be normalized so that $1 = \sum_j w^{(j)}$ and cut off to avoid outliers in samples, which will also remove the prior terms.

Reconstructions. In Fig. 4.5, reconstructed EoSs from different works are plotted for comparison. The χ EFT calculation combined with polytropic extrapolation and the two-solar-mass pulsar constraint is labeled as “ χ EFT+Astro”, showing as a gray band. It is expected that any reasonable predictions should fall within this gray band, since this first-principle calculation sets a theoretical baseline. Additionally, the Bayesian analyses (noted as “ARAA,54,401” of Ozel

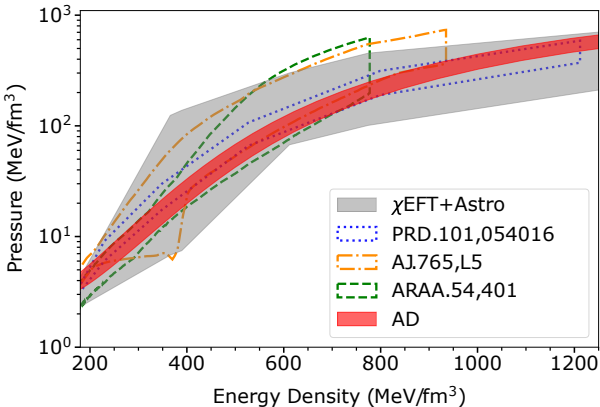


Figure 4.5: The EoS reconstructed from observational data. The gray band locates the χ EFT prediction. The red shaded area represents the automatic differentiaion results (AD [568]). Other results are derived from Bayesian methods (AJ.765,L5 [563] and ARAA.54,401 [528]) and the direct inverse mapping (PRD.101,054016 [594]) are also included.

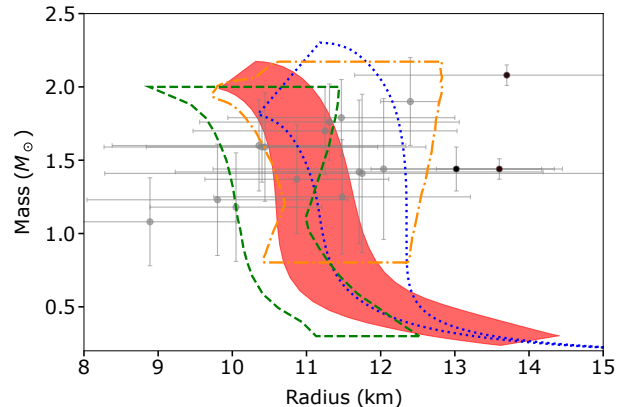


Figure 4.6: M - R contour corresponding to the reconstructed EoSs in the left panel. The dots with uncertainties are fitting observations summarized in Ref. [568], in which black dots are from NICER observations.

et al. [528] and ‘‘AJ.765,L5’’ of Steiner et al. [563]) and the supervised learning result (labelled as ‘‘PRD.101,054016’’ of Fujimoto et al. [594]) are also shown in the figure. It is worth noting that [528] and [594] use the same data set including eight neutron stars in quiescent low-mass X-ray binaries (qLMXB) and six thermonuclear bursters, while [563] uses a subset of the data, i.e., eight of X-ray sources. The AD results (labelled as ‘‘AD’’ of Shriya et al. [568]) are presented as red band, which includes additional four observations: 4U 1702-429 [598], PSR J0437-4715 [599], J0030+0451 [585, 586] and J0740+6620 [587, 588], the three pulsars are from the latest NICER analysis. Figure 4.6 shows the corresponding M - R curves derived from the EoSs in Fig. 4.5. The newest reconstructions certainly consistent with massive neutron stars, i.e., $M \geq 2M_\odot$.

4.2. Constraints from Multimessenger Observations

Multimessenger measurements have provided new insights into ultrahigh-density matter, including gravitational waves (GWs) and electromagnetic (EM) signals. This new era began with the discovery of a binary neutron star merger by the Advanced LIGO and Virgo gravitational wave detectors in 2017 [545]. Because the properties of neutron stars are sensitive to the microscopic interactions that govern the EoS, gravitational waves from the mergers of neutron stars can carry information about the inner cold dense matter. The EoS of dense matter can further be strongly constrained by gravitational wave observations of neutron stars.

Tidal deformability. The finite size of the stars gives rise to tidal interactions that affect the evolution of the binary system during the late stages of the inspiral of coalescing NSs [551]. The tidal field produced by each binary component induces a quadrupole moment on the companion star, resulting in enhanced emission of gravitational radiation and a slight increase in their relative acceleration, accelerating the inspiral phase. The magnitude of the induced quadrupole moment is related to the internal structure of the NS. Larger stars are less compact and thus more easily deformable under the influence of an external field of a given amplitude. The tidal deformability λ is a parameter for the quantification of the effects [600, 601]. Dimensionless tidal deformability Λ is defined as the ratio of the induced quadrupole moment to

the external perturbing tidal field, $\Lambda = \lambda/M^5 = 2k_2/(3\beta^5)$, where k_2 is tidal Love number which is determined as

$$k_2(\beta, y_R) = \frac{8}{5}\beta^5(1-2\beta)^2[2-y_R+2\beta(y_R-1)] \times \{2\beta[6-3y_R+3\beta(5y_R-8)] \\ + 4\beta^3[13-11y_R+\beta(3y_R-2)+2\beta^2(1+y_R)]+3(1-2\beta)^2[2-y_R+2\beta(y_R-1)]\ln(1-2\beta)\}^{-1}, \quad (4.10)$$

where $\beta \equiv M/R$ is dimensionless compactness parameter. $y_R \equiv y(R)$ is the boundary value of $y(r)$, which follows the differential equation

$$\frac{dy(r)}{dr} = -\frac{y(r)^2}{r} - \frac{y(r)}{r}F(r) - rQ(r), \quad (4.11)$$

with

$$F(r) = \left\{1 - 4\pi r^2[\varepsilon(r) - p(r)]\right\} \left[1 - \frac{2m(r)}{r}\right]^{-1}, \quad (4.12)$$

$$Q(r) = 4\pi \left[5\varepsilon(r) + 9p(r) + \frac{\varepsilon(r) + p(r)}{c_s^2(r)} - \frac{6}{r^2}\right] \left[1 - \frac{2m(r)}{r}\right]^{-1} - \frac{4m^2(r)}{r^4} \left[1 + \frac{4\pi r^3 p(r)}{m(r)}\right]^2 \left[1 - \frac{2m(r)}{r}\right]^{-2}. \quad (4.13)$$

The total tidal effect of two compact stars in an inspiraling binary system is given by the mass-weighted (dimensionless) tidal deformability,

$$\tilde{\Lambda} = \frac{16}{13} \frac{(M_1 + 12M_2)M_1^4\Lambda_1 + (M_2 + 12M_1)M_2^4\Lambda_2}{(M_1 + M_2)^5}, \quad (4.14)$$

where the subscripts for Λ and M indicate different stars. For single neutron stars, one can calculate their Λ , predicting the tidal phase contribution for a given binary system from each EOS, for the universality of the nuclear matter EoS. The weighted (dimensionless) deformability $\tilde{\Lambda}$ is usually plotted as a function of the chirp mass $\mathcal{M} = (M_1 M_2)^{3/5}/(M_1 + M_2)^{1/5}$ for asymmetric mass binary systems. See a more systematic introduction in Ref. [551].

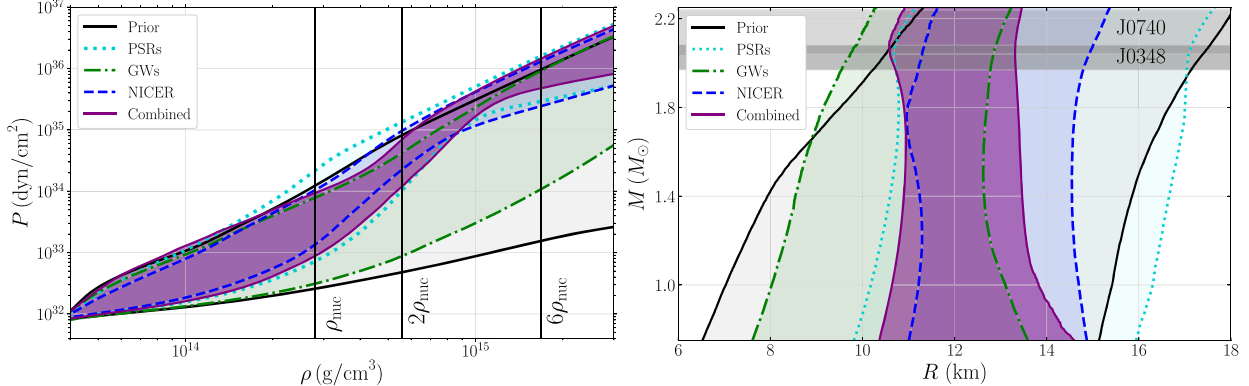


Figure 4.7: In Ref. [602], the authors presented individual-event constraints from various observation classes. The 90% credible intervals for the EoS are displayed in the pressure-density plane (left panel) and the mass-radius plane (right panel). The prior range is indicated by black lines, and the posterior using only heavy pulsar measurements is represented by turquoise lines. The posterior based on only GW data is depicted by green shaded regions, and the posterior using only NICER data is depicted by blue shaded regions. The left panel includes vertical lines marking multiples of the nuclear saturation density, while the right panel includes horizontal shaded regions showing the 68% credible mass estimate for the two heaviest known pulsars. Figures are taken from Ref. [602].

In terms of Bayesian Inference (BI) methods, there are many works using or combining the current GW observations to reconstruct the dense matter EoS [573, 575, 603–605, 605]. As a modern variant of BI methods, the Gaussian Process (GP) has been used to represent the EoS by inferring it from GW observations in the work of Landry et al. [566]. The authors first build a mapping from binary observables $(M_1, M_2, \Lambda_1, \Lambda_2)$ to the GP-represented EoSs and then use MCMC to infer their

corresponding posteriors directly. These synthetic EOSs keep a high flexibility that means covering a large enough interval of stiffnesses and core pressures while satisfying other characteristics introduced in Sec. 4.1.1. The authors validate the inference approach on simulated GW170817-like signals using real detector noise, with reasonable efficiency in recovering a known EOS. Eventually, the authors demonstrate the inferred EOSs and corresponding observables under posterior constraints from the single GW170817 event. In two prior set-ups, the deformability of $\tilde{\Lambda} = 210_{-113}^{+383}(631_{-122}^{+164})$ and $\Lambda_{1.4} = 160_{-113}^{+448}(556_{-172}^{+163})$, maximum mass of $M_{\max} = 2.09_{-0.16}^{+0.37}(2.04_{-0.002}^{+0.22})M_{\odot}$ are consistent with previous analyses [546, 606]. In the following works, Essick et al. [589] extend the analysis, obtaining a more reliable conclusion that is the GW170817 favors a “softer” EoS. Through combining more information from other observations, i.e., maximum masses of NSs, more GW events shown in Table 4.1 and M - R in the newest X-ray observation (J0030+0451). Landry et al. [602] further improve the inference by combining different observations. As a demonstration, individual constraints from different observations can be found in Fig. 4.7. Through combining them, the authors find the radius of the $1.4M_{\odot}$ NS is $R_{1.4} = 12.32_{-1.47}^{+1.09}$ km.

Events	$\mathcal{M}[M_{\odot}]$	$\tilde{\Lambda}$	$\Lambda_{1.4}$
GW170817	$1.186_{-0.001}^{+0.001}$ [545]	300_{-190}^{+500} [607]	190_{-120}^{+390} [546]
GW190425 [547]	$1.44_{-0.02}^{+0.02}$	$\lesssim 600$	—

Table 4.1: Summary of the GW events and their astrophysical observations. It contains the median and uncertainties (90% credible level) of the chirp mass M , and the tidal parameters $\tilde{\Lambda}$ and its corresponding value $\Lambda_{1.4}$ at 1.4 solar mass.

As introduced in Sec. 4.1.2, Morawsk et al. implement deep learning to rebuild EoSs from GW observations [595, 596], in which the learnable inverse mapping consists of mass-radius and tidal deformability as inputs. In Ref [555, 569], the mass-tidal-deformability data of GW170817 event has also contributed to the inference of neural network represented EoSs. In the work of Ferreira et al. [608], the authors prepare training data from a set of metamodeling EoSs. The inverse mapping is learned to predict the parameters of the nuclear matter from the tidal deformability and the radius of the NS. In addition to DNNs, they adopt a classical machine learning method of support vector machine regression (SVM-R). Although the DNNs show a high level of accuracy than the SVM-R in their tests, it provides an alternative way to explore the possible inverse mapping. For classical machine learning algorithms, in Refs. [609, 610], Hernandez et al. develop a random forest regressor algorithm to interpolate the marginalized likelihood for each gravitational-wave observation. It can be utilized in the hierarchical Bayesian Inference for constraining the EoS from GW170817 and GW190425 events directly. They provide a new constraint for the $1.4 M_{\odot}$ neutron star with radius $R = 11.6_{-0.9}^{+1.6}$ km. In addition, the AD framework introduced in Sec. 4.1.3 can conceivably be implemented with the above differentiable formula to combine the observation of tidal deformability with the stellar structures for improving the reconstruction.

Multi-messenger measurements. It is also feasible to explore the nuclear matter EoS from multi-messenger measurements directly with modern deep learning techniques. In Ref. [611], Goncalves et al. examine the Audio Spectrogram Transformer (AST) model for analyzing gravitational-wave data. The AST machine-learning model is a convolution-free classifier that captures long-range global dependencies through a purely attention-based mechanism. In this work, the model is applied to a simulated dataset of inspiral GW signals from binary neutron star coalescences built from five EoSs. It is shown that the model can correctly classify the EOS purely from the gravitational-wave spectra. Additionally, the generalization ability of the machine is investigated in testing data set. Overall, the results suggest that the well-trained attention-based model can infer the cold nuclear matter EOS directly from the GW signals using the simplified setup of noise-free waveforms. In work of Farrell et al. [612], the Transformer model is implemented to deduce EoSs directly

from X-ray spectra of neutron stars. The approach can determine the EoS by analyzing the high-dimensional spectra of observed stars, bypassing the need for intermediate mass-radius calculations. They demonstrate the end-to-end machine slightly but consistently perform better than the two-step method using the intermediate M - R information. The network used in this approach takes into account the sources of uncertainty for each star, enabling a comprehensive propagation of uncertainties to the EOS. These attempts enlighten us that in the future, using deep learning techniques to process more measurements [579](e.g., short gamma-ray burst [613] and subsequent kilonova [614]) will help us to eventually obtain a concrete understanding of the dense matter EoS [615, 616].

4.3. Constraints from Nuclear Physics

4.3.1. Connections with Nuclear Symmetry Energy

One important aspect of the nuclear matter EoS is the symmetry energy, $E_{\text{sym}}(\rho)$, which represents the energy cost of converting neutrons into protons or vice versa. This quantity can affect many properties of nuclei, including the stability of nuclei and nuclear processes [617]. The nucleonic component of the nuclear matter EoS can be expressed in terms of the energy per nucleon ρ as

$$E(\rho, A) = E(\rho, 0) + E_{\text{sym}}(\rho)A^2, \quad (4.15)$$

where $E(\rho, 0) \equiv E_{SNM}(\rho)$ is the energy per nucleon of symmetric nuclear matter(SNM) and $A = (\rho_n - \rho_p)/\rho$ is the isospin asymmetry with $\rho_{n/p}$ being the neutron (proton) density. Thus, as a part of the EoS, the symmetry energy $E_{\text{sym}}(\rho)$ can also be constrained by studying neutron star observations [572, 618]. Around saturation density ρ_0 , $E_{SNM}(\rho)$ can be expanded as $E_0 + K_0x^2/2 + J_0x^3/6$ with $x \equiv (\rho - \rho_0)/(3\rho_0)$. E_0 , K_0 and J_0 are the binding energy, incompressibility, and skewness of symmetric nuclear matter; the symmetry energy can be expanded as $E_{\text{sym}}(\rho) = S_0 + Lx + K_{\text{sym}}x^2/2 + J_{\text{sym}}x^3/6$, where S_0 , L , K_{sym} and J_{sym} are the magnitude, slope, curvature, and skewness of the symmetry energy at ρ_0 . These physical parameters can be determined from NS observables [619]. This information can be further used to improve our understanding of how nuclear matter behaves under extreme conditions and to test nuclear models [620]. In Ref. [621], the authors apply a machine learning approach of support vector machines(SVMs) to predict binding energies of nuclei which are highly related to the outer crust of neutron stars in the density range $\lesssim 10^{-3}\rho_0$. In a series of works from Li et al. [572, 619, 622], they have developed the Bayesian Inference approach to infer, e.g., EoS, phase transitions, symmetry energy and empirical parameters, from observations of neutron stars together with nuclear experiments. See a recent review in Ref. [618].

In Ref. [554], Krastev trains a deep neural network(DNN) to determine the nuclear symmetry energy as a function of density directly from observational neutron star data. The author demonstrates that DNNs can accurately reconstruct the nuclear symmetry energy from a set of available observables of the neutron star, i.e., the masses and the tidal deformabilities. In Ref. [623], Ferreira et al. also use DNNs to analyze the relationship between the cold β -equilibrium matter of NSs and the properties of nuclear matter, which is a non-trivial mapping [624]. Using a Taylor expansion of the energy per particle of homogeneous nuclear matter, they generate a data set of different β -equilibrium neutron star matter scenarios and their corresponding nuclear matter properties. The neural network is trained and achieved high accuracy on the test set. In a real case scenario, they test the neural network on 33 nuclear models and are able to accurately recover the nuclear matter parameters with reasonable standard deviations for both the symmetry energy slope and the nuclear matter incompressibility at saturation. In the work of Thete et al. [625], a DNN is trained to predict EoSs from nuclear

matter saturation parameters, then used as a static module to infer a set of seven nuclear parameters from astrophysical observations.

4.3.2. Constraints from χ EFT, HICs, and pQCD

In addition to using observations from astrophysics, one can improve the performance of the reconstruction by combining more physical priors from other domains of nuclear physics, i.e., relativistic mean-field(RMF) calculations at low-density region [626, 627], heavy-ion collisions (HICs) at mid-density region [4, 526, 628, 629] and perturbative calculations at nuclear matter and quark matter regions respectively [535, 536]. They have been treated as straightforward physics constraints for reducing the dense matter EoS [549, 630, 631].

Chiral effective field theory (χ EFT) is a widely used framework for studying the properties of nuclear matter at moderate densities (see recent reviews [535, 632, 633]). Recent advances in χ EFT have led to a computationally efficient tool for determining the properties of nuclear matter at densities up to $\sim 2 n_0$. In χ EFT, the effective strong interaction *degree of freedoms* are nucleons and pions (and delta isobars), presenting throughout most of the neutron star interior. The effective Lagrangian is formed in an expansion in powers of the momenta of the hadrons and the quark masses, which are the small parameters in the theory. A new framework is introduced for quantifying the correlated uncertainties of the nuclear matter EoS that is derived from χ EFT [634, 635]. This framework uses Gaussian processes with physics-based *multitask* design to efficiently identify theoretical uncertainties from χ EFT truncation errors to derived quantities, e.g., pressure, sound velocity, symmetry energy and its slope. This approach has been applied to the calculations with nucleon-nucleon and three-nucleon interactions up to fourth order in the expansion. At nuclear saturation density, the predicted symmetry energy and its slope are in agreement with various experimental constraints. This work has provided a statistically robust uncertainty estimate in the low density region, which can contribute as a reliable constraint.

The RMF approach uses a relativistic Lagrangian written in terms of baryon and meson fields with simplicity and flexibility [627]. The in-medium coupling constants are chosen to reproduce nuclear physics measurement around $n \simeq n_0$. To determine the EOS based on a relativistic approach with minimal constraints, Malik et al. [636] use the Bayesian approach on a set of models based on the RMF framework with density-dependent coupling parameters and no nonlinear mesonic terms. These models are constrained by the EoS derived from χ EFT and four saturation properties of nuclear matter: density, binding energy per particle, incompressibility, and symmetry energy. The authors have verified that the derived posterior distribution of NS maximum masses, radii, and tidal deformabilities are consistent with recent NS observations. In related works from Li et al. [637, 638], the parametric interactions of RMF models are inferred from astrophysical observations. This is also a promising attempt to understand the nuclear matter from hadron degree of freedom.

Heavy-ion collisions involve the collision of heavy atomic nuclei at high energies, creating a state of matter known as the quark-gluon plasma. This state of matter exists in the cores of neutron stars. The results of heavy-ion collision experiments can be used to study the equation of state of dense matter under these extreme conditions [628, 639]. Bayesian methods have been employed to restrict the density dependence of the QCD EoS for dense nuclear matter using the mean transverse kinetic energy and elliptic flow of protons from HICs [234], in the beam energy range $\sqrt{s_{\text{NN}}} = 2\text{--}10$ GeV. The analysis results in tight constraints on EoS at density $n > 4 n_0$. The extracted EoS is found to be consistent with other observables measured in HIC experiments and constraints from astrophysical observations, which were not used in the analysis.

At extremely high densities, perturbative QCD (pQCD) can vary the order of renormalization scales, which allows one to derive thermodynamical contributions of higher-order corrections [640]. In recent works of Gorda et al. [641, 642], the authors demonstrate that the pQCD calculations provide significant and non-trivial information about the nuclear matter EoS, going beyond what can be obtained from current astrophysical observations. The EoS is extrapolated with a Gaussian process and conditioned with observations and the QCD input. They find that imposing the QCD input does not require extrapolation to a large- n density, while providing strong additional constraints at high densities. In practice, the reliable interpolation between low- and high-density parts can produce an ensemble of EoSs that can be further constrained by astrophysical observations [549].

4.4. Summary

This chapter provides an overview of recent research on nuclear matter EoS inference using statistical learning algorithms (e.g. Bayesian Inference) and advanced deep learning methods (e.g. deep neural networks). The latest measurements, including pulsar masses and radii, are discussed. The neural network EoS and automatic differentiation framework for solving the inverse problem are also introduced. Multimessenger observations and nuclear constraints are discussed as ways to improve reconstruction. As more data is accumulated, such as from GW observations [643, 644], and as prior knowledge (e.g. physical constraints) is incorporated into deep models, the reconstruction performance will be improved continuously.

5. Advanced Developments – Physics Meets ML

In the previous sections, we have reviewed how deep learning can be broadly applied to diverse aspects of high-energy nuclear physics, as a powerful tool for solving specific problems abstracted from physical domains. As we also pointed, rapidly accumulating large amounts of data or, conversely, slowly collecting small amounts of physical observations, they both challenge the ready-to-use deep learning techniques. Indeed, one needs to further improve the efficiency, even the applicability, of deep learning by encoding physics knowledge into the learning process. In the development of deep learning, several attempts have been raised to introduce physics knowledge— *physics-inspired* [67–69], *physics-informed* [90], and *physics-driven* [91] deep learning. In the first approach, physics properties, such as the symmetry or conservation laws, are implemented in the architecture of the network and are strictly enforced. For properties or rules that cannot be encoded in the network setup, one can follow the *physics-informed* approach and include a loss function to punish its violation. Finally, the *physics-driven* approach extends the back-propagation procedure to train network parameters when the output of a network and observables are related by a differentiable function or functional mapping.

The EOS reconstruction from Neutron Star mass and radius observations that was discussed in Sec. 4 is a good example of how these three approaches can be simultaneously implemented in different aspects of a particular problem. One may reconstruct the nuclear matter equation of state, i.e., energy density as a function of pressure $\varepsilon(P)$, from the observation of mass and radius for neutron stars. One may adopt a neural network to represent the inverse of the speed of sound, $c_s^{-2}(P) \equiv d\varepsilon(P)/dP$. Then the causality requirement can be fulfilled by setting the activation function of the output layer to be $\sigma(z) = 1 + e^z$. Such procedure encodes the physics constraint in the setup, and therefore it is a *physics-inspired* procedure. Then prior knowledge from chiral Effective Field Theory(perturbative QCD calculation) can be implemented as a term in the loss function to constrain the low(high)-pressure sector of the equation of state, which fits the definition of *physics-informed* deep learning. Finally, *physics-driven* deep learning would be reflected by the variation analysis of the TOV equation — the functional mapping between $\varepsilon(P)$ and the mass-radius relation — in which the functional derivative of mass and radius with respect to arbitrary change of the equation of state can be computed to guide the optimization of the network parameter in gradient-based training.

In this section, we focus on some works that have been briefly mentioned earlier in the previous sections and expand on their advanced developments of method which implement physics knowledge and/or constraints into the machine learning task.

5.1. Manifesting Physics Properties in NNs

An illustration of physics-inspired deep learning is the integration of physics properties, such as symmetry, into the architecture of a neural network. For further information on this topic, readers can refer to references [32, 80, 81]. Many special neural network architectures have been designed to incorporate specific physics properties. For example, Convolutional Neural Networks (CNNs) are known to be invariant under coordinate translation [32, 82]. The E3NN architecture [85] is designed to preserve rotational invariance, while Group Equivariant Convolutional Networks [83], Point Nets [84] with permutation invariance, and Lorentz group equivariant Neural Networks [645] are other examples.

In the field of nuclear and particle physics, implementing symmetry properties has been applied to reduce the computational complexity of machine learning tasks. This includes point cloud representations for collider event classifications [646], embedding gauge symmetry in normalizing flow for lattice gauge field calculations [87], Feynman path generation using Fourier-flow-based models [398] and the use of CNNs to approximate the inversion of the renormaliza-

tion group transformation in quantum field theory [647]. The last three examples will be discussed in more detail in the remainder of the current subsection.

5.1.1. Gauge Symmetry in Normalizing Flow

As introduced in Section 3.2.4, the flow-based generative machine learning methods offer a promising solution to addressing the critical slowing down(CSD) in lattice simulations. Specifically, in the context of high-energy nuclear physics (HENP) studies of quantum chromodynamics (QCD), lattice gauge field simulations require consideration of special local symmetries. In recent years, learning architectures that encode the relevant symmetries in lattice field theory have been developed ²².

In Ref. [87], a gauge invariant flow model was developed to sample configurations in a $U(1)$ gauge theory. On a lattice, the field configuration can be represented by the gauge variable $U_\mu(x)$, which connects the neighboring sites x and $x + \hat{\mu}$. For a theory with N_d spacetime dimensions (i.e. $\mu = 1, 2, \dots, N_d$), the variable $U(x)$ has G degrees of freedom (e.g. color). The authors defined the lattice volume as V , and the field configurations have dimensions of $G^{N_d V}$. The theory is invariant under a gauge transformation,

$$U_\mu(x) \rightarrow \tilde{U}_\mu(x) = \Omega(x)U_\mu(x)\Omega^\dagger(x + \hat{\mu}), \quad (5.1)$$

where the space-time-dependent $G \times G$ matrices, Ω , act on the intrinsic degrees of freedom. Therefore, the physical distribution shall also be invariant, i.e.,

$$p(U) = p(\tilde{U}). \quad (5.2)$$

In comparison to learning symmetries across a training dataset, the gauge invariant flow model efficiently encodes the invariance of distribution. One may use the normalizing flow method introduced in Sec. 1.2.3, in which the invertible coupling layers (g) are bijective mappings between a $G^{N_d V}$ -dimensional manifold and itself. Equation (5.2) will be fulfilled if two conditions are met: 1) the prior distribution (\mathcal{P}) is symmetrical and 2) each coupling layer commutes with the gauge transformations. While the first criterion can be easily satisfied by setting \mathcal{P} as a uniform distribution, the second requires a specific design for the coupling layer. In [87], each g only acts on some of the gauge links, and one may divide the $G^{N_d V}$ -dimensional manifold into two subsets, U^A and U^B . All elements in the latter are invariant under g : $\forall U \in U^B$, $g(U) = U$; whereas a link in the former ($U^i \in U^A$) is mapped to

$$U'^i \equiv g(U^i) = h(U^i S^i | \boldsymbol{\Pi}_i) (S^i)^\dagger, \quad (5.3)$$

in which S^i is a product of links such that $U^i S^i$ forms a loop ending at the starting point. It belongs to U^B to ensure invertibility, and its explicit form can be determined when a theory is specified. h is a G -to- G dimensional invertible kernel explicitly parametrized by a set of gauge invariant quantities ($\boldsymbol{\Pi}_i$) constructed from the elements of U^B , and satisfies,

$$h(W X W^\dagger) = W h(X) W^\dagger, \quad \forall X, W \in G, \quad (5.4)$$

²²See also the end of Section 3.3.1 where the incorporation of symmetries into neural networks is discussed for a regression task in lattice gauge theory studies.

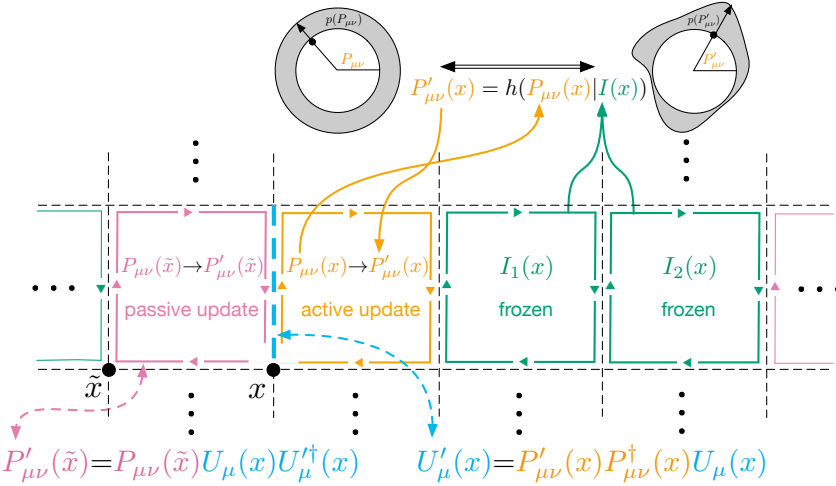


Figure 5.1: Demonstration of gauge invariant normalizing flow. Taken from [87] with permission.

so that g commutes with the gauge transformation:

$$\begin{aligned}
 U'^i &\rightarrow \tilde{U}'^i = h\left(\Omega(x)U^iS^i\Omega^\dagger(x)\right)\left(\Omega(x+\hat{\mu})S^i\Omega^\dagger(x)\right)^\dagger \\
 &= \Omega(x)h(U^iS^i)\Omega^\dagger(x)\Omega(x)(S^i)^\dagger\Omega^\dagger(x+\hat{\mu}) \\
 &= \Omega(x)U'^i\Omega^\dagger(x+\hat{\mu}).
 \end{aligned} \tag{5.5}$$

Taking a U(1) gauge field in $1+1$ dimension as an application example, to which the lattice discretization for this field can be approximated through the Wilson action, defined as:

$$S(U) = -\beta \sum_x \text{Re}P(x), \tag{5.6}$$

where $P(x) = U_0(x)U_1(x+\hat{0})U_0^\dagger(x+\hat{1})U_1^\dagger(x)$ represents the plaquette at x . The choice of S_i is depicted in Fig. 5.1, with U_iS_i representing 1×1 loops adjacent to each U_i . The elements of U^A are sparse enough such that updates do not overlap with one another. With the aforementioned construction of gauge-equivariant coupling layers, a flow-based MCMC scheme was employed on this $1+1$ D U(1) gauge theory at a fixed lattice size ($L = 16$). This resulted in more efficient calculations for topological quantities compared to traditional HMC and Heat Bath algorithms [87].

5.1.2. Inverse Renormalization Group Transformation

In addition to Normalizing Flow method [86–88] which independently samples field configurations in each round, another approach to addressing the CSD using physics-inspired deep learning is the implementation of Convolutional Neural Networks (CNNs) in solving inversion of renormalization group (RG) transformations. This has been independently studied in the context of quantum field theory [647] and spin systems [648].

At the critical point, a thermal system exhibits divergence of the correlation length and therefore there is no length scale remaining in it. As a result, the expectation values of intensive observables are invariant under arbitrary scale transformations. This property is attributed to the theory of RG, which is widely used to study thermodynamics near the critical point. In the typical application of RG, one reduces the size of a system by coarse-graining the configurations of a thermal ensemble, comparing the thermal quantities before and after the operation. The number of RG steps is limited by the original finite size of the system, as the operations always result in a reduction in size. However, one needs to

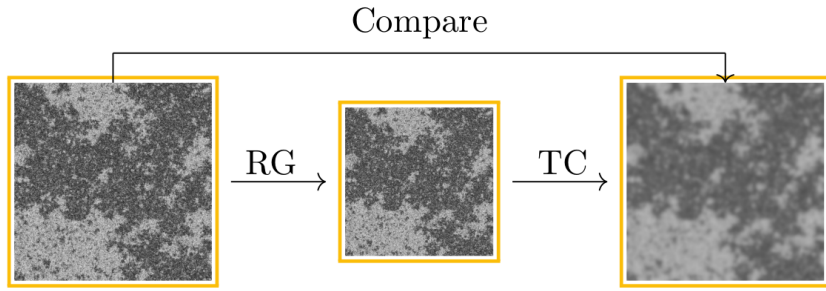


Figure 5.2: Taken from Ref. [647] with permission. Demonstration of the inverse RG training with transposed convolution (TC).

approach the critical behaviors in a large-size limit, which is routinely hindered by computational resources. It has been noted that the coarse-graining operation in real space can be treated as a convolution operation with step 2 and filter size 2×2 . The authors of [647] and [648] supervisedly train a transposed convolution or upsampling layer with filter size 2×2 to approximate the inverse operation of RG²³. Fig. 5.2 gives an illustration of such training using data generated from standard RG procedures. With this tool, it is able to generate large-size configurations from small-size ones with an infinite number of inverse RG steps. One can then accurately determine the location of the critical point and study the critical exponents in its vicinity.

5.1.3. Fourier-flow Model Generating Feynman Paths

Besides embedding symmetries and approximating physical processes with neural networks, it is helpful to deploy the machine learning algorithms in a more efficient physics representation. In Ref. [398], the authors proposed a Fourier flow model(FFM) to simulate the Feynman propagator and generate paths for quantum systems. The Fourier transformation is introduced to approach a Matsubara representation in order to preserve the physics condition for the system. The Euclidean action defined in a discrete time, $S_E[x_n]$, is converted into the Fourier space as, $S_E[X_k]$. The Fourier modes, X_k , represent multi-level correlations in coordinate space. Time-reversal symmetry requires that certain boundary conditions be imposed on the discretized paths x_n . They include invariance under translation ($n \rightarrow n + 1$), inversion ($n \rightarrow -n$), and periodicity ($n \rightarrow n + N$), where n is the index of the site. These conditions are naturally satisfied in Fourier space. The path generator of FFM is validated on the harmonic and anharmonic oscillators as a demonstration. The latter is set as a multimode system in a double-well potential without an analytic solution. The ground-state wave function and low-lying energy levels are accurately estimated.

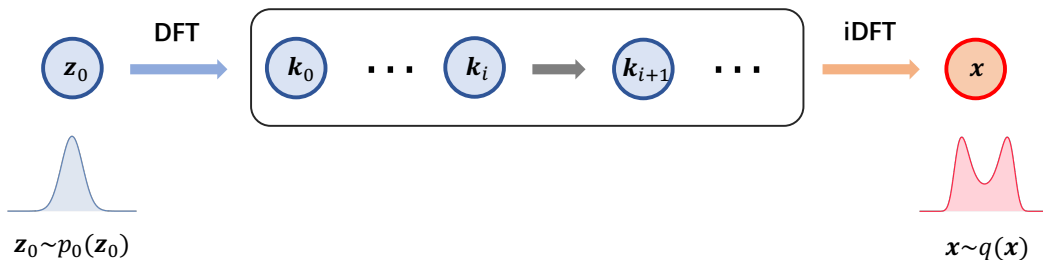


Figure 5.3: Demonstration of the Fourier flow model. The discrete Fourier transformation(DFT) and inverse discrete Fourier transformation(iDFT) are inserted before the input and after the output of a normalizing flow model respectively.

²³See Ref. [649] for details on the involved different convolution arithmetics

It should be noted that the kinetic term of action, $m(\Delta x/\Delta t)^2$ which correlates in coordinate space, will disentangle in frequency space as, $m|X_k|^2$ (see details in Ref. [398]). As a matter of fact, the Feynman path describes the field in 0+1 dimensional field theory. The Fourier transformation converts the dynamical fields to the inverse of the two-point correlation function in frequency space (also known as the inverse power spectral density as discussed in Ref. [399]). It can preserve the dynamical information at least at mean-field level [650]. This method provides a novel way to manifest physics properties, such as time-reversal symmetry and dynamical mean-field theory, in the design of flow-based models.

5.2. Fusing Physics Models into NNs

Another type of physics-inspired machine learning leverages the mathematical similarity between a specific physics model and a neural network architecture, enabling the application of existing deep learning frameworks to solve physics problems with ease. Some pioneer attempts [387, 651–653] have been made in the direction of anti-de Sitter/conformal field theory(AdS-CFT) correspondence. The AdS-CFT correspondence [654–656] is a renowned holographic relation between d -dimensional Quantum Field Theories and $(d+1)$ -dimensional gravity. It has been widely applied in solving problems for strong coupling quantum fields. In the limit of large number of colors (N_c), the generating functional of the CFT boundary and the action of the gravity bulk are related by the Gubser–Klebanov–Polyakov–Witten relation,

$$Z_{\text{QFT}}[J] = \exp(-S_{\text{gravity}}[\phi]), \quad (5.7)$$

where $\phi(x, \eta)$ is the bulk field that satisfies the boundary condition $\phi(x, \eta=0) = J(x)$. It has been argued [652] that AdS/CFT correspondence as a deep Boltzmann machine²⁴. The Boltzmann machines are network models that give a probabilistic distribution of variables v_i that defined as,

$$P(v_i) = \exp\left(-\sum_i a_i v_i - \sum_{i,j} w_{ij} v_i v_j\right), \quad (5.8)$$

with a_i and w_{ij} being network parameters. The deep Boltzmann machines further include hidden variables to enhance the expression ability,

$$P(v_i) = \sum_{h_i^{(k)}} \exp\left(-\sum_{i,j} w_{ij}^{(0)} v_i h_j^{(1)} - \sum_{k=1}^{N-1} \sum_{i,j} w_{i,j}^{(k)} h_i^{(k)} h_j^{(k+1)}\right), \quad (5.9)$$

When comparing with AdS/CFT correspondence, the variables of interest are the quantum fields J , represented as v_i , and the bulk field ϕ corresponds to the hidden variables $h_j^{(k)}$. The bulk field is governed by its equation of motion, which can be modeled through the setup of a deep neural network in the deep Boltzmann machine, as claimed in [651]. For instance, in the $(d+1)$ -dimensional space-time with the metric,

$$ds^2 = -f(\eta)dt^2 + d\eta^2 + g(\eta)(dx_1^2 + \cdots + dx_{d-1}^2), \quad (5.10)$$

with η being the holographic direction, a scalar field theory is defined by the action,

$$S = \frac{1}{2} \int d^{d+1}x \sqrt{|g|} \left(g^{\mu\nu} (\partial_\mu \phi)(\partial_\nu \phi) + m^2 \phi^2 + \frac{\lambda}{2} \phi^4 \right), \quad (5.11)$$

where $\sqrt{|g|} = \sqrt{f(\eta)g^{d-1}(\eta)}$ is the spacetime volume factor. The classical equation of motion for a homogeneous, constant field (ϕ) and its canonical momentum (π) reads

$$\partial_\eta \pi + h(\eta) \pi - m^2 \phi - \lambda \phi^3 = 0, \quad \partial_\eta \phi = \pi. \quad (5.12)$$

²⁴It has also been found that the existence of the exact mapping between the deep Boltzmann machine and the renormalization group [657].

where $h(\eta) \equiv \partial_\eta \ln \sqrt{|g|}$. It has been claimed in [651] that numerically solving (5.12) with Euler's method is equivalent to a DNN with width $w = 2$ at each layer, see Fig. 5.4. Each layer corresponds to an Euler iteration step. The weights at the n^{th} layer are set to be

$$W^{(n)} = \begin{pmatrix} m^2 \delta\eta & 1 - h(\eta^{(n)}) \Delta\eta \\ 1 & \Delta\eta \end{pmatrix}, \quad (5.13)$$

whereas biases are set to zero. Linear activation is set for ϕ and non-linear one is set for π to implement the interaction term $(\lambda\phi^3)$. In Ref. [651], the authors aim to determine the function $h(\eta)$ given the values of π and ϕ at the $\eta = \infty$ and

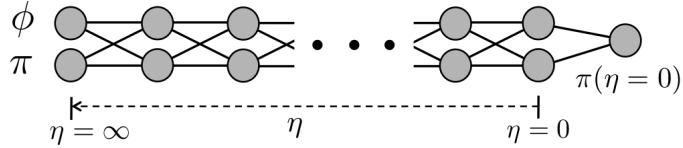


Figure 5.4: Demonstration of solving Eq. (5.12) with DNN. Taken from [651] with permission.

$\eta = 0$ limits. As a mock test, the authors prepared a set of data by solving Eq. (5.12) exactly with a known $h(\eta)$. The parameters of the network $[h(\eta^{(n)})]$ were then trained to match the relationship between the large and small boundary values in the holographic direction. The results showed that the reconstructed metric agreed well with the true values, with a deviation of about 30% in the near-horizon (small η) region.

The procedure has been further improved by parameterizing $h(\eta)$ by polynomials [658]. The loss function and parameter training procedure of the neural ODE [396] are borrowed to learn the polynomial coefficients in $h(\eta)$. Then, the authors trained the machine from lattice QCD results of the quark mass condensate and obtained results that are qualitatively consistent with the temperature dependence of the confinement and the Debye-screening behavior.

5.3. Solving Complex Inverse Problems

problem	quantity of interest $\mathcal{Q}(x)$	observable \mathcal{O}_y	relation
Sec. 3.3.3	in-medium potential $V(r)$	energy spectrum $\{E_n\}$	Schrödinger equation (5.20)
Sec. 4.1	equation of state $\varepsilon(P)$	mass and radius $\{M_i, R_i\}$	TOV equation (4.1)
Sec. 3.3.3	spectral function $\rho(\omega)$	Euclidean correlator $D(k)$	Källen–Lehmann convolution (5.23)

Table 5.1: Complex inverse problems: quantities of interest, observables, and the relation between them.

We finally review how deep learning helps in solving inverse problems. Nuclear physics, and more broadly, physics, presents numerous challenging inverse problems. In these problems, the forward problem is straightforward, but its inversion is not. For instance, consider a quantum system described by the Schrödinger equation with a potential model, if the interaction potential is known, the microscopic properties such as the energy levels and corresponding wave functions can easily be predicted. However, for certain systems like mesons (bound states of quarks and anti-quarks), the energy spectrum can be experimentally measured, but the effective interaction potential remains unclear. In this case, extracting the interaction potential from the given energy spectrum, which is the inverse problem of solving the Schrödinger equation, poses a significant challenge, yet remains an important practical issue. Deep learning has been found suitable for solving such inverse problems, examples include reconstructions of interaction potential [473], spectral function [441, 443, 453–

[457], parton distribution function [478, 486, 659–662], nuclear matter equation of state [567, 568, 592–594], and effective parton mass in a finite-temperature QCD medium [663].

Such inverse problems share similar characteristics. The unknown functions of interest, denoted as $\mathcal{Q}(x)$, are continuous, while the observables which can be either continuous functions or discrete variables, are functionals of $\mathcal{Q}(x)$, i.e. $\mathcal{O}_y = \mathcal{F}_y[\mathcal{Q}(x)]$, where the subscript y labels the continuous argument or discrete index of the observables. A summary of the quantities of interest, observables, and their relationship for the inverse problems discussed in this subsection can be found in Table 5.1.

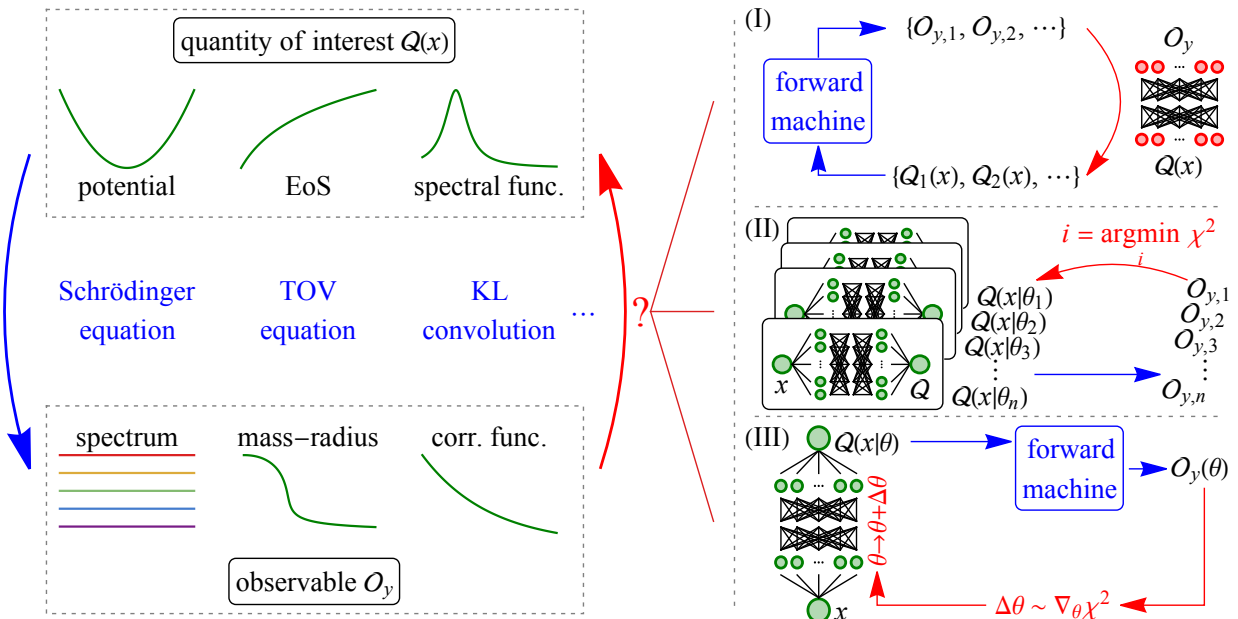


Figure 5.5: Different approaches of solving inverse problems.

Generally speaking, there are three different approaches to solving such inverse problems. They are summarized in Fig. 5.5 and listed as follows.

- (i) The first approach is to parameterize or discretize $\mathcal{Q}(x)$, prepare a sufficiently large ensemble of different \mathcal{Q} 's, compute their corresponding \mathcal{O} 's from the feasible forward modelling and exploit machine learning techniques, such as regression or classification algorithms e.g., with deep neural networks(DNNs) to learn an inverse mapping from the set of $\{\mathcal{O}, \mathcal{Q}\}$ pairs. Such an approach falls in the category of direct supervised learning. Physics priors are implicitly manifested inside the training data collection. This approach has been demonstrated in studies discussed in, e.g., Sections 2.2.1, 2.4.4, 2.3, 3.3.1, and 4.1.2.
- (ii) The second approach is to parameterize the quantity of interest by polynomials, neural networks or Gaussian Process(GP), $\mathcal{Q}(x) = \mathcal{Q}(x|\theta)$, update its parameters according to statistical approach (such as Markov-Chain Monte Carlo within Bayesian Inference) or Heuristic Algorithm (Generic Algorithm), in order to minimize the uncertainty-weighted difference between the target observable and the ones corresponding to $\mathcal{Q}(x|\theta)$,

$$\chi^2 = \sum_y \left(\frac{\mathcal{F}_y[\mathcal{Q}_{\text{NN}}(x|\theta)] - \mathcal{O}_y}{\Delta \mathcal{O}_y} \right)^2, \quad (5.14)$$

where $\Delta\mathcal{O}_y$ is the uncertainty of \mathcal{O}_y and $\sum_y \rightarrow \int dy$ for continuous arguments. Then being integrated into the Bayesian formula one can evaluate the posterior distribution for the target. See Sections 2.2.3, 2.4.2, and 4.1.1 for

typical examples adopted this approach.

(iii) The third approach is similar to the second one, but to update parameters of neural networks according to a gradient-based method,

$$\frac{1}{2} \nabla_{\boldsymbol{\theta}} \chi^2 = \sum_y \frac{\mathcal{F}_y[\mathcal{Q}_{\text{NN}}(x|\boldsymbol{\theta})] - \mathcal{O}_y}{(\Delta \mathcal{O}_y)^2} \int dx \frac{\delta \mathcal{F}_y[\mathcal{Q}(x)]}{\delta \mathcal{Q}(x)} \Big|_{\mathcal{Q}(x)=\mathcal{Q}_{\text{NN}}(x|\boldsymbol{\theta})} \nabla_{\boldsymbol{\theta}} \mathcal{Q}_{\text{NN}}(x|\boldsymbol{\theta}), \quad (5.15)$$

with $\frac{\delta \mathcal{F}_y[\mathcal{Q}(x)]}{\delta \mathcal{Q}(x)}$ being the functional derivative of \mathcal{F}_y with respect to $\mathcal{Q}(x)$. Intuitively, when the chi-square function reaches its minimum, the gradients vanish by definition, $\frac{1}{2} \nabla_{\boldsymbol{\theta}} \chi^2 = 0$, the parameters stop being updated and achieve the optimal point. This approach also allows the fusion of physical model or simulation into the optimization procedure with differentiable programming strategy. See Sections 3.3.3, 4.1.3, and 5.2 for examples using this approach, and in the following we will have details explanations for three typical cases.

Compared to Approach(ii), the physics-driven Approach(iii) directs the parameters to the minimum of χ^2 , rather than random walks. Therefore, it is more efficient for networks with numerous parameters. To apply the third method, the differentiability of $\mathcal{F}_y[\mathcal{Q}(x)]$ is a prerequisite, as shown in Eq. (5.15). In most cases, $\frac{\delta \mathcal{F}_y[\mathcal{Q}(x)]}{\delta \mathcal{Q}(x)}$ can be obtained either through analytical variation analysis or the modern Auto Differentiation framework(e.g., PyTorch, Tensorflow and Paddle); however, in some specific cases, the mapping from $\mathcal{Q}(x)$ to \mathcal{O}_y may be implicit, requiring non-trivial physics knowledge and/or mathematical derivation to compute the functional derivative. In the remainder of this subsection, we provide several examples to highlight the differences between these approaches.

In Sec. 4, we reviewed a few examples of inferring nuclear matter equation of state(EOS) from the neutron star mass-radius relation. In Refs. [567, 568], the authors follow Approach (iii) to implement a Neural Network to represent the EOS and unsupervisedly optimize the network parameter in order to fit the observation data, whereas Refs. [592–594] supervisedly train a network to represent the inverse mapping from mass-radius observations to the EOS. The latter fit into Approach (i) and are natural applications of DL. However, one should carefully prepare the training data set to avoid bias. In this particular case, one should also be careful in ensuring that the sequence of different observations does not alter the result EOS. Also, reliable uncertainty quantification is challenging [592]. The aforementioned challenges can be addressed through unsupervised training. In this approach, a DNN is used as an unbiased parametrization of the EoS and fed into a Bayesian analysis. This enables the extraction of not only the mean value, but also the associated uncertainty.

Inverse TOV equation — The success of unsupervised training lies in designing a physics-driven training process that guides the iteration of parameters towards maximizing likelihood. This can be achieved through the use of automatic differentiation (AD) as discussed in Sec. 4.1, or through analytical derivation. Despite the highly non-linear nature of the TOV equation (4.1) with respect to the EoS, it is still possible to analyze the linear response of observables out of TOV equations to small changes in the EoS.

For the sake of convenience, we reformulate Eq. (4.1) by changing the independent variable from the radius (r) to the logarithmic of pressure, $\ln(P/P_{\text{bnd}})$. P_{bnd} denotes the boundary pressure, and it is small enough such that M and R are insensitive to it. Also, we consider the argument of $v \equiv r^3$ rather than r to avoid numerical divergence. The TOV equation thus becomes,

$$\begin{aligned} \frac{dv}{d \ln \frac{P}{P_{\text{bnd}}}} &= -\mathcal{K}_v(P, \varepsilon, v, m), \\ \frac{dm}{d \ln \frac{P}{P_{\text{bnd}}}} &= -\mathcal{K}_m(P, \varepsilon, v, m), \end{aligned} \quad (5.16)$$

where

$$\begin{aligned}\mathcal{K}_v(P, \varepsilon, v, m) &\equiv \frac{3(v^{\frac{1}{3}} - 2m)}{(m/v + 4\pi P)(1 + \varepsilon/P)}, \\ \mathcal{K}_m(P, \varepsilon, v, m) &\equiv \frac{4\pi(v^{\frac{1}{3}} - 2m)\varepsilon}{(m/v + 4\pi P)(1 + \varepsilon/P)}.\end{aligned}\quad (5.17)$$

For later convenience, we define $\mathcal{K}_{X,Y} \equiv \frac{\partial \mathcal{K}_X}{\partial Y}$ for $X \in \{v, m\}$ and $Y \in \{P, \varepsilon, v, m\}$. Given a small, Dirac- δ function-like perturbation in the EoS, $\varepsilon(P) \rightarrow \varepsilon(P) + \lambda \delta(P - P')$, the change of v and m , denoted as $\Delta v(P|P')$ and $\Delta m(P|P')$, are given by the linear variation of Eq. (5.16),

$$0 = \frac{d\Delta X(P|P')}{d \ln \frac{P}{P_{\text{bnd}}}} + \mathcal{K}_{X,v} \Delta v(P|P') + \mathcal{K}_{X,m} \Delta m(P|P') + \lambda \mathcal{K}_{X,\varepsilon} \delta(P - P'). \quad (5.18)$$

It is obvious that both $\Delta v(P|P')$ and $\Delta m(P|P')$ are linearly depending on the perturbation parameter λ . By solving Eq. (5.18) with parameter $\lambda = 1$ and argument $\ln \frac{P}{P_{\text{bnd}}}$ going from $\ln \frac{P_c}{P_{\text{bnd}}}$ to unity, the functional derivative can be computed as

$$\begin{aligned}\frac{\delta M(P_c)}{\delta \varepsilon(P')} &= \Delta m(P|P' = P_{\text{bnd}}), \\ \frac{\delta R(P_c)}{\delta \varepsilon(P')} &= \left(\Delta v(P|P' = P_{\text{bnd}}) \right)^{1/3}.\end{aligned}\quad (5.19)$$

Consequently, we demonstrate that it is possible to calculate the linear response of a Neutron Star's mass and radius to an infinitesimal perturbation in energy density, thereby supporting the numerical automatic differentiation method outlined in Sec. 4.

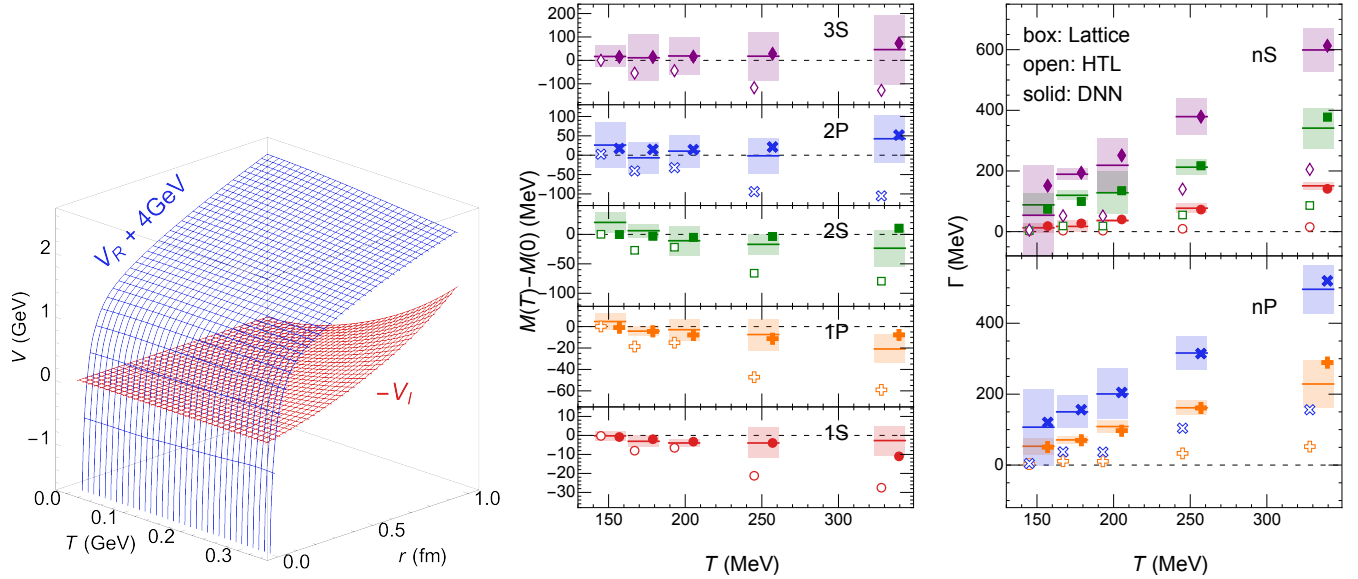


Figure 5.6: (Left) Real (blue) and imaginary (red) part of interaction potentials versus temperature and quark-antiquark distance extracted via DNNs. (Middle and Right) In-medium mass shifts with respect to the vacuum mass (middle) and the thermal widths (right) of different bottomonium states obtained from fits to lattice QCD results of Ref. [471] (lines and shaded bands) using weak-coupling motivated functional forms [664] (open symbols) and DNN based optimization (solid symbols). The points are shifted horizontally for better visualization. $\Upsilon(1S)$, $\chi_{b0}(1P)$, $\Upsilon(2S)$, $\chi_{b0}(2P)$ and $\Upsilon(3S)$ states are represented by red circles, orange pluses, green squares, blue crosses and purple diamonds, respectively. Figures from Ref. [665] with permission.

Inverse Schrödinger equation— Another example of solving inverse problem with physics-driven learning is the reconstruction of finite-temperature interaction potential from the lattice QCD simulation of Bottomonia masses and

thermal widths in the Quark-Gluon Plasma(QGP). The QGP is a new state of matter formed in high energy nuclear collisions and is composed of color-deconfined quarks and gluons, which is in contrast to the low-temperature phase where quarks and gluons are confined within hadrons. The suppression of heavy quarkonium production rates, which are the bound states of a heavy quark and its anti-quark, is evidence of QGP formation in high energy nuclear collisions [109]. Due to the very large mass and small velocity of heavy quarks, one is allowed to employ the Schrödinger equation with an effective finite-temperature potential and study the properties of bottomonium in medium [666, 667],

$$-\frac{\nabla^2}{2m_\mu}\psi_n(r) + V(r)\psi_n(r) = E_n\psi_n(r), \quad (5.20)$$

where the reduced mass is half of the b -quark mass, $m_\mu = m_b/2$, ψ_n the relative wavefunction, and E_n the energy. At finite temperature, the interaction potential becomes complex [463], $V(T, r) = V_R(T, r) + i \cdot V_I(T, r)$, where the imaginary part emerges due to the Landau damping effect and transition between color-singlet and octet and vanishing in the vacuum. Accordingly, the energy eigenvalues are complex, with the real and imaginary parts correspond to the mass, $\text{Re}[E_n] = m - 2m_b$, and width, $\text{Im}[E_n] = -\Gamma$, respectively.

In Ref. [665], it was found that the recent lattice QCD calculation of Bottomonia mass and width (Refs. [470–472]) contradicts the weak-coupling motivated functional forms [664] (shown as open symbols in Fig. 5.6). To address this, the authors developed a model-independent approach for extracting the finite-temperature complex potential directly from the lattice QCD calculation. The complex-valued potential, $\mathcal{Q} \equiv V_R(r, T), V_I(r, T)$, is the quantity of interest, while the observables, the masses and widths for various bound states at different temperatures, $\mathcal{O}_y \equiv m_n(T_j), \Gamma_n(T_j)$, are obtained by solving the eigenvalue problem of a differential equation. This makes the application of general techniques in physics-driven deep learning challenging in computing the parameter gradients in Eq. (5.15).

To compute the functional derivative, one needs to know how the complex-valued energy eigenvalues response to an arbitrary perturbation in potential. Since we only consider small perturbations, the changes of energy eigenvalues are given by the Hellmann–Feynmann theorem in quantum mechanics, $\delta E_n = \int |\psi_n(r)|^2 \delta V(r) dr$. In Ref. [665], the temperature and distance dependence of the real and imaginary potentials are expressed by the DNNs,

$$V_R(r, T) = V_{R,\text{DNN}}(r, T | \boldsymbol{\theta}_R), \quad V_I(r, T) = V_{I,\text{DNN}}(r, T | \boldsymbol{\theta}_I), \quad (5.21)$$

with the network parameters being trained according to the parameter gradients (5.15) with functional derivatives,

$$\begin{aligned} \frac{\delta m_n}{\delta V_R(r)} &= -\frac{\delta \Gamma_n}{\delta V_I(r)} = |\psi_n(r)|^2, \\ \frac{\delta m_n}{\delta V_I(r)} &= \frac{\delta \Gamma_n}{\delta V_R(r)} = 0. \end{aligned} \quad (5.22)$$

The wavefunctions $\psi_n(r)$ are obtained by solving the eigenvalue problem. The validity of this method has been confirmed through a closure test with known potentials. The authors began by using a given formula for complex-valued potentials and solving the Schrödinger equation at six different temperatures to generate a set of pseudo-data, which consists of the mass and width for five eigenstates. This choice of pseudo-data was consistent with the data obtained from lattice QCD calculations [471]. The set of pseudo-data was then used to train the parameters of a DNN, and the resulting $V_{R,\text{DNN}}$ and $V_{I,\text{DNN}}$ were found to be in consistent with the ground-truth. The validated method is then applied to the masses and thermal widths computed from lattice QCD calculation. With the optimized parameter sets for $\boldsymbol{\theta}_R$ and $\boldsymbol{\theta}_I$, the real and imaginary potentials are shown in Fig. 5.6 (left), and the corresponding mass shifts and thermal widths are shown by the solid symbols in Fig. 5.6 (left and middle).

Tackling ill-posed inverse problems — In practice, when solving ill-posed inverse problems, one must introduce additional rules to better control the input function and eliminate degeneracy. This is demonstrated through the example of reconstructing spectral functions, which cannot be directly computed in non-perturbative Monte Carlo calculations such as lattice QCD. Instead, they must be inferred from limited sets of correlation data [434]. The K"allen–Lehmann (KL) correlation functions are among the commonly studied observables,

$$D(k) = \int_0^\infty \frac{1}{\pi} \frac{\omega d\omega}{\omega^2 + k^2} \rho(\omega), \quad (5.23)$$

which is a linear transformation mapping a continuous real function to another continuous real function, and the arguments of both the input and output functions are defined in the real axis. Ref. [441] analytically solved the eigenvalue problem and found the eigenvalues to be $1/(2 \cosh \frac{\pi s}{2})$. Here, $s \in \mathbb{R}$ is a continuous parameter that labels the eigenstates. The eigenvalues can be arbitrarily close to zero for large s , and the eigenvalues of the inverse operation, which are the inverses of those of the KL convolution, can be arbitrarily large. In the inverse operation, a small noise in the realistic numerical calculation of D will be magnified to a large deviation in ρ as shown in Fig. 3.10 of Sec. 3.3.3. Therefore, inverse KL convolution is ill-posed.

Common methods for reconstructing spectral functions include the Tikhonov (TK) regulator [444, 445], the Maximum Entropy Method (MEM) that employs the Shannon–Jaynes entropy [668, 669], and the Bayesian Reconstruction (BR) method [449]. In references [441, 443, 457], the spectral function $\rho(\omega)$ is either formulated as a one-dimensional input and one-dimensional output deep neural network (DNN) that approximates the function (NN-P2P in Figure 5.7), or as a unity-input and N_ω -dimensional output DNN that represents the value of ρ at N_ω points in ω (NN in Figure 5.7). It has been shown [441] that both representations provide non-local regulators and lead to a unique solution of $\rho(\omega)$. To optimize the parameters of network representations $\{\theta\}$ with loss function, the authors implemented gradient-based algorithms. It derives as,

$$\nabla_{\theta} \mathcal{L} = \sum_{j,i} K(k_j, \omega_i) \frac{\partial \mathcal{L}}{\partial D(k_j)} \nabla_{\theta} \rho_i, \quad (5.24)$$

where $K(k, \omega) = \frac{1}{\pi} \frac{\omega}{\omega^2 + k^2}$, and $\nabla_{\theta} \rho_i$ is computed by the standard back-propagation method. The reconstruction error is propagated to parameters of the neural network, combined with gradients derived from automatic differentiation.

As a numerical demonstration, the spectral function formed with two Breit–Wigner peaks is chosen as the ground truth,

$$\rho(\omega) = \sum_{n=1}^2 \frac{4A_n \Gamma_n \omega}{(M_n^2 + \Gamma_n^2 - \omega^2)^2 + 4\Gamma_n^2 \omega^2}, \quad (5.25)$$

with $A_1 = 0.8$, $A_2 = 1.0$, $\Gamma_1 = \Gamma_2 = 0.5$ GeV, $M_1 = 2.0$ GeV, $M_2 = 5.0$ GeV, and compute the corresponding KL correlation functions $D(k_i)$ at $k_i = i \times \Delta k$, with $i = 1, 2, \dots, 100$, and $\Delta k = 0.2$ GeV. To investigate the effects of noise in a realistic situation, mock data were prepared with random noise on the correlation function, i.e. $D_i^{\text{noisy}} = D(k_i) + n_i$. See Refs. [434, 441] for the detailed setup. Then, for points $\omega_a = a \times \Delta \omega$, with $a = 1, 2, \dots, 500$, and $\Delta \omega = 0.04$ GeV, the spectral functions $\rho(\omega)$ were reconstructed.

In Figure 5.8, the spectral functions and their respective correlation functions in both the generalized coordinate and momentum spaces are displayed for three methods: NN and NN-P2P representations, and the widely used Maximum Entropy Method (MEM). To ensure the stability of the MEM results, the number of basis functions, $N_{\text{basis}} = N_k$, has been set to 100. The NN architecture includes three hidden layers with a width of 64, with the input layer consisting

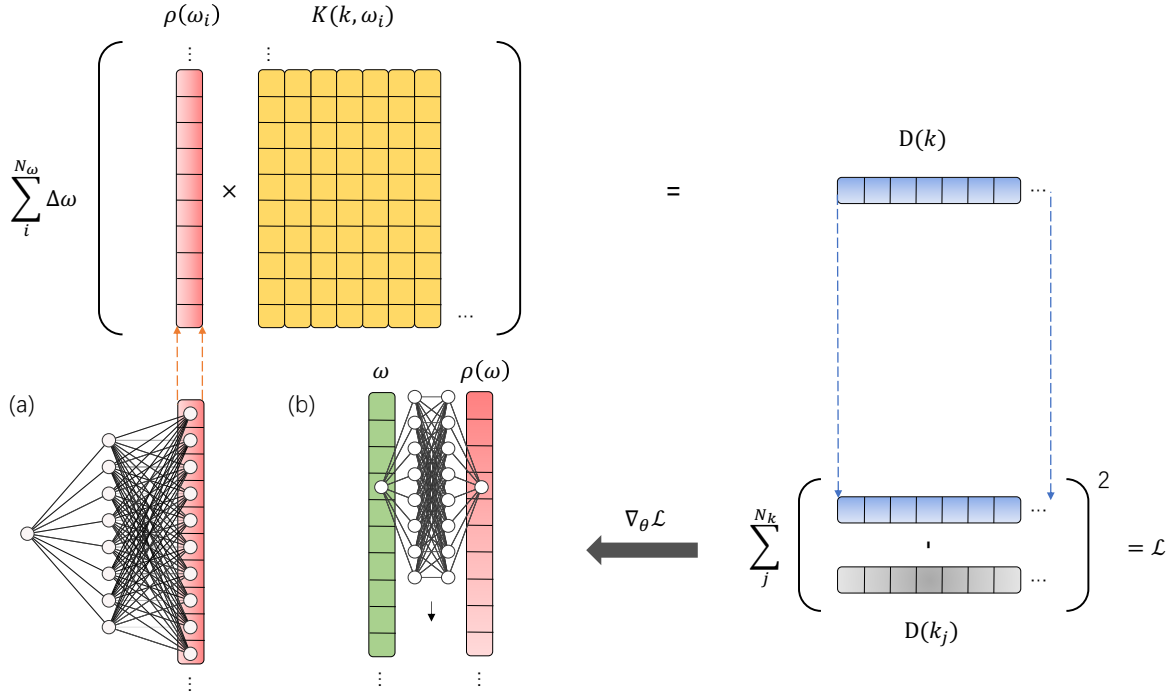


Figure 5.7: Automatic differential framework to reconstruct spectral from observations. (a) NN. Neural networks have outputs as a list representation of spectrum $\rho_i(\omega_i)$. (b) NN-P2P. Neural networks have input and output nodes as (ω_i, ρ_i) pairwise.

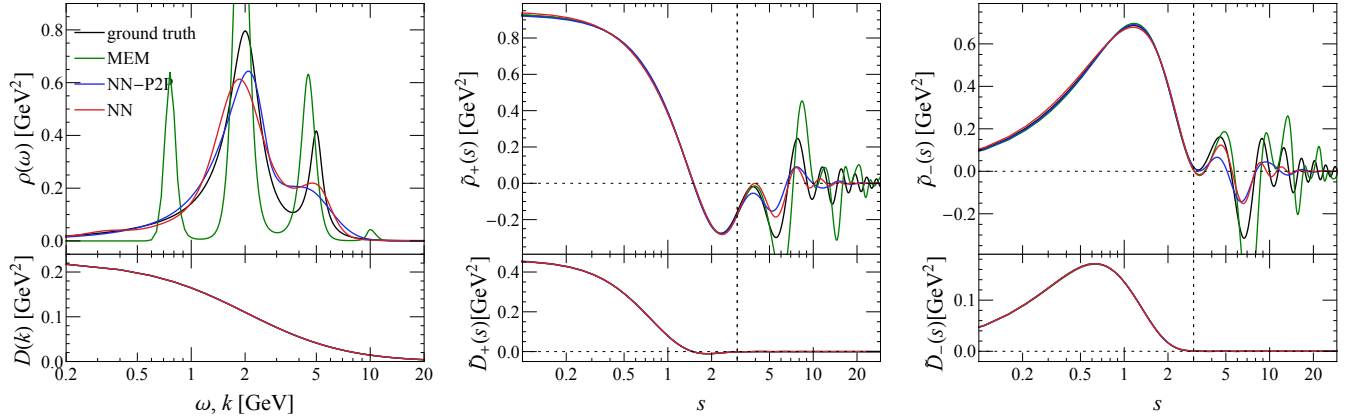


Figure 5.8: Spectral functions using different reconstruction methods (upper panels) and their corresponding KL correlation functions (lower panels) in the generalized coordinate space (left) and generalized momentum space (middle and right). Black curves are for the ground truth using Breit–Wigner spectral functions. Numerically reconstructed functions using NN, NN-P2P, and MEM using $N_{\text{basis}} = 100$ basis are represented by red, blue, and green curves, respectively. Figures reproduced from Ref. [441, 457] with permission.

of a single constant node set to unity. The output layer contains N_ω nodes. For the NN-P2P architecture, the input and hidden layers are unchanged, but the output layer has only one node. All activation functions before the output have been selected as ELU. Although the behavior of $\rho(\omega)$ may vary significantly in the generalized coordinate space, the generalized momentum $\tilde{\rho}_\pm(s)$ exhibits similar behavior for values of s less than or equal to three, as indicated by the vertical dashed lines in Fig. 5.8. This highlights the fundamental challenge in the reconstruction problem. Regardless of the reconstruction method used, one can always accurately recover the low-frequency modes of $\tilde{\rho}$, but the high-frequency modes are prone to being polluted by noise or numerical inaccuracies in the correlation functions, making them nearly impossible to achieve. On the other hand, all D and \tilde{D} values are nearly equal, which is ensured through the χ^2 -fitting.

Thus, it should be noted that all these methods are not guaranteed to provide the correct inversion function when D is of finite precision. Meanwhile, the “biases” introduced in the supervised training data set become helpful in solving ill-posed inverse problems if unwanted biases are carefully avoided. A natural way to implement the physical regulators can be provided by Approach (i). This is demonstrated in studies that employ DNNs to learn the inverse mapping, such as [451, 453, 454, 670, 671]. In these works, an ensemble of ρ ’s that follow the physical properties is generated and the corresponding D ’s are computed. DNNs are then trained to represent the inverse mapping from D to ρ . The trained networks become automatically regularized inverse functions with embedded prior knowledge, but one should be careful about the risk of introducing unwanted biases in the training data.

5.4. Summary

In this section, we reviewed recent advanced developments in embedding more physics priors/knowledge into machine learning methods to improve the efficiency and/or applicability in physics exploration. We illustrate the physics-inspired, informed, and driven deep-learning approaches with taking concrete examples of gauge-invariant sampling of lattice field configurations, inverse renormalization group transformation, Feynman paths generation, and network realization of AdS-CFT calculation, as well as complex inverse problems such as nuclear equation of state reconstruction from neutron star masses and radii, interaction potential extraction from the Schrödinger equation energy spectrum, and spectral function reconstruction from Euclidean correlators. The examples presented in the current section have shown significant advantages of solving physics problems with these advanced developments in ML/DL. We hope that these examples can inspire further work in the near future.

6. Summary and outlook

AI for science has seen a surge in popularity and adoption in general [18]. Especially, paradigms with modern machine- and deep-learning techniques are transforming across broad scientific domains – those are overwhelmed by large-scale intensive computations and/or large amount of high-dimensional data, including high-energy nuclear physics (HENP) [24, 672, 673]. The integration of machine learning techniques has led to remarkable advances and a host of results in the field, opening a new horizon for exploration and discovery. These ML-based methods have revolutionized the way of analyzing data, improved the ability to discover new phenomena and develop more efficient simulations. HENP is an extremely fruitful area in this sense, and many advances have been made in the past decade [4, 13, 579]. We are in the right and exciting era to work in this direction and to further our understanding of QCD matter in extreme conditions.

This review aims to provide an overview of the current applications of ML in HENP theory studies, and to highlight some of the recent developments in this rapidly-evolving crossing field. Several aspects, revolving around ML for theoretical study of extreme QCD matter exploration, are discussed: from data analysis in high energy heavy-ion collisions(HICs) sector, to improving lattice QCD/QFT simulations, and to the inference of Neutron Star(NS) interior matter properties, covering the current efforts for strongly interacting nuclear matter study. Then a refined advanced development summary and discussion is presented in the last chapter to try to form a common ground from a methodology perspective in inspiring further exploration.

In terms of big **data analysis**, HENP indeed forms us a golden playground. Copious amounts of multifarious data can be collected from HIC experiment detectors, astrophysical observatories, and also lattice QCD simulations. Many of the well-established physics models or software/packages also makes it feasible to generate large-scale simulation data, to which the disentangled physics understanding and correlation analysis are yet daunting with conventional methods. Thus, as a modern numerical method to process complex data for hidden pattern decoding, ML and DL techniques have provided a powerful tool for exploring physics across the different disciplines.

Besides being data-rich, a variety of areas in HENP are also **computation intensive**, with many of the accessible measurements such as billions of events from the detectors require understanding from theory simulations but not yet fully calculable in first principle's manner. For the purpose of whatever evolving or confirming our theory understanding, or exploring new physics for discoveries, the ability to perform efficient and prompt simulations is critical for many aspects of HENP. ML and DL have also made significant progresses in HENP computations, e.g., various algorithms have been developed to improve the simulation speed and accuracy [34]. Advanced calculations with faster and optimized models incorporate with ML methodologies allow for better prediction and comprehension in confronting data.

In addition to those head-on applications of ML/DL in HENP, there are still many challenges and questions need to be addressed further. Probably the first-line concern from physicists is the **interpretability** of the ML approaches utilized in HENP research [674]. Detailed understanding on the reason and condition for the used methods to work are desired in physics. More efforts need to be deployed in uncovering the somehow “Black Box” characteristic of ML algorithms, especially those are with huge amounts of parameters. Techniques to reveal the patterns and validate the computations with ML are called for as well. Then per purpose of physics exploration, those practical computation results from the ML methods need to point to or be transferred to physics knowledge or inspirations, which better to be conformed to the well-established language of physics in controlled way, such as with uncertainties properly given. The incorporation of physics priors into those ML paradigms to specific physics studies deserve further development in addressing this concern [90].

Another challenge is how to reliably **connect experimental measurements and physical theory** using ML/DL techniques, with the associated **uncertainties** also properly evaluated. As emphasized, in HENP, to understand the nature of strongly interacting matter, experiments and observations from big scientific infrastructures play crucial role, which need to turn to physics knowledge as per mission. This however is with unprecedented scales and complexities, such as the high dimensionality and highly correlated data stream from measurement, the multi-scale and intricate physics simulations for the dynamical process involved of the measurement. Statistical learning methods such as Bayesian inference [675] and then alternative ML/DL approaches give series of great demonstrations to analyze data for pinning down physics knowledge. Principled uncertainty estimation for results inferred from naive ML/DL applications is not yet fully developed. These methods still have great potential to be unleashed to explore QCD matter.

As future prospects, with ML/DL assisted, important physics properties and hopefully new physics phenomena are expected to be extracted from accumulating measurements in e.g., heavy ion collision experiments or astrophysics observations, to inform physics discovery. Be specific, ever **faster and more efficient analysis** to large amount of data could be anticipated to better connect experiment to physics theory; **smart, controllable and fast simulation** with ML methods such as generative modeling may largely reduce the demand in computational resource for the field, and also mitigate the enormous complexities in disentangling different physics involved for the simulation; in the course of neutron star, it'd be intriguing to explore the possible potential of ML in identifying e.g., presence of exotic phases in NS interiors from observations, and also develop more reliable ways in **combining evidence from multi-source data** such as those from HICs together those from multi-messenger astrophysics. Furthermore, in the lattice QCD sector, while efforts to **improve the efficiency and accuracy of lattice sampling and simulations** continue, it may also be possible to enhance our understanding of QCD from an ML algorithmic perspective. The intersection of HENP and ML is rapidly advancing, and with the continued progress and enthusiasm in ML, we can expect even more exciting developments and remarkable achievements in the near future.

Acknowledgements

We express our sincere gratitude to all collaborators who have made invaluable contributions to our research projects. This work was supported by the Germany BMBF under the ErUM-Data project (KZ), the AI grant of SAMSON AG, Frankfurt (LW and KZ), Xidian-FIAS International Joint Research Center (LW), Huawei Technologies Co., Ltd and the National Natural Science Foundation of China under contract No. 12075098 (LP), and U.S. Department of Energy, Office of Science, Office of Nuclear Physics, grant No. DE-FG88ER40388 (SS).

References

- [1] F. Gross, et al., 50 Years of Quantum Chromodynamics (12 2022). [arXiv:2212.11107](https://arxiv.org/abs/2212.11107).
- [2] K. Yagi, T. Hatsuda, Y. Miake, Quark-gluon plasma: From big bang to little bang, Vol. 23, Cambridge University Press, 2005.
- [3] X.-N. Wang (Ed.), Quark-Gluon Plasma 5, World Scientific, New Jersey, 2016. [doi:10.1142/9533](https://doi.org/10.1142/9533).
- [4] K. Fukushima, B. Mohanty, N. Xu, Little-Bang and Femto-Nova in Nucleus-Nucleus Collisions, APPS Bull. 31 (2021) 1. [arXiv:2009.03006](https://arxiv.org/abs/2009.03006), [doi:10.1007/s43673-021-00002-7](https://doi.org/10.1007/s43673-021-00002-7).
- [5] E. V. Shuryak, The QCD vacuum, hadrons and the superdense matter, Vol. 71, 2004. [doi:10.1142/5367](https://doi.org/10.1142/5367).
- [6] J. Rafelski, Discovery of Quark-Gluon-Plasma: Strangeness Diaries, Eur. Phys. J. ST 229 (1) (2020) 1–140. [arXiv:1911.00831](https://arxiv.org/abs/1911.00831), [doi:10.1140/epjst/e2019-900263-x](https://doi.org/10.1140/epjst/e2019-900263-x).
- [7] X. Luo, Q. Wang, N. Xu, P. Zhuang (Eds.), Properties of QCD Matter at High Baryon Density, Springer, 2022. [doi:10.1007/978-981-19-4441-3](https://doi.org/10.1007/978-981-19-4441-3).
- [8] H.-T. Ding, F. Karsch, S. Mukherjee, Thermodynamics of strong-interaction matter from Lattice QCD, Int. J. Mod. Phys. E 24 (10) (2015) 1530007. [arXiv:1504.05274](https://arxiv.org/abs/1504.05274), [doi:10.1142/S0218301315300076](https://doi.org/10.1142/S0218301315300076).
- [9] F. Karsch, Lattice QCD at non-zero temperature and density (12 2022). [arXiv:2212.03015](https://arxiv.org/abs/2212.03015).
- [10] G. Aarts, et al., Phase Transitions in Particle Physics – Results and Perspectives from Lattice Quantum Chromodynamics, 2023. [arXiv:2301.04382](https://arxiv.org/abs/2301.04382).
- [11] K. Nagata, Finite-density lattice QCD and sign problem: Current status and open problems, Prog. Part. Nucl. Phys. 127 (2022) 103991. [arXiv:2108.12423](https://arxiv.org/abs/2108.12423), [doi:10.1016/j.ppnp.2022.103991](https://doi.org/10.1016/j.ppnp.2022.103991).
- [12] W. Busza, K. Rajagopal, W. van der Schee, Heavy Ion Collisions: The Big Picture, and the Big Questions, Ann. Rev. Nucl. Part. Sci. 68 (2018) 339–376. [arXiv:1802.04801](https://arxiv.org/abs/1802.04801), [doi:10.1146/annurev-nucl-101917-020852](https://doi.org/10.1146/annurev-nucl-101917-020852).
- [13] A. Bzdak, S. Esumi, V. Koch, J. Liao, M. Stephanov, N. Xu, Mapping the Phases of Quantum Chromodynamics with Beam Energy Scan, Phys. Rept. 853 (2020) 1–87. [arXiv:1906.00936](https://arxiv.org/abs/1906.00936), [doi:10.1016/j.physrep.2020.01.005](https://doi.org/10.1016/j.physrep.2020.01.005).
- [14] T. Hogg, B. A. Huberman, Artificial intelligence and large scale computation: A physics perspective, Phys. Rept. 156 (1987) 227. [doi:10.1016/0370-1573\(87\)90096-2](https://doi.org/10.1016/0370-1573(87)90096-2).

[15] Y. K. Dwivedi, L. Hughes, E. Ismagilova, G. Aarts, C. Coombs, T. Crick, Y. Duan, R. Dwivedi, J. Edwards, A. Eirug, V. Galanos, P. V. Ilavarasan, M. Janssen, P. Jones, A. K. Kar, H. Kizgin, B. Kronemann, B. Lal, B. Lucini, R. Medaglia, K. Le Meunier-FitzHugh, L. C. Le Meunier-FitzHugh, S. Misra, E. Mogaji, S. K. Sharma, J. B. Singh, V. Raghavan, R. Raman, N. P. Rana, S. Samothrakis, J. Spencer, K. Tamilmani, A. Tubadji, P. Walton, M. D. Williams, [Artificial intelligence \(ai\): Multidisciplinary perspectives on emerging challenges, opportunities, and agenda for research, practice and policy](#), International Journal of Information Management 57 (2021) 101994. [doi:<https://doi.org/10.1016/j.ijinfomgt.2019.08.002>](https://doi.org/10.1016/j.ijinfomgt.2019.08.002).

URL <https://www.sciencedirect.com/science/article/pii/S026840121930917X>

[16] Y. LeCun, Y. Bengio, G. Hinton, Deep learning, nature 521 (7553) (2015) 436–444.

[17] I. H. Sarker, Deep learning: a comprehensive overview on techniques, taxonomy, applications and research directions, SN Computer Science 2 (6) (2021) 420.

[18] R. Stevens, V. Taylor, J. Nichols, A. B. Maccabe, K. Yelick, D. Brown, [Ai for science: Report on the department of energy \(doe\) town halls on artificial intelligence \(ai\) for science](#) (2 2020). [doi:10.2172/1604756](https://doi.org/10.2172/1604756)

URL <https://www.osti.gov/biblio/1604756>

[19] P. Mehta, M. Bukov, C.-H. Wang, A. G. R. Day, C. Richardson, C. K. Fisher, D. J. Schwab, A high-bias, low-variance introduction to Machine Learning for physicists, Phys. Rept. 810 (2019) 1–124. [arXiv:1803.08823](https://arxiv.org/abs/1803.08823), [doi:10.1016/j.physrep.2019.03.001](https://doi.org/10.1016/j.physrep.2019.03.001).

[20] G. Carleo, I. Cirac, K. Cranmer, L. Daudet, M. Schuld, N. Tishby, L. Vogt-Maranto, L. Zdeborová, Machine learning and the physical sciences, Rev. Mod. Phys. 91 (4) (2019) 045002. [arXiv:1903.10563](https://arxiv.org/abs/1903.10563), [doi:10.1103/RevModPhys.91.045002](https://doi.org/10.1103/RevModPhys.91.045002).

[21] M. Mézard, A. Montanari, [Information, Physics, and Computation](#), Oxford University Press, 2009. [doi:10.1093/acprof:oso/9780198570837.001.0001](https://doi.org/10.1093/acprof:oso/9780198570837.001.0001)

URL <https://doi.org/10.1093/acprof:oso/9780198570837.001.0001>

[22] Y. Bahri, J. Kadmon, J. Pennington, S. S. Schoenholz, J. Sohl-Dickstein, S. Ganguli, [Statistical mechanics of deep learning](#), Annual Review of Condensed Matter Physics 11 (1) (2020) 501–528. [doi:10.1146/annurev-conmatphys-031119-050745](https://doi.org/10.1146/annurev-conmatphys-031119-050745)

URL <https://doi.org/10.1146/annurev-conmatphys-031119-050745>

[23] P. Bedaque, et al., A.I. for nuclear physics, Eur. Phys. J. A 57 (3) (2021) 100. [doi:10.1140/epja/s10050-020-00290-x](https://doi.org/10.1140/epja/s10050-020-00290-x).

[24] A. Boehnlein, et al., Colloquium: Machine learning in nuclear physics, Rev. Mod. Phys. 94 (3) (2022) 031003. [arXiv:2112.02309](https://arxiv.org/abs/2112.02309), [doi:10.1103/RevModPhys.94.031003](https://doi.org/10.1103/RevModPhys.94.031003).

[25] B. Humpert, On the use of neural networks in high-energy physics experiments, Comput. Phys. Commun. 56 (1990) 299–311. [doi:10.1016/0010-4655\(90\)90016-T](https://doi.org/10.1016/0010-4655(90)90016-T).

[26] M. Gyulassy, M. Harlander, Elastic tracking and neural network algorithms for complex pattern recognition, Comput. Phys. Commun. 66 (1991) 31–46. [doi:10.1016/0010-4655\(91\)90005-6](https://doi.org/10.1016/0010-4655(91)90005-6).

[27] S. A. Bass, A. Bischoff, C. Hartnack, J. A. Maruhn, J. Reinhardt, H. Stoecker, W. Greiner, Neural networks for impact parameter determination, *J. Phys. G* 20 (1994) L21–L26. [doi:10.1088/0954-3899/20/1/004](https://doi.org/10.1088/0954-3899/20/1/004).

[28] S. A. Bass, A. Bischoff, J. A. Maruhn, H. Stoecker, W. Greiner, Neural networks for impact parameter determination, *Phys. Rev. C* 53 (1996) 2358–2363. [arXiv:nucl-th/9601024](https://arxiv.org/abs/nucl-th/9601024), [doi:10.1103/PhysRevC.53.2358](https://doi.org/10.1103/PhysRevC.53.2358).

[29] M. Feickert, B. Nachman, A Living Review of Machine Learning for Particle Physics (2 2021). [arXiv:2102.02770](https://arxiv.org/abs/2102.02770).

[30] L. Benato, et al., Shared Data and Algorithms for Deep Learning in Fundamental Physics, *Comput. Softw. Big Sci.* 6 (1) (2022) 9. [arXiv:2107.00656](https://arxiv.org/abs/2107.00656), [doi:10.1007/s41781-022-00082-6](https://doi.org/10.1007/s41781-022-00082-6).

[31] C. M. Bishop, *Pattern Recognition and Machine Learning*, Springer Verlag, Berlin, 2006.

[32] I. Goodfellow, Y. Bengio, A. Courville, *Deep Learning*, The MIT Press, Cambridge, Massachusetts, 2016.

[33] A. Dawid, et al., Modern applications of machine learning in quantum sciences, 2022. [arXiv:2204.04198](https://arxiv.org/abs/2204.04198).

[34] P. Shanahan, et al., Snowmass 2021 Computational Frontier CompF03 Topical Group Report: Machine Learning (9 2022). [arXiv:2209.07559](https://arxiv.org/abs/2209.07559).

[35] K. P. Murphy, *Machine Learning: A Probabilistic Perspective*, The MIT Press, Cambridge, Massachusetts, 2012.

[36] R. Garnett, *Bayesian Optimization*, Cambridge University Press, 2023, to appear.

[37] C. Williams, C. Rasmussen, [Gaussian processes for regression](#), in: D. Touretzky, M. C. Mozer, M. Hasselmo (Eds.), *Adv. Neural Inf. Process. Syst.*, Vol. 8, MIT Press, 1996.
URL <https://proceedings.neurips.cc/paper/1995/file/7cce53cf90577442771720a370c3c723-Paper.pdf>

[38] M. G. Genton, Classes of kernels for machine learning: A statistics perspective 2 (2002) 299–312.

[39] J. Schmidhuber, Deep learning in neural networks: An overview, *Neural networks* 61 (2015) 85–117.

[40] W. S. McCulloch, W. Pitts, A logical calculus of the ideas immanent in nervous activity, *The bulletin of mathematical biophysics* 5 (1943) 115–133.

[41] G. Cybenko, Approximation by superpositions of a sigmoidal function, *Mathematics of control, signals and systems* 2 (4) (1989) 303–314.

[42] K. Hornik, Approximation capabilities of multilayer feedforward networks, *Neural networks* 4 (2) (1991) 251–257.

[43] Y. Lecun, L. Bottou, Y. Bengio, P. Haffner, Gradient-based learning applied to document recognition, *Proceedings of the IEEE* 86 (11) (1998) 2278–2324. [doi:10.1109/5.726791](https://doi.org/10.1109/5.726791).

[44] A. G. Baydin, B. A. Pearlmutter, A. A. Radul, J. M. Siskind, Automatic differentiation in machine learning: a survey, *Journal of Machine Learning Research* 18 (2018) 1–43.

[45] M. Abadi, P. Barham, J. Chen, Z. Chen, A. Davis, J. Dean, M. Devin, S. Ghemawat, G. Irving, M. Isard, et al., Tensorflow: A system for large-scale machine learning., in: *OSDI*, Vol. 16, 2016, pp. 265–283.

[46] A. Paszke, S. Gross, F. Massa, A. Lerer, J. Bradbury, G. Chanan, T. Killeen, Z. Lin, N. Gimelshein, L. Antiga, A. Desmaison, A. Kopf, E. Yang, Z. DeVito, M. Raison, A. Tejani, S. Chilamkurthy, B. Steiner, L. Fang, J. Bai, S. Chintala, Pytorch: An imperative style, high-performance deep learning library, in: Proceedings of the 33rd International Conference on Neural Information Processing Systems, Curran Associates Inc., Red Hook, NY, USA, 2019.

[47] S. S. Schoenholz, E. D. Cubuk, JAX, M.D.: A Framework for Differentiable Physics, arXiv e-prints (2019) arXiv:1912.04232 [arXiv:1912.04232](https://arxiv.org/abs/1912.04232), doi:10.48550/arXiv.1912.04232.

[48] L. Bottou, On-Line Learning and Stochastic Approximations, Cambridge University Press, USA, 1999.

[49] D. P. Kingma, J. Ba, [Adam: A method for stochastic optimization](#), in: Y. Bengio, Y. LeCun (Eds.), 3rd International Conference on Learning Representations, ICLR 2015, San Diego, CA, USA, May 7-9, 2015, Conference Track Proceedings, 2015.
URL <http://arxiv.org/abs/1412.6980>

[50] M. Tschannen, O. Bachem, M. Lucic, Recent advances in autoencoder-based representation learning, arXiv preprint arXiv:1812.05069 (2018).

[51] R. Iten, T. Metger, H. Wilming, L. del Rio, R. Renner, [Discovering physical concepts with neural networks](#), Phys. Rev. Lett. 124 (2020) 010508. doi:10.1103/PhysRevLett.124.010508.
URL <https://link.aps.org/doi/10.1103/PhysRevLett.124.010508>

[52] S. Ladjal, A. Newson, C.-H. Pham, A pca-like autoencoder, arXiv preprint arXiv:1904.01277 (2019).

[53] L. Wang, [Generative models for physicists](#), 2018.
URL "https://wangleiphy.github.io/lectures/GenerativeModels_PIL.pdf"

[54] D. P. Kingma, M. Welling, Auto-Encoding Variational Bayes, arXiv e-prints (2013) arXiv:1312.6114 [arXiv:1312.6114](https://arxiv.org/abs/1312.6114), doi:10.48550/arXiv.1312.6114.

[55] I. J. Goodfellow, J. Pouget-Abadie, M. Mirza, B. Xu, D. Warde-Farley, S. Ozair, A. Courville, Y. Bengio, Generative Adversarial Networks, arXiv e-prints (2014) arXiv:1406.2661 [arXiv:1406.2661](https://arxiv.org/abs/1406.2661), doi:10.48550/arXiv.1406.2661.

[56] A. Odena, C. Olah, J. Shlens, Conditional Image Synthesis With Auxiliary Classifier GANs, arXiv e-prints (2016) arXiv:1610.09585 [arXiv:1610.09585](https://arxiv.org/abs/1610.09585), doi:10.48550/arXiv.1610.09585.

[57] M. Arjovsky, S. Chintala, L. Bottou, Wasserstein GAN, arXiv e-prints (2017) arXiv:1701.07875 [arXiv:1701.07875](https://arxiv.org/abs/1701.07875), doi:10.48550/arXiv.1701.07875.

[58] I. Gulrajani, F. Ahmed, M. Arjovsky, V. Dumoulin, A. Courville, Improved Training of Wasserstein GANs, arXiv e-prints (2017) arXiv:1704.00028 [arXiv:1704.00028](https://arxiv.org/abs/1704.00028), doi:10.48550/arXiv.1704.00028.

[59] M. Germain, K. Gregor, I. Murray, H. Larochelle, MADE: Masked Autoencoder for Distribution Estimation, arXiv e-prints (2015) arXiv:1502.03509 [arXiv:1502.03509](https://arxiv.org/abs/1502.03509), doi:10.48550/arXiv.1502.03509.

[60] A. van den Oord, N. Kalchbrenner, K. Kavukcuoglu, Pixel Recurrent Neural Networks, arXiv e-prints (2016) arXiv:1601.06759 [arXiv:1601.06759](https://arxiv.org/abs/1601.06759), doi:10.48550/arXiv.1601.06759.

[61] A. van den Oord, N. Kalchbrenner, O. Vinyals, L. Espeholt, A. Graves, K. Kavukcuoglu, Conditional Image Generation with PixelCNN Decoders, arXiv e-prints (2016) arXiv:1606.05328 [arXiv:1606.05328](https://arxiv.org/abs/1606.05328), doi:10.48550/[arXiv.1606.05328](https://doi.org/10.48550/arXiv.1606.05328).

[62] T. Salimans, A. Karpathy, X. Chen, D. P. Kingma, PixelCNN++: Improving the PixelCNN with Discretized Logistic Mixture Likelihood and Other Modifications, arXiv e-prints (2017) arXiv:1701.05517 [arXiv:1701.05517](https://arxiv.org/abs/1701.05517), doi:10.48550/[arXiv.1701.05517](https://doi.org/10.48550/arXiv.1701.05517).

[63] D. Jimenez Rezende, S. Mohamed, Variational Inference with Normalizing Flows, arXiv e-prints (2015) arXiv:1505.05770 [arXiv:1505.05770](https://arxiv.org/abs/1505.05770), doi:10.48550/[arXiv.1505.05770](https://doi.org/10.48550/arXiv.1505.05770).

[64] I. Kobyzev, S. J. D. Prince, M. A. Brubaker, Normalizing Flows: An Introduction and Review of Current Methods, arXiv e-prints (2019) arXiv:1908.09257 [arXiv:1908.09257](https://arxiv.org/abs/1908.09257), doi:10.48550/[arXiv.1908.09257](https://doi.org/10.48550/arXiv.1908.09257).

[65] L. Dinh, D. Krueger, Y. Bengio, NICE: Non-linear Independent Components Estimation, arXiv e-prints (2014) arXiv:1410.8516 [arXiv:1410.8516](https://arxiv.org/abs/1410.8516), doi:10.48550/[arXiv.1410.8516](https://doi.org/10.48550/arXiv.1410.8516).

[66] L. Dinh, J. Sohl-Dickstein, S. Bengio, Density estimation using Real NVP, arXiv e-prints (2016) arXiv:1605.08803 [arXiv:1605.08803](https://arxiv.org/abs/1605.08803), doi:10.48550/[arXiv.1605.08803](https://doi.org/10.48550/arXiv.1605.08803).

[67] M. A. Ahmad, c. Özönder, Physics inspired models in artificial intelligence, in: Proceedings of the 26th ACM SIGKDD International Conference on Knowledge Discovery and Data Mining, KDD '20, Association for Computing Machinery, New York, NY, USA, 2020, p. 3535–3536. doi:10.1145/3394486.3406464.
URL <https://doi.org/10.1145/3394486.3406464>

[68] H. Sompolinsky, et al., Statistical mechanics of neural networks, Physics Today 41 (21) (1988) 70–80.

[69] M. Mezard, A. Montanari, Information, physics, and computation, Oxford University Press, 2009.

[70] G. Carleo, M. Troyer, Solving the quantum many-body problem with artificial neural networks, Science 355 (6325) (2017) 602–606. [arXiv:1606.02318](https://arxiv.org/abs/1606.02318), doi:10.1126/science.aag2302.

[71] J. Carrasquilla, Machine Learning for Quantum Matter, Adv. Phys. X 5 (1) (2020) 1797528. [arXiv:2003.11040](https://arxiv.org/abs/2003.11040), doi:10.1080/23746149.2020.1797528.

[72] Z.-A. Jia, B. Yi, R. Zhai, Y.-C. Wu, G.-C. Guo, G.-P. Guo, Quantum neural network states: A brief review of methods and applications, Advanced Quantum Technologies 2 (7-8) (2019) 1800077. doi:<https://doi.org/10.1002/qute.201800077>.

[73] D. H. Ackley, G. E. Hinton, T. J. Sejnowski, A learning algorithm for boltzmann machines, Cognitive science 9 (1) (1985) 147–169.

[74] A. Fischer, C. Igel, An introduction to restricted boltzmann machines, in: Iberoamerican congress on pattern recognition, Springer, 2012, pp. 14–36.

[75] M. M. Bronstein, J. Bruna, Y. LeCun, A. Szlam, P. Vandergheynst, Geometric Deep Learning: Going beyond Euclidean data, IEEE Sig. Proc. Mag. 34 (4) (2017) 18–42. [arXiv:1611.08097](https://arxiv.org/abs/1611.08097), doi:10.1109/MSP.2017.2693418.

[76] M. M. Bronstein, J. Bruna, T. Cohen, P. Veličković, Geometric Deep Learning: Grids, Groups, Graphs, Geodesics, and Gauges (4 2021). [arXiv:2104.13478](https://arxiv.org/abs/2104.13478).

[77] L. Yang, Z. Zhang, Y. Song, S. Hong, R. Xu, Y. Zhao, Y. Shao, W. Zhang, B. Cui, M.-H. Yang, Diffusion models: A comprehensive survey of methods and applications, arXiv preprint arXiv:2209.00796 (2022).

[78] J. Ho, A. Jain, P. Abbeel, Denoising diffusion probabilistic models, in: Proc. 34th Int. Conf. Neural Inf. Process. Syst., NIPS'20, Curran Associates Inc., pp. 6840–6851.

[79] Y. Song, J. Sohl-Dickstein, D. P. Kingma, A. Kumar, S. Ermon, B. Poole, Score-based generative modeling through stochastic differential equations, in: Int. Conf. Learn. Represent. URL <https://openreview.net/forum?id=PxTIG12RRHS>

[80] M. Mattheakis, P. Protopapas, D. Sondak, M. Di Giovanni, E. Kaxiras, Physical Symmetries Embedded in Neural Networks (4 2019). [arXiv:1904.08991](https://arxiv.org/abs/1904.08991).

[81] P. Kicki, P. Skrzypczyński, M. Ozay, A new approach to design symmetry invariant neural networks, in: 2021 International Joint Conference on Neural Networks (IJCNN), 2021, pp. 1–8. [doi:10.1109/IJCNN52387.2021.9533541](https://doi.org/10.1109/IJCNN52387.2021.9533541).

[82] W. Zhang, J. Tanida, K. Itoh, Y. Ichioka, Shift-invariant pattern recognition neural network and its optical architecture, in: Proceedings of annual conference of the Japan Society of Applied Physics, 1988, pp. 2147–2151.

[83] T. Cohen, M. Welling, Group equivariant convolutional networks, in: M. F. Balcan, K. Q. Weinberger (Eds.), Proceedings of The 33rd International Conference on Machine Learning, Vol. 48 of Proceedings of Machine Learning Research, PMLR, New York, New York, USA, 2016, pp. 2990–2999.

[84] C. R. Qi, H. Su, K. Mo, L. J. Guibas, Pointnet: Deep learning on point sets for 3d classification and segmentation, arXiv preprint arXiv:1612.00593 (2016).

[85] M. Geiger, T. Smidt, e3nn: Euclidean neural networks (2022). [doi:10.48550/ARXIV.2207.09453](https://doi.org/10.48550/ARXIV.2207.09453) URL <https://arxiv.org/abs/2207.09453>

[86] M. S. Albergo, G. Kanwar, P. E. Shanahan, Flow-based generative models for Markov chain Monte Carlo in lattice field theory, Phys. Rev. D 100 (3) (2019) 034515. [doi:10.1103/PhysRevD.100.034515](https://doi.org/10.1103/PhysRevD.100.034515).

[87] G. Kanwar, M. S. Albergo, D. Boyda, K. Cranmer, D. C. Hackett, S. Racanière, D. J. Rezende, P. E. Shanahan, Equivariant flow-based sampling for lattice gauge theory, Phys. Rev. Lett. 125 (12) (2020) 121601. [doi:10.1103/PhysRevLett.125.121601](https://doi.org/10.1103/PhysRevLett.125.121601).

[88] M. S. Albergo, D. Boyda, D. C. Hackett, G. Kanwar, K. Cranmer, S. Racanière, D. J. Rezende, P. E. Shanahan, Introduction to Normalizing Flows for Lattice Field Theory (1 2021). [arXiv:2101.08176](https://arxiv.org/abs/2101.08176).

[89] M. Raissi, P. Perdikaris, G. E. Karniadakis, Physics Informed Deep Learning (Part I): Data-driven Solutions of Nonlinear Partial Differential Equations, J. Comput. Phys. 378 (2019) 686–707. [arXiv:1711.10561](https://arxiv.org/abs/1711.10561), [doi:10.1016/j.jcp.2018.10.045](https://doi.org/10.1016/j.jcp.2018.10.045).

[90] G. E. Karniadakis, I. G. Kevrekidis, L. Lu, P. Perdikaris, S. Wang, L. Yang, Physics-informed machine learning, *Nature Reviews Physics* 3 (6) (2021) 422–440. [doi:10.1038/s42254-021-00314-5](https://doi.org/10.1038/s42254-021-00314-5).

[91] N. Thuerey, P. Holl, M. Mueller, P. Schnell, F. Trost, K. Um, Physics-based Deep Learning, *arXiv e-prints* (2021) arXiv:2109.05237 [arXiv:2109.05237](https://arxiv.org/abs/2109.05237).

[92] I. Arsene, et al., Quark gluon plasma and color glass condensate at RHIC? The Perspective from the BRAHMS experiment, *Nucl. Phys. A* 757 (2005) 1–27. [arXiv:nucl-ex/0410020](https://arxiv.org/abs/nucl-ex/0410020), [doi:10.1016/j.nuclphysa.2005.02.130](https://doi.org/10.1016/j.nuclphysa.2005.02.130).

[93] K. Adcox, et al., Formation of dense partonic matter in relativistic nucleus-nucleus collisions at RHIC: Experimental evaluation by the PHENIX collaboration, *Nucl. Phys. A* 757 (2005) 184–283. [arXiv:nucl-ex/0410003](https://arxiv.org/abs/nucl-ex/0410003), [doi:10.1016/j.nuclphysa.2005.03.086](https://doi.org/10.1016/j.nuclphysa.2005.03.086).

[94] B. B. Back, et al., The PHOBOS perspective on discoveries at RHIC, *Nucl. Phys. A* 757 (2005) 28–101. [arXiv:nucl-ex/0410022](https://arxiv.org/abs/nucl-ex/0410022), [doi:10.1016/j.nuclphysa.2005.03.084](https://doi.org/10.1016/j.nuclphysa.2005.03.084).

[95] J. Adams, et al., Experimental and theoretical challenges in the search for the quark gluon plasma: The STAR Collaboration’s critical assessment of the evidence from RHIC collisions, *Nucl. Phys. A* 757 (2005) 102–183. [arXiv:nucl-ex/0501009](https://arxiv.org/abs/nucl-ex/0501009), [doi:10.1016/j.nuclphysa.2005.03.085](https://doi.org/10.1016/j.nuclphysa.2005.03.085).

[96] J. Schukraft, ALICE results from the first Pb-Pb run at the CERN LHC, *J. Phys. G* 38 (2011) 124003. [arXiv:1106.5620](https://arxiv.org/abs/1106.5620), [doi:10.1088/0954-3899/38/12/124003](https://doi.org/10.1088/0954-3899/38/12/124003).

[97] P. Steinberg, Recent Heavy Ion Results with the ATLAS Detector at the LHC, in: Meeting of the APS Division of Particles and Fields, 2011. [arXiv:1110.3352](https://arxiv.org/abs/1110.3352).

[98] B. Wyslouch, Overview of experimental results in PbPb collisions at $\sqrt{s_{NN}} = 2.76$ TeV by the CMS Collaboration, *J. Phys. G* 38 (2011) 124005. [arXiv:1107.2895](https://arxiv.org/abs/1107.2895), [doi:10.1088/0954-3899/38/12/124005](https://doi.org/10.1088/0954-3899/38/12/124005).

[99] G. Baym, RHIC: From dreams to beams in two decades, *Nucl. Phys. A* 698 (2002) XXIII–XXXII. [arXiv:hep-ph/0104138](https://arxiv.org/abs/hep-ph/0104138), [doi:10.1016/S0375-9474\(01\)01342-2](https://doi.org/10.1016/S0375-9474(01)01342-2).

[100] B. Muller, J. Schukraft, B. Wyslouch, First Results from Pb+Pb collisions at the LHC, *Ann. Rev. Nucl. Part. Sci.* 62 (2012) 361–386. [arXiv:1202.3233](https://arxiv.org/abs/1202.3233), [doi:10.1146/annurev-nucl-102711-094910](https://doi.org/10.1146/annurev-nucl-102711-094910).

[101] P. Braun-Munzinger, V. Koch, T. Schäfer, J. Stachel, Properties of hot and dense matter from relativistic heavy ion collisions, *Phys. Rept.* 621 (2016) 76–126. [arXiv:1510.00442](https://arxiv.org/abs/1510.00442), [doi:10.1016/j.physrep.2015.12.003](https://doi.org/10.1016/j.physrep.2015.12.003).

[102] B. Muller, J. L. Nagle, Results from the relativistic heavy ion collider, *Ann. Rev. Nucl. Part. Sci.* 56 (2006) 93–135. [arXiv:nucl-th/0602029](https://arxiv.org/abs/nucl-th/0602029), [doi:10.1146/annurev.nucl.56.080805.140556](https://doi.org/10.1146/annurev.nucl.56.080805.140556).

[103] J. Adam, et al., Global polarization of Λ hyperons in Au+Au collisions at $\sqrt{s_{NN}} = 200$ GeV, *Phys. Rev. C* 98 (2018) 014910. [arXiv:1805.04400](https://arxiv.org/abs/1805.04400), [doi:10.1103/PhysRevC.98.014910](https://doi.org/10.1103/PhysRevC.98.014910).

[104] B. Müller, A. Schäfer, Chiral magnetic effect and an experimental bound on the late time magnetic field strength, *Phys. Rev. D* 98 (7) (2018) 071902. [arXiv:1806.10907](https://arxiv.org/abs/1806.10907), [doi:10.1103/PhysRevD.98.071902](https://doi.org/10.1103/PhysRevD.98.071902).

[105] L. Adamczyk, et al., Global Λ hyperon polarization in nuclear collisions: evidence for the most vortical fluid, *Nature* 548 (2017) 62–65. [arXiv:1701.06657](https://arxiv.org/abs/1701.06657), [doi:10.1038/nature23004](https://doi.org/10.1038/nature23004).

[106] D. Teaney, J. Lauret, E. V. Shuryak, Flow at the SPS and RHIC as a quark gluon plasma signature, *Phys. Rev. Lett.* 86 (2001) 4783–4786. [arXiv:nucl-th/0011058](https://arxiv.org/abs/nucl-th/0011058), [doi:10.1103/PhysRevLett.86.4783](https://doi.org/10.1103/PhysRevLett.86.4783).

[107] J. Rafelski, B. Muller, Strangeness Production in the Quark - Gluon Plasma, *Phys. Rev. Lett.* 48 (1982) 1066, [Erratum: *Phys. Rev. Lett.* 56, 2334 (1986)]. [doi:10.1103/PhysRevLett.48.1066](https://doi.org/10.1103/PhysRevLett.48.1066).

[108] X.-N. Wang, M. Gyulassy, Gluon shadowing and jet quenching in $A + A$ collisions at $s^{**}(1/2) = 200$ -GeV, *Phys. Rev. Lett.* 68 (1992) 1480–1483. [doi:10.1103/PhysRevLett.68.1480](https://doi.org/10.1103/PhysRevLett.68.1480).

[109] T. Matsui, H. Satz, J/ψ Suppression by Quark-Gluon Plasma Formation, *Phys. Lett. B* 178 (1986) 416–422. [doi:10.1016/0370-2693\(86\)91404-8](https://doi.org/10.1016/0370-2693(86)91404-8).

[110] S. Gupta, X. Luo, B. Mohanty, H. G. Ritter, N. Xu, Scale for the Phase Diagram of Quantum Chromodynamics, *Science* 332 (2011) 1525–1528. [arXiv:1105.3934](https://arxiv.org/abs/1105.3934), [doi:10.1126/science.1204621](https://doi.org/10.1126/science.1204621).

[111] X. Luo, N. Xu, Search for the QCD Critical Point with Fluctuations of Conserved Quantities in Relativistic Heavy-Ion Collisions at RHIC : An Overview, *Nucl. Sci. Tech.* 28 (8) (2017) 112. [arXiv:1701.02105](https://arxiv.org/abs/1701.02105), [doi:10.1007/s41365-017-0257-0](https://doi.org/10.1007/s41365-017-0257-0).

[112] E. V. Shuryak, What RHIC experiments and theory tell us about properties of quark-gluon plasma?, *Nucl. Phys. A* 750 (2005) 64–83. [arXiv:hep-ph/0405066](https://arxiv.org/abs/hep-ph/0405066), [doi:10.1016/j.nuclphysa.2004.10.022](https://doi.org/10.1016/j.nuclphysa.2004.10.022).

[113] A. Bazavov, et al., Equation of state and QCD transition at finite temperature, *Phys. Rev. D* 80 (2009) 014504. [arXiv:0903.4379](https://arxiv.org/abs/0903.4379), [doi:10.1103/PhysRevD.80.014504](https://doi.org/10.1103/PhysRevD.80.014504).

[114] S. Borsanyi, et al., Calculation of the axion mass based on high-temperature lattice quantum chromodynamics, *Nature* 539 (7627) (2016) 69–71. [arXiv:1606.07494](https://arxiv.org/abs/1606.07494), [doi:10.1038/nature20115](https://doi.org/10.1038/nature20115).

[115] J. E. Bernhard, Bayesian parameter estimation for relativistic heavy-ion collisions, Ph.D. thesis, Duke U. (4 2018). [arXiv:1804.06469](https://arxiv.org/abs/1804.06469).

[116] J. E. Bernhard, J. S. Moreland, S. A. Bass, Bayesian estimation of the specific shear and bulk viscosity of quark-gluon plasma, *Nature Phys.* 15 (11) (2019) 1113–1117. [doi:10.1038/s41567-019-0611-8](https://doi.org/10.1038/s41567-019-0611-8).

[117] D. Everett, et al., Phenomenological constraints on the transport properties of QCD matter with data-driven model averaging, *Phys. Rev. Lett.* 126 (24) (2021) 242301. [arXiv:2010.03928](https://arxiv.org/abs/2010.03928), [doi:10.1103/PhysRevLett.126.242301](https://doi.org/10.1103/PhysRevLett.126.242301).

[118] G. Nijs, W. van der Schee, U. Gürsoy, R. Snellings, Transverse Momentum Differential Global Analysis of Heavy-Ion Collisions, *Phys. Rev. Lett.* 126 (20) (2021) 202301. [arXiv:2010.15130](https://arxiv.org/abs/2010.15130), [doi:10.1103/PhysRevLett.126.202301](https://doi.org/10.1103/PhysRevLett.126.202301).

[119] X.-N. Wang, Discovery of jet quenching and beyond, *Nucl. Phys. A* 750 (2005) 98–120. [arXiv:nucl-th/0405017](https://arxiv.org/abs/nucl-th/0405017), [doi:10.1016/j.nuclphysa.2004.12.037](https://doi.org/10.1016/j.nuclphysa.2004.12.037).

[120] I. Vitev, M. Gyulassy, High p_T tomography of $d + \text{Au}$ and $\text{Au} + \text{Au}$ at SPS, RHIC, and LHC, *Phys. Rev. Lett.* 89 (2002) 252301. [arXiv:hep-ph/0209161](https://arxiv.org/abs/hep-ph/0209161), [doi:10.1103/PhysRevLett.89.252301](https://doi.org/10.1103/PhysRevLett.89.252301).

[121] K. M. Burke, et al., Extracting the jet transport coefficient from jet quenching in high-energy heavy-ion collisions, *Phys. Rev. C* 90 (1) (2014) 014909. [arXiv:1312.5003](https://arxiv.org/abs/1312.5003), [doi:10.1103/PhysRevC.90.014909](https://doi.org/10.1103/PhysRevC.90.014909).

[122] A. Beraudo, et al., Extraction of Heavy-Flavor Transport Coefficients in QCD Matter, *Nucl. Phys. A* 979 (2018) 21–86. [arXiv:1803.03824](https://arxiv.org/abs/1803.03824), [doi:10.1016/j.nuclphysa.2018.09.002](https://doi.org/10.1016/j.nuclphysa.2018.09.002).

[123] T. Lappi, Theory overview of Heavy Ion collisions, *PoS LHCP2016* (2016) 016. [arXiv:1609.04917](https://arxiv.org/abs/1609.04917), [doi:10.22323/1.276.0016](https://doi.org/10.22323/1.276.0016).

[124] H. Elfner, B. Müller, The exploration of hot and dense nuclear matter: Introduction to relativistic heavy-ion physics (10 2022). [arXiv:2210.12056](https://arxiv.org/abs/2210.12056).

[125] R. D. Woods, D. S. Saxon, Diffuse Surface Optical Model for Nucleon-Nuclei Scattering, *Phys. Rev.* 95 (1954) 577–578. [doi:10.1103/PhysRev.95.577](https://doi.org/10.1103/PhysRev.95.577).

[126] S. Kahana, H. C. Lee, C. K. Scott, Effect of Woods-Saxon Wave Functions on the Calculation of $A=18$, 206, 210 Spectra with a Realistic Interaction, *Phys. Rev.* 180 (1969) 956–966. [doi:10.1103/PhysRev.180.956](https://doi.org/10.1103/PhysRev.180.956).

[127] L. Wilets, [Shape of the nucleus](#), *Science* 129 (3346) (1959) 361–367.
URL <http://www.jstor.org/stable/1758208>

[128] C. Loizides, J. Kamin, D. d'Enterria, Improved Monte Carlo Glauber predictions at present and future nuclear colliders, *Phys. Rev. C* 97 (5) (2018) 054910, [Erratum: *Phys.Rev.C* 99, 019901 (2019)]. [arXiv:1710.07098](https://arxiv.org/abs/1710.07098), [doi:10.1103/PhysRevC.97.054910](https://doi.org/10.1103/PhysRevC.97.054910).

[129] A. H. Mueller, Small x Behavior and Parton Saturation: A QCD Model, *Nucl. Phys. B* 335 (1990) 115–137. [doi:10.1016/0550-3213\(90\)90173-B](https://doi.org/10.1016/0550-3213(90)90173-B).

[130] L. D. McLerran, R. Venugopalan, Gluon distribution functions for very large nuclei at small transverse momentum, *Phys. Rev. D* 49 (1994) 3352–3355. [arXiv:hep-ph/9311205](https://arxiv.org/abs/hep-ph/9311205), [doi:10.1103/PhysRevD.49.3352](https://doi.org/10.1103/PhysRevD.49.3352).

[131] L. D. McLerran, R. Venugopalan, Computing quark and gluon distribution functions for very large nuclei, *Phys. Rev. D* 49 (1994) 2233–2241. [arXiv:hep-ph/9309289](https://arxiv.org/abs/hep-ph/9309289), [doi:10.1103/PhysRevD.49.2233](https://doi.org/10.1103/PhysRevD.49.2233).

[132] L. D. McLerran, R. Venugopalan, Green's functions in the color field of a large nucleus, *Phys. Rev. D* 50 (1994) 2225–2233. [arXiv:hep-ph/9402335](https://arxiv.org/abs/hep-ph/9402335), [doi:10.1103/PhysRevD.50.2225](https://doi.org/10.1103/PhysRevD.50.2225).

[133] T. Lappi, L. McLerran, Some features of the glasma, *Nucl. Phys. A* 772 (2006) 200–212. [arXiv:hep-ph/0602189](https://arxiv.org/abs/hep-ph/0602189), [doi:10.1016/j.nuclphysa.2006.04.001](https://doi.org/10.1016/j.nuclphysa.2006.04.001).

[134] F. Gelis, E. Iancu, J. Jalilian-Marian, R. Venugopalan, The Color Glass Condensate, *Ann. Rev. Nucl. Part. Sci.* 60 (2010) 463–489. [arXiv:1002.0333](https://arxiv.org/abs/1002.0333), [doi:10.1146/annurev.nucl.010909.083629](https://doi.org/10.1146/annurev.nucl.010909.083629).

[135] B. Schenke, P. Tribedy, R. Venugopalan, Fluctuating Glasma initial conditions and flow in heavy ion collisions, *Phys. Rev. Lett.* 108 (2012) 252301. [arXiv:1202.6646](https://arxiv.org/abs/1202.6646), [doi:10.1103/PhysRevLett.108.252301](https://doi.org/10.1103/PhysRevLett.108.252301).

[136] B. Schenke, P. Tribedy, R. Venugopalan, Event-by-event gluon multiplicity, energy density, and eccentricities in ultrarelativistic heavy-ion collisions, *Phys. Rev. C* 86 (2012) 034908. [arXiv:1206.6805](https://arxiv.org/abs/1206.6805), [doi:10.1103/PhysRevC.86.034908](https://doi.org/10.1103/PhysRevC.86.034908).

[137] J. S. Moreland, J. E. Bernhard, S. A. Bass, Alternative ansatz to wounded nucleon and binary collision scaling in high-energy nuclear collisions, *Phys. Rev. C* 92 (1) (2015) 011901. [arXiv:1412.4708](https://arxiv.org/abs/1412.4708), [doi:10.1103/PhysRevC.92.011901](https://doi.org/10.1103/PhysRevC.92.011901).

[138] Z. Xu, K. Zhou, P. Zhuang, C. Greiner, Thermalization of gluons with Bose-Einstein condensation, *Phys. Rev. Lett.* 114 (18) (2015) 182301. [arXiv:1410.5616](https://arxiv.org/abs/1410.5616), [doi:10.1103/PhysRevLett.114.182301](https://doi.org/10.1103/PhysRevLett.114.182301).

[139] H. Stoecker, et al., Glueballs amass at RHIC and LHC Colliders! - The early quarkless 1st order phase transition at $T = 270$ MeV - from pure Yang-Mills glue plasma to GlueBall-Hagedorn states, *J. Phys. G* 43 (1) (2016) 015105. [arXiv:1509.00160](https://arxiv.org/abs/1509.00160), [doi:10.1088/0954-3899/43/1/015105](https://doi.org/10.1088/0954-3899/43/1/015105).

[140] H. Stocker, et al., Under-saturation of quarks at early stages of relativistic nuclear collisions: The hot glue initial scenario and its observable signatures, *Astron. Nachr.* 336 (8/9) (2015) 744–748. [arXiv:1509.07682](https://arxiv.org/abs/1509.07682), [doi:10.1002/asna.201512252](https://doi.org/10.1002/asna.201512252).

[141] K. Zhou, Z. Xu, P. Zhuang, C. Greiner, Kinetic description of Bose-Einstein condensation with test particle simulations, *Phys. Rev. D* 96 (1) (2017) 014020. [arXiv:1703.02495](https://arxiv.org/abs/1703.02495), [doi:10.1103/PhysRevD.96.014020](https://doi.org/10.1103/PhysRevD.96.014020).

[142] J. E. Bernhard, J. S. Moreland, S. A. Bass, J. Liu, U. Heinz, Applying Bayesian parameter estimation to relativistic heavy-ion collisions: simultaneous characterization of the initial state and quark-gluon plasma medium, *Phys. Rev. C* 94 (2) (2016) 024907. [doi:10.1103/PhysRevC.94.024907](https://doi.org/10.1103/PhysRevC.94.024907).

[143] W. Israel, J. M. Stewart, Transient relativistic thermodynamics and kinetic theory, *Annals Phys.* 118 (1979) 341–372. [doi:10.1016/0003-4916\(79\)90130-1](https://doi.org/10.1016/0003-4916(79)90130-1).

[144] P. F. Kolb, U. W. Heinz, Hydrodynamic description of ultrarelativistic heavy ion collisions (2003) 634–714 [arXiv:nucl-th/0305084](https://arxiv.org/abs/nucl-th/0305084).

[145] A. Muronga, Second order dissipative fluid dynamics for ultrarelativistic nuclear collisions, *Phys. Rev. Lett.* 88 (2002) 062302, [Erratum: *Phys. Rev. Lett.* 89, 159901 (2002)]. [arXiv:nucl-th/0104064](https://arxiv.org/abs/nucl-th/0104064), [doi:10.1103/PhysRevLett.88.062302](https://doi.org/10.1103/PhysRevLett.88.062302).

[146] T. Hirano, U. W. Heinz, D. Kharzeev, R. Lacey, Y. Nara, Hadronic dissipative effects on elliptic flow in ultrarelativistic heavy-ion collisions, *Phys. Lett. B* 636 (2006) 299–304. [arXiv:nucl-th/0511046](https://arxiv.org/abs/nucl-th/0511046), [doi:10.1016/j.physletb.2006.03.060](https://doi.org/10.1016/j.physletb.2006.03.060).

[147] A. K. Chaudhuri, Dissipative hydrodynamics in 2+1 dimension, *Phys. Rev. C* 74 (2006) 044904. [arXiv:nucl-th/0604014](https://arxiv.org/abs/nucl-th/0604014), [doi:10.1103/PhysRevC.74.044904](https://doi.org/10.1103/PhysRevC.74.044904).

[148] P. Romatschke, Causal viscous hydrodynamics for central heavy-ion collisions. II. Meson spectra and HBT radii, *Eur. Phys. J. C* 52 (2007) 203–209. [arXiv:nucl-th/0701032](https://arxiv.org/abs/nucl-th/0701032), [doi:10.1140/epjc/s10052-007-0354-z](https://doi.org/10.1140/epjc/s10052-007-0354-z).

[149] K. Dusling, D. Teaney, Simulating elliptic flow with viscous hydrodynamics, *Phys. Rev. C* 77 (2008) 034905. [arXiv:0710.5932](https://arxiv.org/abs/0710.5932), [doi:10.1103/PhysRevC.77.034905](https://doi.org/10.1103/PhysRevC.77.034905).

[150] H. Song, U. W. Heinz, Causal viscous hydrodynamics in 2+1 dimensions for relativistic heavy-ion collisions, *Phys. Rev. C* 77 (2008) 064901. [arXiv:0712.3715](https://arxiv.org/abs/0712.3715), [doi:10.1103/PhysRevC.77.064901](https://doi.org/10.1103/PhysRevC.77.064901).

[151] L. Du, U. Heinz, (3+1)-dimensional dissipative relativistic fluid dynamics at non-zero net baryon density, *Comput. Phys. Commun.* 251 (2020) 107090. [arXiv:1906.11181](https://arxiv.org/abs/1906.11181), doi:10.1016/j.cpc.2019.107090.

[152] G. Inghirami, L. Del Zanna, A. Beraudo, M. H. Moghaddam, F. Becattini, M. Bleicher, Numerical magnetohydrodynamics for relativistic nuclear collisions, *Eur. Phys. J. C* 76 (12) (2016) 659. [arXiv:1609.03042](https://arxiv.org/abs/1609.03042), doi:10.1140/epjc/s10052-016-4516-8.

[153] K. Okamoto, C. Nonaka, A new relativistic viscous hydrodynamics code and its application to the Kelvin–Helmholtz instability in high-energy heavy-ion collisions, *Eur. Phys. J. C* 77 (6) (2017) 383. [arXiv:1703.01473](https://arxiv.org/abs/1703.01473), doi:10.1140/epjc/s10052-017-4944-0.

[154] G. Nijs, W. van der Schee, Predictions and postdictions for relativistic lead and oxygen collisions with the computational simulation code Trajectum, *Phys. Rev. C* 106 (4) (2022) 044903. [arXiv:2110.13153](https://arxiv.org/abs/2110.13153), doi:10.1103/PhysRevC.106.044903.

[155] W. Florkowski, R. Ryblewski, Highly-anisotropic and strongly-dissipative hydrodynamics for early stages of relativistic heavy-ion collisions, *Phys. Rev. C* 83 (2011) 034907. [arXiv:1007.0130](https://arxiv.org/abs/1007.0130), doi:10.1103/PhysRevC.83.034907.

[156] M. Strickland, Highly anisotropic dissipative hydrodynamics, *AIP Conf. Proc.* 1560 (1) (2013) 658–662. [arXiv:1208.2626](https://arxiv.org/abs/1208.2626), doi:10.1063/1.4826864.

[157] B. Schenke, S. Jeon, C. Gale, (3+1)D hydrodynamic simulation of relativistic heavy-ion collisions, *Phys. Rev. C* 82 (2010) 014903. [arXiv:1004.1408](https://arxiv.org/abs/1004.1408), doi:10.1103/PhysRevC.82.014903.

[158] S. Ryu, J. F. Paquet, C. Shen, G. S. Denicol, B. Schenke, S. Jeon, C. Gale, Importance of the Bulk Viscosity of QCD in Ultrarelativistic Heavy-Ion Collisions, *Phys. Rev. Lett.* 115 (13) (2015) 132301. [arXiv:1502.01675](https://arxiv.org/abs/1502.01675), doi:10.1103/PhysRevLett.115.132301.

[159] C. Shen, B. Schenke, Dynamical initial state model for relativistic heavy-ion collisions, *Phys. Rev. C* 97 (2) (2018) 024907. [arXiv:1710.00881](https://arxiv.org/abs/1710.00881), doi:10.1103/PhysRevC.97.024907.

[160] D. Bazow, U. W. Heinz, M. Strickland, Second-order (2+1)-dimensional anisotropic hydrodynamics, *Phys. Rev. C* 90 (5) (2014) 054910. [arXiv:1311.6720](https://arxiv.org/abs/1311.6720), doi:10.1103/PhysRevC.90.054910.

[161] C. Shen, Z. Qiu, H. Song, J. Bernhard, S. Bass, U. Heinz, The iEBE-VISHNU code package for relativistic heavy-ion collisions, *Comput. Phys. Commun.* 199 (2016) 61–85. [arXiv:1409.8164](https://arxiv.org/abs/1409.8164), doi:10.1016/j.cpc.2015.08.039.

[162] T. Pierog, I. Karpenko, J. M. Katzy, E. Yatsenko, K. Werner, EPOS LHC: Test of collective hadronization with data measured at the CERN Large Hadron Collider, *Phys. Rev. C* 92 (3) (2015) 034906. [arXiv:1306.0121](https://arxiv.org/abs/1306.0121), doi:10.1103/PhysRevC.92.034906.

[163] A. Sakai, K. Murase, T. Hirano, Rapidity decorrelation of anisotropic flow caused by hydrodynamic fluctuations, *Phys. Rev. C* 102 (6) (2020) 064903. [arXiv:2003.13496](https://arxiv.org/abs/2003.13496), doi:10.1103/PhysRevC.102.064903.

[164] I. Karpenko, P. Huovinen, M. Bleicher, A 3+1 dimensional viscous hydrodynamic code for relativistic heavy ion collisions, *Comput. Phys. Commun.* 185 (2014) 3016–3027. [arXiv:1312.4160](https://arxiv.org/abs/1312.4160), doi:10.1016/j.cpc.2014.07.010.

[165] L.-G. Pang, H. Petersen, X.-N. Wang, Pseudorapidity distribution and decorrelation of anisotropic flow within the open-computing-language implementation CLVisc hydrodynamics, *Phys. Rev. C* 97 (6) (2018) 064918. [arXiv:1802.04449](https://arxiv.org/abs/1802.04449), [doi:10.1103/PhysRevC.97.064918](https://doi.org/10.1103/PhysRevC.97.064918).

[166] Y. Yin, J. Liao, Hydrodynamics with chiral anomaly and charge separation in relativistic heavy ion collisions, *Phys. Lett. B* 756 (2016) 42–46. [arXiv:1504.06906](https://arxiv.org/abs/1504.06906), [doi:10.1016/j.physletb.2016.02.065](https://doi.org/10.1016/j.physletb.2016.02.065).

[167] K. Hattori, M. Hongo, X.-G. Huang, New Developments in Relativistic Magnetohydrodynamics, *Symmetry* 14 (9) (2022) 1851. [arXiv:2207.12794](https://arxiv.org/abs/2207.12794), [doi:10.3390/sym14091851](https://doi.org/10.3390/sym14091851).

[168] X. Guo, J. Liao, E. Wang, Spin Hydrodynamic Generation in the Charged Subatomic Swirl, *Sci. Rep.* 10 (1) (2020) 2196. [arXiv:1904.04704](https://arxiv.org/abs/1904.04704), [doi:10.1038/s41598-020-59129-6](https://doi.org/10.1038/s41598-020-59129-6).

[169] S. Shi, C. Gale, S. Jeon, From chiral kinetic theory to relativistic viscous spin hydrodynamics, *Phys. Rev. C* 103 (4) (2021) 044906. [arXiv:2008.08618](https://arxiv.org/abs/2008.08618), [doi:10.1103/PhysRevC.103.044906](https://doi.org/10.1103/PhysRevC.103.044906).

[170] M. Bleicher, et al., Relativistic hadron hadron collisions in the ultrarelativistic quantum molecular dynamics model, *J. Phys. G* 25 (1999) 1859–1896. [arXiv:hep-ph/9909407](https://arxiv.org/abs/hep-ph/9909407), [doi:10.1088/0954-3899/25/9/308](https://doi.org/10.1088/0954-3899/25/9/308).

[171] J. Weil, et al., Particle production and equilibrium properties within a new hadron transport approach for heavy-ion collisions, *Phys. Rev. C* 94 (5) (2016) 054905. [arXiv:1606.06642](https://arxiv.org/abs/1606.06642), [doi:10.1103/PhysRevC.94.054905](https://doi.org/10.1103/PhysRevC.94.054905).

[172] M. Gyulassy, X.-n. Wang, Multiple collisions and induced gluon Bremsstrahlung in QCD, *Nucl. Phys. B* 420 (1994) 583–614. [arXiv:nucl-th/9306003](https://arxiv.org/abs/nucl-th/9306003), [doi:10.1016/0550-3213\(94\)90079-5](https://doi.org/10.1016/0550-3213(94)90079-5).

[173] X.-N. Wang, M. Gyulassy, M. Plumer, The LPM effect in QCD and radiative energy loss in a quark gluon plasma, *Phys. Rev. D* 51 (1995) 3436–3446. [arXiv:hep-ph/9408344](https://arxiv.org/abs/hep-ph/9408344), [doi:10.1103/PhysRevD.51.3436](https://doi.org/10.1103/PhysRevD.51.3436).

[174] R. Baier, Y. L. Dokshitzer, A. H. Mueller, S. Peigne, D. Schiff, Radiative energy loss and p(T) broadening of high-energy partons in nuclei, *Nucl. Phys. B* 484 (1997) 265–282. [arXiv:hep-ph/9608322](https://arxiv.org/abs/hep-ph/9608322), [doi:10.1016/S0550-3213\(96\)00581-0](https://doi.org/10.1016/S0550-3213(96)00581-0).

[175] R. Baier, Y. L. Dokshitzer, S. Peigne, D. Schiff, Induced gluon radiation in a QCD medium, *Phys. Lett. B* 345 (1995) 277–286. [arXiv:hep-ph/9411409](https://arxiv.org/abs/hep-ph/9411409), [doi:10.1016/0370-2693\(94\)01617-L](https://doi.org/10.1016/0370-2693(94)01617-L).

[176] R. Baier, Y. L. Dokshitzer, A. H. Mueller, S. Peigne, D. Schiff, Radiative energy loss of high-energy quarks and gluons in a finite volume quark - gluon plasma, *Nucl. Phys. B* 483 (1997) 291–320. [arXiv:hep-ph/9607355](https://arxiv.org/abs/hep-ph/9607355), [doi:10.1016/S0550-3213\(96\)00553-6](https://doi.org/10.1016/S0550-3213(96)00553-6).

[177] B. G. Zakharov, Fully quantum treatment of the Landau-Pomeranchuk-Migdal effect in QED and QCD, *JETP Lett.* 63 (1996) 952–957. [arXiv:hep-ph/9607440](https://arxiv.org/abs/hep-ph/9607440), [doi:10.1134/1.567126](https://doi.org/10.1134/1.567126).

[178] U. A. Wiedemann, Gluon radiation off hard quarks in a nuclear environment: Opacity expansion, *Nucl. Phys. B* 588 (2000) 303–344. [arXiv:hep-ph/0005129](https://arxiv.org/abs/hep-ph/0005129), [doi:10.1016/S0550-3213\(00\)00457-0](https://doi.org/10.1016/S0550-3213(00)00457-0).

[179] X.-f. Guo, X.-N. Wang, Multiple scattering, parton energy loss and modified fragmentation functions in deeply inelastic e A scattering, *Phys. Rev. Lett.* 85 (2000) 3591–3594. [arXiv:hep-ph/0005044](https://arxiv.org/abs/hep-ph/0005044), [doi:10.1103/PhysRevLett.85.3591](https://doi.org/10.1103/PhysRevLett.85.3591).

[180] X.-N. Wang, X.-f. Guo, Multiple parton scattering in nuclei: Parton energy loss, *Nucl. Phys. A* 696 (2001) 788–832. [arXiv:hep-ph/0102230](https://arxiv.org/abs/hep-ph/0102230), doi:10.1016/S0375-9474(01)01130-7.

[181] B.-W. Zhang, X.-N. Wang, Multiple parton scattering in nuclei: Beyond helicity amplitude approximation, *Nucl. Phys. A* 720 (2003) 429–451. [arXiv:hep-ph/0301195](https://arxiv.org/abs/hep-ph/0301195), doi:10.1016/S0375-9474(03)01003-0.

[182] A. Schafer, X.-N. Wang, B.-W. Zhang, Multiple Parton Scattering in Nuclei: Quark-quark Scattering, *Nucl. Phys. A* 793 (2007) 128–170. [arXiv:0704.0106](https://arxiv.org/abs/0704.0106), doi:10.1016/j.nuclphysa.2007.06.009.

[183] Y. He, T. Luo, X.-N. Wang, Y. Zhu, Linear Boltzmann Transport for Jet Propagation in the Quark-Gluon Plasma: Elastic Processes and Medium Recoil, *Phys. Rev. C* 91 (2015) 054908, [Erratum: *Phys. Rev. C* 97, 019902 (2018)]. [arXiv:1503.03313](https://arxiv.org/abs/1503.03313), doi:10.1103/PhysRevC.91.054908.

[184] S. Cao, T. Luo, G.-Y. Qin, X.-N. Wang, Linearized Boltzmann transport model for jet propagation in the quark-gluon plasma: Heavy quark evolution, *Phys. Rev. C* 94 (1) (2016) 014909. [arXiv:1605.06447](https://arxiv.org/abs/1605.06447), doi:10.1103/PhysRevC.94.014909.

[185] J. Casalderrey-Solana, D. C. Gulhan, J. G. Milhano, D. Pablos, K. Rajagopal, A Hybrid Strong/Weak Coupling Approach to Jet Quenching, *JHEP* 10 (2014) 019, [Erratum: *JHEP* 09, 175 (2015)]. [arXiv:1405.3864](https://arxiv.org/abs/1405.3864), doi:10.1007/JHEP09(2015)175.

[186] S. Shi, J. Liao, M. Gyulassy, Global constraints from RHIC and LHC on transport properties of QCD fluids in CUJET/CIBJET framework, *Chin. Phys. C* 43 (4) (2019) 044101. [arXiv:1808.05461](https://arxiv.org/abs/1808.05461), doi:10.1088/1674-1137/43/4/044101.

[187] S. Cao, X.-N. Wang, Jet quenching and medium response in high-energy heavy-ion collisions: a review, *Rept. Prog. Phys.* 84 (2) (2021) 024301. [arXiv:2002.04028](https://arxiv.org/abs/2002.04028), doi:10.1088/1361-6633/abc22b.

[188] G.-Y. Qin, X.-N. Wang, Jet quenching in high-energy heavy-ion collisions, *Int. J. Mod. Phys. E* 24 (11) (2015) 1530014. [arXiv:1511.00790](https://arxiv.org/abs/1511.00790), doi:10.1142/S0218301315300143.

[189] A. Majumder, M. Van Leeuwen, The Theory and Phenomenology of Perturbative QCD Based Jet Quenching, *Prog. Part. Nucl. Phys.* 66 (2011) 41–92. [arXiv:1002.2206](https://arxiv.org/abs/1002.2206), doi:10.1016/j.ppnp.2010.09.001.

[190] N. Armesto, et al., Comparison of Jet Quenching Formalisms for a Quark-Gluon Plasma 'Brick', *Phys. Rev. C* 86 (2012) 064904. [arXiv:1106.1106](https://arxiv.org/abs/1106.1106), doi:10.1103/PhysRevC.86.064904.

[191] G.-Y. Qin, J. Ruppert, C. Gale, S. Jeon, G. D. Moore, Jet energy loss, photon production, and photon-hadron correlations at RHIC, *Phys. Rev. C* 80 (2009) 054909. [arXiv:0906.3280](https://arxiv.org/abs/0906.3280), doi:10.1103/PhysRevC.80.054909.

[192] S. Jeon, G. D. Moore, Energy loss of leading partons in a thermal QCD medium, *Phys. Rev. C* 71 (2005) 034901. [arXiv:hep-ph/0309332](https://arxiv.org/abs/hep-ph/0309332), doi:10.1103/PhysRevC.71.034901.

[193] J. Noronha-Hostler, B. Betz, J. Noronha, M. Gyulassy, Event-by-event hydrodynamics + jet energy loss: A solution to the $R_{AA} \otimes v_2$ puzzle, *Phys. Rev. Lett.* 116 (25) (2016) 252301. [arXiv:1602.03788](https://arxiv.org/abs/1602.03788), doi:10.1103/PhysRevLett.116.252301.

[194] C. Andrés, N. Armesto, M. Luzum, C. A. Salgado, P. Zurita, Energy versus centrality dependence of the jet quenching parameter \hat{q} at RHIC and LHC: a new puzzle?, *Eur. Phys. J. C* 76 (9) (2016) 475. [arXiv:1606.04837](https://arxiv.org/abs/1606.04837), [doi:10.1140/epjc/s10052-016-4320-5](https://doi.org/10.1140/epjc/s10052-016-4320-5).

[195] E. Bianchi, J. Elledge, A. Kumar, A. Majumder, G.-Y. Qin, C. Shen, The x and Q^2 dependence of \hat{q} , quasi-particles and the JET puzzle (2 2017). [arXiv:1702.00481](https://arxiv.org/abs/1702.00481).

[196] Y.-T. Chien, A. Emerman, Z.-B. Kang, G. Ovanesyan, I. Vitev, Jet Quenching from QCD Evolution, *Phys. Rev. D* 93 (7) (2016) 074030. [arXiv:1509.02936](https://arxiv.org/abs/1509.02936), [doi:10.1103/PhysRevD.93.074030](https://doi.org/10.1103/PhysRevD.93.074030).

[197] C. Andres, N. Armesto, H. Niemi, R. Paatelainen, C. A. Salgado, Jet quenching as a probe of the initial stages in heavy-ion collisions, *Phys. Lett. B* 803 (2020) 135318. [arXiv:1902.03231](https://arxiv.org/abs/1902.03231), [doi:10.1016/j.physletb.2020.135318](https://doi.org/10.1016/j.physletb.2020.135318).

[198] R. M. Yazdi, S. Shi, C. Gale, S. Jeon, Leading order, next-to-leading order, and nonperturbative parton collision kernels: Effects in static and evolving media, *Phys. Rev. C* 106 (6) (2022) 064902. [arXiv:2206.05855](https://arxiv.org/abs/2206.05855), [doi:10.1103/PhysRevC.106.064902](https://doi.org/10.1103/PhysRevC.106.064902).

[199] S. Shi, R. Modarresi Yazdi, C. Gale, S. Jeon, Comparing the MARTINI and CUJET models for jet-quenching: I. medium modification of jets and jet substructure (12 2022). [arXiv:2212.05944](https://arxiv.org/abs/2212.05944).

[200] T. Sjöstrand, The PYTHIA Event Generator: Past, Present and Future, *Comput. Phys. Commun.* 246 (2020) 106910. [arXiv:1907.09874](https://arxiv.org/abs/1907.09874), [doi:10.1016/j.cpc.2019.106910](https://doi.org/10.1016/j.cpc.2019.106910).

[201] S. Cao, et al., Multistage Monte-Carlo simulation of jet modification in a static medium, *Phys. Rev. C* 96 (2) (2017) 024909. [arXiv:1705.00050](https://arxiv.org/abs/1705.00050), [doi:10.1103/PhysRevC.96.024909](https://doi.org/10.1103/PhysRevC.96.024909).

[202] M. Kordell, A. Majumder, Event-by-Event Simulations of Jet Modification Using the MATTER Event Generator, in: 8th International Conference on Hard and Electromagnetic Probes of High-energy Nuclear Collisions: Hard Probes 2016, 2017. [arXiv:1702.05862](https://arxiv.org/abs/1702.05862).

[203] B. Schenke, C. Gale, S. Jeon, MARTINI: An Event generator for relativistic heavy-ion collisions, *Phys. Rev. C* 80 (2009) 054913. [arXiv:0909.2037](https://arxiv.org/abs/0909.2037), [doi:10.1103/PhysRevC.80.054913](https://doi.org/10.1103/PhysRevC.80.054913).

[204] D. Pablos, Jet quenching with strong coupling, *Nucl. Phys. A* 967 (2017) 169–176. [doi:10.1016/j.nuclphysa.2017.04.040](https://doi.org/10.1016/j.nuclphysa.2017.04.040).

[205] S. A. Bass, J. Bernhard, J. S. Moreland, [Determination of quark-gluon-plasma parameters from a global Bayesian analysis](#), *Nucl. Phys. A* 967 (2017) 67–73, the 26th International Conference on Ultra-relativistic Nucleus-Nucleus Collisions: Quark Matter 2017. [doi:10.1016/j.nuclphysa.2017.05.052](https://doi.org/10.1016/j.nuclphysa.2017.05.052).
URL <https://www.sciencedirect.com/science/article/pii/S0375947417301690>

[206] L.-G. Pang, K. Zhou, N. Su, H. Petersen, H. Stöcker, X.-N. Wang, An equation-of-state-meter of quantum chromodynamics transition from deep learning, *Nature Commun.* 9 (1) (2018) 210. [doi:10.1038/s41467-017-02726-3](https://doi.org/10.1038/s41467-017-02726-3).

[207] J. Steinheimer, L. Pang, K. Zhou, V. Koch, J. Randrup, H. Stoecker, A machine learning study to identify spinodal clumping in high energy nuclear collisions, *JHEP* 12 (2019) 122. [doi:10.1007/JHEP12\(2019\)122](https://doi.org/10.1007/JHEP12(2019)122).

[208] J. He, W.-B. He, Y.-G. Ma, S. Zhang, Machine-learning-based identification for initial clustering structure in relativistic heavy-ion collisions (9 2021). [arXiv:2109.06277](https://arxiv.org/abs/2109.06277).

[209] M. L. Miller, K. Reygers, S. J. Sanders, P. Steinberg, Glauber modeling in high energy nuclear collisions, *Ann. Rev. Nucl. Part. Sci.* 57 (2007) 205–243. [arXiv:nucl-ex/0701025](https://arxiv.org/abs/nucl-ex/0701025), doi:10.1146/annurev.nucl.57.090506.123020.

[210] S. Kagamaster, R. Reed, M. Lisa, Centrality determination with a forward detector in the RHIC Beam Energy Scan, *Phys. Rev. C* 103 (4) (2021) 044902. [arXiv:2009.01483](https://arxiv.org/abs/2009.01483), doi:10.1103/PhysRevC.103.044902.

[211] C. David, M. Freslier, J. Aichelin, Impact parameter determination for heavy-ion collisions by use of a neural network, *Phys. Rev. C* 51 (1995) 1453–1459. doi:10.1103/PhysRevC.51.1453.

[212] F. Haddad, K. Hagel, J. Li, N. Mdeiwayeh, J. B. Natowitz, R. Wada, B. Xiao, C. David, M. Freslier, J. Aichelin, Impact parameter determination in experimental analysis using neural network, *Phys. Rev. C* 55 (1997) 1371–1375. doi:10.1103/PhysRevC.55.1371.

[213] J. D. Sanctis, M. Masotti, M. Bruno, M. D’Agostino, E. Geraci, G. Vannini, A. Bonasera, [Classification of the impact parameter in nucleus–nucleus collisions by a support vector machine method](#), *Journal of Physics G: Nuclear and Particle Physics* 36 (1) (2008) 015101. doi:10.1088/0954-3899/36/1/015101.
URL <https://dx.doi.org/10.1088/0954-3899/36/1/015101>

[214] L. Li, X. Chen, Y. Cui, Z. Li, Y. Zhang, Fluctuation mechanism and reconstruction of impact parameter distributions with two-observables for intermediate energy heavy ion collisions (1 2022). [arXiv:2201.12586](https://arxiv.org/abs/2201.12586).

[215] F. Li, Y. Wang, H. Lü, P. Li, Q. Li, F. Liu, Application of artificial intelligence in the determination of impact parameter in heavy-ion collisions at intermediate energies, *J. Phys. G* 47 (11) (2020) 115104. [arXiv:2008.11540](https://arxiv.org/abs/2008.11540), doi:10.1088/1361-6471/abb1f9.

[216] F. Li, Y. Wang, Z. Gao, P. Li, H. Lü, H. Lv, Q. Li, C. Y. Tsang, M. B. Tsang, Application of machine learning in the determination of impact parameter in the $^{132}\text{Sn} + ^{124}\text{Sn}$ system, *Phys. Rev. C* 104 (3) (2021) 034608. [arXiv:2105.08912](https://arxiv.org/abs/2105.08912), doi:10.1103/PhysRevC.104.034608.

[217] X. Zhang, et al., Determining impact parameters of heavy-ion collisions at low-intermediate incident energies using deep learning with convolutional neural networks, *Phys. Rev. C* 105 (3) (2022) 034611. [arXiv:2111.06597](https://arxiv.org/abs/2111.06597), doi:10.1103/PhysRevC.105.034611.

[218] C. Y. Tsang, et al., Applying machine learning to determine impact parameter in nuclear physics experiments (7 2021). [arXiv:2107.13985](https://arxiv.org/abs/2107.13985).

[219] P. Xiang, Y.-S. Zhao, X.-G. Huang, Determination of the impact parameter in high-energy heavy-ion collisions via deep learning *, *Chin. Phys. C* 46 (7) (2022) 074110. [arXiv:2112.03824](https://arxiv.org/abs/2112.03824), doi:10.1088/1674-1137/ac6490.

[220] N. Mallick, S. Tripathy, A. N. Mishra, S. Deb, R. Sahoo, Estimation of Impact Parameter and Transverse Spherocity in heavy-ion collisions at the LHC energies using Machine Learning (3 2021). [arXiv:2103.01736](https://arxiv.org/abs/2103.01736).

[221] A. Saha, D. Dan, S. Sanyal, Machine-learning model-driven prediction of the initial geometry in heavy-ion collision experiments, *Phys. Rev. C* 106 (1) (2022) 014901. [arXiv:2203.15433](https://arxiv.org/abs/2203.15433), doi:10.1103/PhysRevC.106.014901.

[222] M. Omana Kuttan, J. Steinheimer, K. Zhou, A. Redelbach, H. Stoecker, A fast centrality-meter for heavy-ion collisions at the CBM experiment, *Phys. Lett. B* 811 (2020) 135872. [arXiv:2009.01584](https://arxiv.org/abs/2009.01584), [doi:10.1016/j.physletb.2020.135872](https://doi.org/10.1016/j.physletb.2020.135872).

[223] M. Omana Kuttan, J. Steinheimer, K. Zhou, A. Redelbach, H. Stoecker, Deep Learning Based Impact Parameter Determination for the CBM Experiment, *Particles* 4 (1) (2021) 47–52. [doi:10.3390/particles4010006](https://doi.org/10.3390/particles4010006).

[224] A. Bzdak, V. Koch, D. Oliinychenko, J. Steinheimer, Large proton cumulants from the superposition of ordinary multiplicity distributions, *Phys. Rev. C* 98 (5) (2018) 054901. [arXiv:1804.04463](https://arxiv.org/abs/1804.04463), [doi:10.1103/PhysRevC.98.054901](https://doi.org/10.1103/PhysRevC.98.054901).

[225] X. Luo, Energy Dependence of Moments of Net-Proton and Net-Charge Multiplicity Distributions at STAR, *PoS CPOD2014* (2015) 019. [arXiv:1503.02558](https://arxiv.org/abs/1503.02558), [doi:10.22323/1.217.0019](https://doi.org/10.22323/1.217.0019).

[226] P. Thaprasop, K. Zhou, J. Steinheimer, C. Herold, Unsupervised Outlier Detection in Heavy-Ion Collisions, *Phys. Scripta* 96 (6) (2021) 064003. [arXiv:2007.15830](https://arxiv.org/abs/2007.15830), [doi:10.1088/1402-4896/abf214](https://doi.org/10.1088/1402-4896/abf214).

[227] B. Bally, et al., Imaging the initial condition of heavy-ion collisions and nuclear structure across the nuclide chart (9 2022). [arXiv:2209.11042](https://arxiv.org/abs/2209.11042).

[228] D. Adhikari, et al., Accurate Determination of the Neutron Skin Thickness of ^{208}Pb through Parity-Violation in Electron Scattering, *Phys. Rev. Lett.* 126 (17) (2021) 172502. [arXiv:2102.10767](https://arxiv.org/abs/2102.10767), [doi:10.1103/PhysRevLett.126.172502](https://doi.org/10.1103/PhysRevLett.126.172502).

[229] L.-G. Pang, K. Zhou, X.-N. Wang, Interpretable deep learning for nuclear deformation in heavy ion collisions (6 2019). [arXiv:1906.06429](https://arxiv.org/abs/1906.06429).

[230] S. Bailey, T. Kokalova, M. Freer, C. Wheldon, R. Smith, J. Walshe, N. Soić, L. Prepolec, V. Tokić, F. M. Marqués, L. Achouri, F. Delaunay, M. Parlog, Q. Deshayes, B. Fernández-Dominguez, B. Jacquot, The identification of α -clustered doorway states in $^{44,48,52}\text{Ti}$ using machine learning, *Eur. Phys. J. A* 57 (3) (2021) 108. [doi:10.1140/epja/s10050-021-00357-3](https://doi.org/10.1140/epja/s10050-021-00357-3).
URL <https://doi.org/10.1140/epja/s10050-021-00357-3>

[231] J. Jia, C.-J. Zhang, Scaling approach to nuclear structure in high-energy heavy-ion collisions (11 2021). [arXiv:2111.15559](https://arxiv.org/abs/2111.15559).

[232] Y.-L. Cheng, S. Shi, Y.-G. Ma, H. Stöcker, K. Zhou, How does Bayesian analysis infer the nucleon distributions in isobar collisions? (1 2023). [arXiv:2301.03910](https://arxiv.org/abs/2301.03910).

[233] S. Pratt, E. Sangaline, P. Sorensen, H. Wang, Constraining the Eq. of State of Super-Hadronic Matter from Heavy-Ion Collisions, *Phys. Rev. Lett.* 114 (2015) 202301. [doi:10.1103/PhysRevLett.114.202301](https://doi.org/10.1103/PhysRevLett.114.202301).

[234] M. Omana Kuttan, J. Steinheimer, K. Zhou, H. Stöcker, The QCD EoS of dense nuclear matter from Bayesian analysis of heavy ion collision data (11 2022). [arXiv:2211.11670](https://arxiv.org/abs/2211.11670).

[235] L.-G. Pang, K. Zhou, N. Su, H. Petersen, H. Stöcker, X.-N. Wang, Classify QCD phase transition with deep learning, *Nucl. Phys. A* 982 (2019) 867–870. [doi:10.1016/j.nuclphysa.2018.10.077](https://doi.org/10.1016/j.nuclphysa.2018.10.077).

[236] K. Zhou, L.-G. Pang, N. Su, H. Petersen, H. Stoecker, X.-N. Wang, Identifying QCD Transition Using Deep Learning, EPJ Web Conf. 171 (2018) 16005. [doi:10.1051/epjconf/201817116005](https://doi.org/10.1051/epjconf/201817116005).

[237] Y.-L. Du, K. Zhou, J. Steinheimer, L.-G. Pang, A. Motornenko, H.-S. Zong, X.-N. Wang, H. Stöcker, Identifying the nature of the QCD transition in relativistic collision of heavy nuclei with deep learning, Eur. Phys. J. C 80 (6) (2020) 516. [arXiv:1910.11530](https://arxiv.org/abs/1910.11530), [doi:10.1140/epjc/s10052-020-8030-7](https://doi.org/10.1140/epjc/s10052-020-8030-7).

[238] Y.-L. Du, K. Zhou, J. Steinheimer, L.-G. Pang, A. Motornenko, H.-S. Zong, X.-N. Wang, H. Stöcker, Identifying the nature of the QCD transition in heavy-ion collisions with deep learning, Nucl. Phys. A 1005 (2021) 121891. [arXiv:2009.03059](https://arxiv.org/abs/2009.03059), [doi:10.1016/j.nuclphysa.2020.121891](https://doi.org/10.1016/j.nuclphysa.2020.121891).

[239] L. Jiang, L. Wang, K. Zhou, Deep learning stochastic processes with QCD phase transition, Phys. Rev. D 103 (11) (2021) 116023. [arXiv:2103.04090](https://arxiv.org/abs/2103.04090), [doi:10.1103/PhysRevD.103.116023](https://doi.org/10.1103/PhysRevD.103.116023).

[240] L. Wang, L. Jiang, K. Zhou, Learning Langevin dynamics with QCD phase transition, EPJ Web Conf. 259 (2022) 10017. [arXiv:2108.03987](https://arxiv.org/abs/2108.03987), [doi:10.1051/epjconf/202225910017](https://doi.org/10.1051/epjconf/202225910017).

[241] M. Nahrgang, S. Leupold, C. Herold, M. Bleicher, Nonequilibrium chiral fluid dynamics including dissipation and noise, Phys. Rev. C 84 (2011) 024912. [arXiv:1105.0622](https://arxiv.org/abs/1105.0622), [doi:10.1103/PhysRevC.84.024912](https://doi.org/10.1103/PhysRevC.84.024912).

[242] Y. Kvasiuk, E. Zabrodin, L. Bravina, I. Didur, M. Frolov, Classification of Equation of State in Relativistic Heavy-Ion Collisions Using Deep Learning, JHEP 07 (2020) 133. [arXiv:2004.14409](https://arxiv.org/abs/2004.14409), [doi:10.1007/JHEP07\(2020\)133](https://doi.org/10.1007/JHEP07(2020)133).

[243] F. Sergeev, E. Bratkovskaya, I. Kisel, I. Vassiliev, Deep learning for quark-gluon plasma detection in the CBM experiment, Int. J. Mod. Phys. A 35 (33) (2020) 2043002. [doi:10.1142/S0217751X20430022](https://doi.org/10.1142/S0217751X20430022).

[244] R. Wang, Y.-G. Ma, R. Wada, L.-W. Chen, W.-B. He, H.-L. Liu, K.-J. Sun, Nuclear liquid-gas phase transition with machine learning, Phys. Rev. Res. 2 (4) (2020) 043202. [arXiv:2010.15043](https://arxiv.org/abs/2010.15043), [doi:10.1103/PhysRevResearch.2.043202](https://doi.org/10.1103/PhysRevResearch.2.043202).

[245] Y. Wang, F. Li, Q. Li, H. Lü, K. Zhou, Finding signatures of the nuclear symmetry energy in heavy-ion collisions with deep learning, Phys. Lett. B 822 (2021) 136669. [arXiv:2107.11012](https://arxiv.org/abs/2107.11012), [doi:10.1016/j.physletb.2021.136669](https://doi.org/10.1016/j.physletb.2021.136669).

[246] M. Omana Kuttan, K. Zhou, J. Steinheimer, A. Redelbach, H. Stoecker, An equation-of-state-meter for CBM using PointNet, JHEP 21 (2020) 184. [arXiv:2107.05590](https://arxiv.org/abs/2107.05590), [doi:10.1007/JHEP10\(2021\)184](https://doi.org/10.1007/JHEP10(2021)184).

[247] Y. Huang, L.-G. Pang, X. Luo, X.-N. Wang, Probing criticality with deep learning in relativistic heavy-ion collisions, Phys. Lett. B 827 (2022) 137001. [arXiv:2107.11828](https://arxiv.org/abs/2107.11828), [doi:10.1016/j.physletb.2022.137001](https://doi.org/10.1016/j.physletb.2022.137001).

[248] B. Settles, Active learning literature survey, 2009.

[249] D. Mroczek, M. Hjorth-Jensen, J. Noronha-Hostler, P. Parotto, C. Ratti, R. Vilalta, [Mapping out the thermodynamic stability of a qcd equation of state with a critical point using active learning](#) (2022). [doi:10.48550/ARXIV.2203.13876](https://doi.org/10.48550/ARXIV.2203.13876).
URL <https://arxiv.org/abs/2203.13876>

[250] X. An, et al., The BEST framework for the search for the QCD critical point and the chiral magnetic effect, Nucl. Phys. A 1017 (2022) 122343. [arXiv:2108.13867](https://arxiv.org/abs/2108.13867), [doi:10.1016/j.nuclphysa.2021.122343](https://doi.org/10.1016/j.nuclphysa.2021.122343).

[251] U. W. Heinz, H. Song, A. K. Chaudhuri, Dissipative hydrodynamics for viscous relativistic fluids, *Phys. Rev. C* 73 (2006) 034904. [arXiv:nucl-th/0510014](https://arxiv.org/abs/nucl-th/0510014), [doi:10.1103/PhysRevC.73.034904](https://doi.org/10.1103/PhysRevC.73.034904).

[252] P. Romatschke, U. Romatschke, Viscosity Information from Relativistic Nuclear Collisions: How Perfect is the Fluid Observed at RHIC?, *Phys. Rev. Lett.* 99 (2007) 172301. [arXiv:0706.1522](https://arxiv.org/abs/0706.1522), [doi:10.1103/PhysRevLett.99.172301](https://doi.org/10.1103/PhysRevLett.99.172301).

[253] H. Song, S. A. Bass, U. Heinz, T. Hirano, C. Shen, 200 A GeV Au+Au collisions serve a nearly perfect quark-gluon liquid, *Phys. Rev. Lett.* 106 (2011) 192301, [Erratum: *Phys. Rev. Lett.* 109, 139904 (2012)]. [arXiv:1011.2783](https://arxiv.org/abs/1011.2783), [doi:10.1103/PhysRevLett.106.192301](https://doi.org/10.1103/PhysRevLett.106.192301).

[254] A. Buchel, J. T. Liu, Universality of the shear viscosity in supergravity, *Phys. Rev. Lett.* 93 (2004) 090602. [arXiv:hep-th/0311175](https://arxiv.org/abs/hep-th/0311175), [doi:10.1103/PhysRevLett.93.090602](https://doi.org/10.1103/PhysRevLett.93.090602).

[255] D. Teaney, The Effects of viscosity on spectra, elliptic flow, and HBT radii, *Phys. Rev. C* 68 (2003) 034913. [arXiv:nucl-th/0301099](https://arxiv.org/abs/nucl-th/0301099), [doi:10.1103/PhysRevC.68.034913](https://doi.org/10.1103/PhysRevC.68.034913).

[256] H. Niemi, K. J. Eskola, R. Paatelainen, Event-by-event fluctuations in a perturbative QCD + saturation + hydrodynamics model: Determining QCD matter shear viscosity in ultrarelativistic heavy-ion collisions, *Phys. Rev. C* 93 (2) (2016) 024907. [arXiv:1505.02677](https://arxiv.org/abs/1505.02677), [doi:10.1103/PhysRevC.93.024907](https://doi.org/10.1103/PhysRevC.93.024907).

[257] C. Gale, S. Jeon, B. Schenke, P. Tribedy, R. Venugopalan, Event-by-event anisotropic flow in heavy-ion collisions from combined Yang-Mills and viscous fluid dynamics, *Phys. Rev. Lett.* 110 (1) (2013) 012302. [arXiv:1209.6330](https://arxiv.org/abs/1209.6330), [doi:10.1103/PhysRevLett.110.012302](https://doi.org/10.1103/PhysRevLett.110.012302).

[258] H. Song, S. Bass, U. W. Heinz, Spectra and elliptic flow for identified hadrons in 2.76A TeV Pb + Pb collisions, *Phys. Rev. C* 89 (3) (2014) 034919. [arXiv:1311.0157](https://arxiv.org/abs/1311.0157), [doi:10.1103/PhysRevC.89.034919](https://doi.org/10.1103/PhysRevC.89.034919).

[259] J. Novak, K. Novak, S. Pratt, J. Vredevoogd, C. Coleman-Smith, R. Wolpert, Determining Fundamental Properties of Matter Created in Ultrarelativistic Heavy-Ion Collisions, *Phys. Rev. C* 89 (3) (2014) 034917. [arXiv:1303.5769](https://arxiv.org/abs/1303.5769), [doi:10.1103/PhysRevC.89.034917](https://doi.org/10.1103/PhysRevC.89.034917).

[260] D. Everett, et al., Multisystem Bayesian constraints on the transport coefficients of QCD matter, *Phys. Rev. C* 103 (5) (2021) 054904. [arXiv:2011.01430](https://arxiv.org/abs/2011.01430), [doi:10.1103/PhysRevC.103.054904](https://doi.org/10.1103/PhysRevC.103.054904).

[261] G. Nijs, W. van der Schee, U. Gürsoy, R. Snellings, Bayesian analysis of heavy ion collisions with the heavy ion computational framework Trajectum, *Phys. Rev. C* 103 (5) (2021) 054909. [arXiv:2010.15134](https://arxiv.org/abs/2010.15134), [doi:10.1103/PhysRevC.103.054909](https://doi.org/10.1103/PhysRevC.103.054909).

[262] Y. Xu, J. E. Bernhard, S. A. Bass, M. Nahrgang, S. Cao, Data-driven analysis for the temperature and momentum dependence of the heavy-quark diffusion coefficient in relativistic heavy-ion collisions, *Phys. Rev. C* 97 (1) (2018) 014907. [doi:10.1103/PhysRevC.97.014907](https://doi.org/10.1103/PhysRevC.97.014907).

[263] R. Soltz, Bayesian extraction of \hat{q} with multi-stage jet evolution approach, *PoS HardProbes2018* (2019) 048. [doi:10.22323/1.345.0048](https://doi.org/10.22323/1.345.0048).

[264] Y. He, L.-G. Pang, X.-N. Wang, Bayesian extraction of jet energy loss distributions in heavy-ion collisions, *Phys. Rev. Lett.* 122 (25) (2019) 252302. [arXiv:1808.05310](https://arxiv.org/abs/1808.05310), [doi:10.1103/PhysRevLett.122.252302](https://doi.org/10.1103/PhysRevLett.122.252302).

[265] M. Xie, W. Ke, H. Zhang, X.-N. Wang, Information field based global Bayesian inference of the jet transport coefficient (6 2022). [arXiv:2206.01340](https://arxiv.org/abs/2206.01340).

[266] A. J. Larkoski, I. Moult, B. Nachman, Jet Substructure at the Large Hadron Collider: A Review of Recent Advances in Theory and Machine Learning, *Phys. Rept.* 841 (2020) 1–63. [arXiv:1709.04464](https://arxiv.org/abs/1709.04464), [doi:10.1016/j.physrep.2019.11.001](https://doi.org/10.1016/j.physrep.2019.11.001).

[267] G. Louppe, K. Cho, C. Becot, K. Cranmer, QCD-Aware Recursive Neural Networks for Jet Physics, *JHEP* 01 (2019) 057. [arXiv:1702.00748](https://arxiv.org/abs/1702.00748), [doi:10.1007/JHEP01\(2019\)057](https://doi.org/10.1007/JHEP01(2019)057).

[268] F. A. Dreyer, G. Soyez, A. Takacs, Quarks and gluons in the Lund plane, *JHEP* 08 (2022) 177. [arXiv:2112.09140](https://arxiv.org/abs/2112.09140), [doi:10.1007/JHEP08\(2022\)177](https://doi.org/10.1007/JHEP08(2022)177).

[269] R. T. de Lima, Sequence-based Machine Learning Models in Jet Physics (2 2021). [arXiv:2102.06128](https://arxiv.org/abs/2102.06128).

[270] A. Romero, D. Whiteson, M. Fenton, J. Collado, P. Baldi, Safety of Quark/Gluon Jet Classification (3 2021). [arXiv:2103.09103](https://arxiv.org/abs/2103.09103).

[271] P. Konar, V. S. Ngairangbam, M. Spannowsky, Energy-weighted message passing: an infra-red and collinear safe graph neural network algorithm, *JHEP* 02 (2022) 060. [arXiv:2109.14636](https://arxiv.org/abs/2109.14636), [doi:10.1007/JHEP02\(2022\)060](https://doi.org/10.1007/JHEP02(2022)060).

[272] G. Karagiorgi, G. Kasieczka, S. Kravitz, B. Nachman, D. Shih, Machine Learning in the Search for New Fundamental Physics (12 2021). [arXiv:2112.03769](https://arxiv.org/abs/2112.03769).

[273] T. Q. Nguyen, Searches for Nonresonant Higgs Boson Pair Production and Long-Lived Particles at the LHC and Machine-Learning Solutions for the High-Luminosity LHC Era, Ph.D. thesis, Caltech (2021). [doi:10.7907/knfz-q495](https://doi.org/10.7907/knfz-q495).

[274] M. A. Luchmann, Making the most of LHC data - Bayesian neural networks and SMEFT global analysis, Ph.D. thesis, U. Heidelberg (main) (2022).

[275] S. Gong, Q. Meng, J. Zhang, H. Qu, C. Li, S. Qian, W. Du, Z.-M. Ma, T.-Y. Liu, An efficient Lorentz equivariant graph neural network for jet tagging, *JHEP* 07 (2022) 030. [arXiv:2201.08187](https://arxiv.org/abs/2201.08187), [doi:10.1007/JHEP07\(2022\)030](https://doi.org/10.1007/JHEP07(2022)030).

[276] F. Bedeschi, L. Gouskos, M. Selvaggi, Jet flavour tagging for future colliders with fast simulation, *Eur. Phys. J. C* 82 (7) (2022) 646. [arXiv:2202.03285](https://arxiv.org/abs/2202.03285), [doi:10.1140/epjc/s10052-022-10609-1](https://doi.org/10.1140/epjc/s10052-022-10609-1).

[277] H. Qu, C. Li, S. Qian, Particle Transformer for Jet Tagging (2 2022). [arXiv:2202.03772](https://arxiv.org/abs/2202.03772).

[278] Reconstruction of decays to merged photons using end-to-end deep learning with domain continuation in the CMS detector (4 2022). [arXiv:2204.12313](https://arxiv.org/abs/2204.12313).

[279] P. Cal, J. Thaler, W. J. Waalewijn, Power counting energy flow polynomials, *JHEP* 09 (2022) 021. [arXiv:2205.06818](https://arxiv.org/abs/2205.06818), [doi:10.1007/JHEP09\(2022\)021](https://doi.org/10.1007/JHEP09(2022)021).

[280] K. Cranmer, M. Drnevich, S. Macaluso, D. Pappadopulo, Reframing Jet Physics with New Computational Methods, *EPJ Web Conf.* 251 (2021) 03059. [arXiv:2105.10512](https://arxiv.org/abs/2105.10512), [doi:10.1051/epjconf/202125103059](https://doi.org/10.1051/epjconf/202125103059).

[281] M. Rossi, Deep Learning Applications to Particle Physics: From Monte Carlo Simulation Acceleration to Protodune Reconstruction, Ph.D. thesis, Milan U., Milan U. (2023). [arXiv:2302.03343](https://arxiv.org/abs/2302.03343).

[282] Y.-T. Chien, Probing heavy ion collisions using quark and gluon jet substructure with machine learning, *Nucl. Phys. A* 982 (2019) 619–622. [arXiv:1808.04708](https://arxiv.org/abs/1808.04708), [doi:10.1016/j.nuclphysa.2018.11.009](https://doi.org/10.1016/j.nuclphysa.2018.11.009).

[283] Y.-L. Du, D. Pablos, K. Tywoniuk, Classification of quark and gluon jets in hot QCD medium with deep learning, *PoS PANIC2021* (2022) 224. [arXiv:2112.00681](https://arxiv.org/abs/2112.00681), [doi:10.22323/1.380.0224](https://doi.org/10.22323/1.380.0224).

[284] L. Apolinário, N. F. Castro, M. Crispim Romão, J. G. Milhano, R. Pedro, F. C. R. Peres, Deep Learning for the classification of quenched jets, *JHEP* 11 (2021) 219. [arXiv:2106.08869](https://arxiv.org/abs/2106.08869), [doi:10.1007/JHEP11\(2021\)219](https://doi.org/10.1007/JHEP11(2021)219).

[285] Y.-L. Du, D. Pablos, K. Tywoniuk, Deep learning jet modifications in heavy-ion collisions, *JHEP* 21 (2020) 206. [doi:10.1007/JHEP03\(2021\)206](https://doi.org/10.1007/JHEP03(2021)206).

[286] Y.-L. Du, D. Pablos, K. Tywoniuk, Jet tomography in heavy ion collisions with deep learning (6 2021). [arXiv:2106.11271](https://arxiv.org/abs/2106.11271).

[287] Z. Yang, Y. He, W. Chen, W.-Y. Ke, L.-G. Pang, X.-N. Wang, Deep learning assisted jet tomography for the study of Mach cones in QGP (6 2022). [arXiv:2206.02393](https://arxiv.org/abs/2206.02393).

[288] K. Lee, J. Mulligan, M. Płoskoń, F. Ringer, F. Yuan, Machine learning-based jet and event classification at the Electron-Ion Collider with applications to hadron structure and spin physics (10 2022). [arXiv:2210.06450](https://arxiv.org/abs/2210.06450).

[289] M. Arratia, Y. Furletova, T. Hobbs, F. I. Olness, S. J. Sekula, Charm jets as a probe for strangeness at the future electron-ion collider, *Physical Review D* 103 (2020).

[290] J. Arrington, et al., EIC Physics from An All-Silicon Tracking Detector (2 2021). [arXiv:2102.08337](https://arxiv.org/abs/2102.08337).

[291] S. Caletti, O. Fedkevych, S. Marzani, D. Reichelt, Tagging the initial-state gluon, *Eur. Phys. J. C* 81 (9) (2021) 844. [arXiv:2108.10024](https://arxiv.org/abs/2108.10024), [doi:10.1140/epjc/s10052-021-09648-x](https://doi.org/10.1140/epjc/s10052-021-09648-x).

[292] H. G. Baumgardt, J. U. Schott, Y. Sakamoto, E. Schopper, H. Stoecker, J. Hofmann, W. Scheid, W. Greiner, Shock Waves and MACH Cones in Fast Nucleus-Nucleus Collisions, *Z. Phys. A* 273 (1975) 359–371. [doi:10.1007/BF01435578](https://doi.org/10.1007/BF01435578).

[293] D. H. Rischke, H. Stoecker, W. Greiner, Flow in Conical Shock Waves: A Signal for the Deconfinement Transition?, *Phys. Rev. D* 42 (1990) 2283–2292. [doi:10.1103/PhysRevD.42.2283](https://doi.org/10.1103/PhysRevD.42.2283).

[294] J. Casalderrey-Solana, E. V. Shuryak, D. Teaney, Conical flow induced by quenched QCD jets, *J. Phys. Conf. Ser.* 27 (2005) 22–31. [arXiv:hep-ph/0411315](https://arxiv.org/abs/hep-ph/0411315), [doi:10.1088/1742-6596/27/1/003](https://doi.org/10.1088/1742-6596/27/1/003).

[295] L. M. Satarov, H. Stoecker, I. N. Mishustin, Mach shocks induced by partonic jets in expanding quark-gluon plasma, *Phys. Lett. B* 627 (2005) 64–70. [arXiv:hep-ph/0505245](https://arxiv.org/abs/hep-ph/0505245), [doi:10.1016/j.physletb.2005.08.102](https://doi.org/10.1016/j.physletb.2005.08.102).

[296] I. M. Dremin, Ring-like events: Cerenkov gluons or mach waves?, *Nucl. Phys. A* 767 (2006) 233–247. [arXiv:hep-ph/0507167](https://arxiv.org/abs/hep-ph/0507167), [doi:10.1016/j.nuclphysa.2005.12.015](https://doi.org/10.1016/j.nuclphysa.2005.12.015).

[297] V. Koch, A. Majumder, X.-N. Wang, Cerenkov radiation from jets in heavy-ion collisions, *Phys. Rev. Lett.* 96 (2006) 172302. [arXiv:nucl-th/0507063](https://arxiv.org/abs/nucl-th/0507063), doi:10.1103/PhysRevLett.96.172302.

[298] G. L. Ma, et al., Time evolution of Mach-like structure in a partonic transport model (10 2006). [arXiv:nucl-th/0610088](https://arxiv.org/abs/nucl-th/0610088).

[299] S. S. Gubser, S. S. Pufu, A. Yarom, Sonic booms and diffusion wakes generated by a heavy quark in thermal AdS/CFT, *Phys. Rev. Lett.* 100 (2008) 012301. [arXiv:0706.4307](https://arxiv.org/abs/0706.4307), doi:10.1103/PhysRevLett.100.012301.

[300] B. Betz, M. Gyulassy, D. H. Rischke, H. Stocker, G. Torrieri, Jet Propagation and Mach Cones in (3+1)d Ideal Hydrodynamics, *J. Phys. G* 35 (2008) 104106. [arXiv:0804.4408](https://arxiv.org/abs/0804.4408), doi:10.1088/0954-3899/35/10/104106.

[301] R. B. Neufeld, Mach cones in the quark-gluon plasma: Viscosity, speed of sound, and effects of finite source structure, *Phys. Rev. C* 79 (2009) 054909. [arXiv:0807.2996](https://arxiv.org/abs/0807.2996), doi:10.1103/PhysRevC.79.054909.

[302] G. Torrieri, B. Betz, J. Noronha, M. Gyulassy, Mach cones in heavy ion collisions, *Acta Phys. Polon. B* 39 (2008) 3281–3308. [arXiv:0901.0230](https://arxiv.org/abs/0901.0230).

[303] G. Y. Qin, A. Majumder, H. Song, U. Heinz, Energy and momentum deposited into a QCD medium by a jet shower, *Phys. Rev. Lett.* 103 (2009) 152303. [arXiv:0903.2255](https://arxiv.org/abs/0903.2255), doi:10.1103/PhysRevLett.103.152303.

[304] V. Roy, A. K. Chaudhuri, Equation of state dependence of Mach cone like structures in Au+Au collisions, *J. Phys. G* 37 (2010) 035105. [arXiv:0905.2807](https://arxiv.org/abs/0905.2807), doi:10.1088/0954-3899/37/3/035105.

[305] Y. Tachibana, T. Hirano, Interplay between Mach cone and radial expansion and its signal in γ -jet events, *Phys. Rev. C* 93 (5) (2016) 054907. [arXiv:1510.06966](https://arxiv.org/abs/1510.06966), doi:10.1103/PhysRevC.93.054907.

[306] K. Fukushima, D. E. Kharzeev, H. J. Warringa, The Chiral Magnetic Effect, *Phys. Rev. D* 78 (2008) 074033. [arXiv:0808.3382](https://arxiv.org/abs/0808.3382), doi:10.1103/PhysRevD.78.074033.

[307] D. E. Kharzeev, The Chiral Magnetic Effect and Anomaly-Induced Transport, *Prog. Part. Nucl. Phys.* 75 (2014) 133–151. [arXiv:1312.3348](https://arxiv.org/abs/1312.3348), doi:10.1016/j.ppnp.2014.01.002.

[308] D. E. Kharzeev, J. Liao, S. A. Voloshin, G. Wang, Chiral magnetic and vortical effects in high-energy nuclear collisions—A status report, *Prog. Part. Nucl. Phys.* 88 (2016) 1–28. [arXiv:1511.04050](https://arxiv.org/abs/1511.04050), doi:10.1016/j.ppnp.2016.01.001.

[309] J. Zhao, F. Wang, Experimental searches for the chiral magnetic effect in heavy-ion collisions, *Prog. Part. Nucl. Phys.* 107 (2019) 200–236. [arXiv:1906.11413](https://arxiv.org/abs/1906.11413), doi:10.1016/j.ppnp.2019.05.001.

[310] W. Li, G. Wang, Chiral Magnetic Effects in Nuclear Collisions, *Ann. Rev. Nucl. Part. Sci.* 70 (2020) 293–321. [arXiv:2002.10397](https://arxiv.org/abs/2002.10397), doi:10.1146/annurev-nucl-030220-065203.

[311] Y.-S. Zhao, L. Wang, K. Zhou, X.-G. Huang, Detecting the chiral magnetic effect via deep learning, *Phys. Rev. C* 106 (5) (2022) L051901. [arXiv:2105.13761](https://arxiv.org/abs/2105.13761), doi:10.1103/PhysRevC.106.L051901.

[312] Z.-W. Lin, C. M. Ko, B.-A. Li, B. Zhang, S. Pal, A Multi-phase transport model for relativistic heavy ion collisions, *Phys. Rev. C* 72 (2005) 064901. [arXiv:nucl-th/0411110](https://arxiv.org/abs/nucl-th/0411110), doi:10.1103/PhysRevC.72.064901.

[313] G.-L. Ma, B. Zhang, Effects of final state interactions on charge separation in relativistic heavy ion collisions, *Phys. Lett. B* 700 (2011) 39–43. [arXiv:1101.1701](https://arxiv.org/abs/1101.1701), [doi:10.1016/j.physletb.2011.04.057](https://doi.org/10.1016/j.physletb.2011.04.057).

[314] X. Jin, J. Chen, Z. Lin, G. Ma, Y. Ma, S. Zhang, Explore the QCD phase transition phenomena from a multiphase transport model, *Sci. China Phys. Mech. Astron.* 62 (1) (2019) 11012. [doi:10.1007/s11433-018-9272-4](https://doi.org/10.1007/s11433-018-9272-4).

[315] S. Shi, Y. Jiang, E. Lilleskov, J. Liao, Anomalous Chiral Transport in Heavy Ion Collisions from Anomalous-Viscous Fluid Dynamics, *Annals Phys.* 394 (2018) 50–72. [arXiv:1711.02496](https://arxiv.org/abs/1711.02496), [doi:10.1016/j.aop.2018.04.026](https://doi.org/10.1016/j.aop.2018.04.026).

[316] S. Shi, H. Zhang, D. Hou, J. Liao, Chiral Magnetic Effect in Isobaric Collisions from Anomalous-Viscous Fluid Dynamics (AVFD), *Nucl. Phys. A* 982 (2019) 539–542. [arXiv:1807.05604](https://arxiv.org/abs/1807.05604), [doi:10.1016/j.nuclphysa.2018.10.007](https://doi.org/10.1016/j.nuclphysa.2018.10.007).

[317] S. Shi, H. Zhang, D. Hou, J. Liao, Signatures of Chiral Magnetic Effect in the Collisions of Isobars, *Phys. Rev. Lett.* 125 (2020) 242301. [arXiv:1910.14010](https://arxiv.org/abs/1910.14010), [doi:10.1103/PhysRevLett.125.242301](https://doi.org/10.1103/PhysRevLett.125.242301).

[318] Z. Liu, W. Zhao, H. Song, Principal Component Analysis of collective flow in Relativistic Heavy-Ion Collisions, *Eur. Phys. J. C* 79 (10) (2019) 870. [arXiv:1903.09833](https://arxiv.org/abs/1903.09833), [doi:10.1140/epjc/s10052-019-7379-y](https://doi.org/10.1140/epjc/s10052-019-7379-y).

[319] D. Higdon, J. D. McDonnell, N. Schunck, J. Sarich, S. M. Wild, A bayesian approach for parameter estimation and prediction using a computationally intensive model, *Journal of Physics G: Nuclear and Particle Physics* 42 (3) (2015) 034009.

[320] D. Higdon, J. Gattiker, B. Williams, M. Rightley, Computer model calibration using high-dimensional output, *Journal of the American Statistical Association* 103 (482) (2008) 570–583.

[321] D. Liyanage, Y. Ji, D. Everett, M. Heffernan, U. Heinz, S. Mak, J.-F. Paquet, Efficient emulation of relativistic heavy ion collisions with transfer learning, *Phys. Rev. C* 105 (3) (2022) 034910. [arXiv:2201.07302](https://arxiv.org/abs/2201.07302), [doi:10.1103/PhysRevC.105.034910](https://doi.org/10.1103/PhysRevC.105.034910).

[322] H. Huang, B. Xiao, Z. Liu, Z. Wu, Y. Mu, H. Song, Applications of deep learning to relativistic hydrodynamics, *Phys. Rev. Res.* 3 (2) (2021) 023256. [arXiv:1801.03334](https://arxiv.org/abs/1801.03334), [doi:10.1103/PhysRevResearch.3.023256](https://doi.org/10.1103/PhysRevResearch.3.023256).

[323] K. Taradiy, K. Zhou, J. Steinheimer, R. V. Poberezhnyuk, V. Vovchenko, H. Stoecker, Machine learning based approach to fluid dynamics (6 2021). [arXiv:2106.02841](https://arxiv.org/abs/2106.02841).

[324] S. Cai, Z. Mao, Z. Wang, M. Yin, G. E. Karniadakis, Physics-informed neural networks (PINNs) for fluid mechanics: a review, *Acta Mechanica Sinica* 37 (12) (2021) 1727–1738. [arXiv:2105.09506](https://arxiv.org/abs/2105.09506), [doi:10.1007/s10409-021-01148-1](https://doi.org/10.1007/s10409-021-01148-1).

[325] C. Rao, H. Sun, Y. Liu, Physics-informed deep learning for incompressible laminar flows, *Theoretical and Applied Mechanics Letters* 10 (3) (2020) 207–212. [doi:https://doi.org/10.1016/j.taml.2020.01.039](https://doi.org/10.1016/j.taml.2020.01.039).
URL <https://www.sciencedirect.com/science/article/pii/S2095034920300350>

[326] J. Bai, Y. Zhou, Y. Ma, H. Jeong, H. Zhan, C. Rathnayaka, E. Sauret, Y. Gu, A general neural particle method for hydrodynamics modeling, *Computer Methods in Applied Mechanics and Engineering* 393 (2022) 114740. [doi:https://doi.org/10.1016/j.cma.2022.114740](https://doi.org/10.1016/j.cma.2022.114740).
URL <https://www.sciencedirect.com/science/article/pii/S0045782522000962>

[327] D. M. Habashy, M. Y. El-Bakry, W. Scheinast, M. Hanafy, Entropy per Rapidity in Pb-Pb Central Collisions using Thermal and Artificial Neural Network (ANN) Models at LHC Energies, *Chin. Phys. C* 46 (7) (2022) 073103. [arXiv:2110.15026](https://arxiv.org/abs/2110.15026), doi:10.1088/1674-1137/ac5f9d.

[328] R. M. A. Rahman, M. Y. El-Bakry, D. M. Habashy, A. N. Tawfik, M. Hanafy, Particle ratios with in Hadron Resonance Gas (HRG) and Artificial Neural Network (ANN) models (1 2022). [arXiv:2201.04444](https://arxiv.org/abs/2201.04444).

[329] D. M. Habashy, M. Y. El-Bakry, A. N. Tawfik, R. M. Abdel Rahman, M. Hanafy, Particles multiplicity based on rapidity in Landau and artificial neural network (ANN) models, *Int. J. Mod. Phys. A* 37 (02) (2022) 2250002. [arXiv:2109.07191](https://arxiv.org/abs/2109.07191), doi:10.1142/S0217751X22500026.

[330] K. V. Yousefnia, A. Kotibhaskar, R. Bhalerao, J.-Y. Ollitrault, Bayesian approach to long-range correlations and multiplicity fluctuations in nucleus-nucleus collisions, *Phys. Rev. C* 105 (1) (2022) 014907. [arXiv:2108.03471](https://arxiv.org/abs/2108.03471), doi:10.1103/PhysRevC.105.014907.

[331] C. S. Fischer, QCD at finite temperature and chemical potential from Dyson–Schwinger equations, *Prog. Part. Nucl. Phys.* 105 (2019) 1–60. [arXiv:1810.12938](https://arxiv.org/abs/1810.12938), doi:10.1016/j.ppnp.2019.01.002.

[332] K. G. Wilson, Confinement of Quarks, *Phys. Rev. D* 10 (1974) 2445–2459. doi:10.1103/PhysRevD.10.2445.

[333] S. Duane, A. D. Kennedy, B. J. Pendleton, D. Roweth, Hybrid Monte Carlo, *Phys. Lett. B* 195 (1987) 216–222. doi:10.1016/0370-2693(87)91197-X.

[334] F. Knechtli, M. Günther, M. Peardon, Lattice Quantum Chromodynamics: Practical Essentials, *SpringerBriefs in Physics*, Springer, 2017. doi:10.1007/978-94-024-0999-4.

[335] K. Fukushima, T. Hatsuda, The phase diagram of dense QCD, *Rept. Prog. Phys.* 74 (2011) 014001. [arXiv:1005.4814](https://arxiv.org/abs/1005.4814), doi:10.1088/0034-4885/74/1/014001.

[336] O. Philipsen, The QCD equation of state from the lattice, *Prog. Part. Nucl. Phys.* 70 (2013) 55–107. [arXiv:1207.5999](https://arxiv.org/abs/1207.5999), doi:10.1016/j.ppnp.2012.09.003.

[337] J. N. Guenther, Overview of the QCD phase diagram: Recent progress from the lattice, *Eur. Phys. J. A* 57 (4) (2021) 136. [arXiv:2010.15503](https://arxiv.org/abs/2010.15503), doi:10.1140/epja/s10050-021-00354-6.

[338] C. Ratti, Lattice QCD and heavy ion collisions: a review of recent progress, *Rept. Prog. Phys.* 81 (8) (2018) 084301. [arXiv:1804.07810](https://arxiv.org/abs/1804.07810), doi:10.1088/1361-6633/aabb97.

[339] U. Wolff, CRITICAL SLOWING DOWN, *Nucl. Phys. B Proc. Suppl.* 17 (1990) 93–102. doi:10.1016/0920-5632(90)90224-I.

[340] D. Boyda, et al., Applications of Machine Learning to Lattice Quantum Field Theory, in: 2022 Snowmass Summer Study, 2022. [arXiv:2202.05838](https://arxiv.org/abs/2202.05838).

[341] W. Krauth, Statistical mechanics: algorithms and computations, Vol. 13, OUP Oxford, 2006.

[342] N. Metropolis, A. W. Rosenbluth, M. N. Rosenbluth, A. H. Teller, E. Teller, [Equation of state calculations by fast computing machines](#), *The Journal of Chemical Physics* 21 (6) (1953) 1087–1092. doi:10.1063/1.1699114. URL <https://doi.org/10.1063/1.1699114>

[343] W. K. Hastings, Monte Carlo sampling methods using Markov chains and their applications, *Biometrika* 57 (1) (1970) 97–109. [doi:10.1093/biomet/57.1.97](https://doi.org/10.1093/biomet/57.1.97).
 URL <https://doi.org/10.1093/biomet/57.1.97>

[344] L. Del Debbio, G. M. Manca, E. Vicari, Critical slowing down of topological modes, *Phys. Lett. B* 594 (2004) 315–323. [arXiv:hep-lat/0403001](https://arxiv.org/abs/hep-lat/0403001), [doi:10.1016/j.physletb.2004.05.038](https://doi.org/10.1016/j.physletb.2004.05.038).

[345] S. Schaefer, R. Sommer, F. Virotta, Critical slowing down and error analysis in lattice QCD simulations, *Nucl. Phys. B* 845 (2011) 93–119. [doi:10.1016/j.nuclphysb.2010.11.020](https://doi.org/10.1016/j.nuclphysb.2010.11.020).

[346] M. Troyer, U.-J. Wiese, Computational complexity and fundamental limitations to fermionic quantum Monte Carlo simulations, *Phys. Rev. Lett.* 94 (2005) 170201. [arXiv:cond-mat/0408370](https://arxiv.org/abs/cond-mat/0408370), [doi:10.1103/PhysRevLett.94.170201](https://doi.org/10.1103/PhysRevLett.94.170201).

[347] G. Aarts, Introductory lectures on lattice QCD at nonzero baryon number, *J. Phys. Conf. Ser.* 706 (2) (2016) 022004. [arXiv:1512.05145](https://arxiv.org/abs/1512.05145), [doi:10.1088/1742-6596/706/2/022004](https://doi.org/10.1088/1742-6596/706/2/022004).

[348] C. E. Berger, L. Rammelmüller, A. C. Loheac, F. Ehmann, J. Braun, J. E. Drut, Complex Langevin and other approaches to the sign problem in quantum many-body physics, *Phys. Rept.* 892 (2021) 1–54. [arXiv:1907.10183](https://arxiv.org/abs/1907.10183), [doi:10.1016/j.physrep.2020.09.002](https://doi.org/10.1016/j.physrep.2020.09.002).

[349] A. Alexandru, G. Basar, P. F. Bedaque, N. C. Warrington, Complex paths around the sign problem, *Rev. Mod. Phys.* 94 (1) (2022) 015006. [arXiv:2007.05436](https://arxiv.org/abs/2007.05436), [doi:10.1103/RevModPhys.94.015006](https://doi.org/10.1103/RevModPhys.94.015006).

[350] M. Hasenbusch, Fighting topological freezing in the two-dimensional CP^{N-1} model, *EPJ Web Conf.* 175 (2018) 02004. [arXiv:1709.09460](https://arxiv.org/abs/1709.09460), [doi:10.1051/epjconf/201817502004](https://doi.org/10.1051/epjconf/201817502004).

[351] Z. Liu, S. P. Rodrigues, W. Cai, Simulating the Ising Model with a Deep Convolutional Generative Adversarial Network, *arXiv e-prints* (2017) arXiv:1710.04987 [arXiv:1710.04987](https://arxiv.org/abs/1710.04987), [doi:10.48550/arXiv.1710.04987](https://doi.org/10.48550/arXiv.1710.04987).

[352] K. Zhou, G. Endrődi, L.-G. Pang, H. Stöcker, Regressive and generative neural networks for scalar field theory, *Phys. Rev. D* 100 (1) (2019) 011501. [arXiv:1810.12879](https://arxiv.org/abs/1810.12879), [doi:10.1103/PhysRevD.100.011501](https://doi.org/10.1103/PhysRevD.100.011501).

[353] K. Zhou, G. Endrődi, L.-G. Pang, H. Stöcker, Neural Network Study for 1+1d-Complex Scalar Field Theory, *Nucl. Phys. A* 1005 (2021) 121847. [doi:10.1016/j.nuclphysa.2020.121847](https://doi.org/10.1016/j.nuclphysa.2020.121847).

[354] K. Zhou, G. Endrodi, L.-G. Pang, H. Stöcker, Generative Model Study for 1+1d-Complex Scalar Field Theory, *PoS AISIS2019* (2020) 007. [doi:10.22323/1.372.0007](https://doi.org/10.22323/1.372.0007).

[355] A. Singha, D. Chakrabarti, V. Arora, Generative learning for the problem of critical slowing down in lattice Gross-Neveu model, *SciPost Phys. Core* 5 (2022) 052. [arXiv:2111.00574](https://arxiv.org/abs/2111.00574), [doi:10.21468/SciPostPhysCore.5.4.052](https://doi.org/10.21468/SciPostPhysCore.5.4.052).

[356] J. Singh, M. Scheurer, V. Arora, Conditional generative models for sampling and phase transition indication in spin systems, *SciPost Physics* 11 (2) (2021) 043. [arXiv:2006.11868](https://arxiv.org/abs/2006.11868), [doi:10.21468/SciPostPhys.11.2.043](https://doi.org/10.21468/SciPostPhys.11.2.043).

[357] J. M. Pawłowski, J. M. Urban, Reducing Autocorrelation Times in Lattice Simulations with Generative Adversarial Networks, *Mach. Learn. Sci. Tech.* 1 (2020) 045011. [arXiv:1811.03533](https://arxiv.org/abs/1811.03533), [doi:10.1088/2632-2153/abae73](https://doi.org/10.1088/2632-2153/abae73).

[358] J. Liu, Y. Qi, Z. Y. Meng, L. Fu, Self-learning Monte Carlo method, *Physical Review B* 95 (4) (2017) 041101. [arXiv:1610.03137](https://arxiv.org/abs/1610.03137), doi:10.1103/PhysRevB.95.041101.

[359] Y. Nagai, M. Okumura, K. Kobayashi, M. Shiga, Self-learning hybrid monte carlo: A first-principles approach, *Phys. Rev. B* 102 (2020) 041124. doi:10.1103/PhysRevB.102.041124. URL <https://link.aps.org/doi/10.1103/PhysRevB.102.041124>

[360] G. E. Hinton, Training Products of Experts by Minimizing Contrastive Divergence, *Neural Computation* 14 (8) (2002) 1771–1800. [arXiv:https://direct.mit.edu/neco/article-pdf/14/8/1771/815447/089976602760128018.pdf](https://arxiv.org/abs/https://direct.mit.edu/neco/article-pdf/14/8/1771/815447/089976602760128018.pdf), doi:10.1162/089976602760128018. URL <https://doi.org/10.1162/089976602760128018>

[361] L. Huang, L. Wang, Accelerated monte carlo simulations with restricted boltzmann machines, *Phys. Rev. B* 95 (2017) 035105. doi:10.1103/PhysRevB.95.035105. URL <https://link.aps.org/doi/10.1103/PhysRevB.95.035105>

[362] G. Torlai, R. G. Melko, Learning thermodynamics with Boltzmann machines, *Phys. Rev. B* 94 (16) (2016) 165134. [arXiv:1606.02718](https://arxiv.org/abs/1606.02718), doi:10.1103/PhysRevB.94.165134.

[363] L. Wang, Exploring cluster monte carlo updates with boltzmann machines, *Phys. Rev. E* 96 (2017) 051301. doi:10.1103/PhysRevE.96.051301. URL <https://link.aps.org/doi/10.1103/PhysRevE.96.051301>

[364] S. Pilati, E. M. Inack, P. Pieri, Self-learning projective quantum Monte Carlo simulations guided by restricted Boltzmann machines, *Phys. Rev. E* 100 (4) (2019) 043301. [arXiv:1907.00907](https://arxiv.org/abs/1907.00907), doi:10.1103/PhysRevE.100.043301.

[365] J. Liu, H. Shen, Y. Qi, Z. Y. Meng, L. Fu, Self-learning Monte Carlo method and cumulative update in fermion systems, *Physical Review B* 95 (24) (2017) 241104. doi:10.1103/PhysRevB.95.241104.

[366] X. Y. Xu, Y. Qi, J. Liu, L. Fu, Z. Y. Meng, Self-learning quantum Monte Carlo method in interacting fermion systems, *Physical Review B* 96 (4) (2017) 041119. [arXiv:1612.03804](https://arxiv.org/abs/1612.03804), doi:10.1103/PhysRevB.96.041119.

[367] Y. Nagai, H. Shen, Y. Qi, J. Liu, L. Fu, Self-learning Monte Carlo method: Continuous-time algorithm, *Physical Review B* 96 (16) (2017) 161102. [arXiv:1705.06724](https://arxiv.org/abs/1705.06724), doi:10.1103/PhysRevB.96.161102.

[368] H. Shen, J. Liu, L. Fu, Self-learning Monte Carlo with deep neural networks, *Physical Review B* 97 (20) (2018) 205140. [arXiv:1801.01127](https://arxiv.org/abs/1801.01127), doi:10.1103/PhysRevB.97.205140.

[369] Y. Nagai, M. Okumura, A. Tanaka, Self-learning monte carlo method with behler-parrinello neural networks, *Phys. Rev. B* 101 (2020) 115111. doi:10.1103/PhysRevB.101.115111. URL <https://link.aps.org/doi/10.1103/PhysRevB.101.115111>

[370] T. Song, H. Lee, Accelerated continuous time quantum Monte Carlo method with machine learning, *Phys. Rev. B* 100 (4) (2019) 045153. [arXiv:1901.01501](https://arxiv.org/abs/1901.01501), doi:10.1103/PhysRevB.100.045153.

[371] Y. Nagai, A. Tanaka, A. Tomyia, Self-learning Monte-Carlo for non-abelian gauge theory with dynamical fermions (10 2020). [arXiv:2010.11900](https://arxiv.org/abs/2010.11900).

[372] A. Tomiya, Y. Nagai, Gauge covariant neural network for 4 dimensional non-abelian gauge theory (3 2021). [arXiv:2103.11965](https://arxiv.org/abs/2103.11965).

[373] P. E. Shanahan, D. Trewartha, W. Detmold, Machine learning action parameters in lattice quantum chromodynamics, Phys. Rev. D 97 (9) (2018) 094506. [arXiv:1801.05784](https://arxiv.org/abs/1801.05784), [doi:10.1103/PhysRevD.97.094506](https://doi.org/10.1103/PhysRevD.97.094506).

[374] R. Peierls, [On a minimum property of the free energy](#), Phys. Rev. 54 (1938) 918–919. [doi:10.1103/PhysRev.54.918](https://doi.org/10.1103/PhysRev.54.918).
URL <https://link.aps.org/doi/10.1103/PhysRev.54.918>

[375] K. Symanzik, [Proof and refinements of an inequality of feynman](#), Journal of Mathematical Physics 6 (7) (1965) 1155–1156. [arXiv:https://doi.org/10.1063/1.1704383](https://arxiv.org/abs/https://doi.org/10.1063/1.1704383), [doi:10.1063/1.1704383](https://doi.org/10.1063/1.1704383).
URL <https://doi.org/10.1063/1.1704383>

[376] J. L. Lebowitz, E. H. Lieb, [Existence of thermodynamics for real matter with coulomb forces](#), Phys. Rev. Lett. 22 (1969) 631–634. [doi:10.1103/PhysRevLett.22.631](https://doi.org/10.1103/PhysRevLett.22.631).
URL <https://link.aps.org/doi/10.1103/PhysRevLett.22.631>

[377] D. Wu, L. Wang, P. Zhang, Solving Statistical Mechanics Using Variational Autoregressive Networks, Physical Review Letter 122 (8) (2019) 080602. [arXiv:1809.10606](https://arxiv.org/abs/1809.10606), [doi:10.1103/PhysRevLett.122.080602](https://doi.org/10.1103/PhysRevLett.122.080602).

[378] J.-G. Liu, L. Mao, P. Zhang, L. Wang, [Solving quantum statistical mechanics with variational autoregressive networks and quantum circuits](#), Machine Learning: Science and Technology 2 (2) (2021) 025011. [doi:10.1088/2632-2153/aba19d](https://doi.org/10.1088/2632-2153/aba19d).
URL <https://dx.doi.org/10.1088/2632-2153/aba19d>

[379] A. Tomiya, [Schwinger model at finite temperature and density with beta VQE](#) (5 2022). [arXiv:2205.08860](https://arxiv.org/abs/2205.08860).

[380] L. Wang, Y. Jiang, L. He, K. Zhou, Continuous-Mixture Autoregressive Networks Learning the Kosterlitz-Thouless Transition, Chin. Phys. Lett. 39 (12) (2022) 120502. [arXiv:2005.04857](https://arxiv.org/abs/2005.04857), [doi:10.1088/0256-307X/39/12/120502](https://doi.org/10.1088/0256-307X/39/12/120502).

[381] D. Wu, R. Rossi, G. Carleo, Unbiased Monte Carlo cluster updates with autoregressive neural networks, Physical Review Research 3 (4) (2021) L042024. [arXiv:2105.05650](https://arxiv.org/abs/2105.05650), [doi:10.1103/PhysRevResearch.3.L042024](https://doi.org/10.1103/PhysRevResearch.3.L042024).

[382] S.-H. Li, L. Wang, Neural Network Renormalization Group, Phys. Rev. Lett. 121 (26) (2018) 260601. [arXiv:1802.02840](https://arxiv.org/abs/1802.02840), [doi:10.1103/PhysRevLett.121.260601](https://doi.org/10.1103/PhysRevLett.121.260601).

[383] K. A. Nicoli, C. J. Anders, L. Funcke, T. Hartung, K. Jansen, P. Kessel, S. Nakajima, P. Stornati, Estimation of Thermodynamic Observables in Lattice Field Theories with Deep Generative Models, Phys. Rev. Lett. 126 (3) (2021) 032001. [doi:10.1103/PhysRevLett.126.032001](https://doi.org/10.1103/PhysRevLett.126.032001).

[384] T. Müller, B. Mcwilliams, F. Rousselle, M. Gross, J. Novák, [Neural importance sampling](#), ACM Trans. Graph. 38 (5) (oct 2019). [doi:10.1145/3341156](https://doi.org/10.1145/3341156).
URL <https://doi.org/10.1145/3341156>

[385] A. Singha, D. Chakrabarti, V. Arora, Conditional normalizing flow for Markov chain Monte Carlo sampling in the critical region of lattice field theory, Phys. Rev. D 107 (1) (2023) 014512. [doi:10.1103/PhysRevD.107.014512](https://doi.org/10.1103/PhysRevD.107.014512).

[386] L. Del Debbio, J. Marsh Rossney, M. Wilson, Efficient modeling of trivializing maps for lattice ϕ^4 theory using normalizing flows: A first look at scalability, Phys. Rev. D 104 (2021) 094507. [doi:10.1103/PhysRevD.104.094507](https://doi.org/10.1103/PhysRevD.104.094507). URL <https://link.aps.org/doi/10.1103/PhysRevD.104.094507>

[387] H.-Y. Hu, S.-H. Li, L. Wang, Y.-Z. You, Machine Learning Holographic Mapping by Neural Network Renormalization Group, Phys. Rev. Res. 2 (2) (2020) 023369. [arXiv:1903.00804](https://arxiv.org/abs/1903.00804), [doi:10.1103/PhysRevResearch.2.023369](https://doi.org/10.1103/PhysRevResearch.2.023369).

[388] S. Foreman, X.-Y. Jin, J. C. Osborn, Deep learning Hamiltonian Monte Carlo, in: 9th International Conference on Learning Representations, 2021. [arXiv:2105.03418](https://arxiv.org/abs/2105.03418).

[389] D. Boyda, G. Kanwar, S. Racanière, D. J. Rezende, M. S. Albergo, K. Cranmer, D. C. Hackett, P. E. Shanahan, Sampling using $SU(N)$ gauge equivariant flows, Phys. Rev. D 103 (7) (2021) 074504. [arXiv:2008.05456](https://arxiv.org/abs/2008.05456), [doi:10.1103/PhysRevD.103.074504](https://doi.org/10.1103/PhysRevD.103.074504).

[390] M. S. Albergo, G. Kanwar, S. Racanière, D. J. Rezende, J. M. Urban, D. Boyda, K. Cranmer, D. C. Hackett, P. E. Shanahan, Flow-based sampling for fermionic lattice field theories, Phys. Rev. D 104 (11) (2021) 114507. [doi:10.1103/PhysRevD.104.114507](https://doi.org/10.1103/PhysRevD.104.114507).

[391] R. Abbott, et al., Gauge-equivariant flow models for sampling in lattice field theories with pseudofermions, Phys. Rev. D 106 (7) (2022) 074506. [arXiv:2207.08945](https://arxiv.org/abs/2207.08945), [doi:10.1103/PhysRevD.106.074506](https://doi.org/10.1103/PhysRevD.106.074506).

[392] M. Lüscher, Trivializing maps, the Wilson flow and the HMC algorithm, Commun. Math. Phys. 293 (2010) 899–919. [arXiv:0907.5491](https://arxiv.org/abs/0907.5491), [doi:10.1007/s00220-009-0953-7](https://doi.org/10.1007/s00220-009-0953-7).

[393] S. Foreman, T. Izubuchi, L. Jin, X.-Y. Jin, J. C. Osborn, A. Tomiya, HMC with Normalizing Flows, PoS LATTICE2021 (2022) 073. [arXiv:2112.01586](https://arxiv.org/abs/2112.01586), [doi:10.22323/1.396.0073](https://doi.org/10.22323/1.396.0073).

[394] D. Albandea, L. Del Debbio, P. Hernández, R. Kenway, J. M. Rossney, A. Ramos, Learning Trivializing Flows (2 2023). [arXiv:2302.08408](https://arxiv.org/abs/2302.08408).

[395] M. Gerdes, P. de Haan, C. Rainone, R. Bondesan, M. C. N. Cheng, Learning Lattice Quantum Field Theories with Equivariant Continuous Flows (7 2022). [arXiv:2207.00283](https://arxiv.org/abs/2207.00283).

[396] R. T. Q. Chen, Y. Rubanova, J. Bettencourt, D. Duvenaud, Neural Ordinary Differential Equations, arXiv e-prints (2018) arXiv:1806.07366 [arXiv:1806.07366](https://arxiv.org/abs/1806.07366), [doi:10.48550/arXiv.1806.07366](https://doi.org/10.48550/arXiv.1806.07366).

[397] D. C. Hackett, C.-C. Hsieh, M. S. Albergo, D. Boyda, J.-W. Chen, K.-F. Chen, K. Cranmer, G. Kanwar, P. E. Shanahan, Flow-based sampling for multimodal distributions in lattice field theory (7 2021). [arXiv:2107.00734](https://arxiv.org/abs/2107.00734).

[398] S. Chen, O. Savchuk, S. Zheng, B. Chen, H. Stoecker, L. Wang, K. Zhou, Fourier-Flow model generating Feynman paths (11 2022). [arXiv:2211.03470](https://arxiv.org/abs/2211.03470).

[399] J. Komijani, M. K. Marinkovic, Generative models for scalar field theories: how to deal with poor scaling?, in: 39th International Symposium on Lattice Field Theory, 2023. [arXiv:2301.01504](https://arxiv.org/abs/2301.01504).

[400] R. Abbott, et al., Sampling QCD field configurations with gauge-equivariant flow models, PoS LATTICE2022 (2023) 036. [arXiv:2208.03832](https://arxiv.org/abs/2208.03832), [doi:10.22323/1.430.0036](https://doi.org/10.22323/1.430.0036).

[401] R. Abbott, et al., Aspects of scaling and scalability for flow-based sampling of lattice QCD (11 2022). [arXiv:2211.07541](#).

[402] J. Carrasquilla, R. G. Melko, Machine learning phases of matter, *Nature Physics* 13 (5) (2017) 431–434. [arXiv:1605.01735](#), [doi:10.1038/nphys4035](#).

[403] P. Broecker, J. Carrasquilla, R. G. Melko, S. Trebst, Machine learning quantum phases of matter beyond the fermion sign problem, *Scientific Reports* 7 (2017) 8823. [arXiv:1608.07848](#), [doi:10.1038/s41598-017-09098-0](#).

[404] A. Tanaka, A. Tomya, Detection of phase transition via convolutional neural network, *J. Phys. Soc. Jap.* 86 (6) (2017) 063001. [arXiv:1609.09087](#), [doi:10.7566/JPSJ.86.063001](#).

[405] X. Li, R. Guo, Y. Zhou, K. Liu, J. Zhao, F. Long, Y. Wu, Z. Li, Machine learning phase transitions of the three-dimensional Ising universality class (12 2021). [arXiv:2112.13987](#).

[406] L. Wang, Discovering phase transitions with unsupervised learning, *Physical Review B* 94 (19) (2016) 195105. [arXiv:1606.00318](#), [doi:10.1103/PhysRevB.94.195105](#).

[407] W. Hu, R. R. P. Singh, R. T. Scalettar, Discovering phases, phase transitions, and crossovers through unsupervised machine learning: A critical examination, *Physical Review E* 95 (6) (2017) 062122. [arXiv:1704.00080](#), [doi:10.1103/PhysRevE.95.062122](#).

[408] E. P. L. van Nieuwenburg, Y.-H. Liu, S. D. Huber, Learning phase transitions by confusion, *Nature Physics* 13 (5) (2017) 435–439. [arXiv:1610.02048](#), [doi:10.1038/nphys4037](#).

[409] M. J. S. Beach, A. Golubeva, R. G. Melko, Machine learning vortices at the Kosterlitz-Thouless transition, *Physical Review B* 97 (4) (2018) 045207. [arXiv:1710.09842](#), [doi:10.1103/PhysRevB.97.045207](#).

[410] S. J. Wetzel, Unsupervised learning of phase transitions: From principal component analysis to variational autoencoders, *Physical Review E* 96 (2) (2017) 022140. [arXiv:1703.02435](#), [doi:10.1103/PhysRevE.96.022140](#).

[411] N. Walker, K.-M. Tam, M. Jarrell, Deep learning on the 2-dimensional Ising model to extract the crossover region with a variational autoencoder, *Scientific Reports* 10 (2020) 13047. [arXiv:2005.13742](#), [doi:10.1038/s41598-020-69848-5](#).

[412] K. Kottmann, P. Huembeli, M. Lewenstein, A. Acín, Unsupervised Phase Discovery with Deep Anomaly Detection, *Physical Review Letter* 125 (17) (2020) 170603. [arXiv:2003.09905](#), [doi:10.1103/PhysRevLett.125.170603](#).

[413] D. Contessi, E. Ricci, A. Recati, M. Rizzi, Detection of Berezinskii-Kosterlitz-Thouless transition via Generative Adversarial Networks, *SciPost Phys.* 12 (3) (2022) 107. [arXiv:2110.05383](#), [doi:10.21468/SciPostPhys.12.3.107](#).

[414] P. Ponte, R. G. Melko, Kernel methods for interpretable machine learning of order parameters, *Phys. Rev. B* 96 (20) (2017) 205146. [arXiv:1704.05848](#), [doi:10.1103/PhysRevB.96.205146](#).

[415] K. Liu, J. Greitemann, L. Pollet, Learning multiple order parameters with interpretable machines, *Phys. Rev. B* 99 (10) (2019) 104410. [arXiv:1810.05538](#), [doi:10.1103/PhysRevB.99.104410](#).

[416] J. Greitemann, K. Liu, L. Pollet, Probing hidden spin order with interpretable machine learning, *Phys. Rev. B* 99 (6) (2019) 060404. [arXiv:1804.08557](https://arxiv.org/abs/1804.08557), [doi:10.1103/PhysRevB.99.060404](https://doi.org/10.1103/PhysRevB.99.060404).

[417] S. J. Wetzel, M. Scherzer, Machine Learning of Explicit Order Parameters: From the Ising Model to SU(2) Lattice Gauge Theory, *Phys. Rev. B* 96 (18) (2017) 184410. [arXiv:1705.05582](https://arxiv.org/abs/1705.05582), [doi:10.1103/PhysRevB.96.184410](https://doi.org/10.1103/PhysRevB.96.184410).

[418] S. Blücher, L. Kades, J. M. Pawłowski, N. Strodthoff, J. M. Urban, Towards novel insights in lattice field theory with explainable machine learning, *Phys. Rev. D* 101 (9) (2020) 094507. [arXiv:2003.01504](https://arxiv.org/abs/2003.01504), [doi:10.1103/PhysRevD.101.094507](https://doi.org/10.1103/PhysRevD.101.094507).

[419] D. Bachtis, G. Aarts, B. Lucini, Extending machine learning classification capabilities with histogram reweighting, *Phys. Rev. E* 102 (3) (2020) 033303. [arXiv:2004.14341](https://arxiv.org/abs/2004.14341), [doi:10.1103/PhysRevE.102.033303](https://doi.org/10.1103/PhysRevE.102.033303).

[420] D. Bachtis, G. Aarts, B. Lucini, Mapping distinct phase transitions to a neural network, *Phys. Rev. E* 102 (5) (2020) 053306. [arXiv:2007.00355](https://arxiv.org/abs/2007.00355), [doi:10.1103/PhysRevE.102.053306](https://doi.org/10.1103/PhysRevE.102.053306).

[421] D. L. Boyda, M. N. Chernodub, N. V. Gerasimeniuk, V. A. Goy, S. D. Liubimov, A. V. Molochkov, Finding the deconfinement temperature in lattice Yang-Mills theories from outside the scaling window with machine learning, *Phys. Rev. D* 103 (1) (2021) 014509. [arXiv:2009.10971](https://arxiv.org/abs/2009.10971), [doi:10.1103/PhysRevD.103.014509](https://doi.org/10.1103/PhysRevD.103.014509).

[422] S. Bulusu, M. Favoni, A. Ipp, D. I. Müller, D. Schuh, Generalization capabilities of translationally equivariant neural networks, *Phys. Rev. D* 104 (7) (2021) 074504. [arXiv:2103.14686](https://arxiv.org/abs/2103.14686), [doi:10.1103/PhysRevD.104.074504](https://doi.org/10.1103/PhysRevD.104.074504).

[423] B. Yoon, T. Bhattacharya, R. Gupta, Machine Learning Estimators for Lattice QCD Observables, *Phys. Rev. D* 100 (1) (2019) 014504. [arXiv:1807.05971](https://arxiv.org/abs/1807.05971), [doi:10.1103/PhysRevD.100.014504](https://doi.org/10.1103/PhysRevD.100.014504).

[424] T. S. Cohen, M. Welling, Group Equivariant Convolutional Networks, arXiv e-prints (2016) arXiv:1602.07576 [arXiv:1602.07576](https://arxiv.org/abs/1602.07576), [doi:10.48550/arXiv.1602.07576](https://doi.org/10.48550/arXiv.1602.07576).

[425] T. S. Cohen, M. Weiler, B. Kicanaoglu, M. Welling, Gauge Equivariant Convolutional Networks and the Icosahedral CNN, arXiv e-prints (2019) arXiv:1902.04615 [arXiv:1902.04615](https://arxiv.org/abs/1902.04615), [doi:10.48550/arXiv.1902.04615](https://doi.org/10.48550/arXiv.1902.04615).

[426] A. Bogatskiy, et al., Symmetry Group Equivariant Architectures for Physics, in: 2022 Snowmass Summer Study, 2022. [arXiv:2203.06153](https://arxiv.org/abs/2203.06153).

[427] M. Favoni, A. Ipp, D. I. Müller, D. Schuh, Lattice Gauge Equivariant Convolutional Neural Networks, *Phys. Rev. Lett.* 128 (3) (2022) 032003. [arXiv:2012.12901](https://arxiv.org/abs/2012.12901), [doi:10.1103/PhysRevLett.128.032003](https://doi.org/10.1103/PhysRevLett.128.032003).

[428] J. Chen, S. Cheng, H. Xie, L. Wang, T. Xiang, Equivalence of restricted Boltzmann machines and tensor network states, *Phys. Rev. B* 97 (8) (2018) 085104. [arXiv:1701.04831](https://arxiv.org/abs/1701.04831), [doi:10.1103/PhysRevB.97.085104](https://doi.org/10.1103/PhysRevB.97.085104).

[429] K. Choo, G. Carleo, N. Regnault, T. Neupert, Symmetries and Many-Body Excitations with Neural-Network Quantum States, *Physical Review Letter* 121 (16) (2018) 167204. [arXiv:1807.03325](https://arxiv.org/abs/1807.03325), [doi:10.1103/PhysRevLett.121.167204](https://doi.org/10.1103/PhysRevLett.121.167204).

[430] M. Noormandipour, Y. Sun, B. Haghhighat, Restricted Boltzmann machine representation for the groundstate and excited states of Kitaev Honeycomb model, *Mach. Learn. Sci. Tech.* 3 (1) (2022) 015010. [arXiv:2003.07280](https://arxiv.org/abs/2003.07280), [doi:10.1088/2632-2153/ac3ddf](https://doi.org/10.1088/2632-2153/ac3ddf).

[431] O. Sharir, Y. Levine, N. Wies, G. Carleo, A. Shashua, Deep Autoregressive Models for the Efficient Variational Simulation of Many-Body Quantum Systems, *Phys. Rev. Lett.* 124 (2) (2020) 020503. [arXiv:1902.04057](https://arxiv.org/abs/1902.04057), doi: [10.1103/PhysRevLett.124.020503](https://doi.org/10.1103/PhysRevLett.124.020503).

[432] J. Carrasquilla, G. Torlai, How To Use Neural Networks To Investigate Quantum Many-Body Physics, *PRX Quantum* 2 (4) (2021) 040201. doi: [10.1103/PRXQuantum.2.040201](https://doi.org/10.1103/PRXQuantum.2.040201).

[433] J. Carrasquilla, G. Torlai, Neural networks in quantum many-body physics: a hands-on tutorial, *arXiv e-prints* (2021) arXiv:2101.11099 [arXiv:2101.11099](https://arxiv.org/abs/2101.11099), doi: [10.48550/arXiv.2101.11099](https://doi.org/10.48550/arXiv.2101.11099).

[434] M. Asakawa, T. Hatsuda, Y. Nakahara, Maximum entropy analysis of the spectral functions in lattice QCD, *Prog. Part. Nucl. Phys.* 46 (2001) 459–508. [arXiv:hep-lat/0011040](https://arxiv.org/abs/hep-lat/0011040), doi: [10.1016/S0146-6410\(01\)00150-8](https://doi.org/10.1016/S0146-6410(01)00150-8).

[435] A. Rothkopf, Inverse problems, real-time dynamics and lattice simulations, *EPJ Web Conf.* 274 (2022) 01004. [arXiv:2211.10680](https://arxiv.org/abs/2211.10680), doi: [10.1051/epjconf/202227401004](https://doi.org/10.1051/epjconf/202227401004).

[436] A. Rothkopf, Heavy Quarkonium in Extreme Conditions, *Phys. Rept.* 858 (2020) 1–117. [arXiv:1912.02253](https://arxiv.org/abs/1912.02253), doi: [10.1016/j.physrep.2020.02.006](https://doi.org/10.1016/j.physrep.2020.02.006).

[437] J. Zhao, K. Zhou, S. Chen, P. Zhuang, Heavy flavors under extreme conditions in high energy nuclear collisions, *Prog. Part. Nucl. Phys.* 114 (2020) 103801. [arXiv:2005.08277](https://arxiv.org/abs/2005.08277), doi: [10.1016/j.ppnp.2020.103801](https://doi.org/10.1016/j.ppnp.2020.103801).

[438] X. Ji, Y.-S. Liu, Y. Liu, J.-H. Zhang, Y. Zhao, Large-momentum effective theory, *Rev. Mod. Phys.* 93 (3) (2021) 035005. [arXiv:2004.03543](https://arxiv.org/abs/2004.03543), doi: [10.1103/RevModPhys.93.035005](https://doi.org/10.1103/RevModPhys.93.035005).

[439] M. Constantinou, The x-dependence of hadronic parton distributions: A review on the progress of lattice QCD, *Eur. Phys. J. A* 57 (2) (2021) 77. [arXiv:2010.02445](https://arxiv.org/abs/2010.02445), doi: [10.1140/epja/s10050-021-00353-7](https://doi.org/10.1140/epja/s10050-021-00353-7).

[440] A. Candido, L. Del Debbio, T. Giani, G. Petrillo, Inverse Problems in PDF determinations, *PoS LATTICE2022* (2023) 098. [arXiv:2302.14731](https://arxiv.org/abs/2302.14731), doi: [10.22323/1.430.0098](https://doi.org/10.22323/1.430.0098).

[441] S. Shi, L. Wang, K. Zhou, Rethinking the ill-posedness of the spectral function reconstruction — Why is it fundamentally hard and how Artificial Neural Networks can help, *Comput. Phys. Commun.* 282 (2023) 108547. [arXiv:2201.02564](https://arxiv.org/abs/2201.02564), doi: [10.1016/j.cpc.2022.108547](https://doi.org/10.1016/j.cpc.2022.108547).

[442] J. G. McWhirter, E. R. Pike, [On the numerical inversion of the laplace transform and similar fredholm integral equations of the first kind](#), *Journal of Physics A: Mathematical and General* 11 (9) (1978) 1729. doi: [10.1088/0305-4470/11/9/007](https://doi.org/10.1088/0305-4470/11/9/007).
URL <https://dx.doi.org/10.1088/0305-4470/11/9/007>

[443] L. Wang, S. Shi, K. Zhou, Reconstructing spectral functions via automatic differentiation, *Phys. Rev. D* 106 (5) (2022) L051502. [arXiv:2111.14760](https://arxiv.org/abs/2111.14760), doi: [10.1103/PhysRevD.106.L051502](https://doi.org/10.1103/PhysRevD.106.L051502).

[444] A. N. Tikhonov, On the stability of inverse problems, *Proceedings of the USSR Academy of Sciences* 39 (1943) 195–198.

[445] A. N. Tikhonov, A. Goncharsky, V. V. Stepanov, A. G. Yagola, *Numerical methods for the solution of ill-posed problems*, Vol. 328, Springer Science & Business Media, 1995.

[446] J. Otsuki, M. Ohzeki, H. Shinaoka, K. Yoshimi, [Sparse modeling approach to analytical continuation of imaginary-time quantum monte carlo data](#), Phys. Rev. E 95 (2017) 061302. [doi:10.1103/PhysRevE.95.061302](https://doi.org/10.1103/PhysRevE.95.061302).
 URL <https://link.aps.org/doi/10.1103/PhysRevE.95.061302>

[447] E. Itou, Y. Nagai, Sparse modeling approach to obtaining the shear viscosity from smeared correlation functions, JHEP 07 (2020) 007. [arXiv:2004.02426](https://arxiv.org/abs/2004.02426), [doi:10.1007/JHEP07\(2020\)007](https://doi.org/10.1007/JHEP07(2020)007).

[448] M. Jarrell, J. Gubernatis, [Bayesian inference and the analytic continuation of imaginary-time quantum monte carlo data](#), Physics Reports 269 (3) (1996) 133–195. [doi:https://doi.org/10.1016/0370-1573\(95\)00074-7](https://doi.org/10.1016/0370-1573(95)00074-7).
 URL <https://www.sciencedirect.com/science/article/pii/0370157395000747>

[449] Y. Burnier, A. Rothkopf, Bayesian Approach to Spectral Function Reconstruction for Euclidean Quantum Field Theories, Phys. Rev. Lett. 111 (2013) 182003. [arXiv:1307.6106](https://arxiv.org/abs/1307.6106), [doi:10.1103/PhysRevLett.111.182003](https://doi.org/10.1103/PhysRevLett.111.182003).

[450] L.-F. Arsenault, R. Neuberg, L. A. Hannah, A. J. Millis, Projected Regression Methods for Inverting Fredholm Integrals: Formalism and Application to Analytical Continuation, arXiv e-prints (2016) arXiv:1612.04895 [arXiv:1612.04895](https://arxiv.org/abs/1612.04895), [doi:10.48550/arXiv.1612.04895](https://doi.org/10.48550/arXiv.1612.04895).

[451] H. Yoon, J.-H. Sim, M. J. Han, Analytic continuation via domain knowledge free machine learning, Physical Review B 98 (24) (2018) 245101. [arXiv:1806.03841](https://arxiv.org/abs/1806.03841), [doi:10.1103/PhysRevB.98.245101](https://doi.org/10.1103/PhysRevB.98.245101).

[452] R. Fournier, L. Wang, O. V. Yazyev, Q. Wu, [Artificial neural network approach to the analytic continuation problem](#), Phys. Rev. Lett. 124 (2020) 056401. [doi:10.1103/PhysRevLett.124.056401](https://doi.org/10.1103/PhysRevLett.124.056401).
 URL <https://link.aps.org/doi/10.1103/PhysRevLett.124.056401>

[453] L. Kades, J. M. Pawłowski, A. Rothkopf, M. Scherzer, J. M. Urban, S. J. Wetzel, N. Wink, F. P. G. Ziegler, Spectral Reconstruction with Deep Neural Networks, Phys. Rev. D 102 (9) (2020) 096001. [arXiv:1905.04305](https://arxiv.org/abs/1905.04305), [doi:10.1103/PhysRevD.102.096001](https://doi.org/10.1103/PhysRevD.102.096001).

[454] S. Y. Chen, H. T. Ding, F. Y. Liu, G. Papp, C. B. Yang, Machine learning spectral functions in lattice QCD (10 2021). [arXiv:2110.13521](https://arxiv.org/abs/2110.13521).

[455] M. Zhou, F. Gao, J. Chao, Y.-X. Liu, H. Song, Application of radial basis functions neutral networks in spectral functions, Phys. Rev. D 104 (7) (2021) 076011. [arXiv:2106.08168](https://arxiv.org/abs/2106.08168), [doi:10.1103/PhysRevD.104.076011](https://doi.org/10.1103/PhysRevD.104.076011).

[456] J. Horak, J. M. Pawłowski, J. Rodríguez-Quintero, J. Turnwald, J. M. Urban, N. Wink, S. Zafeiropoulos, Reconstructing QCD Spectral Functions with Gaussian Processes (7 2021). [arXiv:2107.13464](https://arxiv.org/abs/2107.13464).

[457] L. Wang, S. Shi, K. Zhou, Automatic differentiation approach for reconstructing spectral functions with neural networks, in: 35th Conference on Neural Information Processing Systems, 2021. [arXiv:2112.06206](https://arxiv.org/abs/2112.06206).

[458] B. Chen, K. Zhou, P. Zhuang, Mean Field Effect on J/ψ Production in Heavy Ion Collisions, Phys. Rev. C 86 (2012) 034906. [arXiv:1202.3523](https://arxiv.org/abs/1202.3523), [doi:10.1103/PhysRevC.86.034906](https://doi.org/10.1103/PhysRevC.86.034906).

[459] X. Zhao, R. Rapp, Charmonium in Medium: From Correlators to Experiment, Phys. Rev. C 82 (2010) 064905. [arXiv:1008.5328](https://arxiv.org/abs/1008.5328), [doi:10.1103/PhysRevC.82.064905](https://doi.org/10.1103/PhysRevC.82.064905).

[460] K. Zhou, N. Xu, Z. Xu, P. Zhuang, Medium effects on charmonium production at ultrarelativistic energies available at the CERN Large Hadron Collider, *Phys. Rev. C* 89 (5) (2014) 054911. [arXiv:1401.5845](https://arxiv.org/abs/1401.5845), doi: [10.1103/PhysRevC.89.054911](https://doi.org/10.1103/PhysRevC.89.054911).

[461] S. Chatrchyan, et al., Indications of suppression of excited Υ states in PbPb collisions at $\sqrt{S_{NN}} = 2.76$ TeV, *Phys. Rev. Lett.* 107 (2011) 052302. [arXiv:1105.4894](https://arxiv.org/abs/1105.4894), doi: [10.1103/PhysRevLett.107.052302](https://doi.org/10.1103/PhysRevLett.107.052302).

[462] S. Chatrchyan, et al., Observation of Sequential Upsilon Suppression in PbPb Collisions, *Phys. Rev. Lett.* 109 (2012) 222301, [Erratum: *Phys. Rev. Lett.* 120, 199903 (2018)]. [arXiv:1208.2826](https://arxiv.org/abs/1208.2826), doi: [10.1103/PhysRevLett.109.222301](https://doi.org/10.1103/PhysRevLett.109.222301).

[463] M. Laine, O. Philipsen, P. Romatschke, M. Tassler, Real-time static potential in hot QCD, *JHEP* 03 (2007) 054. [arXiv:hep-ph/0611300](https://arxiv.org/abs/hep-ph/0611300), doi: [10.1088/1126-6708/2007/03/054](https://doi.org/10.1088/1126-6708/2007/03/054).

[464] A. Beraudo, J. P. Blaizot, C. Ratti, Real and imaginary-time Q anti-Q correlators in a thermal medium, *Nucl. Phys. A* 806 (2008) 312–338. [arXiv:0712.4394](https://arxiv.org/abs/0712.4394), doi: [10.1016/j.nuclphysa.2008.03.001](https://doi.org/10.1016/j.nuclphysa.2008.03.001).

[465] N. Brambilla, J. Ghiglieri, A. Vairo, P. Petreczky, Static quark-antiquark pairs at finite temperature, *Phys. Rev. D* 78 (2008) 014017. [arXiv:0804.0993](https://arxiv.org/abs/0804.0993), doi: [10.1103/PhysRevD.78.014017](https://doi.org/10.1103/PhysRevD.78.014017).

[466] N. Brambilla, M. A. Escobedo, J. Ghiglieri, J. Soto, A. Vairo, Heavy Quarkonium in a weakly-coupled quark-gluon plasma below the melting temperature, *JHEP* 09 (2010) 038. [arXiv:1007.4156](https://arxiv.org/abs/1007.4156), doi: [10.1007/JHEP09\(2010\)038](https://doi.org/10.1007/JHEP09(2010)038).

[467] A. Rothkopf, T. Hatsuda, S. Sasaki, Complex Heavy-Quark Potential at Finite Temperature from Lattice QCD, *Phys. Rev. Lett.* 108 (2012) 162001. [arXiv:1108.1579](https://arxiv.org/abs/1108.1579), doi: [10.1103/PhysRevLett.108.162001](https://doi.org/10.1103/PhysRevLett.108.162001).

[468] Y. Burnier, O. Kaczmarek, A. Rothkopf, Static quark-antiquark potential in the quark-gluon plasma from lattice QCD, *Phys. Rev. Lett.* 114 (8) (2015) 082001. [arXiv:1410.2546](https://arxiv.org/abs/1410.2546), doi: [10.1103/PhysRevLett.114.082001](https://doi.org/10.1103/PhysRevLett.114.082001).

[469] Y. Burnier, O. Kaczmarek, A. Rothkopf, Quarkonium at finite temperature: Towards realistic phenomenology from first principles, *JHEP* 12 (2015) 101. [arXiv:1509.07366](https://arxiv.org/abs/1509.07366), doi: [10.1007/JHEP12\(2015\)101](https://doi.org/10.1007/JHEP12(2015)101).

[470] R. Larsen, S. Meinel, S. Mukherjee, P. Petreczky, Thermal broadening of bottomonia: Lattice nonrelativistic QCD with extended operators, *Phys. Rev. D* 100 (7) (2019) 074506. [arXiv:1908.08437](https://arxiv.org/abs/1908.08437), doi: [10.1103/PhysRevD.100.074506](https://doi.org/10.1103/PhysRevD.100.074506).

[471] R. Larsen, S. Meinel, S. Mukherjee, P. Petreczky, Excited bottomonia in quark-gluon plasma from lattice QCD, *Phys. Lett. B* 800 (2020) 135119. [arXiv:1910.07374](https://arxiv.org/abs/1910.07374), doi: [10.1016/j.physletb.2019.135119](https://doi.org/10.1016/j.physletb.2019.135119).

[472] R. Larsen, S. Meinel, S. Mukherjee, P. Petreczky, Bethe-Salpeter amplitudes of Upsilon, *Phys. Rev. D* 102 (2020) 114508. [arXiv:2008.00100](https://arxiv.org/abs/2008.00100), doi: [10.1103/PhysRevD.102.114508](https://doi.org/10.1103/PhysRevD.102.114508).

[473] S. Shi, K. Zhou, J. Zhao, S. Mukherjee, P. Zhuang, Heavy Quark Potential in QGP: DNN meets LQCD (5 2021). [arXiv:2105.07862](https://arxiv.org/abs/2105.07862).

[474] H.-W. Lin, et al., Parton distributions and lattice QCD calculations: a community white paper, *Prog. Part. Nucl. Phys.* 100 (2018) 107–160. [arXiv:1711.07916](https://arxiv.org/abs/1711.07916), doi: [10.1016/j.ppnp.2018.01.007](https://doi.org/10.1016/j.ppnp.2018.01.007).

[475] S. Forte, S. Carrazza, Parton distribution functions (8 2020). [arXiv:2008.12305](https://arxiv.org/abs/2008.12305).

[476] S. Forte, L. Garrido, J. I. Latorre, A. Piccione, Neural network parametrization of deep inelastic structure functions, JHEP 05 (2002) 062. [arXiv:hep-ph/0204232](https://arxiv.org/abs/hep-ph/0204232), doi:10.1088/1126-6708/2002/05/062.

[477] R. D. Ball, L. Del Debbio, S. Forte, A. Guffanti, J. I. Latorre, A. Piccione, J. Rojo, M. Ubiali, Precision determination of electroweak parameters and the strange content of the proton from neutrino deep-inelastic scattering, Nucl. Phys. B 823 (2009) 195–233. [arXiv:0906.1958](https://arxiv.org/abs/0906.1958), doi:10.1016/j.nuclphysb.2009.08.003.

[478] R. D. Ball, L. Del Debbio, S. Forte, A. Guffanti, J. I. Latorre, J. Rojo, M. Ubiali, A first unbiased global NLO determination of parton distributions and their uncertainties, Nucl. Phys. B 838 (2010) 136–206. doi:10.1016/j.nuclphysb.2010.05.008.

[479] R. D. Ball, et al., Parton distributions with LHC data, Nucl. Phys. B 867 (2013) 244–289. [arXiv:1207.1303](https://arxiv.org/abs/1207.1303), doi:10.1016/j.nuclphysb.2012.10.003.

[480] R. D. Ball, et al., Parton distributions for the LHC Run II, JHEP 04 (2015) 040. [arXiv:1410.8849](https://arxiv.org/abs/1410.8849), doi:10.1007/JHEP04(2015)040.

[481] V. Bertone, S. Carrazza, N. P. Hartland, E. R. Nocera, J. Rojo, A determination of the fragmentation functions of pions, kaons, and protons with faithful uncertainties, Eur. Phys. J. C 77 (8) (2017) 516. [arXiv:1706.07049](https://arxiv.org/abs/1706.07049), doi:10.1140/epjc/s10052-017-5088-y.

[482] R. Abdul Khalek, J. J. Ethier, J. Rojo, Nuclear parton distributions from lepton-nucleus scattering and the impact of an electron-ion collider, Eur. Phys. J. C 79 (6) (2019) 471. doi:10.1140/epjc/s10052-019-6983-1.

[483] R. Abdul Khalek, J. J. Ethier, J. Rojo, G. van Weelden, nNNPDF2.0: quark flavor separation in nuclei from LHC data, JHEP 09 (2020) 183. [arXiv:2006.14629](https://arxiv.org/abs/2006.14629), doi:10.1007/JHEP09(2020)183.

[484] R. Abdul Khalek, R. Gauld, T. Giani, E. R. Nocera, T. R. Rabemananjara, J. Rojo, nNNPDF3.0: evidence for a modified partonic structure in heavy nuclei, Eur. Phys. J. C 82 (6) (2022) 507. [arXiv:2201.12363](https://arxiv.org/abs/2201.12363), doi:10.1140/epjc/s10052-022-10417-7.

[485] J. Karpie, K. Orginos, A. Rothkopf, S. Zafeiropoulos, Reconstructing parton distribution functions from Ioffe time data: from Bayesian methods to Neural Networks, JHEP 04 (2019) 057. doi:10.1007/JHEP04(2019)057.

[486] X. Gao, A. D. Hanlon, N. Karthik, S. Mukherjee, P. Petreczky, P. Scior, S. Shi, S. Syritsyn, Y. Zhao, K. Zhou, Continuum-extrapolated NNLO Valence PDF of Pion at the Physical Point (8 2022). [arXiv:2208.02297](https://arxiv.org/abs/2208.02297).

[487] S. Forte, J. I. Latorre, L. Magnea, A. Piccione, Determination of alpha(s) from scaling violations of truncated moments of structure functions, Nucl. Phys. B 643 (2002) 477–500. [arXiv:hep-ph/0205286](https://arxiv.org/abs/hep-ph/0205286), doi:10.1016/S0550-3213(02)00688-0.

[488] R. Zhang, Z. Fan, R. Li, H.-W. Lin, B. Yoon, Machine-learning prediction for quasiparton distribution function matrix elements, Phys. Rev. D 101 (3) (2020) 034516. doi:10.1103/PhysRevD.101.034516.

[489] L. Del Debbio, T. Giani, J. Karpie, K. Orginos, A. Radyushkin, S. Zafeiropoulos, Neural-network analysis of Parton Distribution Functions from Ioffe-time pseudodistributions, JHEP 02 (2021) 138. doi:10.1007/JHEP02(2021)138.

[490] L. Del Debbio, T. Giani, M. Wilson, Bayesian approach to inverse problems: an application to NNPDF closure testing, *Eur. Phys. J. C* 82 (4) (2022) 330. [arXiv:2111.05787](https://arxiv.org/abs/2111.05787), [doi:10.1140/epjc/s10052-022-10297-x](https://doi.org/10.1140/epjc/s10052-022-10297-x).

[491] A. M. Ferrenberg, R. H. Swendsen, New Monte Carlo Technique for Studying Phase Transitions, *Phys. Rev. Lett.* 61 (1988) 2635–2638. [doi:10.1103/PhysRevLett.61.2635](https://doi.org/10.1103/PhysRevLett.61.2635).

[492] F. Wang, D. P. Landau, Efficient, Multiple-Range Random Walk Algorithm to Calculate the Density of States, *Phys. Rev. Lett.* 86 (10) (2001) 2050. [arXiv:cond-mat/0011174](https://arxiv.org/abs/cond-mat/0011174), [doi:10.1103/PhysRevLett.86.2050](https://doi.org/10.1103/PhysRevLett.86.2050).

[493] C. R. Allton, S. Ejiri, S. J. Hands, O. Kaczmarek, F. Karsch, E. Laermann, C. Schmidt, L. Scorzato, The QCD thermal phase transition in the presence of a small chemical potential, *Phys. Rev. D* 66 (2002) 074507. [arXiv:hep-lat/0204010](https://arxiv.org/abs/hep-lat/0204010), [doi:10.1103/PhysRevD.66.074507](https://doi.org/10.1103/PhysRevD.66.074507).

[494] S. Borsányi, Fluctuations at finite temperature and density, *PoS LATTICE2015* (2016) 015. [arXiv:1511.06541](https://arxiv.org/abs/1511.06541), [doi:10.22323/1.251.0015](https://doi.org/10.22323/1.251.0015).

[495] P. de Forcrand, O. Philipsen, The QCD phase diagram for small densities from imaginary chemical potential, *Nucl. Phys. B* 642 (2002) 290–306. [arXiv:hep-lat/0205016](https://arxiv.org/abs/hep-lat/0205016), [doi:10.1016/S0550-3213\(02\)00626-0](https://doi.org/10.1016/S0550-3213(02)00626-0).

[496] P. de Forcrand, Simulating QCD at finite density, *PoS LAT2009* (2009) 010. [arXiv:1005.0539](https://arxiv.org/abs/1005.0539), [doi:10.22323/1.091.0010](https://doi.org/10.22323/1.091.0010).

[497] P. Rossi, U. Wolff, Lattice QCD With Fermions at Strong Coupling: A Dimer System, *Nucl. Phys. B* 248 (1984) 105–122. [doi:10.1016/0550-3213\(84\)90589-3](https://doi.org/10.1016/0550-3213(84)90589-3).

[498] G. Parisi, Y.-s. Wu, Perturbation Theory Without Gauge Fixing, *Sci. Sin.* 24 (1981) 483.

[499] G. Aarts, L. Bongiovanni, E. Seiler, D. Sexty, I.-O. Stamatescu, Controlling complex Langevin dynamics at finite density, *Eur. Phys. J. A* 49 (2013) 89. [arXiv:1303.6425](https://arxiv.org/abs/1303.6425), [doi:10.1140/epja/i2013-13089-4](https://doi.org/10.1140/epja/i2013-13089-4).

[500] F. Attanasio, B. Jäger, F. P. G. Ziegler, Complex Langevin simulations and the QCD phase diagram: Recent developments, *Eur. Phys. J. A* 56 (10) (2020) 251. [arXiv:2006.00476](https://arxiv.org/abs/2006.00476), [doi:10.1140/epja/s10050-020-00256-z](https://doi.org/10.1140/epja/s10050-020-00256-z).

[501] N. Rom, D. M. Charutz, D. Neuhauser, Shifted-contour auxiliary-field Monte Carlo: circumventing the sign difficulty for electronic-structure calculations, *Chemical Physics Letters* 270 (3) (1997) 382–386. [doi:10.1016/S0009-2614\(97\)00370-9](https://doi.org/10.1016/S0009-2614(97)00370-9).

[502] M. Cristoforetti, F. Di Renzo, L. Scorzato, New approach to the sign problem in quantum field theories: High density QCD on a Lefschetz thimble, *Phys. Rev. D* 86 (2012) 074506. [arXiv:1205.3996](https://arxiv.org/abs/1205.3996), [doi:10.1103/PhysRevD.86.074506](https://doi.org/10.1103/PhysRevD.86.074506).

[503] M. Cristoforetti, F. Di Renzo, A. Mukherjee, L. Scorzato, Monte Carlo simulations on the Lefschetz thimble: Taming the sign problem, *Phys. Rev. D* 88 (5) (2013) 051501. [arXiv:1303.7204](https://arxiv.org/abs/1303.7204), [doi:10.1103/PhysRevD.88.051501](https://doi.org/10.1103/PhysRevD.88.051501).

[504] A. Alexandru, G. Basar, P. F. Bedaque, G. W. Ridgway, N. C. Warrington, Sign problem and Monte Carlo calculations beyond Lefschetz thimbles, *JHEP* 05 (2016) 053. [arXiv:1512.08764](https://arxiv.org/abs/1512.08764), [doi:10.1007/JHEP05\(2016\)053](https://doi.org/10.1007/JHEP05(2016)053).

[505] J. Nishimura, S. Shimasaki, Combining the complex Langevin method and the generalized Lefschetz-thimble method, *JHEP* 06 (2017) 023. [arXiv:1703.09409](https://arxiv.org/abs/1703.09409), [doi:10.1007/JHEP06\(2017\)023](https://doi.org/10.1007/JHEP06(2017)023).

[506] A. Alexandru, P. F. Bedaque, H. Lamm, S. Lawrence, Deep Learning Beyond Lefschetz Thimbles, *Phys. Rev. D* 96 (9) (2017) 094505. [arXiv:1709.01971](https://arxiv.org/abs/1709.01971), [doi:10.1103/PhysRevD.96.094505](https://doi.org/10.1103/PhysRevD.96.094505).

[507] J.-L. Wynen, E. Berkowitz, S. Krieg, T. Luu, J. Ostmeyer, Machine learning to alleviate Hubbard-model sign problems, *Physical Review B* 103 (12) (2021) 125153. [arXiv:2006.11221](https://arxiv.org/abs/2006.11221), [doi:10.1103/PhysRevB.103.125153](https://doi.org/10.1103/PhysRevB.103.125153).

[508] M. Rodekamp, E. Berkowitz, C. Gärtgen, S. Krieg, T. Luu, J. Ostmeyer, Mitigating the Hubbard sign problem with complex-valued neural networks, *Physical Review B* 106 (12) (2022) 125139. [arXiv:2203.00390](https://arxiv.org/abs/2203.00390), [doi:10.1103/PhysRevB.106.125139](https://doi.org/10.1103/PhysRevB.106.125139).

[509] M. Rodekamp, C. Gärtgen, Mitigating the Hubbard Sign Problem. A Novel Application of Machine Learning (11 2022). [arXiv:2211.09584](https://arxiv.org/abs/2211.09584).

[510] S. Lawrence, Y. Yamauchi, Normalizing Flows and the Real-Time Sign Problem, *Phys. Rev. D* 103 (11) (2021) 114509. [arXiv:2101.05755](https://arxiv.org/abs/2101.05755), [doi:10.1103/PhysRevD.103.114509](https://doi.org/10.1103/PhysRevD.103.114509).

[511] Y. Yamauchi, S. Lawrence, Normalizing flows for the real-time sign problem, *PoS LATTICE2021* (2022) 621. [arXiv:2112.15035](https://arxiv.org/abs/2112.15035), [doi:10.22323/1.396.0621](https://doi.org/10.22323/1.396.0621).

[512] S. Lawrence, H. Oh, Y. Yamauchi, Lattice scalar field theory at complex coupling, *Phys. Rev. D* 106 (11) (2022) 114503. [arXiv:2205.12303](https://arxiv.org/abs/2205.12303), [doi:10.1103/PhysRevD.106.114503](https://doi.org/10.1103/PhysRevD.106.114503).

[513] J. M. Pawłowski, J. M. Urban, Flow-based density of states for complex actions (3 2022). [arXiv:2203.01243](https://arxiv.org/abs/2203.01243).

[514] Z.-Q. Wan, S.-X. Zhang, H. Yao, Mitigating the fermion sign problem by automatic differentiation, *Phys. Rev. B* 106 (24) (2022) L241109. [arXiv:2010.01141](https://arxiv.org/abs/2010.01141), [doi:10.1103/PhysRevB.106.L241109](https://doi.org/10.1103/PhysRevB.106.L241109).

[515] Y. Mori, K. Kashiwa, A. Ohnishi, Toward solving the sign problem with path optimization method, *Phys. Rev. D* 96 (11) (2017) 111501. [arXiv:1705.05605](https://arxiv.org/abs/1705.05605), [doi:10.1103/PhysRevD.96.111501](https://doi.org/10.1103/PhysRevD.96.111501).

[516] Y. Mori, K. Kashiwa, A. Ohnishi, Application of a neural network to the sign problem via the path optimization method, *PTEP* 2018 (2) (2018) 023B04. [arXiv:1709.03208](https://arxiv.org/abs/1709.03208), [doi:10.1093/ptep/ptx191](https://doi.org/10.1093/ptep/ptx191).

[517] K. Kashiwa, Y. Mori, A. Ohnishi, Application of the path optimization method to the sign problem in an effective model of QCD with a repulsive vector-type interaction, *Phys. Rev. D* 99 (11) (2019) 114005. [arXiv:1903.03679](https://arxiv.org/abs/1903.03679), [doi:10.1103/PhysRevD.99.114005](https://doi.org/10.1103/PhysRevD.99.114005).

[518] K. Kashiwa, Y. Mori, A. Ohnishi, Controlling the model sign problem via the path optimization method: Monte Carlo approach to a QCD effective model with Polyakov loop, *Phys. Rev. D* 99 (1) (2019) 014033. [arXiv:1805.08940](https://arxiv.org/abs/1805.08940), [doi:10.1103/PhysRevD.99.014033](https://doi.org/10.1103/PhysRevD.99.014033).

[519] F. Bursa, M. Kroyter, A simple approach towards the sign problem using path optimisation, *JHEP* 12 (2018) 054. [arXiv:1805.04941](https://arxiv.org/abs/1805.04941), [doi:10.1007/JHEP12\(2018\)054](https://doi.org/10.1007/JHEP12(2018)054).

[520] Y. Mori, K. Kashiwa, A. Ohnishi, Path optimization in 0 + 1D QCD at finite density, *PTEP* 2019 (11) (2019) 113B01. [arXiv:1904.11140](https://arxiv.org/abs/1904.11140), [doi:10.1093/ptep/ptz111](https://doi.org/10.1093/ptep/ptz111).

[521] W. Detmold, G. Kanwar, H. Lamm, M. L. Wagman, N. C. Warrington, Path integral contour deformations for observables in $SU(N)$ gauge theory, Phys. Rev. D 103 (9) (2021) 094517. [arXiv:2101.12668](https://arxiv.org/abs/2101.12668), doi:10.1103/PhysRevD.103.094517.

[522] A. Alexandru, P. F. Bedaque, H. Lamm, S. Lawrence, Finite-Density Monte Carlo Calculations on Sign-Optimized Manifolds, Phys. Rev. D 97 (9) (2018) 094510. [arXiv:1804.00697](https://arxiv.org/abs/1804.00697), doi:10.1103/PhysRevD.97.094510.

[523] A. Alexandru, P. F. Bedaque, H. Lamm, S. Lawrence, N. C. Warrington, Fermions at Finite Density in 2+1 Dimensions with Sign-Optimized Manifolds, Phys. Rev. Lett. 121 (19) (2018) 191602. [arXiv:1808.09799](https://arxiv.org/abs/1808.09799), doi:10.1103/PhysRevLett.121.191602.

[524] Y. Namekawa, K. Kashiwa, A. Ohnishi, H. Takase, Gauge invariant input to neural network for path optimization method, Phys. Rev. D 105 (3) (2022) 034502. [arXiv:2109.11710](https://arxiv.org/abs/2109.11710), doi:10.1103/PhysRevD.105.034502.

[525] Y. Namekawa, K. Kashiwa, H. Matsuda, A. Ohnishi, H. Takase, Improving efficiency of the path optimization method for a gauge theory (10 2022). [arXiv:2210.05402](https://arxiv.org/abs/2210.05402).

[526] V. Dexheimer, J. Noronha, J. Noronha-Hostler, C. Ratti, N. Yunes, Future physics perspectives on the equation of state from heavy ion collisions to neutron stars, J. Phys. G 48 (7) (2021) 073001. [arXiv:2010.08834](https://arxiv.org/abs/2010.08834), doi:10.1088/1361-6471/abe104.

[527] A. L. Watts, et al., Colloquium : Measuring the neutron star equation of state using x-ray timing, Rev. Mod. Phys. 88 (2) (2016) 021001. [arXiv:1602.01081](https://arxiv.org/abs/1602.01081), doi:10.1103/RevModPhys.88.021001.

[528] F. Özel, P. Freire, Masses, Radii, and the Equation of State of Neutron Stars, Ann. Rev. Astron. Astrophys. 54 (2016) 401–440. [arXiv:1603.02698](https://arxiv.org/abs/1603.02698), doi:10.1146/annurev-astro-081915-023322.

[529] G. Baym, T. Hatsuda, T. Kojo, P. D. Powell, Y. Song, T. Takatsuka, From hadrons to quarks in neutron stars: a review, Rept. Prog. Phys. 81 (5) (2018) 056902. [arXiv:1707.04966](https://arxiv.org/abs/1707.04966), doi:10.1088/1361-6633/aaae14.

[530] L. Baiotti, Gravitational waves from neutron star mergers and their relation to the nuclear equation of state, Prog. Part. Nucl. Phys. 109 (2019) 103714. [arXiv:1907.08534](https://arxiv.org/abs/1907.08534), doi:10.1016/j.ppnp.2019.103714.

[531] T. Kojo, QCD equations of state and speed of sound in neutron stars, AAPPS Bull. 31 (1) (2021) 11. [arXiv:2011.10940](https://arxiv.org/abs/2011.10940), doi:10.1007/s43673-021-00011-6.

[532] J. M. Lattimer, Neutron Stars and the Nuclear Matter Equation of State, Ann. Rev. Nucl. Part. Sci. 71 (2021) 433–464. doi:10.1146/annurev-nucl-102419-124827.

[533] K. Fukushima, C. Sasaki, The phase diagram of nuclear and quark matter at high baryon density, Prog. Part. Nucl. Phys. 72 (2013) 99–154. [arXiv:1301.6377](https://arxiv.org/abs/1301.6377), doi:10.1016/j.ppnp.2013.05.003.

[534] G. F. Burgio, H. J. Schulze, I. Vidana, J. B. Wei, Neutron stars and the nuclear equation of state, Prog. Part. Nucl. Phys. 120 (2021) 103879. [arXiv:2105.03747](https://arxiv.org/abs/2105.03747), doi:10.1016/j.ppnp.2021.103879.

[535] C. Drischler, J. W. Holt, C. Wellenhofer, Chiral Effective Field Theory and the High-Density Nuclear Equation of State, Ann. Rev. Nucl. Part. Sci. 71 (2021) 403–432. [arXiv:2101.01709](https://arxiv.org/abs/2101.01709), doi:10.1146/annurev-nucl-102419-041903.

[536] J. Ghiglieri, A. Kurkela, M. Strickland, A. Vuorinen, Perturbative Thermal QCD: Formalism and Applications, *Phys. Rept.* 880 (2020) 1–73. [arXiv:2002.10188](https://arxiv.org/abs/2002.10188), [doi:10.1016/j.physrep.2020.07.004](https://doi.org/10.1016/j.physrep.2020.07.004).

[537] M. C. Miller, Astrophysical Constraints on Dense Matter in Neutron Stars, *Astrophys. Space Sci. Libr.* 461 (2020) 1–51. [arXiv:1312.0029](https://arxiv.org/abs/1312.0029), [doi:10.1007/978-3-662-62110-3_1](https://doi.org/10.1007/978-3-662-62110-3_1).

[538] M. C. Miller, F. K. Lamb, Observational Constraints on Neutron Star Masses and Radii, *Eur. Phys. J. A* 52 (3) (2016) 63. [arXiv:1604.03894](https://arxiv.org/abs/1604.03894), [doi:10.1140/epja/i2016-16063-8](https://doi.org/10.1140/epja/i2016-16063-8).

[539] Z. Arzoumanian, K. C. Gendreau, C. L. Baker, T. Cazeau, P. Hestnes, J. W. Kellogg, S. J. Kenyon, R. P. Kozon, K.-C. Liu, S. S. Manthripragada, C. B. Markwardt, A. L. Mitchell, J. W. Mitchell, C. A. Monroe, T. Okajima, S. E. Pollard, D. F. Powers, B. J. Savadkin, L. B. Winternitz, P. T. Chen, M. R. Wright, R. Foster, G. Prigozhin, R. Remillard, J. Doty, [The neutron star interior composition explorer \(NICER\): mission definition](#), in: T. Takahashi, J.-W. A. den Herder, M. Bautz (Eds.), *Space Telescopes and Instrumentation 2014: Ultraviolet to Gamma Ray*, Vol. 9144, International Society for Optics and Photonics, SPIE, 2014, p. 914420. [doi:10.1117/12.2056811](https://doi.org/10.1117/12.2056811).
URL <https://doi.org/10.1117/12.2056811>

[540] K. Gendreau, Z. Arzoumanian, Searching for a pulse, *Nature Astronomy* 1 (12) (2017) 895–895.

[541] N. Yunes, M. C. Miller, K. Yagi, Gravitational-wave and X-ray probes of the neutron star equation of state, *Nature Rev. Phys.* 4 (4) (2022) 237–246. [arXiv:2202.04117](https://arxiv.org/abs/2202.04117), [doi:10.1038/s42254-022-00420-y](https://doi.org/10.1038/s42254-022-00420-y).

[542] K. Yagi, N. Yunes, I-Love-Q, *Science* 341 (2013) 365–368. [arXiv:1302.4499](https://arxiv.org/abs/1302.4499), [doi:10.1126/science.1236462](https://doi.org/10.1126/science.1236462).

[543] B. P. Abbott, et al., GWTC-1: A Gravitational-Wave Transient Catalog of Compact Binary Mergers Observed by LIGO and Virgo during the First and Second Observing Runs, *Phys. Rev. X* 9 (3) (2019) 031040. [arXiv:1811.12907](https://arxiv.org/abs/1811.12907), [doi:10.1103/PhysRevX.9.031040](https://doi.org/10.1103/PhysRevX.9.031040).

[544] R. Abbott, et al., GWTC-2: Compact Binary Coalescences Observed by LIGO and Virgo During the First Half of the Third Observing Run, *Phys. Rev. X* 11 (2021) 021053. [arXiv:2010.14527](https://arxiv.org/abs/2010.14527), [doi:10.1103/PhysRevX.11.021053](https://doi.org/10.1103/PhysRevX.11.021053).

[545] B. P. Abbott, et al., GW170817: Observation of Gravitational Waves from a Binary Neutron Star Inspiral, *Phys. Rev. Lett.* 119 (16) (2017) 161101. [arXiv:1710.05832](https://arxiv.org/abs/1710.05832), [doi:10.1103/PhysRevLett.119.161101](https://doi.org/10.1103/PhysRevLett.119.161101).

[546] B. P. Abbott, et al., GW170817: Measurements of neutron star radii and equation of state, *Phys. Rev. Lett.* 121 (16) (2018) 161101. [arXiv:1805.11581](https://arxiv.org/abs/1805.11581), [doi:10.1103/PhysRevLett.121.161101](https://doi.org/10.1103/PhysRevLett.121.161101).

[547] B. P. Abbott, et al., GW190425: Observation of a Compact Binary Coalescence with Total Mass $\sim 3.4M_{\odot}$, *Astrophys. J. Lett.* 892 (1) (2020) L3. [arXiv:2001.01761](https://arxiv.org/abs/2001.01761), [doi:10.3847/2041-8213/ab75f5](https://doi.org/10.3847/2041-8213/ab75f5).

[548] R. Abbott, et al., Observation of Gravitational Waves from Two Neutron Star–Black Hole Coalescences, *Astrophys. J. Lett.* 915 (1) (2021) L5. [arXiv:2106.15163](https://arxiv.org/abs/2106.15163), [doi:10.3847/2041-8213/ac082e](https://doi.org/10.3847/2041-8213/ac082e).

[549] E. Annala, T. Gorda, E. Katerini, A. Kurkela, J. Nättilä, V. Paschalidis, A. Vuorinen, Multimessenger Constraints for Ultradense Matter, *Phys. Rev. X* 12 (1) (2022) 011058. [arXiv:2105.05132](https://arxiv.org/abs/2105.05132), [doi:10.1103/PhysRevX.12.011058](https://doi.org/10.1103/PhysRevX.12.011058).

[550] C. J. Fluke, C. Jacobs, Surveying the reach and maturity of machine learning and artificial intelligence in astronomy, *WIREs Data Mining and Knowledge Discovery* 10 (2) (2020) e1349. [arXiv:1912.02934](https://arxiv.org/abs/1912.02934), [doi:10.1002/widm.1349](https://doi.org/10.1002/widm.1349).

[551] J. Schaffner-Bielich, Compact Star Physics, Cambridge University Press, 2020. [doi:10.1017/9781316848357](https://doi.org/10.1017/9781316848357).

[552] R. C. Tolman, Static solutions of Einstein's field equations for spheres of fluid, *Phys. Rev.* 55 (1939) 364–373. [doi:10.1103/PhysRev.55.364](https://doi.org/10.1103/PhysRev.55.364).

[553] J. R. Oppenheimer, G. M. Volkoff, On massive neutron cores, *Phys. Rev.* 55 (1939) 374–381. [doi:10.1103/PhysRev.55.374](https://doi.org/10.1103/PhysRev.55.374).

[554] P. G. Krastev, Translating Neutron Star Observations to Nuclear Symmetry Energy via Deep Neural Networks, *Galaxies* 10 (1) (2022) 16. [arXiv:2112.04089](https://arxiv.org/abs/2112.04089), [doi:10.3390/galaxies10010016](https://doi.org/10.3390/galaxies10010016).

[555] M.-Z. Han, J.-L. Jiang, S.-P. Tang, Y.-Z. Fan, Bayesian Nonparametric Inference of the Neutron Star Equation of State via a Neural Network, *Astrophys. J.* 919 (1) (2021) 11. [arXiv:2103.05408](https://arxiv.org/abs/2103.05408), [doi:10.3847/1538-4357/ac11f8](https://doi.org/10.3847/1538-4357/ac11f8).

[556] P. Demorest, T. Pennucci, S. Ransom, M. Roberts, J. Hessels, Shapiro Delay Measurement of A Two Solar Mass Neutron Star, *Nature* 467 (2010) 1081–1083. [arXiv:1010.5788](https://arxiv.org/abs/1010.5788), [doi:10.1038/nature09466](https://doi.org/10.1038/nature09466).

[557] R. V. Lobato, E. V. Chimanski, C. A. Bertulani, Unsupervised machine learning correlations in EoS of neutron stars, PoS XVHadronPhysics (2022) 062. [arXiv:2202.13940](https://arxiv.org/abs/2202.13940), [doi:10.22323/1.408.0062](https://doi.org/10.22323/1.408.0062).

[558] L. Lindblom, Spectral Representations of Neutron-Star Equations of State, *Phys. Rev. D* 82 (2010) 103011. [arXiv:1009.0738](https://arxiv.org/abs/1009.0738), [doi:10.1103/PhysRevD.82.103011](https://doi.org/10.1103/PhysRevD.82.103011).

[559] L. Lindblom, Improved spectral representations of neutron-star equations of state, *Phys. Rev. D* 105 (6) (2022) 063031. [arXiv:2202.12285](https://arxiv.org/abs/2202.12285), [doi:10.1103/PhysRevD.105.063031](https://doi.org/10.1103/PhysRevD.105.063031).

[560] J. S. Read, B. D. Lackey, B. J. Owen, J. L. Friedman, Constraints on a phenomenologically parameterized neutron-star equation of state, *Phys. Rev. D* 79 (2009) 124032. [arXiv:0812.2163](https://arxiv.org/abs/0812.2163), [doi:10.1103/PhysRevD.79.124032](https://doi.org/10.1103/PhysRevD.79.124032).

[561] F. Ozel, D. Psaltis, Reconstructing the Neutron-Star Equation of State from Astrophysical Measurements, *Phys. Rev. D* 80 (2009) 103003. [arXiv:0905.1959](https://arxiv.org/abs/0905.1959), [doi:10.1103/PhysRevD.80.103003](https://doi.org/10.1103/PhysRevD.80.103003).

[562] A. W. Steiner, J. M. Lattimer, E. F. Brown, The Equation of State from Observed Masses and Radii of Neutron Stars, *Astrophys. J.* 722 (2010) 33–54. [arXiv:1005.0811](https://arxiv.org/abs/1005.0811), [doi:10.1088/0004-637X/722/1/33](https://doi.org/10.1088/0004-637X/722/1/33).

[563] A. W. Steiner, J. M. Lattimer, E. F. Brown, The Neutron Star Mass-Radius Relation and the Equation of State of Dense Matter, *Astrophys. J. Lett.* 765 (2013) L5. [arXiv:1205.6871](https://arxiv.org/abs/1205.6871), [doi:10.1088/2041-8205/765/1/L5](https://doi.org/10.1088/2041-8205/765/1/L5).

[564] C. A. Raithel, F. Ozel, D. Psaltis, From Neutron Star Observables to the Equation of State: An Optimal Parametrization, *Astrophys. J.* 831 (1) (2016) 44. [arXiv:1605.03591](https://arxiv.org/abs/1605.03591), [doi:10.3847/0004-637X/831/1/44](https://doi.org/10.3847/0004-637X/831/1/44).

[565] C. A. Raithel, F. Özel, D. Psaltis, From Neutron Star Observables to the Equation of State. II. Bayesian Inference of Equation of State Pressures, *Astrophys. J.* 844 (2) (2017) 156. [arXiv:1704.00737](https://arxiv.org/abs/1704.00737), [doi:10.3847/1538-4357/aa7a5a](https://doi.org/10.3847/1538-4357/aa7a5a).

[566] P. Landry, R. Essick, Nonparametric inference of the neutron star equation of state from gravitational wave observations, *Phys. Rev. D* 99 (8) (2019) 084049. [arXiv:1811.12529](https://arxiv.org/abs/1811.12529), [doi:10.1103/PhysRevD.99.084049](https://doi.org/10.1103/PhysRevD.99.084049).

[567] S. Soma, L. Wang, S. Shi, H. Stöcker, K. Zhou, Neural network reconstruction of the dense matter equation of state from neutron star observables, *JCAP* 08 (2022) 071. [arXiv:2201.01756](https://arxiv.org/abs/2201.01756), [doi:10.1088/1475-7516/2022/08/071](https://doi.org/10.1088/1475-7516/2022/08/071).

[568] S. Soma, L. Wang, S. Shi, H. Stöcker, K. Zhou, Reconstructing the neutron star equation of state from observational data via automatic differentiation (9 2022). [arXiv:2209.08883](https://arxiv.org/abs/2209.08883).

[569] M.-Z. Han, S.-P. Tang, Y.-Z. Fan, Nonparametric Representation of Neutron Star Equation of State Using Variational Auto-Encoder (5 2022). [arXiv:2205.03855](https://arxiv.org/abs/2205.03855).

[570] J. Margueron, R. Hoffmann Casali, F. Gulminelli, Equation of state for dense nucleonic matter from metamodeling. I. Foundational aspects, *Phys. Rev. C* 97 (2) (2018) 025805. [arXiv:1708.06894](https://arxiv.org/abs/1708.06894), [doi:10.1103/PhysRevC.97.025805](https://doi.org/10.1103/PhysRevC.97.025805).

[571] J. Margueron, R. Hoffmann Casali, F. Gulminelli, Equation of state for dense nucleonic matter from metamodeling. II. Predictions for neutron star properties, *Phys. Rev. C* 97 (2) (2018) 025806. [arXiv:1708.06895](https://arxiv.org/abs/1708.06895), [doi:10.1103/PhysRevC.97.025806](https://doi.org/10.1103/PhysRevC.97.025806).

[572] W.-J. Xie, B.-A. Li, Bayesian Inference of High-density Nuclear Symmetry Energy from Radii of Canonical Neutron Stars, *Astrophys. J.* 883 (2019) 174. [arXiv:1907.10741](https://arxiv.org/abs/1907.10741), [doi:10.3847/1538-4357/ab3f37](https://doi.org/10.3847/1538-4357/ab3f37).

[573] L. Brandes, W. Weise, N. Kaiser, Inference of the sound speed and related properties of neutron stars (8 2022). [arXiv:2208.03026](https://arxiv.org/abs/2208.03026).

[574] S. Altiparmak, C. Ecker, L. Rezzolla, On the Sound Speed in Neutron Stars, *Astrophys. J. Lett.* 939 (2) (2022) L34. [arXiv:2203.14974](https://arxiv.org/abs/2203.14974), [doi:10.3847/2041-8213/ac9b2a](https://doi.org/10.3847/2041-8213/ac9b2a).

[575] C. Ecker, L. Rezzolla, A General, Scale-independent Description of the Sound Speed in Neutron Stars, *Astrophys. J. Lett.* 939 (2) (2022) L35. [arXiv:2207.04417](https://arxiv.org/abs/2207.04417), [doi:10.3847/2041-8213/ac8674](https://doi.org/10.3847/2041-8213/ac8674).

[576] J.-L. Jiang, C. Ecker, L. Rezzolla, Bayesian analysis of neutron-star properties with parameterized equations of state: the role of the likelihood functions (10 2022). [arXiv:2211.00018](https://arxiv.org/abs/2211.00018).

[577] G. D'Agostini, Bayesian inference in processing experimental data: principles and basic applications, *Reports on Progress in Physics* 66 (9) (2003) 1383.

[578] J. Berkson, Minimum chi-square, not maximum likelihood!, *The Annals of Statistics* 8 (3) (1980) 457–487.

[579] S. Bogdanov, et al., Snowmass 2021 Cosmic Frontier White Paper: The Dense Matter Equation of State and QCD Phase Transitions, in: 2022 Snowmass Summer Study, 2022. [arXiv:2209.07412](https://arxiv.org/abs/2209.07412).

[580] P. B. Demorest, T. Pennucci, S. M. Ransom, M. S. E. Roberts, J. W. T. Hessels, A two-solar-mass neutron star measured using Shapiro delay, *Nature* 467 (7319) (2010) 1081–1083. [arXiv:1010.5788](https://arxiv.org/abs/1010.5788), [doi:10.1038/nature09466](https://doi.org/10.1038/nature09466).

[581] J. Antoniadis, P. C. C. Freire, N. Wex, T. M. Tauris, R. S. Lynch, M. H. van Kerkwijk, M. Kramer, C. Bassa, V. S. Dhillon, T. Driebe, J. W. T. Hessels, V. M. Kaspi, V. I. Kondratiev, N. Langer, T. R. Marsh, M. A. McLaughlin, T. T. Pennucci, S. M. Ransom, I. H. Stairs, J. van Leeuwen, J. P. W. Verbiest, D. G. Whelan, A Massive Pulsar in a Compact Relativistic Binary, *Science* 340 (6131) (2013) 448. [arXiv:1304.6875](https://arxiv.org/abs/1304.6875), [doi:10.1126/science.1233232](https://doi.org/10.1126/science.1233232).

[582] H. T. Cromartie, E. Fonseca, S. M. Ransom, P. B. Demorest, Z. Arzoumanian, H. Blumer, P. R. Brook, M. E. DeCesar, T. Dolch, J. A. Ellis, R. D. Ferdman, E. C. Ferrara, N. Garver-Daniels, P. A. Gentile, M. L. Jones, M. T. Lam, D. R. Lorimer, R. S. Lynch, M. A. McLaughlin, C. Ng, D. J. Nice, T. T. Pennucci, R. Spiewak, I. H. Stairs, K. Stovall, J. K. Swiggum, W. W. Zhu, Relativistic Shapiro delay measurements of an extremely massive millisecond pulsar, *Nature Astronomy* 4 (2020) 72–76. [arXiv:1904.06759](https://arxiv.org/abs/1904.06759), doi:10.1038/s41550-019-0880-2.

[583] P. Landry, B. Kumar, Constraints on the moment of inertia of PSR J0737-3039A from GW170817, *Astrophys. J. Lett.* 868 (2) (2018) L22. [arXiv:1807.04727](https://arxiv.org/abs/1807.04727), doi:10.3847/2041-8213/aaee76.

[584] Z. Miao, A. Li, Z.-G. Dai, On the moment of inertia of PSR J0737-3039 A from LIGO/Virgo and NICER, *Mon. Not. Roy. Astron. Soc.* 515 (4) (2022) 5071–5080. [arXiv:2107.07979](https://arxiv.org/abs/2107.07979), doi:10.1093/mnras/stac2015.

[585] M. C. Miller, et al., PSR J0030+0451 Mass and Radius from *NICER* Data and Implications for the Properties of Neutron Star Matter, *Astrophys. J. Lett.* 887 (1) (2019) L24. [arXiv:1912.05705](https://arxiv.org/abs/1912.05705), doi:10.3847/2041-8213/ab50c5.

[586] T. E. Riley, et al., A *NICER* View of PSR J0030+0451: Millisecond Pulsar Parameter Estimation, *Astrophys. J. Lett.* 887 (1) (2019) L21. [arXiv:1912.05702](https://arxiv.org/abs/1912.05702), doi:10.3847/2041-8213/ab481c.

[587] M. C. Miller, et al., The Radius of PSR J0740+6620 from NICER and XMM-Newton Data, *Astrophys. J. Lett.* 918 (2) (2021) L28. [arXiv:2105.06979](https://arxiv.org/abs/2105.06979), doi:10.3847/2041-8213/ac089b.

[588] T. E. Riley, et al., A NICER View of the Massive Pulsar PSR J0740+6620 Informed by Radio Timing and XMM-Newton Spectroscopy, *Astrophys. J. Lett.* 918 (2) (2021) L27. [arXiv:2105.06980](https://arxiv.org/abs/2105.06980), doi:10.3847/2041-8213/ac0a81.

[589] R. Essick, P. Landry, D. E. Holz, Nonparametric Inference of Neutron Star Composition, Equation of State, and Maximum Mass with GW170817, *Phys. Rev. D* 101 (6) (2020) 063007. [arXiv:1910.09740](https://arxiv.org/abs/1910.09740), doi:10.1103/PhysRevD.101.063007.

[590] L. Lindblom, Determining the Nuclear Equation of State from Neutron-Star Masses and Radii, *Astrophysical Journal* 398 (1992) 569. doi:10.1086/171882.

[591] L.-G. Pang, K. Zhou, X.-N. Wang, Deep learning for nuclear physics 37 (3) 720–726. doi:10.11804/NuclPhysRev.37.2019CNPC41.

[592] Y. Fujimoto, K. Fukushima, K. Murase, Extensive Studies of the Neutron Star Equation of State from the Deep Learning Inference with the Observational Data Augmentation, *JHEP* 03 (2021) 273. [arXiv:2101.08156](https://arxiv.org/abs/2101.08156), doi:10.1007/JHEP03(2021)273.

[593] Y. Fujimoto, K. Fukushima, K. Murase, Methodology study of machine learning for the neutron star equation of state, *Phys. Rev. D* 98 (2) (2018) 023019. [arXiv:1711.06748](https://arxiv.org/abs/1711.06748), doi:10.1103/PhysRevD.98.023019.

[594] Y. Fujimoto, K. Fukushima, K. Murase, Mapping neutron star data to the equation of state using the deep neural network, *Phys. Rev. D* 101 (5) (2020) 054016. [arXiv:1903.03400](https://arxiv.org/abs/1903.03400), doi:10.1103/PhysRevD.101.054016.

[595] F. Morawski, M. Bejger, Neural network reconstruction of the dense matter equation of state derived from the parameters of neutron stars, *Astron. Astrophys.* 642 (2020) A78. [arXiv:2006.07194](https://arxiv.org/abs/2006.07194), doi:10.1051/0004-6361/202038130.

[596] F. Morawski, M. Bejger, Detecting dense-matter phase transition signatures in neutron star mass-radius measurements as data anomalies using normalizing flows, *Phys. Rev. C* 106 (6) (2022) 065802. [arXiv:2212.05480](https://arxiv.org/abs/2212.05480), [doi:10.1103/PhysRevC.106.065802](https://doi.org/10.1103/PhysRevC.106.065802).

[597] S. Traversi, P. Char, Structure of Quark Star: A Comparative Analysis of Bayesian Inference and Neural Network Based Modeling, *Astrophys. J.* 905 (1) (2020) 9. [arXiv:2007.10239](https://arxiv.org/abs/2007.10239), [doi:10.3847/1538-4357/abbfb4](https://doi.org/10.3847/1538-4357/abbfb4).

[598] J. Nättilä, M. C. Miller, A. W. Steiner, J. J. E. Kajava, V. F. Suleimanov, J. Poutanen, Neutron star mass and radius measurements from atmospheric model fits to X-ray burst cooling tail spectra, *Astron. Astrophys.* 608 (2017) A31. [arXiv:1709.09120](https://arxiv.org/abs/1709.09120), [doi:10.1051/0004-6361/201731082](https://doi.org/10.1051/0004-6361/201731082).

[599] S. Bogdanov, et al., Constraining the Neutron Star Mass–Radius Relation and Dense Matter Equation of State with *NICER*. I. The Millisecond Pulsar X-Ray Data Set, *Astrophys. J. Lett.* 887 (1) (2019) L25. [arXiv:1912.05706](https://arxiv.org/abs/1912.05706), [doi:10.3847/2041-8213/ab53eb](https://doi.org/10.3847/2041-8213/ab53eb).

[600] E. E. Flanagan, T. Hinderer, Constraining neutron star tidal Love numbers with gravitational wave detectors, *Phys. Rev. D* 77 (2008) 021502. [arXiv:0709.1915](https://arxiv.org/abs/0709.1915), [doi:10.1103/PhysRevD.77.021502](https://doi.org/10.1103/PhysRevD.77.021502).

[601] T. Hinderer, Tidal Love numbers of neutron stars, *Astrophys. J.* 677 (2008) 1216–1220. [arXiv:0711.2420](https://arxiv.org/abs/0711.2420), [doi:10.1086/533487](https://doi.org/10.1086/533487).

[602] P. Landry, R. Essick, K. Chatzioannou, Nonparametric constraints on neutron star matter with existing and upcoming gravitational wave and pulsar observations, *Phys. Rev. D* 101 (12) (2020) 123007. [arXiv:2003.04880](https://arxiv.org/abs/2003.04880), [doi:10.1103/PhysRevD.101.123007](https://doi.org/10.1103/PhysRevD.101.123007).

[603] Z. Miao, J.-L. Jiang, A. Li, L.-W. Chen, Bayesian Inference of Strange Star Equation of State Using the GW170817 and GW190425 Data, *Astrophys. J. Lett.* 917 (2) (2021) L22. [arXiv:2107.13997](https://arxiv.org/abs/2107.13997), [doi:10.3847/2041-8213/ac194d](https://doi.org/10.3847/2041-8213/ac194d).

[604] J. Golomb, C. Talbot, Hierarchical Inference of Binary Neutron Star Mass Distribution and Equation of State with Gravitational Waves, *Astrophys. J.* 926 (1) (2022) 79. [arXiv:2106.15745](https://arxiv.org/abs/2106.15745), [doi:10.3847/1538-4357/ac43bc](https://doi.org/10.3847/1538-4357/ac43bc).

[605] E. V. Chimanski, R. V. Lobato, A. R. Goncalves, C. A. Bertulani, Bayesian Inference of Phenomenological EoS of Neutron Stars with Recent Observations (5 2022). [arXiv:2205.01174](https://arxiv.org/abs/2205.01174).

[606] S. De, D. Finstad, J. M. Lattimer, D. A. Brown, E. Berger, C. M. Biwer, Tidal Deformabilities and Radii of Neutron Stars from the Observation of GW170817, *Phys. Rev. Lett.* 121 (9) (2018) 091102, [Erratum: *Phys. Rev. Lett.* 121, 259902 (2018)]. [arXiv:1804.08583](https://arxiv.org/abs/1804.08583), [doi:10.1103/PhysRevLett.121.091102](https://doi.org/10.1103/PhysRevLett.121.091102).

[607] B. P. Abbott, et al., Properties of the binary neutron star merger GW170817, *Phys. Rev. X* 9 (1) (2019) 011001. [arXiv:1805.11579](https://arxiv.org/abs/1805.11579), [doi:10.1103/PhysRevX.9.011001](https://doi.org/10.1103/PhysRevX.9.011001).

[608] M. a. Ferreira, C. Providênci, Unveiling the nuclear matter EoS from neutron star properties: a supervised machine learning approach, *JCAP* 07 (2021) 011. [arXiv:1910.05554](https://arxiv.org/abs/1910.05554), [doi:10.1088/1475-7516/2021/07/011](https://doi.org/10.1088/1475-7516/2021/07/011).

[609] F. Hernandez Vivanco, R. Smith, E. Thrane, P. D. Lasky, C. Talbot, V. Raymond, [Measuring the neutron star equation of state with gravitational waves: The first forty binary neutron star merger observations](#), *Phys. Rev. D*

100 (2019) 103009. [doi:10.1103/PhysRevD.100.103009](https://doi.org/10.1103/PhysRevD.100.103009).

URL <https://link.aps.org/doi/10.1103/PhysRevD.100.103009>

[610] F. Hernandez Vivanco, R. Smith, E. Thrane, P. D. Lasky, A scalable random forest regressor for combining neutron-star equation of state measurements: A case study with GW170817 and GW190425, *Mon. Not. Roy. Astron. Soc.* 499 (4) (2020) 5972–5977. [arXiv:2008.05627](https://arxiv.org/abs/2008.05627), [doi:10.1093/mnras/staa3243](https://doi.org/10.1093/mnras/staa3243).

[611] G. Gonçalves, M. Ferreira, J. a. Aveiro, A. Onofre, F. F. Freitas, C. Providênci, J. A. Font, Machine-Learning Love: classifying the equation of state of neutron stars with Transformers (10 2022). [arXiv:2210.08382](https://arxiv.org/abs/2210.08382).

[612] D. Farrell, P. Baldi, J. Ott, A. Ghosh, A. W. Steiner, A. Kavikar, L. Lindblom, D. Whiteson, F. Weber, Deducing neutron star equation of state parameters directly from telescope spectra with uncertainty-aware machine learning, *JCAP* 02 (2023) 016. [arXiv:2209.02817](https://arxiv.org/abs/2209.02817), [doi:10.1088/1475-7516/2023/02/016](https://doi.org/10.1088/1475-7516/2023/02/016).

[613] P. D’Avanzo, Short gamma-ray bursts: A review, *JHEAp* 7 (2015) 73–80. [doi:10.1016/j.jheap.2015.07.002](https://doi.org/10.1016/j.jheap.2015.07.002).

[614] P. S. Cowperthwaite, et al., The Electromagnetic Counterpart of the Binary Neutron Star Merger LIGO/Virgo GW170817. II. UV, Optical, and Near-infrared Light Curves and Comparison to Kilonova Models, *Astrophys. J. Lett.* 848 (2) (2017) L17. [arXiv:1710.05840](https://arxiv.org/abs/1710.05840), [doi:10.3847/2041-8213/aa8fc7](https://doi.org/10.3847/2041-8213/aa8fc7).

[615] Y.-J. Huang, L. Baiotti, T. Kojo, K. Takami, H. Sotani, H. Togashi, T. Hatsuda, S. Nagataki, Y.-Z. Fan, Merger and Postmerger of Binary Neutron Stars with a Quark-Hadron Crossover Equation of State, *Phys. Rev. Lett.* 129 (18) (2022) 181101. [arXiv:2203.04528](https://arxiv.org/abs/2203.04528), [doi:10.1103/PhysRevLett.129.181101](https://doi.org/10.1103/PhysRevLett.129.181101).

[616] Y. Fujimoto, K. Fukushima, K. Hotokezaka, K. Kyutoku, Gravitational Wave Signal for Quark Matter with Realistic Phase Transition (5 2022). [arXiv:2205.03882](https://arxiv.org/abs/2205.03882).

[617] M. Baldo, G. F. Burgio, The nuclear symmetry energy, *Prog. Part. Nucl. Phys.* 91 (2016) 203–258. [arXiv:1606.08838](https://arxiv.org/abs/1606.08838), [doi:10.1016/j.ppnp.2016.06.006](https://doi.org/10.1016/j.ppnp.2016.06.006).

[618] B.-A. Li, B.-J. Cai, W.-J. Xie, N.-B. Zhang, Progress in Constraining Nuclear Symmetry Energy Using Neutron Star Observables Since GW170817, *Universe* 7 (6) (2021) 182. [arXiv:2105.04629](https://arxiv.org/abs/2105.04629), [doi:10.3390/universe7060182](https://doi.org/10.3390/universe7060182).

[619] N.-B. Zhang, B.-A. Li, J. Xu, Combined Constraints on the Equation of State of Dense Neutron-rich Matter from Terrestrial Nuclear Experiments and Observations of Neutron Stars, *Astrophys. J.* 859 (2) (2018) 90. [arXiv:1801.06855](https://arxiv.org/abs/1801.06855), [doi:10.3847/1538-4357/aac027](https://doi.org/10.3847/1538-4357/aac027).

[620] B.-A. Li, P. G. Krastev, D.-H. Wen, N.-B. Zhang, Towards Understanding Astrophysical Effects of Nuclear Symmetry Energy, *Eur. Phys. J. A* 55 (7) (2019) 117. [arXiv:1905.13175](https://arxiv.org/abs/1905.13175), [doi:10.1140/epja/i2019-12780-8](https://doi.org/10.1140/epja/i2019-12780-8).

[621] M. U. Anil, K. Banerjee, T. Malik, C. Providênci, The neutron star outer crust equation of state: a machine learning approach, *JCAP* 01 (01) (2022) 045. [arXiv:2004.14196](https://arxiv.org/abs/2004.14196), [doi:10.1088/1475-7516/2022/01/045](https://doi.org/10.1088/1475-7516/2022/01/045).

[622] W.-J. Xie, B.-A. Li, Bayesian inference of the dense-matter equation of state encapsulating a first-order hadron-quark phase transition from observables of canonical neutron stars, *Phys. Rev. C* 103 (3) (2021) 035802. [arXiv:2009.13653](https://arxiv.org/abs/2009.13653), [doi:10.1103/PhysRevC.103.035802](https://doi.org/10.1103/PhysRevC.103.035802).

[623] M. Ferreira, V. Carvalho, C. Providênci, Extracting nuclear matter properties from the neutron star matter equation of state using deep neural networks, *Phys. Rev. D* 106 (10) (2022) 103023. [arXiv:2209.09085](https://arxiv.org/abs/2209.09085), doi: [10.1103/PhysRevD.106.103023](https://doi.org/10.1103/PhysRevD.106.103023).

[624] C. Mondal, F. Gulminelli, Can we decipher the composition of the core of a neutron star?, *Phys. Rev. D* 105 (8) (2022) 083016. [arXiv:2111.04520](https://arxiv.org/abs/2111.04520), doi: [10.1103/PhysRevD.105.083016](https://doi.org/10.1103/PhysRevD.105.083016).

[625] A. Thete, K. Banerjee, T. Malik, Inferring the dense matter equation of state from neutron star observations via artificial neural networks (8 2022). [arXiv:2208.13163](https://arxiv.org/abs/2208.13163).

[626] B. D. Serot, J. D. Walecka, The Relativistic Nuclear Many Body Problem, *Adv. Nucl. Phys.* 16 (1986) 1–327.

[627] M. Oertel, M. Hempel, T. Klähn, S. Typel, Equations of state for supernovae and compact stars, *Rev. Mod. Phys.* 89 (1) (2017) 015007. [arXiv:1610.03361](https://arxiv.org/abs/1610.03361), doi: [10.1103/RevModPhys.89.015007](https://doi.org/10.1103/RevModPhys.89.015007).

[628] S. Huth, et al., Constraining Neutron-Star Matter with Microscopic and Macroscopic Collisions, *Nature* 606 (2022) 276–280. [arXiv:2107.06229](https://arxiv.org/abs/2107.06229), doi: [10.1038/s41586-022-04750-w](https://doi.org/10.1038/s41586-022-04750-w).

[629] A. Sorensen, et al., Dense Nuclear Matter Equation of State from Heavy-Ion Collisions (1 2023). [arXiv:2301.13253](https://arxiv.org/abs/2301.13253).

[630] T. Demircik, C. Ecker, M. Järvinen, Dense and Hot QCD at Strong Coupling, *Phys. Rev. X* 12 (4) (2022) 041012. [arXiv:2112.12157](https://arxiv.org/abs/2112.12157), doi: [10.1103/PhysRevX.12.041012](https://doi.org/10.1103/PhysRevX.12.041012).

[631] S. Shirke, S. Ghosh, D. Chatterjee, Constraining the equation of state of hybrid stars using recent information from multidisciplinary physics (10 2022). [arXiv:2210.09077](https://arxiv.org/abs/2210.09077).

[632] F. Sammarruca, R. Millerson, Nuclear Forces in the Medium: Insight From the Equation of State, *Front. in Phys.* 7 (2019) 213. doi: [10.3389/fphy.2019.00213](https://doi.org/10.3389/fphy.2019.00213).

[633] C. Drischler, W. Haxton, K. McElvain, E. Mereghetti, A. Nicholson, P. Vranas, A. Walker-Loud, Towards grounding nuclear physics in QCD, *Prog. Part. Nucl. Phys.* 121 (2021) 103888. [arXiv:1910.07961](https://arxiv.org/abs/1910.07961), doi: [10.1016/j.ppnp.2021.103888](https://doi.org/10.1016/j.ppnp.2021.103888).

[634] C. Drischler, R. J. Furnstahl, J. A. Melendez, D. R. Phillips, How Well Do We Know the Neutron-Matter Equation of State at the Densities Inside Neutron Stars? A Bayesian Approach with Correlated Uncertainties, *Phys. Rev. Lett.* 125 (20) (2020) 202702. [arXiv:2004.07232](https://arxiv.org/abs/2004.07232), doi: [10.1103/PhysRevLett.125.202702](https://doi.org/10.1103/PhysRevLett.125.202702).

[635] C. Drischler, J. A. Melendez, R. J. Furnstahl, D. R. Phillips, Quantifying uncertainties and correlations in the nuclear-matter equation of state, *Phys. Rev. C* 102 (5) (2020) 054315. [arXiv:2004.07805](https://arxiv.org/abs/2004.07805), doi: [10.1103/PhysRevC.102.054315](https://doi.org/10.1103/PhysRevC.102.054315).

[636] T. Malik, M. Ferreira, B. K. Agrawal, C. Providênci, Relativistic Description of Dense Matter Equation of State and Compatibility with Neutron Star Observables: A Bayesian Approach, *Astrophys. J.* 930 (1) (2022) 17. [arXiv:2201.12552](https://arxiv.org/abs/2201.12552), doi: [10.3847/1538-4357/ac5d3c](https://doi.org/10.3847/1538-4357/ac5d3c).

[637] Z. Zhu, A. Li, T. Liu, A Bayesian inference of relativistic mean-field model for neutron star matter from observation of NICER and GW170817/AT2017gfo (11 2022). [arXiv:2211.02007](https://arxiv.org/abs/2211.02007).

[638] X. Sun, Z. Miao, B. Sun, A. Li, Astrophysical Implications on Hyperon Couplings and Hyperon Star Properties with Relativistic Equations of States, *Astrophys. J.* 942 (1) (2023) 55. [arXiv:2205.10631](https://arxiv.org/abs/2205.10631), [doi:10.3847/1538-4357/ac9d9a](https://doi.org/10.3847/1538-4357/ac9d9a).

[639] A. Lovato, et al., Long Range Plan: Dense matter theory for heavy-ion collisions and neutron stars (11 2022). [arXiv:2211.02224](https://arxiv.org/abs/2211.02224).

[640] A. Kurkela, P. Romatschke, A. Vuorinen, Cold Quark Matter, *Phys. Rev. D* 81 (2010) 105021. [arXiv:0912.1856](https://arxiv.org/abs/0912.1856), [doi:10.1103/PhysRevD.81.105021](https://doi.org/10.1103/PhysRevD.81.105021).

[641] T. Gorda, O. Komoltsev, A. Kurkela, Ab-initio QCD calculations impact the inference of the neutron-star-matter equation of state (4 2022). [arXiv:2204.11877](https://arxiv.org/abs/2204.11877).

[642] T. Gorda, K. Hebeler, A. Kurkela, A. Schwenk, A. Vuorinen, Constraints on strong phase transitions in neutron stars (12 2022). [arXiv:2212.10576](https://arxiv.org/abs/2212.10576).

[643] R. Abbott, et al., Open data from the first and second observing runs of Advanced LIGO and Advanced Virgo, *SoftwareX* 13 (2021) 100658. [arXiv:1912.11716](https://arxiv.org/abs/1912.11716), [doi:10.1016/j.softx.2021.100658](https://doi.org/10.1016/j.softx.2021.100658).

[644] R. Abbott, et al., Open data from the third observing run of LIGO, Virgo, KAGRA and GEO (2 2023). [arXiv:2302.03676](https://arxiv.org/abs/2302.03676).

[645] A. Bogatskiy, B. Anderson, J. T. Offermann, M. Roussi, D. W. Miller, R. Kondor, Lorentz group equivariant neural network for particle physics, in: Proceedings of the 37th International Conference on Machine Learning, ICML'20, JMLR.org, 2020.

[646] P. Onyisi, D. Shen, J. Thaler, Comparing Point Cloud Strategies for Collider Event Classification (12 2022). [arXiv:2212.10659](https://arxiv.org/abs/2212.10659).

[647] D. Bachtis, G. Aarts, F. Di Renzo, B. Lucini, Inverse Renormalization Group in Quantum Field Theory, *Phys. Rev. Lett.* 128 (8) (2022) 081603. [arXiv:2107.00466](https://arxiv.org/abs/2107.00466), [doi:10.1103/PhysRevLett.128.081603](https://doi.org/10.1103/PhysRevLett.128.081603).

[648] K. Shiina, H. Mori, Y. Tomita, H. K. Lee, Y. Okabe, Inverse renormalization group based on image super-resolution using deep convolutional networks, *Sci. Rep.* 11 (1) (2021) 9617. [arXiv:2104.04482](https://arxiv.org/abs/2104.04482), [doi:10.1038/s41598-021-88605-w](https://doi.org/10.1038/s41598-021-88605-w).

[649] V. Dumoulin, F. Visin, A guide to convolution arithmetic for deep learning, arXiv e-prints (2016) arXiv:1603.07285 [arXiv:1603.07285](https://arxiv.org/abs/1603.07285), [doi:10.48550/arXiv.1603.07285](https://doi.org/10.48550/arXiv.1603.07285).

[650] A. Georges, G. Kotliar, W. Krauth, M. J. Rozenberg, Dynamical mean-field theory of strongly correlated fermion systems and the limit of infinite dimensions, *Rev. Mod. Phys.* 68 (1996) 13–125. [doi:10.1103/RevModPhys.68.13](https://doi.org/10.1103/RevModPhys.68.13).

[651] K. Hashimoto, S. Sugishita, A. Tanaka, A. Tomiya, Deep learning and the AdS/CFT correspondence, *Phys. Rev. D* 98 (4) (2018) 046019. [arXiv:1802.08313](https://arxiv.org/abs/1802.08313), [doi:10.1103/PhysRevD.98.046019](https://doi.org/10.1103/PhysRevD.98.046019).

[652] K. Hashimoto, AdS/CFT correspondence as a deep Boltzmann machine, *Phys. Rev. D* 99 (10) (2019) 106017. [doi:10.1103/PhysRevD.99.106017](https://doi.org/10.1103/PhysRevD.99.106017).

[653] K. Hashimoto, K. Ohashi, T. Sumimoto, Deriving the dilaton potential in improved holographic QCD from the meson spectrum, *Phys. Rev. D* 105 (10) (2022) 106008. [arXiv:2108.08091](https://arxiv.org/abs/2108.08091), [doi:10.1103/PhysRevD.105.106008](https://doi.org/10.1103/PhysRevD.105.106008).

[654] J. M. Maldacena, The Large N limit of superconformal field theories and supergravity, *Adv. Theor. Math. Phys.* 2 (1998) 231–252. [arXiv:hep-th/9711200](https://arxiv.org/abs/hep-th/9711200), [doi:10.1023/A:1026654312961](https://doi.org/10.1023/A:1026654312961).

[655] S. S. Gubser, I. R. Klebanov, A. M. Polyakov, Gauge theory correlators from noncritical string theory, *Phys. Lett. B* 428 (1998) 105–114. [arXiv:hep-th/9802109](https://arxiv.org/abs/hep-th/9802109), [doi:10.1016/S0370-2693\(98\)00377-3](https://doi.org/10.1016/S0370-2693(98)00377-3).

[656] E. Witten, Anti-de Sitter space and holography, *Adv. Theor. Math. Phys.* 2 (1998) 253–291. [arXiv:hep-th/9802150](https://arxiv.org/abs/hep-th/9802150), [doi:10.4310/ATMP.1998.v2.n2.a2](https://doi.org/10.4310/ATMP.1998.v2.n2.a2).

[657] P. Mehta, D. J. Schwab, An exact mapping between the variational renormalization group and deep learning, arXiv preprint [arXiv:1410.3831](https://arxiv.org/abs/1410.3831) (2014).

[658] K. Hashimoto, H.-Y. Hu, Y.-Z. You, Neural ordinary differential equation and holographic quantum chromodynamics, *Mach. Learn. Sci. Tech.* 2 (3) (2021) 035011. [arXiv:2006.00712](https://arxiv.org/abs/2006.00712), [doi:10.1088/2632-2153/abe527](https://doi.org/10.1088/2632-2153/abe527).

[659] L. Del Debbio, S. Forte, J. I. Latorre, A. Piccione, J. Rojo, Neural network determination of parton distributions: The Nonsinglet case, *JHEP* 03 (2007) 039. [arXiv:hep-ph/0701127](https://arxiv.org/abs/hep-ph/0701127), [doi:10.1088/1126-6708/2007/03/039](https://doi.org/10.1088/1126-6708/2007/03/039).

[660] R. D. Ball, V. Bertone, F. Cerutti, L. Del Debbio, S. Forte, A. Guffanti, N. P. Hartland, J. I. Latorre, J. Rojo, M. Ubiali, Reweighting and Unweighting of Parton Distributions and the LHC W lepton asymmetry data, *Nucl. Phys. B* 855 (2012) 608–638. [doi:10.1016/j.nuclphysb.2011.10.018](https://doi.org/10.1016/j.nuclphysb.2011.10.018).

[661] R. D. Ball, V. Bertone, F. Cerutti, L. Del Debbio, S. Forte, A. Guffanti, J. I. Latorre, J. Rojo, M. Ubiali, Unbiased global determination of parton distributions and their uncertainties at NNLO and at LO, *Nucl. Phys. B* 855 (2012) 153–221. [doi:10.1016/j.nuclphysb.2011.09.024](https://doi.org/10.1016/j.nuclphysb.2011.09.024).

[662] E. R. Nocera, R. D. Ball, S. Forte, G. Ridolfi, J. Rojo, A first unbiased global determination of polarized PDFs and their uncertainties, *Nucl. Phys. B* 887 (2014) 276–308. [doi:10.1016/j.nuclphysb.2014.08.008](https://doi.org/10.1016/j.nuclphysb.2014.08.008).

[663] F.-P. Li, H.-L. Lü, L.-G. Pang, G.-Y. Qin, Deep-learning quasi-particle masses from QCD equation of state (11 2022). [arXiv:2211.07994](https://arxiv.org/abs/2211.07994).

[664] D. Lafferty, A. Rothkopf, Improved Gauss law model and in-medium heavy quarkonium at finite density and velocity, *Phys. Rev. D* 101 (5) (2020) 056010. [arXiv:1906.00035](https://arxiv.org/abs/1906.00035), [doi:10.1103/PhysRevD.101.056010](https://doi.org/10.1103/PhysRevD.101.056010).

[665] S. Shi, K. Zhou, J. Zhao, S. Mukherjee, P. Zhuang, Heavy quark potential in the quark-gluon plasma: Deep neural network meets lattice quantum chromodynamics, *Phys. Rev. D* 105 (1) (2022) 014017. [arXiv:2105.07862](https://arxiv.org/abs/2105.07862), [doi:10.1103/PhysRevD.105.014017](https://doi.org/10.1103/PhysRevD.105.014017).

[666] H. Satz, Colour deconfinement and quarkonium binding, *J. Phys. G* 32 (2006) R25. [arXiv:hep-ph/0512217](https://arxiv.org/abs/hep-ph/0512217), [doi:10.1088/0954-3899/32/3/R01](https://doi.org/10.1088/0954-3899/32/3/R01).

[667] X. Guo, S. Shi, P. Zhuang, Relativistic Correction to Charmonium Dissociation Temperature, *Phys. Lett. B* 718 (2012) 143–146. [arXiv:1209.5873](https://arxiv.org/abs/1209.5873), [doi:10.1016/j.physletb.2012.10.032](https://doi.org/10.1016/j.physletb.2012.10.032).

[668] R. Narayan, R. Nityananda, Maximum entropy image restoration in astronomy, *Ann. Rev. Astron. Astrophys.* 24 (1986) 127–170. [doi:10.1146/annurev.aa.24.090186.001015](https://doi.org/10.1146/annurev.aa.24.090186.001015).

[669] M. Jarrell, J. E. Gubernatis, Bayesian inference and the analytic continuation of imaginary-time quantum Monte Carlo data, *Phys. Rept.* 269 (1996) 133–195. [doi:10.1016/0370-1573\(95\)00074-7](https://doi.org/10.1016/0370-1573(95)00074-7).

[670] R. Fournier, L. Wang, O. V. Yazyev, Q. Wu, Artificial Neural Network Approach to the Analytic Continuation Problem, *Physical Review Letter* 124 (5) (2020) 056401. [doi:10.1103/PhysRevLett.124.056401](https://doi.org/10.1103/PhysRevLett.124.056401).

[671] H. Li, J. Schwab, S. Antholzer, M. Haltmeier, NETT: solving inverse problems with deep neural networks, *Inverse Problems* 36 (6) (2020) 065005. [doi:10.1088/1361-6420/ab6d57](https://doi.org/10.1088/1361-6420/ab6d57).

[672] W.-B. He, Y.-G. Ma, L.-G. Pang, H. Song, K. Zhou, High energy nuclear physics meets Machine Learning (3 2023). [arXiv:2303.06752](https://arxiv.org/abs/2303.06752).

[673] P. Calafiura, D. Rousseau, K. Terao (Eds.), *Artificial Intelligence for High Energy Physics*, World Scientific, 2022. [doi:10.1142/12200](https://doi.org/10.1142/12200).

[674] M. S. Neubauer, A. Roy, Explainable AI for High Energy Physics, in: 2022 Snowmass Summer Study, 2022. [arXiv:2206.06632](https://arxiv.org/abs/2206.06632).

[675] K. Cranmer, J. Brehmer, G. Louppe, The frontier of simulation-based inference, *Proc. Nat. Acad. Sci.* 117 (48) (2020) 30055–30062. [arXiv:1911.01429](https://arxiv.org/abs/1911.01429), [doi:10.1073/pnas.1912789117](https://doi.org/10.1073/pnas.1912789117).